Imperial College London

Aerodynamic Optimisation of Aerofoils for Martian Rotorcraft using Direct Numerical Simulations

---

By

Lidia Caros Roca

Supervised by

Prof Peter Vincent and Prof Oliver Buxton

Thesis submitted in part fulfilment of the requirements for the degree of Doctor of Philosophy in Aeronautics of Imperial College London

Department of Aeronautics

Faculty of Engineering

Imperial College London

August 2024

Declaration of Originality

I hereby declare that all the work and material presented in this thesis is composed and reported as my own. All information and data obtained from external sources are properly acknowledged and cited in text with the full list of references given in the final bibliography section.

Lidia Caros Roca

Copyright Declaration

The copyright of this thesis rests with the author. Unless otherwise indicated, its contents are licensed under a Creative Commons Attribution-Non Commercial 4.0 International Licence (CC BY-NC).

Under this licence, you may copy and redistribute the material in any medium or format. You may also create and distribute modified versions of the work. This is on the condition that: you credit the author and do not use it, or any derivative works, for a commercial purpose.

When reusing or sharing this work, ensure you make the licence terms clear to others by naming the licence and linking to the licence text. Where a work has been adapted, you should indicate that the work has been changed and describe those changes.

Please seek permission from the copyright holder for uses of this work that are not included in this licence or permitted under UK Copyright Law.

Acknowledgements

I would like to take this opportunity to acknowledge several people who have supported me throughout my PhD journey.

Firstly, I express my deepest gratitude to my supervisors, Prof Peter Vincent and Prof Oliver Buxton. Their invaluable technical advice and personal guidance have been crucial to my development, helping me achieve and surpass the goals of my PhD. Their constant support and understanding have been indispensable throughout this process.

I must also acknowledge the EPSRC for funding my PhD through Grant No. EP/R030340/1, which provided essential financial support during this period. Additionally, I am sincerely grateful for the Amelia Earhart Fellowship and the Vertical Flight Foundation Scholarship. These contributions have facilitated my participation in various conferences, including VFS Forum 78, VFS Forum 79, ICCFD11, PASC23 and AIAA SciTech 2024, and have allowed me to participate in invaluable meetings at NASA Ames and Tohoku University.

I would like to extend my heartfelt gratitude to the ROAMX team at NASA Ames, including Witold Koning, Haley Cummings, and Natalia Perez Perez, as well as the Mars Wind Tunnel team in Japan, including Prof Taku Nonomura, Dr Takayuki Nagata, Yudai Kanzaki, Miku Kasai, and Miyagi Muku. Their unwavering kindness and generosity throughout our collaboration have been inspiring, particularly in hosting us at their institutions and fostering an environment of mutual learning and cooperation.

I am profoundly grateful for the friendships I have formed during this shared PhD experience, they have been my anchor during my time at Imperial. They have shown me persistent support and encouraged me to reach further. I would like to express my sincere thanks to Filippo, Francisco, Josephine, Steffi, Kazuki, Grace, Maria, Henrik, Chi Hin, Nicola, and especially Christian, who has consistently accompanied me through this journey, supporting me through difficulties and celebrating my achievements.

Lastly, I want to express my gratitude to my mother and sister, who continue to inspire me with their bravery, resilience, and perseverance. This thesis is dedicated to my late father, whose memory encourages me every day.

Abstract

Martian conditions present unique challenges for rotorcraft design due to the planet's lower atmospheric density and lower speed of sound compared to Earth. Consequently, Martian rotorcraft blades operate in a low-Reynolds-number compressible flow regime, a relatively unexplored domain atypical for terrestrial helicopters. Non-conventional aerofoils with sharp edges and flat surfaces have demonstrated improved performance under these conditions, inducing earlier separation and unsteady vortex roll-up on the suction side. Several studies have performed optimisation using Reynolds-Averaged Navier-Stokes (RANS) and Unsteady RANS (URANS) solvers. However, given the unsteady, vortex-dominated, and transitional nature of the flow, RANS/URANS solvers have limited predictive capability. This thesis overcomes these limitations by employing high-order accurate Direct Numerical Simulations (DNS) via PyFR to optimise aerofoils for Martian rotorcraft. First, DNS results are compared against experimental data, contributing to the understanding of Martian aerodynamics and demonstrating the utility of DNS in accurately resolving Martian flow over triangular aerofoils. Next, DNS shape optimisation of triangular aerofoils maximising lift and minimising drag is performed, revealing optimised aerofoils that achieve up to a 48% increase in lift or a 28% reduction in drag compared to a reference aerofoil previously studied experimentally. Flow characteristics of optimal aerofoils are analysed to elucidate flow physics that yield optimal performance. The sensitivity of these optimal aerofoils to free-stream perturbations is then explored by injecting eddies upstream of the aerofoils. Findings show that such disturbances lead to a breakdown of coherent vortices and a reduction in aerodynamic forces. This motivates an optimisation that includes free-stream eddies, revealing that optimal aerofoil shapes are sensitive to free-stream conditions. The work in this thesis constitutes the first use of DNS for aerodynamic shape optimisation.

Contents

1 Introduction **1**

1.1 Motivation 1

1.2 Objectives 4

1.3 Thesis Outline 5

1.4 Publications 6

1.4.1 International Journals 6

1.4.2 International Conferences 7

1.4.3 Online Seminars 7

1.5 Scholarships and Awards received during the PhD 7

2 Literature Review **8**

2.1 Martian Aerodynamics 8

2.1.1 Sub-Critical Regime on Conventional Aerofoils 9

2.1.2 Sharp Leading Edge Aerofoils 11

2.1.3 Previous Experimental and Numerical Studies 12

2.2 Aerodynamic Shape Optimisation of Aerofoils for Martian Rotorcraft 15

2.3 Novelty of this Research 16

3 Numerical Methods **17**

3.1 Direct Numerical Simulations with PyFR 18

3.1.1 Flux Reconstruction Approach 18

3.1.2 Governing Equations 22

3.1.3 Synthetic Eddy Method 23

3.1.4 Simulation Setup 26

3.2 Multi-Objective Genetic Algorithm Optimisation with `pymoo` 26

3.2.1 Genetic Algorithms 27

3.2.2 Optimisation Process 28

4 Direct Numerical Simulations of a Triangular Aerofoil under Martian Conditions 32

4.1 Test Case 33

4.2 Effects of Domain Span 35

4.2.1 Overview 35

4.2.2 Setup 35

4.2.3 Results 38

4.3 Effects of Wind Tunnel Walls 41

4.3.1 Overview 41

4.3.2 Setup 44

4.3.3 Results 46

4.4 Summary 55

5 Optimisation of Aerofoils for Martian Rotorcraft using Direct Numerical Simulations and Genetic Algorithms **56**

5.1 Methodology 57

5.1.1 Optimisation 57

5.1.2 Evaluation 58

5.2 Comparison of 2D DNS vs 3D DNS as Evaluation 61

5.2.1 Low Angle of Attack, $\alpha = 6^\circ$ 62

5.2.2 High Angle of Attack, $\alpha = 12^\circ$ 67

5.3 Optimisation Results at $\alpha = 12^\circ$ using 3D DNS 73

5.3.1 Optimal Aerofoils 73

5.3.2 Q-criterion Isosurfaces and Lift Time Series 74

5.3.3 Pressure Coefficient Distribution 76

5.3.4 Velocity Line Integral Convolutions (LICs) and Skin Friction Distribution . . . 78

5.4 Summary 80

6 Effects of Free-Stream Eddies on Genetic Algorithm Optimisation of Aerofoils for Martian Rotorcraft using Direct Numerical Simulations 83

6.1 Methodology 84

6.2 Effects of Free-Stream Eddies on Optimised Aerofoils from 3D-DNS-12_{2DS} 85

6.2.1 Aerodynamic Performance 86

6.2.2 Q-criterion Isosurfaces and Lift Time Series 88

6.2.3 Pressure Coefficient Distribution 93

6.2.4 Skin Friction Distribution 95

6.2.5 Outcomes 97

6.3 Optimisation with Free-Stream Eddies 97

6.3.1 Optimal Aerofoils 98

6.3.2 Instantaneous Density Gradient and Static Pressure 101

6.3.3 Time-Averaged Pressure Coefficient on the Surface 102

6.3.4 Q-criterion Isosurfaces and Lift Time Series 103

6.3.5 Velocity Line Integral Convolutions (LICs) and Skin Friction Distribution . . . 105

6.4 Summary 107

7 Conclusions and Future Work **109**

7.1 Conclusions 109

7.2 Future Work 113

7.2.1 Discrepancies between the Virtual Wind Tunnel DNS and Associated Mars Wind Tunnel Data 113

7.2.2 Acceleration Techniques for DNS Optimisation 116

7.2.3 Multi-Point Optimisation 118

7.2.4 Increased Design Complexity 118

Bibliography **119**

List of Figures

1.1 Artist's impression of the NASA Ingenuity Helicopter (a) and the NASA Sample Recovery Helicopter (b). Source: NASA. 2

2.1 Plot of density gradient from a DNS with PyFR showing the vortex roll-up due to the Kelvin-Helmholtz (K-H) instability of a separated shear layer from a sharp-leading-edge aerofoil. 11

2.2 Imperial College London team, consisting of Prof Peter Vincent, Prof Oliver Buxton and Lidia Caros (author) visiting and discussing the Mars Wind Tunnel experiments at Tohoku University, Japan, in collaboration with the ROAMX team from NASA Ames, consisting of Haley Cummings, Witold Koning and Natalia Perez Perez, and the experimental team at Tohoku University, consisting of Associate Prof Taku Nonomura, Dr Takayuki Nagata, Yudai Kanzaki, Miku Kasai and Miyagi Muku. 13

3.1 Flowchart of the optimisation process. 29

4.1 Schematic of the Reference aerofoil studied experimentally and numerically by Munday et al. [15] and used as validation case. 34

4.2 View of mesh in the streamwise-vertical xy-plane used for 2D and span-wise periodic 3D DNS with $\alpha = 12^\circ$ of the Reference aerofoil. The origin in the streamwise-vertical xy-plane is located at the leading edge of the aerofoil when $\alpha = 0^\circ$. 37

4.3 Plots of Δ/η in the mid-span plane as a function of y at $x = 3$, $x = 5$ and $x = 7$ (a) and as a function of x at $y = 0.2$ (b) for span-wise periodic 3D DNS with $\alpha = 15^\circ$ and $\delta_z = 0.9$ of the Reference aerofoil. 38

4.4 Plots of time-averaged lift coefficient $\overline{C}_L$ (a) and drag coefficient $\overline{C}_D$ (b) as a function of angle of attack α obtained from the MWT experiments of Munday et al. [15], span-wise periodic DNS with $\delta_z = 0.3$ of Munday et al. [15], 2D DNS using PyFR, span-wise periodic DNS with $\delta_z = 0.3$, $\delta_z = 0.6$, $\delta_z = 0.9$ using PyFR, and DNS in a virtual wind tunnel using PyFR. 39

4.5 Plots of pressure coefficient $\overline{C}_P$ as a function of $\tilde{x}$ for angles of attack $\alpha = 6^\circ$ (a) and $\alpha = 12^\circ$ (b) on the suction surface of the aerofoil obtained from the MWT experiments of Munday et al. [15], span-wise periodic DNS with $\delta_z = 0.3$ of Munday et al. [15], 2D DNS using PyFR, span-wise periodic DNS with $\delta_z = 0.3$, $\delta_z = 0.6$, $\delta_z = 0.9$ using PyFR, and DNS in a virtual wind tunnel using PyFR. 41

4.6 Images of instantaneous Q-criterion isosurfaces $Q = 1$, coloured by velocity magnitude $|v|$, for $\alpha = 12^\circ$ when $\delta_z = 0.3$ (a), (b) and (c), and $\delta_z = 0.9$ (d), (e) and (f), at different points in the shedding cycle: maximum lift (a) and (d), intermediate lift (b) and (e), and minimum lift (c) and (f). 42

4.7 Images of instantaneous density gradient magnitude $|\nabla\rho|$, at the instant of maximum lift in a specific shedding cycle, for $\alpha = 12^\circ$ when $\delta_z = 0.3$ (a), (b) and (c), and $\delta_z = 0.9$ (d), (e) and (f), in different y-z planes: (a) and (d) show a plane at the trailing edge, (b) and (e) show a plane half a chord downstream from the trailing edge, and (c) and (f) show a plane one chord downstream from the trailing edge. Note that for the case with $\delta_z = 0.3$ the periodic data is repeated three times to facilitate comparison with the $\delta_z = 0.9$ case. 43

4.8 View of the computational mesh used for the virtual wind tunnel DNS with $\alpha = 12^\circ$. The origin in the streamwise-vertical xy-plane is located at the leading edge of the aerofoil when $\alpha = 0^\circ$. 45

4.9 Plots of Δ/η in the mid-span plane as a function of y at $x = 3$, $x = 5$ and $x = 7$ (a) and as a function of x at $y = 0.2$ (b) for DNS in a virtual wind tunnel with $\alpha = 15^\circ$. . 46

4.10 Plot of the boundary layer thickness δ_{99} as a function of $\mathbf{x}$ for the virtual wind tunnel DNS with $\alpha = 11^\circ$ on the lower and right-hand-side walls, measured at the mid-span and mid-height respectively, alongside the Blasius laminar boundary layer thickness. . 47

4.11 Plots of $\overline{C}_P$ distribution on the suction surface of the wing obtained by experimental studies of Munday et al. [15] (a) and DNS in a virtual wind tunnel using PyFR (b). . 49

4.12 Images of instantaneous Q-criterion isosurfaces $Q = 1$, coloured by velocity magnitude $|v|$, for angles of attack $\alpha = 6°$ (a) and (b), $\alpha = 8°$ (c) and (d), and $\alpha = 15°$ (e) and (f), from span-wise periodic DNS with span $\delta_z = 0.9$ (a), (c) and (e), and virtual wind tunnel DNS (b), (d) and (f). 50

4.13 Images of time-averaged velocity magnitude $|v|$ in the mid-span plane with superimposed velocity Line Integral Convolutions (LICs) for angles of attack $\alpha = 7°$ (a) and (b), $\alpha = 8°$ (c) and (d), and $\alpha = 9°$ (e) and (f), from span-wise periodic DNS with span $\delta_z = 0.9$ (a), (c) and (e), and virtual wind tunnel DNS (b), (d) and (f). 51

4.14 Images of time-averaged wall shear stress magnitude $|\tau|$ on the suction surface of the aerofoil with superimposed time-averaged wall shear stress Line Integral Convolutions (LICs) for angles of attack $\alpha = 7°$ (a), $\alpha = 8°$ (b), and $\alpha = 9°$ (c) from virtual wind tunnel DNS. 52

4.15 Plots of friction coefficient $\overline{C}_f$ on the suction surface of the aerofoil in the mid-span plane as a function of $\tilde{x}$ for angles of attack $\alpha = 7°$ (a), $\alpha = 8°$ (b), and $\alpha = 9°$ (c) from span-wise periodic DNS with $\delta_z = 0.9$ and virtual wind tunnel DNS. 53

5.1 Triangular aerofoil with design variables x_a and y_a. 57

5.2 C_L as a function of time for a subset of 9 aerofoils from the initial population of the 2D-DNS-12$_{\text{2DS}}$ optimisation. The horizontal red line marks $\overline{C}_L$. The vertical dotted lines mark the start and end of the Data Extraction Period. 59

5.3 Plots of Δ/η in the mid-span plane as a function of y at $x = 3$, $x = 5$ and $x = 7$ (a) and as a function of x at $y = 0.2$ (b) for a representative Pareto optimal aerofoil from 3D-DNS-12$_{\text{2DS}}$ (Group 1). 60

5.4 Plots of Δ/η in the mid-span plane as a function of y at $x = 3$, $x = 5$ and $x = 7$ (a) and as a function of x at $y = 0.2$ (b) for a representative Pareto optimal aerofoil from 3D-DNS-12$_{\text{2DS}}$ (Group 2). 60

5.5 Plots of Δ/η in the mid-span plane as a function of y at $x = 3$, $x = 5$ and $x = 7$ (a) and as a function of x at $y = 0.2$ (b) for a representative Pareto optimal aerofoil from 3D-DNS-12_{2DS} (Group 3). 61

5.6 Plots of Δ/η in the mid-span plane as a function of y at $x = 3$, $x = 5$ and $x = 7$ (a) and as a function of x at $y = 0.2$ (b) for a representative Pareto optimal aerofoil from 3D-DNS-12_{2DS} (Group 4). 61

5.7 Normalised hypervolume convergence as a function of the number of generations for 2D-DNS-6_{LHS} (a) and 3D-DNS-6_{LHS} (b). 63

5.8 Design space with plots of x_a, y_a (a) and plots of $\overline{C}_L$, $\overline{C}_D$ (b) for the initial population of 2D-DNS-6_{LHS} and 3D-DNS-6_{LHS}, and the Reference aerofoil at $\alpha = 6°$. 64

5.9 Plots of x_a, y_a for the Pareto optimal aerofoils of 2D-DNS-6_{LHS} and 3D-DNS-6_{LHS}, with the minimum $\overline{C}_D$, maximum $\overline{C}_L/\overline{C}_D$, and maximum $\overline{C}_L$ aerofoils and the Reference aerofoil represented with lines (a). Plots of $\overline{C}_L$, $\overline{C}_D$ (b) for the Pareto optimal aerofoils of 2D-DNS-6_{LHS} and 3D-DNS-6_{LHS}, the Reference aerofoil at $\alpha = 6°$ and 2D-DNS-6_{LHS} Pareto optimal aerofoils run with 3D DNS (b). 65

5.10 Images of time-averaged velocity magnitude in the midspan plane with superimposed velocity line integral convolutions (LICs) on the left (a),(c),(e) and images of instantaneous Q-criterion isosurfaces $Q = 1$, coloured by velocity magnitude $|\mathbf{v}|$, on the right (b),(d),(f) for the Pareto optimal aerofoils with minimum $\overline{C}_D$ (a),(b), maximum $\overline{C}_L/\overline{C}_D$ (c),(d), and maximum $\overline{C}_L$ (e),(f) obtained from 2D-DNS-6_{LHS} run with 3D DNS. . . . 66

5.11 Normalised hypervolume convergence as a function of the number of generations for 2D-DNS-12_{LHS} (a) and 3D-DNS-12_{LHS} (b). Note that 3D-DNS-12_{LHS} does not show convergence and was not run further due to limited resources. 68

5.12 Design space with plots of x_a, y_a (a) and plots of $\overline{C}_L$, $\overline{C}_D$ (b) for the initial population of 2D-DNS-12_{LHS} and 3D-DNS-12_{LHS}, and the Reference aerofoil at $\alpha = 12°$. 69

5.13 Plots of x_a, y_a for the Pareto optimal aerofoils of 2D-DNS-12_{LHS} and 3D-DNS-12_{LHS}, with the minimum $\overline{C}_D$, maximum $\overline{C}_L/\overline{C}_D$, and maximum $\overline{C}_L$ aerofoils and the Reference aerofoil represented with lines (a). Plots of $\overline{C}_L$, $\overline{C}_D$ (b) for the Pareto optimal aerofoils of 2D-DNS-12_{LHS} and 3D-DNS-12_{LHS}, the Reference aerofoil at $\alpha = 12°$ and 2D-DNS-12_{LHS} Pareto optimal aerofoils run with 3D DNS (b). 70

5.14 Images of time-averaged velocity magnitude in the midspan plane with superimposed velocity line integral convolutions (LICs) on the left (a),(c),(e) and images of instantaneous Q-criterion isosurfaces $Q = 1$, coloured by velocity magnitude $|\mathbf{v}|$, on the right (b),(d),(f) for the Pareto optimal aerofoils with minimum $\overline{C}_D$ (a),(b), maximum $\overline{C}_L/\overline{C}_D$ (c),(d), and maximum $\overline{C}_L$ (e),(f) obtained from 3D-DNS-12_{LHS}. 72

5.15 Normalised hypervolume convergence as a function of the number of generations for 3D-DNS-12_{LHS} and 3D-DNS-12_{2DS}. Note that it is normalised by its value at the last generation of 3D-DNS-12_{2DS}. 74

5.16 Plots of x_a, y_a for the initial population (hollow circles), and optimal aerofoils (solid circles), from 3D-DNS-12_{2DS} and the Reference aerofoil (a). Plots of $\overline{C}_L$, $\overline{C}_D$ for the initial population (hollow circles), and optimal aerofoils (solid circles), forming the Pareto front, from 3D-DNS-12_{2DS} and the Reference aerofoil (b). 75

5.17 Instantaneous Q-criterion isosurfaces coloured by velocity magnitude $|v|$ (left), C_L time-series (middle) and C_L spectra (right) for one representative aerofoil of each group on the Pareto front from 3D-DNS-12_{2DS} and the Reference aerofoil. 77

5.18 Plots of mid-span $\overline{C}_p$ distributions on the surface of a representative aerofoil from each group on the Pareto front from 3D-DNS-12_{2DS}, and the Reference aerofoil, as a function of $\tilde{x}$. The dashed lines show the position of the apex for each aerofoil. 78

5.19 Time-averaged velocity magnitude $|v|$ in a span-wise constant plane, with superimposed time-averaged velocity LICs (left), and mid-span $\overline{C}_f$ distributions on the suction surface as a function of $\tilde{x}$ (right), for a representative aerofoil from each group on the Pareto front from 3D-DNS-12_{2DS}, and the Reference aerofoil. The dashed lines show the position of the apex for each aerofoil. 79

6.1 Computational mesh for the Reference aerofoil. The box within which free-stream eddies were injected is shaded red for a specific characteristic length scale of $ls = 0.1$. . 85

6.2 Plots of x_a, y_a for the optimal aerofoils from 3D-DNS-12_{2DS} in grey with one aerofoil representative from each of the groups identified delineated with dashed lines and colours (a). Plots of $\overline{C}_L$, $\overline{C}_D$ (b), (c), (d), (e), (f) for the optimal aerofoils from 3D-DNS-12_{2DS} in grey with values of the representative (coloured) aerofoils under the influence of free-stream eddies with target values of turbulent intensity of TI=1% and TI=0.5% and characteristic length scales of $ls = 0.1$ and $ls = 0.05$. 87

6.3 Instantaneous Q-criterion isosurfaces coloured by velocity magnitude $|v|$ (left), C_L time series (middle) and C_L spectra (right) for different free-stream conditions for the representative aerofoil from Group 1 on the Pareto front from 3D-DNS-12_{2DS}. 89

6.4 Instantaneous Q-criterion isosurfaces coloured by velocity magnitude $|v|$ (left), C_L time series (middle) and C_L spectra (right) for different free-stream conditions for the representative aerofoil from Group 2 on the Pareto front from 3D-DNS-12_{2DS}. 90

6.5 Instantaneous Q-criterion isosurfaces coloured by velocity magnitude $|v|$ (left), C_L time series (middle) and C_L spectra (right) for different free-stream conditions for the representative aerofoil from Group 3 on the Pareto front from 3D-DNS-12_{2DS}. 91

6.6 Instantaneous Q-criterion isosurfaces coloured by velocity magnitude $|v|$ (left), C_L time series (middle) and C_L spectra (right) for different free-stream conditions for the representative aerofoil from Group 4 on the Pareto front from 3D-DNS-12_{2DS}. 92

6.7 Plots of mid-span $\overline{C}_p$ distributions as a function of $\tilde{x}$ on the surface of the representative aerofoil from each group on the Pareto front from 3D-DNS-12_{2DS} when evaluated with uniform inflow as well as when affected by free-stream eddies with different target turbulence intensities, TI, and different target characteristic length scales, ls. 94

6.8 Plots of mid-span $\overline{C}_f$ distributions on the suction surface as a function of $\tilde{x}$ for the representative aerofoils from each group on the Pareto front from 3D-DNS-12_{2DS} when evaluated with uniform inflow as well as when affected by free-stream eddies with different target turbulence intensities, TI, and different target characteristic length scales, ls. 96

6.9 Normalised hypervolume convergence as a function of the number of generations for 3D-DNS-12-FSE_{3DS}. 98

6.10 Plots of x_a, y_a for all tested aerofoils (hollow) and Pareto optimal aerofoils (filled) for 3D-DNS-12_{2DS} (circles) and 3D-DNS-12-FSE_{3DS} (squares) with the minimum $\overline{C}_D$ aerofoil (left), the maximum $\overline{C}_L/\overline{C}_D$ aerofoil (middle) and the maximum $\overline{C}_L$ aerofoil (right) represented with dashed lines (a). Plots of $\overline{C}_L$, $\overline{C}_D$ for all tested aerofoils (hollow) and Pareto optimal aerofoils (filled) for 3D-DNS-12_{2DS} (circles) and 3D-DNS-12-FSE_{3DS} (squares), and 3D-DNS-12_{2DS} Pareto optimal aerofoils run with free-stream eddies (brown squares) and 3D-DNS-12-FSE_{3DS} Pareto optimal aerofoils run with uniform free-stream (magenta circles) (b). 100

6.11 Images of instantaneous density gradient magnitude $|\boldsymbol{\nabla}\rho|$ (left) and instantaneous static pressure p (right) for three aerofoils on the Pareto front from 3D-DNS-12-FSE_{3DS} (a), (c) and (e), and three from 3D-DNS-12_{2DS} (b), (d) and (f). 102

6.12 Plots of mid-span $\overline{C}_p$ distributions on the surface of three aerofoils on the Pareto front from 3D-DNS-12-FSE_{3DS} and three from 3D-DNS-12_{2DS} as a function of $\tilde{x}$. 103

6.13 Instantaneous Q-criterion isosurfaces coloured by velocity magnitude $|v|$ (left) and lift time series C_L (right) for three aerofoils on the Pareto front from 3D-DNS-12-FSE_{3DS} (a), (c) and (e), and three from 3D-DNS-12_{2DS} (b), (d) and (f). 104

6.14 Time-averaged velocity magnitude $|v|$ in a span-wise constant plane, with superimposed time-averaged velocity LICs for three aerofoils on the Pareto front from 3D-DNS-12-FSE_{3DS} (a), (c) and (e), and three from 3D-DNS-12_{2DS} (b), (d) and (f). 105

6.15 Plots of mid-span $\overline{C}_f$ distributions on the suction surface of three aerofoils on the Pareto front from 3D-DNS-12-FSE_{3DS} and three from 3D-DNS-12_{2DS} as a function of $\tilde{x}$. . . 106

7.1 Plots of time-averaged lift coefficient $\overline{C}_L$ (a) and drag coefficient $\overline{C}_D$ (b) as a function of angle of attack α showing the data presented in Chapter 4 Figure 4.4 including DNS of the triangular aerofoil with rounded leading and trailing edges in a virtual wind tunnel using PyFR. 114

7.2 Plots of time-averaged lift coefficient $\overline{C}_L$ (a) and drag coefficient $\overline{C}_D$ (b) as a function of angle of attack α showing the data presented in Chapter 4 Figure 4.4 including DNS of the triangular aerofoil with periodic boundary conditions at the sides and a span of 0.6 chords using PyFR with injected free-stream eddies of various turbulence intensities and characteristic length scales. 115

7.3 IGD+ metric as a function of DNS evaluations comparing the convergence of DNS-based optimisation against surrogate-assisted optimisation DNS infill. 118

List of Tables

5.1 Flow characteristics associated with each of the four distinct groups of aerofoils on the Pareto front from 3D-DNS-12_{2DS}, and flow characteristics associated with the Reference aerofoil. 76

Nomenclature

α	Angle of attack
Δ	Estimate of the local solution point spacing, $\frac{\sqrt[3]{V}}{\wp+1}$
δ_v	Local diffusive length scale of a Blasius boundary layer solution
δ_{99}	Boundary layer thickness
η	Kolmogorov length scale, $\left(\frac{\nu^3}{\varepsilon}\right)^{1/4}$
$\mathbf{v}$	Fluid velocity, $\{v_x, v_y, v_z\}$
μ	Dynamic viscosity of the fluid
ν	Kinematic viscosity
ρ	Fluid density
ε	Dissipation rate, $2\nu s_{ij} s_{ij}$
$\wp$	Solution polynomial order for the PyFR simulations
A	Airfoil platform area
a	Speed of sound
c	Characteristic length
C_D	Drag coefficient, $\frac{F_D}{q_\infty A}$
C_L	Lift coefficient, $\frac{F_L}{q_\infty A}$
C_P	Pressure coefficient, $\frac{p-p_\infty}{q_\infty}$
C_{Pa}	Pressure coefficient normalised by the pressure at the apex, $\frac{p-p_a}{q_\infty}$

F_D	Drag force
F_L	Lift force
M	Mach number, $M = \frac{v_\infty}{a}$
p	Static pressure
p_∞	Free-stream static pressure
p_a	Static pressure measured at the apex
p_e	Static pressure measured at the entrance of the test section
p_{Ts}	Total pressure measured in the settling chamber
p_T	Total pressure
q	Dynamic pressure, $\frac{1}{2}\rho u^2$
Re	Reynolds number, $Re = \frac{\rho_\infty c v_\infty}{\mu}$
s_{ij}	Fluctuating rate-of-strain tensor
t_c	Simulation time in convective time units, $\frac{c}{v_\infty}$
t_e	Simulation Data Extraction Period
t_t	Simulation transient period
T_T	Total temperature
V	Local element volume

Chapter 1

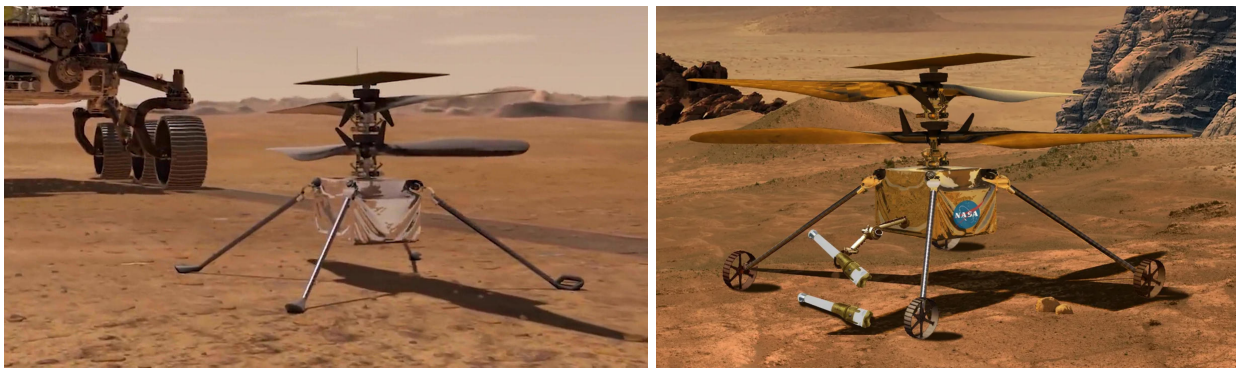
Introduction

1.1 Motivation

Martian aerial exploration offers the potential to revolutionise our understanding of the Red Planet. Numerous advances in Mars exploration have resulted from both in-orbit [1, 2] and ground-based missions [3–8]. Satellite missions, while providing extensive data from orbit, lack the ability to conduct close-up investigations and cannot access specific locations of interest on the Martian surface. Ground-based vehicles, such as rovers, allow for more detailed exploration, being able to take samples from the surface and analyse the atmosphere. However, they are limited by the planet's rocky surface, which can impede mobility and restrict access to scientifically valuable but otherwise inaccessible regions. Additionally, the presence of dust, large boulders, and steep slopes further complicates navigation and increases the risk of mission failure.

Martian aerial vehicles, such as drones and helicopters, can overcome these limitations, providing unprecedented access to diverse geological formations, polar ice caps, and deep canyons. Furthermore, aerial vehicles can cover larger areas in shorter timeframes compared to rovers, significantly enhancing the efficiency of exploration missions. By hovering or landing at points of interest, they can conduct detailed observations and collect high-resolution data from multiple vantage points. Additionally, air vehicles can be equipped with instruments for atmospheric sampling, weather monitoring, and magnetic field studies, complementing the scientific capabilities of ground-based and in-orbit missions and enhancing the safety and success rate of future robotic and human missions.

On April 19, 2021, NASA's Ingenuity Helicopter, shown in Figure 1.1 (a), achieved a historic milestone by performing the first-ever heavier-than-air flight on another planet, in particular, on Mars [9]. This pioneering flight demonstrated the feasibility of aerial exploration on Mars, paving the way for future missions. The next mission in sight is the Mars Sample Return (MSR) mission [10], a collaborative effort between NASA and the European Space Agency (ESA) to bring Martian soil and rock samples back to Earth. Central to this mission is the Sample Recovery Helicopter (SRH) [11], illustrated in Figure 1.1 (b), which will be deployed to retrieve sample containers left on the Martian surface by the Perseverance rover. One or multiple of these helicopters will play a crucial role in transporting the samples to the Mars Ascent Vehicle, which will launch them into orbit for subsequent capture and return to Earth.



(a) (b)

Figure 1.1: Artist's impression of the NASA Ingenuity Helicopter (a) and the NASA Sample Recovery Helicopter (b). Source: NASA.

The conditions under which rotorcraft must operate on Mars present numerous challenges for their design. Mars has a thin atmosphere with a significantly lower density at the surface compared to Earth, about 1% of Earth's air density at sea level, which drastically reduces the performance of conventional blades. Although the gravity on Mars is lower ($g = 3.72\ m/s^2$), this difference does not compensate for the reduced lifting force of the rotorcraft. Additionally, the speed of sound on Mars is approximately 72% of that on Earth due to its low surface temperatures and atmospheric composition, which is predominantly carbon dioxide. This lower speed of sound imposes further constraints on rotor operation, as it results in higher Mach numbers at the blade tip at lower rotational velocities compared to Earth, potentially leading to compressibility effects and shock wave formation. These unique conditions necessitate that Martian rotor blades operate in a low-Reynolds-number compressible flow regime, a relatively unexplored domain due to the absence of similar conditions in

terrestrial applications.

When conventional terrestrial aerofoils are tested under Martian atmospheric conditions, they show a significantly reduced aerodynamic performance since they are not optimised for these conditions. This underscores the need for the development of new aerofoils specifically designed for the Martian atmosphere. Recent studies by Konig et al. [12–14] and Munday et al. [15] have investigated the use of unconventional aerofoils with sharp leading edges and flat surfaces that rely on unsteady lift generation mechanisms. These induce earlier separation compared to conventional aerofoils, leading to an unsteady roll-up of coherent vortices on the suction side of the aerofoil, which improves performance.

Several studies [12,13,16] have explored unconventional aerofoils using Genetic Algorithm (GA) shape optimisations to find optimal designs. Such optimisations involve a high number of evaluations, which, when combined with computationally intensive Computational Fluid Dynamics (CFD) simulations, significantly increase the time required to find optimal shapes. Consequently, it is crucial to solve each geometry with the lowest computational cost possible. These studies employ a Reynolds Averaged Navier-Stokes (RANS) or Unsteady RANS (URANS) approach, which reduces computational costs compared to higher-resolution CFD approaches. However, given the nature of the flow around unconventional aerofoils under Martian conditions — which is unsteady, vortex-dominated, and transitional — RANS/URANS solvers have limited predictive capability, especially at higher angles of attack where the aforementioned flow physics are more acute [14].

The work presented in this thesis overcomes this limitation by optimising Martian aerofoils using high-order accurate Direct Numerical Simulations (DNS) via PyFR [17]. DNS provides a more detailed resolution of the flow field by directly solving the Navier-Stokes equations without any turbulence modelling. This high-fidelity approach is able to accurately capture the complex flow phenomena associated with low-Reynolds-number compressible flows around unconventional sharp-leading-edge aerofoils. The capabilities of PyFR, an open-source Python-based high-order-accurate CFD solver for unstructured grids, enable DNS that are both highly accurate and run efficiently on a range of hardware platforms. Additionally, this research investigates the flow physics associated with unconventional optimal aerofoils, analysing their performance under various conditions to achieve a deeper understanding of this relatively unexplored domain.

The insights gained from this analysis are expected to contribute to the field of Martian rotorcraft

design, ultimately contributing to the development of more efficient aerial vehicles for planetary exploration. Additionally, this work provides a robust framework for optimising aerofoils in other similar flow conditions, benefiting a range of aerospace applications, such as the design of micro-air-vehicle blades or low-pressure turbine blades for commercial jet engines.

1.2 Objectives

Given the unique challenges posed by the Martian atmosphere, it is essential to design efficient aerofoil shapes for Martian rotorcraft to enhance and advance the aerial exploration of Mars. This thesis aims to develop a robust and efficient methodology for optimising aerofoil designs targeting aerodynamic performance under Martian atmospheric conditions, whilst investigating the flow physics of novel unconventional aerofoils through high-fidelity DNS. More specifically, the thesis focuses on the following objectives:

- **Objective 1:** Validate the DNS setup and framework against experimental data to ensure accurate representation of the flow over aerofoils under Martian atmospheric conditions.
- **Objective 2:** Develop an aerodynamic shape optimisation framework by integrating a GA optimisation tool with DNS via PyFR. This includes investigating the most appropriate simulation setup and post-processing in the evaluation step for a cost- and time-effective optimisation.
- **Objective 3:** Identify novel optimal unconventional aerofoil designs through the optimisation framework and thoroughly investigate the flow physics that enhance their performance, comparing them against the flow physics of sub-optimal aerofoils.
- **Objective 4:** Examine the effects of free-stream eddies on the aerodynamic performance of the optimised aerofoil shapes to assess their robustness, and analyse the impact on their flow physics to contribute to the field of Martian aerodynamics.
- **Objective 5:** Find optimal unconventional aerofoil designs under the effects of free-stream eddies and investigate the differences between these designs and those optimised for laminar free-stream conditions, extracting general design conclusions for Martian rotorcraft aerofoil design.

By leveraging high-fidelity simulations via PyFR and optimisation techniques, this research aims to contribute to the advancement of Martian rotorcraft aerofoil design.

1.3 Thesis Outline

This introduction sets the stage by detailing the motivation and objectives of the research. The subsequent chapters will present the state-of-the-art and theoretical foundations that underpin this study. Following this, the main body of the manuscript will present the DNS validation against experimental data, optimisation results, and investigation of the flow physics under different conditions. The thesis will conclude with a discussion of the key findings and directions for future work. A more detailed overview of each chapter is provided below:

- **Chapter 2: Literature Review**

  Chapter 2 provides a comprehensive review of the existing literature relevant to the aerodynamic optimisation of aerofoils for Martian rotorcraft. It includes a discussion on the challenges presented by the Martian atmosphere, previous computational and experimental research on Martian aerodynamics and the state-of-the-art in design optimisation of Martian rotorcraft aerofoils.

- **Chapter 3: Numerical Methods**

  Chapter 3 presents the numerical methods utilised in this thesis for the aerodynamic optimisation of aerofoils for Martian rotorcraft. Two primary methodologies form the backbone of this research: Direct Numerical Simulations (DNS) via PyFR for aerodynamic analysis and Genetic Algorithms (GAs) for design optimisation via `pymoo`.

- **Chapter 4: Direct Numerical Simulations of a Triangular Aerofoil under Martian Conditions**

  Chapter 4 validates the DNS setup by comparing simulation results against published experimental data. It discusses the effects of domain span and wind tunnel walls on the flow physics around a specific triangular aerofoil under Martian conditions.

- **Chapter 5: Optimisation of Aerofoils for Martian Rotorcraft using Direct Numerical Simulations and a Genetic Algorithms**

Chapter 5 presents an optimisation of Martian aerofoils using DNS via PyFR and GAs via `pymoo`. First, it compares the use of two-dimensional and three-dimensional DNS as cost function evaluation for the optimisation at different angles of attack. Next, it focuses on the optimisation results and it analyses the flow physics induced by the optimal aerofoils to understand their enhanced performance.

- **Chapter 6: Effects of Free-Stream Eddies on Genetic Algorithm Optimisation of Aerofoils for Martian Rotorcraft using Direct Numerical Simulations**
  Chapter 6 first examines the impact of free-stream eddies on the performance and flow physics of optimised aerofoils from Chapter 5. Next, it investigates the effect of injecting free-stream eddies when evaluating aerofoils within the optimisation, comparing the resulting optimal aerofoil shapes against results obtained in Chapter 5.

- **Chapter 7: Conclusions and Future Work**
  Chapter 7 summarises the key findings of this research and suggests directions for future work to further advance the field.

1.4 Publications

The list of publications from the author during this period is documented below.

1.4.1 International Journals

- Caros, L., Buxton, O., and Vincent, P., Optimization of Triangular Airfoils for Martian Helicopters using Direct Numerical Simulations, AIAAJ, Vol. 61, No. 11 (2023), pp. 4935-4945 DOI: 10.2514/1.J063164

- Caros, L., Buxton, O., Shigeta, T., Nagata, T., Nonomura, T., Asai, K., and Vincent, P., Direct Numerical Simulation of Flow over a Triangular Airofoil under Martian Conditions, AIAAJ, Vol. 60, No. 7 (2022), pp. 3961-3972 DOI: 10.2514/1.J061454

1.4.2 International Conferences

- Caros, L., Buxton, O., and Vincent, P., The Effects of Free-Stream Eddies on Optimized Martian Rotorcraft Airofoils, AIAA SciTech 2024, Jan 2024.
- Caros, L., Buxton, O., and Vincent, P., Optimization of Non-Conventional Airofoils for Martian Rotorcraft using Direct Numerical Simulations, ICCFD11, July 2022.
- Caros, L., Blank, J., Buxton, O., and Vincent, P., Comparing Strategies for DNS-based Optimization of Airofoils for Martian Rotorcraft, VFS F78, May 2022.

1.4.3 Online Seminars

- Caros, L., DNS-based Optimization of Airofoils for Martian Helicopters using PyFR, PyFR Seminar Series on Cassyni, June 2023, DOI: 10.52843/cassyni.6r5ry1
- Caros, L., Martian Aerodynamics with PyFR, PyFR Seminar Series on Cassyni, May 2021, DOI: 10.52843/47ly7q

1.5 Scholarships and Awards received during the PhD

- NASA Group Achievement Award: Award for contributions to the ROAMX (Rotorcraft Optimization for the Advancement of Mars eXploration) team for developing aerodynamic design technologies for Martian rotorcraft.
- Vertical Flight Foundation Scholarship: Award by the Vertical Flight Society Foundation to the world's most talented engineering students interested in vertical flight. Monetary award $5,000.
- Zonta International Amelia Earhart Fellowship: Award for women pursuing a PhD who demonstrate a superior academic record conducting research applied to aerospace engineering or space sciences. Monetary award $10,000.

Chapter 2

Literature Review

This chapter provides a review of the existing literature relevant to the aerodynamic optimisation of aerofoils for Martian rotorcraft. First, an overview of the Martian atmosphere's unique challenges and their implications for rotorcraft design is presented. Following this, the chapter delves into previous experimental and numerical studies related to Martian aerodynamics, including research on both conventional and unconventional aerofoil shapes. Additionally, the state-of-the-art in design optimisation of Martian rotorcraft aerofoils is presented. Finally, the chapter identifies the gaps in the current literature that motivated the work in this thesis and outlines how this work aims to address them.

2.1 Martian Aerodynamics

The Martian atmosphere presents significant challenges for the aerodynamic design of rotorcraft due to its unique flow conditions, which differ markedly from those encountered on Earth. The primary characteristic impacting rotorcraft design is the Martian atmosphere's very low density ($\rho \approx 0.017\,\mathrm{kg/m^3}$) – around 1% of Earth's density at the surface – and pressure ($P \approx 600\,\mathrm{Pa}$) at the surface. These quantities vary through the seasons due to the carbon dioxide freezing at the poles, with the air pressure ranging from 100 Pa to 900 Pa. The very low air density at the surface results in a substantial reduction in rotor lifting force and efficiency, only partially compensated by Mars' lower gravity ($g = 3.71\,\mathrm{m/s^2}$), which is about 38% of Earth's gravity. The lower density of the Martian atmosphere leads to a low Reynolds number flow, involving distinct flow physics compared to those typically studied for terres-

trial helicopters. Furthermore, the Martian atmosphere is composed predominantly of carbon dioxide (95%), with a surface temperature ranging $-163°C$ to $-28°C$, with an average of around $-63°C$. This composition and temperature result in a lower speed of sound ($a \approx 244.2\,\text{m/s}$), about 72% of that on Earth. This lower speed of sound places the rotorcraft flow within a compressible regime, where the Mach number increases rapidly, thereby constraining the rotor's operational speed range to avoid high Mach numbers at the rotor tips. Future Martian rotorcraft are expected to employ a co-axial rotor system with a mass of approximately $m = 1.8$ kg and a rotor diameter of $D = 1.2$ m, with blade chords ranging between 10% and 15% of the rotor radius. These rotors are anticipated to operate at speeds of up to 2,800 RPM. During hover in the Martian atmosphere, the tip speed is estimated to be approximately $V_{tip} = 177$ m/s, with a corresponding tip Mach number of $M_{tip} = 0.76$ [13]. Given the low density of the Martian atmosphere and the aforementioned blade dimensions and speeds, the resulting Reynolds number is significantly lower than in typical terrestrial rotorblade conditions.

The unique combination of low-Reynolds-number and compressible flow conditions on Mars has not been extensively studied compared to more common flow regimes, such as high-Reynolds-number compressible flow or low-Reynolds-number incompressible flow. This results in distinctive aerofoil performance characteristics that differ significantly from conventional aerodynamics.

2.1.1 Sub-Critical Regime on Conventional Aerofoils

The dimensions of future Mars helicopters are planned to be relatively small [11, 13, 16, 18–22], and considering the low density of the Martian atmosphere close to the surface, a low chord-based Reynolds number flow ($Re \approx 10^3$ to 10^4) is expected. An overview of the aerodynamic implications of a low Reynolds number is presented below.

At the considered Reynolds number, conventional aerofoils experience flow in the subcritical regime, where laminar to turbulent transition in the boundary layer does not occur. At higher Reynolds numbers, conventional aerofoils often undergo a laminar to turbulent transition in the boundary layer due to the growth of convective instabilities. This transition enables relatively high lift-to-drag ratios since turbulent boundary layers are more likely to remain attached. A turbulent boundary layer implies higher shear stresses, causing higher friction drag, but also the increase in momentum in the boundary layer prevents separation, and thus prevents an increment of the pressure drag. Conversely,

at lower Reynolds numbers, viscous forces become more dominant relative to inertial forces. This increased dominance of viscous forces reduces flow disturbances, resulting in a delayed or nonexistent transition. The consequent laminar boundary layer tends to suffer from early separation as it can only sustain small adverse pressure gradients [23]. Laminar boundary layers with an early separation provoke a reduced lift, and more importantly, the separated flow significantly increases the pressure drag; altogether making the aerofoil performance drop [24].

The behaviour of the reattachment process following flow separation is crucial to understanding the aerodynamics of aerofoils. Initially, viscous-type Tollmien-Schlichting (T-S) waves dominate the instability leading up to flow separation [25,26]. However, once separation occurs, the shear layer becomes susceptible to inviscid Kelvin-Helmholtz (K-H) instability. The inflectional velocity profile of the separated shear layer induces oscillations that can cause the shear layer to roll up, forming K-H vortices downstream [27, 28]. These vortices may merge through mutual induction, ultimately resulting in large-scale vortex shedding [29].

Laminar separation bubbles (LSBs) play a significant role in the non-linear characteristics of the lift coefficient curves for aerofoils at low Reynolds numbers [26,30]. These bubbles arise when the laminar boundary layer separates due to an adverse pressure gradient, transitions to turbulence, and then reattaches. The process leads to a deviation from the linear lift behavior predicted by Prandtl's thin aerofoil theory, even at small angles of attack.

The position and size of LSBs vary with Reynolds number and angle of attack [31]. At low angles of attack, aerofoils typically exhibit trailing edge separation without reattachment. As angle of attack increases, the adverse pressure gradient intensifies, moving the separation point upstream and promoting earlier transition. When the separation point is sufficiently upstream, the flow transitions to turbulent and reattaches. Further increases in angle of attack shift the separation point towards the leading edge, and at sufficiently high angles of attack, the adverse pressure gradient becomes so strong that the turbulent boundary layer detaches completely, resulting in massive separation and stall [32].

Transition within separation bubbles occurs at much lower Reynolds numbers compared to classical natural transition thresholds [31,33]. While T-S wave amplification is similar to natural transition, the adverse pressure gradient triggers K-H instability in the separated shear layer earlier, causing vortex roll-up and eventual transition to turbulence. The turbulent flow effectively transports momentum

towards the wall, facilitating reattachment of the separation bubble. This reattachment process can exhibit unsteady behavior, known as bubble flapping, where large spanwise structures are shed into the turbulent boundary layer [25, 30, 34].

2.1.2 Sharp Leading Edge Aerofoils

Studies by Munday et al. [15] and Koning et al. [12–14], amongst others, have investigated the use of aerofoils with sharp leading edges and flat surfaces for Martian applications that rely on unsteady lift generation mechanisms. These induce earlier separation compared to conventional aerofoils, leading to an unsteady roll-up of coherent vortices on the suction side of the aerofoil, which improves performance.

When introducing non-conventional aerofoils with sharp leading edges, a higher adverse pressure gradient compared to conventional aerofoils is induced at the leading edge, generating laminar flow destabilisation. This effect, together with the K-H instabilty, cause the roll-up of coherent vortices on the suction side of the aerofoil, without immediate laminar-turbulent transition. This vortex roll-up of the separated shear layer from a sharp-leading-edge aerofoil is shown by a density gradient plot from a DNS with PyFR in Figure 2.1. The wave length of the K-H vortices increases as the Reynolds number decreases. Additionally, at higher angles of attack or at an increased strength of the adverse pressure gradient, the shear layer oscillations occur earlier and stronger with larger observed K-H vortices.

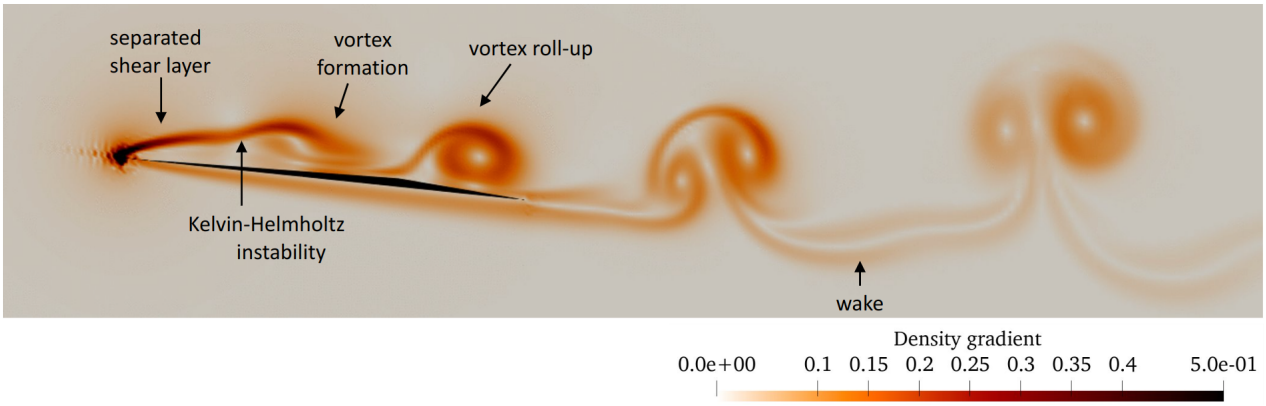


Figure 2.1: Plot of density gradient from a DNS with PyFR showing the vortex roll-up due to the Kelvin-Helmholtz (K-H) instability of a separated shear layer from a sharp-leading-edge aerofoil.

The increased performance for these sharp-leading-edge aerofoils at low Reynolds numbers relies on this roll-up of coherent vortices that mitigate the negative effects of laminar flow separation and generate an area of high suction in the time-averaged sense by the vortices rolling close to the surface.

This lift-generation mechanism differs significantly from the conventional aerofoil flow behavior, where the laminar separation with vortex shedding typically signifies poor aerofoil performance. The sharp leading edge is also a good choice for a Mars rotorcraft as it has shown relative Mach number insensitivity for $0.15 < M_\infty < 0.7$ and stability of the laminar separated shear layer for higher Mach numbers [12, 15].

It is important to point out that the performance of sharp leading edge aerofoils at low Reynolds numbers might be very sensitive to perturbations in the flow, since these can interact with the separated shear layer on which they depend. Several studies [35–37] have investigated the effects of free-stream turbulence on the flow over conventional aerofoils and conclude that under low Reynolds number conditions, the level of turbulence intensity affects the flow characteristics and that higher angles of attack with flow separation are more impacted by free-stream turbulence. Furthermore, in [37], it was concluded that free-stream turbulence can induce transition in the separated shear layer, which may, in turn, induce reattachment. It is understood that the Martian atmosphere is characterised by high levels of free-stream turbulence [38, 39], although very little actual data on the atmospheric turbulent properties has been published. Additionally, there have been no studies about the effect of free-stream turbulence or perturbations in the flow on the performance and flow physics of unconventional Martian aerofoils.

2.1.3 Previous Experimental and Numerical Studies

A small number of wind tunnels have been constructed specifically for Martian atmospheric exploration and research. Most of these facilities primarily focus on geological and planetary studies [40, 41], with only a few dedicated to Martian aerodynamic research. The Mars Wind Tunnel (MWT) at Tohoku University [42], shown in Figure 2.2, substantially enhanced the research of Martian aerodynamics over unconventional aerofoils with its dedicated facility to Martian flows. This facility can simulate low-Reynolds-number compressible flows by placing the induction wind tunnel inside a vacuum chamber. This setup allows for the testing of aerofoil performance using either air or carbon dioxide to replicate Martian atmospheric conditions. Various conventional and unconventional aerofoil shapes have been tested in the MWT, including the NACA0012 aerofoil [43, 44], the Ishii aerofoil [45, 46], flat plates [43] and triangular aerofoils [15, 47].

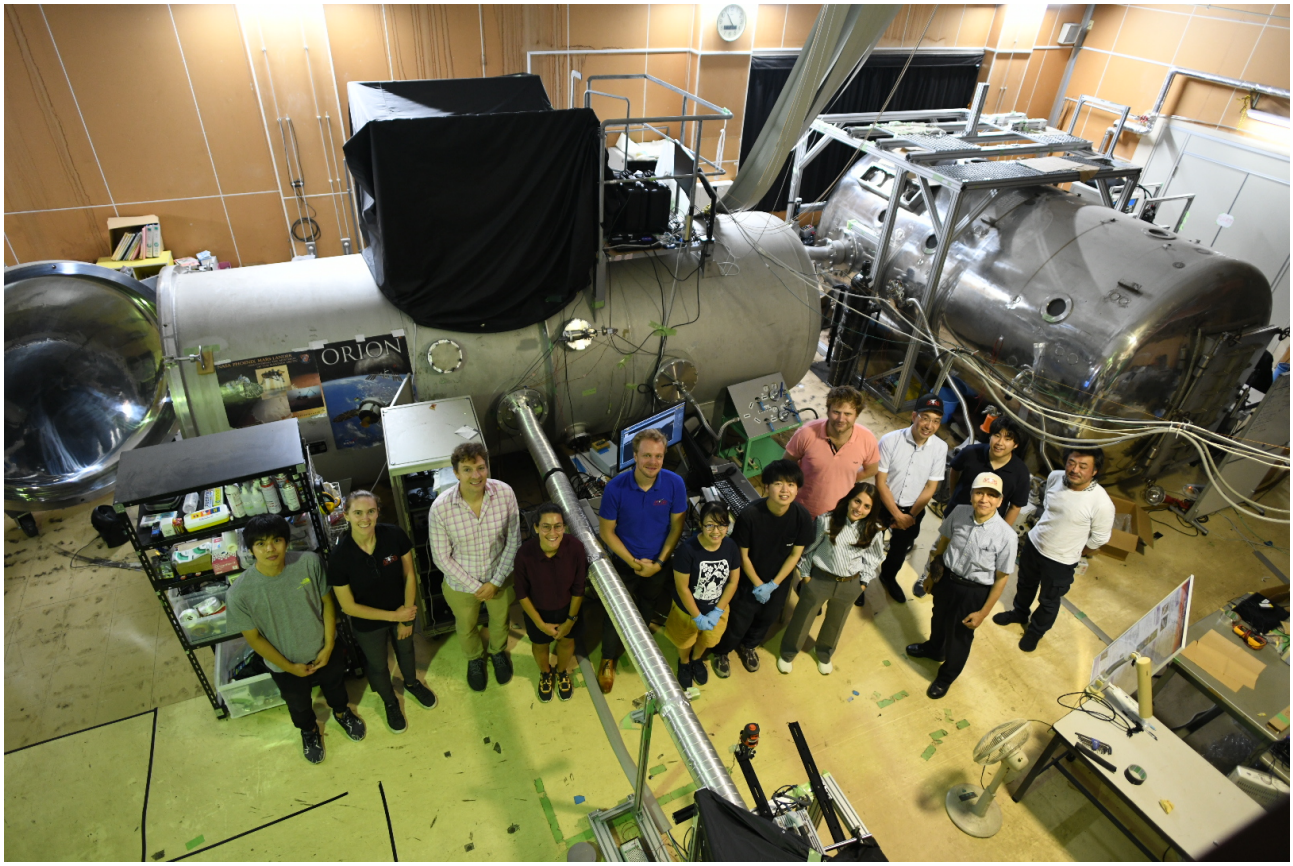


Figure 2.2: Imperial College London team, consisting of Prof Peter Vincent, Prof Oliver Buxton and Lidia Caros (author) visiting and discussing the Mars Wind Tunnel experiments at Tohoku University, Japan, in collaboration with the ROAMX team from NASA Ames, consisting of Haley Cummings, Witold Koning and Natalia Perez Perez, and the experimental team at Tohoku University, consisting of Associate Prof Taku Nonomura, Dr Takayuki Nagata, Yudai Kanzaki, Miku Kasai and Miyagi Muku.

The majority of other wind tunnel experiments for Mars vehicles have focused on studying the behaviour of flow around aerodynamic surfaces at low Reynolds numbers (1,000 to 10,000). Initial experimental research for low Reynolds numbers includes studies by McGhee et al. [48] which explored the Eppler 387 aerofoil and studies by Ol et al. [49] on the SD7003 aerofoil, two popular conventional aerofoils for low Reynolds numbers. Another conventional aerofoil that acquired interest for Martian flight is the Ishii aerofoil, tested in the Mars Wind Tunnel [45, 46]. Several studies also tested the NACA0012 aerofoil under different Martian-like conditions [43, 44, 50]. Recently, there has also been substantial focus on testing scaled models of aircraft [51] and rotors [52–58] in conditions close to the ones encountered on Mars. On the side of unconventional aerofoils with sharp edges, recent research has looked at dragonfly-inspired aerofoils [59, 60], angular aerofoils [61], thin flat and cambered plates [43, 44], and triangular aerofoils [15, 47] which have demonstrated superior aerodynamic

performance at low Reynolds numbers compared to the previously mentioned conventional aerofoils designed for low Reynolds numbers.

Computational Fluid Dynamics (CFD) studies of conventional aerofoils targeting low Reynolds numbers include Large Eddy Simulation (LES) studies on the Eppler 387 and Ishii aerofoils [45] and Implicit LES (ILES) [62, 63] and Direct Numerical Simulations (DNS) [63] studies the SD7003 aerofoil. These aerofoils, under low Reynolds number conditions and at low-to-moderate angles of attack, exhibit a LSB, and, as the angle of attack is increased, they induce laminar separation without reattachment. These investigations have shown to accurately predict the separation and reattachment of the flow against experimental data.

There have been relatively few studies on unconventional aerofoils for Martian rotorcraft. These include, but are not limited to, studies on the triangular aerofoil investigated experimentally at the Mars Wind Tunnel [15, 47]. These investigations employ Reynolds Averaged Navier-Stokes (RANS) simulations, both with [12,13] and without [64] a transition model, as well as commercial finite volume Navier-Stokes solvers [65] and DNS [15] of the same case. The investigated triangular aerofoil exhibits a non-linear behaviour in its lift coefficient as the angle of attack increases. This non-linearity arises from the shift in the flow separation from the apex of the triangle to the leading edge, in a time-averaged sense, as the angle of attack increases. When the flow separates from the sharp leading edge, the K-H instability in the separated shear layer triggers the previously described roll-up of vortices on the suction side of the aerofoil, resulting in a highly unsteady phenomenon. DNS results were found to qualitatively capture the experimentally observed non-linearity in the lift curve, with quantitative differences remaining at high angles of attack. The RANS simulations showed, in general, an over-prediction of the aerodynamic forces, especially at angles of attack where the flow separates from the sharp leading edge.

A recent study by Koning et al. [14] on performance evaluation methods of aerofoils at low Reynolds Numbers underscores the importance of employing unsteady Navier-Stokes simulations without turbulence modelling to accurately capture the unsteady and transitional phenomena of vortex roll-up, which serves as the lifting mechanism for these aerofoils.

2.2 Aerodynamic Shape Optimisation of Aerofoils for Martian Rotorcraft

The potential benefits of aerodynamic optimisation were recognised early on [66,67], but the efforts in this area were constrained by the computational resources and algorithms available at the time. Now, with advances in computer processing speeds and the development of new algorithms, aerodynamic optimisations involving multiple design variables, multiple objectives, and expensive cost functions have become feasible. When considering aerodynamic shape optimisation, different optimisation methods can be used. These are generally classified into two broad categories: gradient-based and gradient-free approaches. Each approach has their strengths and weaknesses and the choice is typically problem dependent. Gradient-based methods use the derivatives of the objective function with respect to design variables to find the optimal solution. These methods are efficient and converge quickly but can get trapped in local minima and require the objective function to be differentiable. In contrast, gradient-free methods do not require derivative information and can handle non-differentiable, noisy, and multi-modal objective functions. Genetic Algorithms (GA), a popular gradient-free method, mimic the process of natural selection by generating a population of solutions and evolving them through selection, crossover, and mutation operations. While computationally expensive, GAs are robust and can explore a large design space [68]. Numerous studies have utilised GAs to optimise aerodynamic shapes [69–74,74–81] for a wide range of aerospace applications, including aircraft wings, UAV wings, and wind turbine blades, among others. Given that these algorithms typically require a large number of cost function evaluations, they have usually been coupled with low-computational-cost evaluation methods, such as potential flow solvers, or moderately expensive ones, like RANS solvers. Higher-fidelity methods, such as LES, have also been successfully coupled with GAs for optimisation in specific applications. For instance, Tyacke et al. [82] optimised labyrinth seals for gas turbines using highly resolved LES (quasi-DNS) to capture the complex unsteady flow behaviour around these geometries, where conventional RANS approaches had been shown to inadequately model. Similarly, Watson and Tucker [83] employed wall-modelled LES (WMLES) in conjunction with GAs to optimise the aerodynamics of turbine blades in the trailing edge region.

The study of aerofoils for Martian rotorcraft is a relatively new and unexplored field. In recent years, there has been a notable increase in research specifically dedicated to the design of aerofoils for Martian

vehicles. Notably, the "Rotor Optimization for the Advancement of Mars eXploration" (ROAMX) team has been at the forefront of this effort, investigating various potential aerofoil shapes for Martian rotorcraft [11–14, 21, 22]. Other research groups [16, 56, 84–96] have also contributed to exploring and analysing several Martian helicopter design ideas and configurations.

Given the unique flow conditions in the Martian atmosphere and the unexplored domain of unconventional aerofoils for Martian rotorcraft, aerodynamic shape optimisation offers significant potential to accelerate the discovery of optimal designs. In this context, it is important to highlight studies by Koning et al. [12, 13] and Sasaki et al. [16] which optimised unconventional aerofoils by integrating RANS and unsteady RANS (URANS) solvers with GAs. However, given the nature of the flow – which is unsteady, vortex-dominated, and transitional – RANS/URANS solvers have limited predictive capability, especially at higher angles of attack where the aforementioned flow physics are more acute [13, 14]. Scale-resolving simulations, such as DNS and LES, offer higher accuracy by resolving a wider range of scales in the flow. These approaches would be computationally prohibitive for optimisation at high Reynolds numbers flows, but they are feasible for the low Reynolds number flows typical of Martian conditions. To date, there has been no DNS-based aerodynamic shape optimisation.

2.3 Novelty of this Research

The research presented in this thesis addresses the limitations in the field by utilising high-order DNS for aerodynamic optimisation, which enables the resolution of the unsteady transitional flow physics associated with sharp-leading-edge aerofoils under Martian conditions. Additionally, this study allows for an enhanced understanding of the impact of simulation accuracy on Martian aerodynamic design. Furthermore, it explores new unconventional Martian aerofoil designs under various conditions, expanding the current knowledge of Martian aerodynamics and identifying the flow characteristics that contribute to the superior performance of optimal aerofoils.

Chapter 3

Numerical Methods

This chapter presents the numerical methods utilised for aerodynamic optimisation of aerofoils designed for Martian rotorcraft. The unique atmospheric conditions on Mars necessitate accurate simulation tools and cost-effective optimisation techniques to obtain aerofoil designs in a feasible manner. Two primary methodologies form the backbone of this research: Direct Numerical Simulations (DNS) for accurate aerodynamic analysis and Genetic Algorithms (GAs) for design optimisation.

The DNS are performed using PyFR [17], an open-source Python-based high-order accurate framework for solving advection-diffusion type problems on streaming architectures. PyFR allows for a detailed resolution of the flow phenomena around unconventional Martian aerofoils, which is critical given the unsteady, separated, vortex-dominated and transitional low-Reynolds-number flow. Additionally, PyFR is designed to run across modern hardware platforms and has shown an excellent computational efficiency, allowing for a feasible cost- and time-effective design optimisation that involves many cost function evaluations.

For the optimisation process, the `pymoo` [97] framework is employed, a tool for multi-objective optimisation using evolutionary algorithms. In particular, GAs within `pymoo` are selected, since they facilitate the exploration of a wide design space based on multiple performance criteria, which is particularly beneficial for the unexplored domain of Martian rotorcraft aerodynamics.

3.1 Direct Numerical Simulations with PyFR

PyFR is a cross-platform solver providing high-order accurate solutions on unstructured grids. It leverages the Flux Reconstruction approach, which enables it to achieve high-order accuracy while maintaining computational efficiency. PyFR can be deployed on a wide range of hardware platforms, including multi-core CPUs and GPUs, which is particularly advantageous to accelerate the multiple large-scale simulations required in this research.

3.1.1 Flux Reconstruction Approach

The Flux Reconstruction (FR) method [98] is a high-order numerical technique used to solve partial differential equations (PDEs) in fluid dynamics, providing high accuracy on unstructured grids. This method integrates nodal Discontinuous Galerkin (DG) schemes and Spectral Difference (SD) methods, achieving high-order accuracy and element locality, which is advantageous for efficient use of modern computational hardware. An overview of the FR approach is presented below, see [17] for a more detailed description of the implementation in PyFR, and [98, 99] for the extended formulation.

Consider a general advection-diffusion problem within a domain $\mathbf{\Omega}$ in N_D dimensions

$$\frac{\partial u_\beta}{\partial t} + \nabla \cdot \mathbf{f}_\beta = 0 \tag{3.1}$$

where $u_\beta = u_\beta(\mathbf{x}, t)$ represents the conserved quantity for a particular field variable β where $\mathbf{x}$ is the spatial coordinate vector and t is time, and $\mathbf{f}_\beta = \mathbf{f}_\beta(u, \nabla u)$ denotes the flux of this particular field variable, which is a function of all field variables u and their gradients ∇u.

Eq. (3.1) can be re-written as a first-order system by using $\mathbf{q}$ as an auxiliary variable such that

$$\frac{\partial u_\beta}{\partial t} + \nabla \cdot \mathbf{f}_\beta(u, \mathbf{q}) = 0, \tag{3.2a}$$

$$\mathbf{q}_\beta - \nabla u_\beta = 0. \tag{3.2b}$$

To solve this problem, the domain $\mathbf{\Omega}$ is partitioned into a mesh of N non-overlapping elements such

that

$$\boldsymbol{\Omega} = \bigcup_{e=0}^{N-1} \boldsymbol{\Omega}_e, \qquad \bigcap_{e=0}^{N-1} \boldsymbol{\Omega}_e = \emptyset.$$

Each element $\boldsymbol{\Omega}_e$ is mapped to a standard element $\hat{\boldsymbol{\Omega}}_e$ in a transformed space through

$$\mathbf{x} = \boldsymbol{\mathcal{M}}_e(\tilde{\mathbf{x}}), \qquad \tilde{\mathbf{x}} = \boldsymbol{\mathcal{M}}_e^{-1}(\mathbf{x})$$

where $\tilde{\mathbf{x}}$ are the coordinates in the transformed space, and the Jacobian matrices

$$\mathbf{J}_e = J_{eij} = \frac{\partial \mathcal{M}_{ei}}{\partial \tilde{x}_j}, \quad J_e = \det \mathbf{J}_e,$$

$$\mathbf{J}_e^{-1} = J_{eij}^{-1} = \frac{\partial \mathcal{M}_{ei}^{-1}}{\partial x_j}, \quad J_e^{-1} = \det \mathbf{J}_e^{-1} = \frac{1}{J_e}$$

which allow for quantities to be transformed to and from standard element space. The governing equations are then transformed as follows

$$\frac{\partial u_{e\beta}}{\partial t} + J_e^{-1} \tilde{\nabla} \cdot \tilde{\mathbf{f}}_{e\beta} = 0, \tag{3.3a}$$

$$\tilde{\mathbf{q}}_{e\beta} - \tilde{\nabla} \tilde{u}_{e\beta} = 0, \tag{3.3b}$$

where

$$\tilde{\mathbf{f}}_{e\beta} = \tilde{\mathbf{f}}_{e\beta}(\tilde{\mathbf{x}}, t) = J_e(\tilde{\mathbf{x}}) \mathbf{J}_e^{-1}(\boldsymbol{\mathcal{M}}_e(\tilde{\mathbf{x}})) \mathbf{f}_{e\beta}(\boldsymbol{\mathcal{M}}_e(\tilde{\mathbf{x}}), t),$$

$$\tilde{\mathbf{q}}_{e\beta} = \tilde{\mathbf{q}}_{e\beta}(\tilde{\mathbf{x}}, t) = \mathbf{J}_e^T(\tilde{\mathbf{x}}) \mathbf{q}_{e\beta}(\boldsymbol{\mathcal{M}}_e(\tilde{\mathbf{x}}), t),$$

$$\tilde{u}_{e\beta} = \tilde{u}_{e\beta}(\tilde{\mathbf{x}}, t) = J_e(\tilde{\mathbf{x}}) u_{e\beta}(\boldsymbol{\mathcal{M}}_e(\tilde{\mathbf{x}}), t).$$

Within each standard element, a set of solution points $\tilde{x}_\rho^{(u)}$ and flux points $\tilde{x}_\rho^{(f)}$ are identified, where $0 \leq \rho < N(\wp)$, where $\wp$ is the polynomial order. Every pair of flux points along an interface must have identical coordinates in physical space. These points are used to construct a nodal basis set $\ell_\rho^{(u)}(\tilde{\mathbf{x}})$ such that $\ell_\rho^{(u)}(\tilde{\mathbf{x}}_\sigma^{(u)}) = \delta_{\rho\sigma}$. This set is obtained by computing the elements of the generalised Vandermonde matrix $\mathcal{V}_{\rho\sigma} = \psi_\rho(\tilde{\mathbf{x}}_\sigma^{(u)})$, where $\psi_\rho(\tilde{\mathbf{x}})$ represents a basis that spans a chosen polynomial space of order $\wp$ inside $\boldsymbol{\Omega}_e$. Then, the nodal basis set can be constructed as $\ell_\rho^{(u)}(\tilde{\mathbf{x}}) = \mathcal{V}_{\rho\sigma}^{-1} \psi_\sigma(\tilde{\mathbf{x}})$.

The discontinuous solution for the field variable β at solution points is extrapolated to a discontinuous solution at the flux points through the following relationship

$$u_{e\sigma\beta}^{(f)} = u_{e\rho\beta}^{(u)} \ell_{\rho}^{(u)}(\tilde{\mathbf{x}}_{\sigma}^{(f)}). \tag{3.5}$$

The two values from each side at the flux points with $u_L = u_{e\rho\beta}^{(f)}$ being the solution on the left and $u_R = u_{\widetilde{e}\rho\beta}^{(f)}$ being the solution on the right for the element e, flux point ρ, and field variable β, are then used to compute a common solution. The common solution is obtained through $\mathcal{C}_{\beta}(u_L, u_R)$, a scalar function that takes two values at a point and returns a common value. Then, the common solution can be represented as

$$\mathcal{C}_{\beta} u_{e\rho\beta}^{(f)} = \mathcal{C}_{\beta} u_{\widetilde{e}\rho\beta}^{(f)} = \mathcal{C}_{\beta}(u_{e\rho\beta}^{(f)}, u_{\widetilde{e}\rho\beta}^{(f)}). \tag{3.6}$$

Each flux point is associated with a vector correction function $\mathbf{g}_{\rho}^{(f)}(\tilde{\mathbf{x}})$ such that $\hat{\tilde{\mathbf{n}}}_{\sigma}^{(f)} \cdot \mathbf{g}_{\rho}^{(f)}(\tilde{\mathbf{x}}_{\sigma}^{(f)}) = \delta_{\rho\sigma}$, where $\hat{\tilde{\mathbf{n}}}_{\sigma}^{(f)}$ is the normalised outward-pointing normal vector at the flux point. The divergence of this correction function is in the same polynomial space as the solution, maintaining high-order accuracy.

Then, the solution to Eq. (3.3b) can be expressed as

$$\tilde{\mathbf{q}}_{e\sigma\beta}^{(u)} = \left[\hat{\tilde{\mathbf{n}}}_{\rho}^{(f)} \cdot \tilde{\nabla} \mathbf{g}_{\rho}^{(f)}(\tilde{\mathbf{x}}) \left\{ \mathcal{C}_{\beta} u_{e\rho\beta}^{(f)} - u_{e\rho\beta}^{(f)} \right\} + u_{ev\beta}^{(u)} \tilde{\nabla} \ell_{v}^{(u)}(\tilde{\mathbf{x}}) \right]_{\tilde{\mathbf{x}} = \tilde{\mathbf{x}}_{\sigma}^{(u)}}, \tag{3.7}$$

where $u_{ev\beta}^{(u)} \tilde{\nabla} \ell_{v}^{(u)}(\tilde{\mathbf{x}})$ is an order $\wp - 1$ approximation of the gradient obtained by differentiating the discontinuous solution polynomial. Following the approaches of Kopriva [100] and Sun et al. [101], physical gradients can be computed to obtain

$$\mathbf{q}_{e\sigma\beta}^{(u)} = \mathbf{J}_{e\sigma}^{-T(u)} \tilde{\mathbf{q}}_{e\sigma\beta}^{(u)}, \tag{3.8}$$

$$\mathbf{q}_{e\sigma\beta}^{(f)} = \ell_{\rho}^{(u)}(\tilde{\mathbf{x}}_{\sigma}^{(f)}) \mathbf{q}_{e\rho\beta}^{(u)} \tag{3.9}$$

where $\mathbf{J}_{e\sigma}^{-T(u)}$ the inverse transpose of the Jacobian matrix.

Then, the transformed flux $\tilde{\mathbf{f}}_{e\rho\beta}^{(u)}$ can be evaluated at the solution points using the physical gradients and the Jacobian matrices, which allows computing the normal transformed flux at each of the flux

points

$$\tilde{f}^{(f\perp)}_{e\sigma\beta} = \ell^{(u)}_{\rho}(\tilde{\mathbf{x}}^{(f)}_{\sigma})\hat{\tilde{\mathbf{n}}}^{(f)}_{\sigma} \cdot \tilde{\mathbf{f}}^{(u)}_{e\rho\beta}. \tag{3.10}$$

For the physical normals at the flux points

$$\mathbf{n}^{(f)}_{e\sigma} = n^{(f)}_{e\sigma}\hat{\mathbf{n}}^{(f)}_{e\sigma} = \mathbf{J}^{-T(f)}_{e\sigma}\hat{\tilde{\mathbf{n}}}^{(f)}_{\sigma} \tag{3.11}$$

where $\mathbf{n}^{(f)}_{e\sigma}$ is the outward-facing normal vector in physical space with magnitude $n^{(f)}_{e\sigma} > 0$. At the interfaces where two elements are adjacent, the condition $\hat{\mathbf{n}}^{(f)}_{e\sigma} = -\hat{\mathbf{n}}^{(f)}_{\widetilde{e\sigma}}$ must be met so that the normal vector of one element is the negative of the normal vector of the adjacent element, ensuring continuity across the interface. $\widetilde{e\sigma}$ refers to the adjoining point at the interface of element e and flux point ρ.

Then, the common normal flux at a flux point pair can be expressed as

$$\mathcal{F}_{\beta}f^{(f\perp)}_{e\sigma\beta} = -\mathcal{F}_{\beta}f^{(f\perp)}_{\widetilde{e\sigma}\beta} = \mathcal{F}_{\beta}\left(u^{(f)}_{e\sigma}, u^{(f)}_{\widetilde{e\sigma}}, \mathbf{q}^{(f)}_{e\sigma}, \mathbf{q}^{(f)}_{\widetilde{e\sigma}}, \hat{\mathbf{n}}^{(f)}_{e\sigma}\right), \tag{3.12}$$

which can be taken into transformed space via $\tilde{f}^{(f\perp)}_{e\sigma\beta} = J^{(f)}_{e\sigma\beta}n^{(f)}_{e\sigma\beta}\mathcal{F}_{\beta}f^{(f\perp)}_{e\sigma\beta}$.

Then, an approximation of the divergence of the continuous flux, analogous to Eq. (3.7), can be computed as

$$(\tilde{\nabla}\cdot\tilde{\mathbf{f}})^{(u)}_{e\rho\beta} = \left[\tilde{\nabla}\cdot\mathbf{g}^{(f)}_{\sigma}(\tilde{\mathbf{x}})\left\{\mathcal{F}_{\beta}\tilde{f}^{(f\perp)}_{e\sigma\beta} - \tilde{f}^{(f\perp)}_{e\sigma\beta}\right\} + \tilde{\mathbf{f}}^{(u)}_{ev\beta}\cdot\tilde{\nabla}\ell^{(u)}_{v}(\tilde{\mathbf{x}})\right]_{\tilde{\mathbf{x}}=\tilde{\mathbf{x}}^{(u)}_{\rho}}, \tag{3.13}$$

which can then be used to obtain a spatially discretised system of ordinary differential equations with respect to t as

$$\frac{\partial u^{(u)}_{e\rho\beta}}{\partial t} = -J^{-1(u)}_{e\rho}(\tilde{\nabla}\cdot\tilde{\mathbf{f}})^{(u)}_{e\rho\beta} \tag{3.14}$$

which can be solved using various time-stepping schemes.

3.1.2 Governing Equations

In this work, PyFR [17] is used to solve the compressible Navier-Stokes equations for an ideal gas with constant viscosity. These can be written as

$$\frac{\partial \mathbf{u}}{\partial t} + \boldsymbol{\nabla} \cdot \mathbf{f} = 0, \tag{3.15}$$

where $\mathbf{u} = \mathbf{u}(\mathbf{x}, t) = (\rho, \rho v_x, \rho v_y, \rho v_z, E)$ is the solution with ρ the fluid density, $\mathbf{v} = (v_x, v_y, v_z)$ the fluid velocity and E the total energy per unit volume, and where $\mathbf{f} = \mathbf{f}(\mathbf{u}, \boldsymbol{\nabla}\mathbf{u}) = \mathbf{f^i} - \mathbf{f^v}$ is the flux, with $\mathbf{f^i}$ the inviscid flux given by

$$\mathbf{f^i} = \begin{Bmatrix} \rho v_x & \rho v_y & \rho v_z \\ \rho v_x^2 + p & \rho v_y v_x & \rho v_z v_x \\ \rho v_x v_y & \rho v_y^2 + p & \rho v_z v_y \\ \rho v_x v_z & \rho v_y v_z & \rho v_z^2 + p \\ v_x(E+p) & v_y(E+p) & v_z(E+p) \end{Bmatrix}, \tag{3.16}$$

where p is the pressure, which for an ideal gas is given by

$$p = (\gamma - 1)\left(E - \frac{1}{2}\rho \|\mathbf{v}\|^2\right), \tag{3.17}$$

with $\gamma = c_p/c_v$, where c_p and c_v are specific heat capacities at constant pressure and volume, respectively, and $\mathbf{f^v}$ is the viscous flux given by

$$\mathbf{f^v} = \begin{Bmatrix} 0 & 0 & 0 \\ \mathscr{T}_{xx} & \mathscr{T}_{yx} & \mathscr{T}_{zx} \\ \mathscr{T}_{xy} & \mathscr{T}_{yy} & \mathscr{T}_{zy} \\ \mathscr{T}_{xz} & \mathscr{T}_{yz} & \mathscr{T}_{zz} \\ v_i\mathscr{T}_{ix} + \Delta\partial_x T & v_i\mathscr{T}_{iy} + \Delta\partial_y T & v_i\mathscr{T}_{iz} + \Delta\partial_z T \end{Bmatrix}, \tag{3.18}$$

where the stress-energy tensor is given by

$$\mathscr{T}_{ij} = \mu(\partial_i v_j + \partial_j v_i) - \frac{2}{3}\mu\delta_{ij}\boldsymbol{\nabla} \cdot \mathbf{v}, \tag{3.19}$$

with μ the dynamic viscosity, $\Delta = \mu c_p/Pr$, with Pr the Prandtl number, and T is the temperature, which for an ideal gas is given by

$$T = \frac{1}{c_v}\frac{1}{\gamma - 1}\frac{p}{\rho}. \tag{3.20}$$

In the current study, values of $\gamma = 1.4$ and $Pr = 0.71$ are used, corresponding to the properties of air at ambient temperature. While values of $\gamma = 1.29$ and $Pr = 1.18$ are more representative of the Martian atmosphere, the chosen values were selected to align with the published experimental data used for validating the PyFR simulations (see Chapter 4).

Flow conditions of Mach number $M = 0.15$ and chord-based Reynolds number $Re = 3,000$ are employed throughout this work. Note that the continuum approximation is valid at $M = 0.15$ and $Re = 3,000$ since the Knudsen number $K \approx M/\sqrt{Re} < 0.01$ [102, 103].

3.1.3 Synthetic Eddy Method

PyFR employs the synthetic eddy method (SEM) [104–106] to generate free-stream turbulence in the computational domain. The SEM is a technique for generating synthetic turbulence by injecting fictitious coherent eddies into the flow. The SEM implemented in PyFR is based on the work of Giangaspero et al. [107], and it uses a source term formulation that allows isotropic eddies to be injected into any portion of the domain, where the turbulence intensity and characteristic length scale of the eddies can be specified. The characteristic length scale ls defines the spatial size of the synthetic eddies, which aims to determine the size of the largest energy-containing eddies or integral length scale in the resulting injected turbulence. Since the flow resulting from the injected eddies does not develop into turbulence due to the low Reynolds number ($Re = 3,000$), ls here refers primarily to the injected eddy size. A brief explanation of the SEM implemented in PyFR is presented below, for a more extensive detailed explanation of the approach see [107].

The SEM aims to define a stochastic signal $\tilde{u}_j(\mathbf{x}, t)$ where $\mathbf{x} = (x, y, z)$. This signal must satisfy the following conditions

$$\langle \tilde{u}_j \rangle = 0 \tag{3.21a}$$

$$\langle \tilde{u}_j^2 \rangle = 1 \tag{3.21b}$$

$$\langle \tilde{u}_i \tilde{u}_j \rangle_{i \neq j} = 0 \tag{3.21c}$$

Here, $\langle\cdot\rangle$ denotes the averaging operator, and $i = j = \{1, 2, 3\}$. The velocity components are given by $\tilde{\mathbf{u}} = \tilde{u}_j = (\tilde{u}, \tilde{v}, \tilde{w})$.

The instantaneous velocity field $u_k(\mathbf{x}, t) = (u, v, w)$ is obtained from the mean velocity $U_k = (U, V, W)$ combined with the stochastic signal as

$$u_k(\mathbf{x}, t) = U_k(\mathbf{x}) + u'_k(\mathbf{x}, t) = U_k(\mathbf{x}) + \sum_j A_{kj}(\mathbf{x})\tilde{u}_j(\mathbf{x}, t) \tag{3.22}$$

where $A_{kj}(\mathbf{x})$ results from the Cholesky decomposition of the target Reynolds stresses $\mathbf{R} = \mathbf{A}\mathbf{A}^T$, which for isotropic homogeneous turbulence

$$\mathbf{A} = \begin{bmatrix} R_{11}^{1/2} & 0 & 0 \\ 0 & R_{22}^{1/2} & 0 \\ 0 & 0 & R_{33}^{1/2} \end{bmatrix} \qquad \text{and} \qquad R_{11} = R_{22} = R_{33}.$$

Eddies are generated through a source term formulation within a box that can be placed anywhere in the domain. The position of each eddy n at time t is computed as

$$x_n(t) = x_n(t_0) + U_b(t - t_0), \quad y_n(t) = y_n(t_0), \quad z_n(t) = z_n(t_0)$$

where U_b is the bulk velocity at which the eddies are advected through the box. Once an eddy reaches the end of the box, a new eddy is generated at the beginning of the box. The injected eddies are translated through the box of eddies with a fixed structure, with all eddies having the same characteristic length scale/wavenumber. When they leave the box, they interact with the mean flow and each other, governed by the Navier-Stokes equations, developing into a broader spectrum in space/time.

The field $\tilde{u}_j(\mathbf{x})$ is computed as

$$\tilde{u}_j(\mathbf{x}) = \sum_{n=1}^{N} \varepsilon_{jn} g_j \left(\frac{\mathbf{x} - \mathbf{x}_n}{l} \right) \tag{3.23}$$

where ε_{jn} is the sign (+1 or -1) of eddy n for component j, which are drawn randomly from a uniform

distribution to satisfy condition (3.21c), and where

$$g_j\left(\frac{\mathbf{x}-\mathbf{x}_n}{\mathbf{l}}\right)=\prod_{i=1}^{3}G_{ij}\left(\frac{x_i-x_{ni}}{l_i}\right) \tag{3.24}$$

where G_{ij} are the shape functions, and l_i are the characteristic length scales in each direction. The injected eddies in this work are isotropic, therefore, $l_x = l_y = l_z$. The shape of each eddy is defined by G_{ij}. These have compact support on $[-1, 1]$, ensuring that the eddies are spatially localised. To satisfy condition (3.21b), the functions G_{ij} must satisfy the equation

$$\frac{1}{2}\int_{-1}^{+1}G_{ij}^2(\xi)\,d\xi=1. \tag{3.25}$$

Additionally, G_{ij} must be symmetric with respect to $\xi = 0$ to satisfy condition (3.21a). Finally, the corresponding correlation functions are given by

$$R_{ij}(r)=\frac{1}{2}\int_{-1}^{+1}G_{ij}(\xi)G_{ij}(\xi+r)\,d\xi. \tag{3.26}$$

The SEM implemented in PyFR employs a source term formulation to introduce the synthetic turbulence into the Navier-Stokes equations, similar to the approach proposed by Schmidt and Breuer [108] for the digital filter method. This approach allows the turbulence to be injected away from boundaries, closer to regions of interest. For the incompressible solver, the source term S_{uk} added to the momentum equations is:

$$S_{uk}(\mathbf{x},t)=\frac{u_k'(\mathbf{x},t)}{t_k(\mathbf{x})}\mathcal{F}\left(\frac{x-x_{\text{in}}}{l_{xk}^{\text{clip}}}\right)$$

where $u_k'(\mathbf{x}, t)$ are the velocity fluctuations, $t_k(\mathbf{x}) = l_{xk}^{\text{clip}}/U_b$ is the characteristic turbulent time scale, $\mathcal{F}(\xi) = \exp(-\frac{\pi}{2}\xi^2)$ is a smoothing function to avoid strong variations of the source term across the domain [108], x_{in} is the streamwise location of the centre of the injection domain and l_{xk}^{clip} is the clipping length. For the compressible solver, source terms are added to the density, momentum, and energy equations. To compute the density fluctuations, a strong Reynolds analogy (SRA) originally proposed by Morkovin [109] for adiabatic wall turbulence is used, which provides a good approximation close to a nonadiabatic wall [110]. The density fluctuations are then given by

$$\rho'(\mathbf{x},t)=\langle\rho\rangle(\gamma-1)\langle M\rangle^2\frac{u_x'(\mathbf{x},t)}{U_b}. \tag{3.27}$$

The implementation in PyFR is designed to scale efficiently and minimise memory bandwidth requirements. Specifically, by precomputing and caching element intersections of every injected eddy before the simulation starts, the cost of the implementation is able to scale as the number of eddies intersecting an element at a given time — which for sensible grid resolutions will remain small — as opposed to scaling with the overall number of injected eddies, which can be substantial for large domains and small turbulent length scales.

3.1.4 Simulation Setup

For all simulations presented in this work, fourth-order polynomials were used to represent the solution within each element of the mesh, thus nominally achieving fifth-order accuracy in space. A Rusanov Riemann solver was used to calculate the inter-element inviscid fluxes and the Local Discontinuous Galerkin [111] approach was used to calculate the inter-element viscous fluxes. An explicit 5th stage 4th order Runge-Kutta time-stepping scheme, specifically version RK45[2R+] [112], with a fixed time-step was employed to advance the solution in time. These schemes are designed to have large time step stability limits and have been widely adopted in a range of other high-order simulations [113,114]. No anti-aliasing was employed, and all runs were performed using double-precision arithmetic.

The validation of using PyFR for DNS of aerofoils under Martian atmospheric conditions is detailed in Chapter 4 where various simulation configurations are explored and compared against published experimental data to ensure an accurate representation of the physics.

3.2 Multi-Objective Genetic Algorithm Optimisation with pymoo

pymoo [97] is an open-source Python-based framework which supports various single, multi, and many-objective test problems, automatic differentiation for gradients, parallelised evaluation, and tools for multi-criteria decision-making, and includes various evolutionary algorithms. The framework's design enables integration with external software, making it adaptable for complex workflows. Its extensive customisation options facilitate coupling with various tools, such as PyFR and Gmsh. Gmsh [115] is the open-source meshing tool that has been used in this work to make automated unstructured meshes around the geometries.

3.2.1 Genetic Algorithms

Genetic Algorithms (GAs) [68] are used for the optimisation. These algorithms mimic the process of natural selection to find optimal solutions. They are particularly well-suited for problems where the design space is large and complex. Specifically, GAs explore the design space to find the fittest set of design variables for the given objective functions by evolving populations of individuals through generations. Although these algorithms require multiple evaluations to converge, they are suitable for problems with multiple objectives and nonlinear objective spaces with various local optima. Moreover, they do not require gradient information, which is challenging to obtain for the chaotic unsteady flow solutions produced by DNS. The particular GA used here is the Non-dominated Sorting Genetic Algorithm II (NSGA-II), first presented by Srinivas and Deb [116] as NSGA and later improved by Deb et al. [117] to NSGA-II.

Population Size and Number of Offspring: The population size remains constant throughout the optimisation process, meaning that the optimal individuals from generation n can be replaced by superior offspring in generation $n+1$. NSGA-II employs an elitist-preserving approach, ensuring that the best individuals are retained and transferred to the next generation. This strategy significantly enhances the performance of the GA and helps prevent the loss of high-quality solutions once they are discovered. The number of offspring determines how many new individuals are generated and evaluated by the optimiser at each generation. The number of offspring does not necessarily need to be the same as the population size. If a more greedy approach is desired and the evaluations are expensive, the number of offspring can take a lower value.

Selection: Selection is the process of determining the best-performing solutions based on a fitness function to be parents for the next generation. Various selection methods, such as roulette wheel, tournament, or rank-based selection, can be used. The operator used in this work is Tournament Selection [118]. Tournament selection involves randomly selecting a subset of individuals from the population and choosing the best among them based on their fitness scores. The advantages of this method include efficiency, diversity and simplicity.

Crossover: Crossover is the process of combining pairs of parent solutions to produce offspring, facilitating the exchange of genetic material between solutions to explore the design space. Various crossover methods, such as single-point, two-point, or uniform crossover, can be applied. In this work, the Simulated Binary Crossover (SBX) operator [119] is used, which is particularly suitable for real-valued variables. SBX mimics the genetic recombination process observed in nature by producing offspring that are likely to inherit traits from both parents while maintaining diversity in the population. The SBX operator generates two offspring from two parent solutions by creating a blend of their genetic information.

Mutation: Mutation is the process of introducing random variations to offspring to maintain genetic diversity within the population and to help avoid premature convergence to local minima. By slightly altering solution parameters, mutation ensures that the search process remains explorative and capable of discovering new and potentially better solutions. In this work, Polynomial Mutation [119] is used, which is particularly effective for real-valued variables. Polynomial Mutation operates by perturbing each variable of an offspring with a certain probability, known as the mutation probability. This operator is designed to create small variations in the offspring, mimicking the effect of mutation in natural evolution.

3.2.2 Optimisation Process

Figure 3.1 shows the optimisation flowchart. The optimisation process consists of a set of executable scripts that autonomously interact with each other. All optimisations presented in this work have been run on the Piz Daint supercomputer at the Swiss National Supercomputing Centre (CSCS). pymoo and Gmsh were invoked on the login node (Intel Xeon E5-2650 v3 2.30GHz CPU) via Bash scripts and PyFR was invoked on the compute nodes (Tesla P100-16GB GPUs).

Initial Sampling

The initial sampling in GA optimisation is the first population in the optimisation. The initial sampling can be designed to maximize exploration of the design space or can be strategically biased using domain knowledge to improve the search process. In this work, Latin Hypercube Sampling (LHS) is primarily

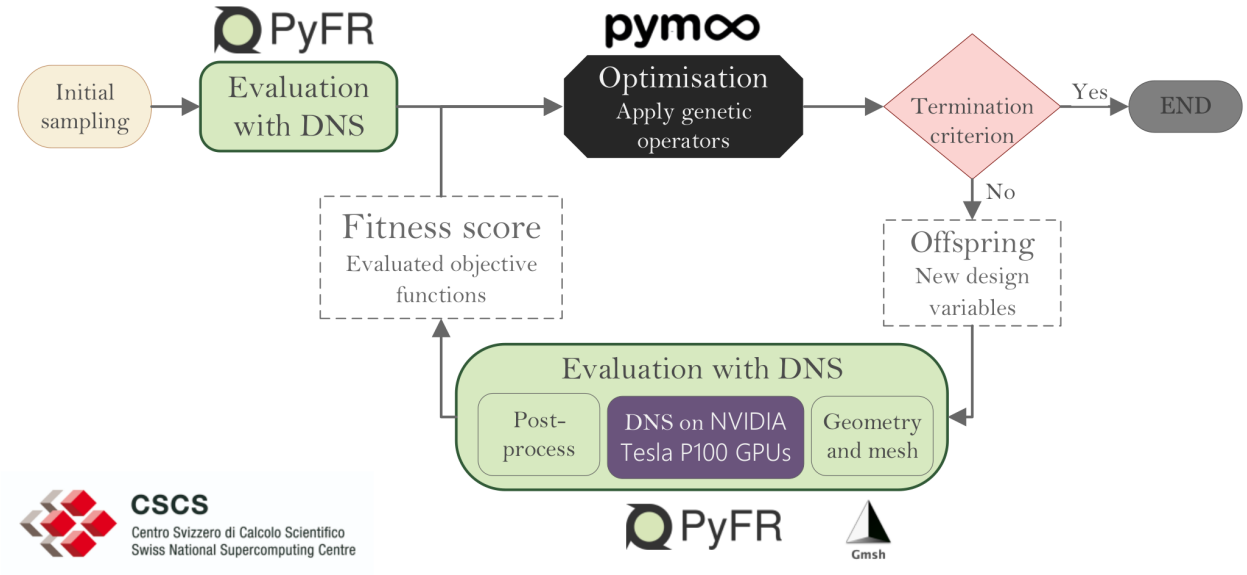


Figure 3.1: Flowchart of the optimisation process.

employed for the initial sampling. LHS is a technique used to generate a well-distributed set of points within the design space targeting domain exploration. The specific details of the initial sampling methods used for each optimisation are presented in the methodology sections of their respective chapters.

Design Space and Design Variables

The range of possible aerofoil shapes constitutes the design space, and the variables within that space are the design variables. This work focuses on optimising triangular aerofoils, where the design variables are the coordinates of the apex of the triangle. Constraints are incorporated to ensure feasible aerofoil designs, such as minimum aerofoil thickness and maximum sharpness of the edges to ensure manufacturability. At each generation, a restriction step is applied, in which any individuals violating the design space constraints are moved to the nearest point within the design space. More details can be found in the methodology sections of each optimisation.

Objective Space and Objective Functions

The metrics that define the fitness score of each individual in the optimisation process are the objective functions, which form the objective space. This work employs a multi-objective optimisation approach resulting in multiple Pareto-optimal solutions. The Pareto front represents a set of non-dominated design solutions. Each solution on the Pareto front ensures that no other solution in the design space can improve one objective without degrading another. This trade-off between objectives is fundamental to multi-objective optimisation, providing a spectrum of optimal solutions rather than a single design. The objective functions in this work are maximising lift and minimising drag. Detailed descriptions of the cost function evaluations are provided in the methodology sections of each optimisation.

Evaluation

Evaluation involves assessing the fitness score of the offspring regarding the objective functions. In this work, this step consists of three main stages. The first stage is the geometry and mesh generation with Gmsh. A notable feature of Gmsh is that it can be scripted via a Python application programming interface (API). This allows for the mesh automation around each aerofoil proposed by the optimiser and for easy integration with the `pymoo` optimisation framework. Then, DNS are run for each aerofoil shape to assess their aerodynamic performance. `pymoo` supports parallelised evaluations, enabling DNS of multiple individuals to be run simultaneously. Additionally, each simulation is parallelised on multiple Nvidia Tesla P100-16GB GPUs. Finally, the fitness score for each aerofoil is calculated by post-processing the DNS output based on the two objectives: maximising lift and minimising drag. More details on each stage are provided in each optimisation's methodology section.

Genetic Operations

Selection, crossover, and mutation are applied to generate new aerofoil shapes. These genetic operations are iteratively applied to evolve the population towards better-performing solutions.

Convergence and Termination Criterion

The optimisation process is repeated until convergence is achieved. The termination criterion in this work is set based on a specific number of evaluations, considering the available computational resources. Convergence is assessed by using a hypervolume metric [120], which is calculated as the area dominated by the Pareto front at a particular generation with respect to a reference point. Hypervolume is a widely used performance metric [121] as it is Pareto compliant [122] and captures both convergence and diversity in a single value [123]. Convergence plots for each optimisation can be found in their respective methodology sections.

Chapter 4

Direct Numerical Simulations of a Triangular Aerofoil under Martian Conditions

In this chapter, a triangular aerofoil studied both experimentally and computationally by Munday et al. [15], hereafter referred to as Reference aerofoil, is analysed using high-order accurate DNS with PyFR, as described in Chapter 3, to validate the simulations against experimental data and to assess the effect of both domain span and wind tunnel walls on DNS accuracy. Specifically, span-wise periodic DNS are undertaken with various domain spans, as well as full-span DNS in a virtual wind tunnel including no-slip walls, representative of the real wind tunnel, for a range of angles of attack, with a fixed free-stream Mach number $M = 0.15$ and a chord-based Reynolds number $Re = 3,000$.

The work presented in this chapter has been published in the AIAA Journal [124].

4.1 Test Case

The experimental studies of Munday et al. [15] were carried out in the Mars Wind Tunnel (MWT) at Tohoku University [42]. The test section of the MWT measures 400 mm in length, 150 mm in height, and 100 mm in width; with the top and bottom walls of the test section inclined at 1.3 degrees to compensate for boundary layer growth. The triangular aerofoil was placed in the middle of the test section. It had a chord of 30 mm, a maximum thickness of 1.5 mm at 9 mm from the leading edge, and spanned the width of the wind-tunnel test section; with a span-to-chord ratio of 3.33. Figure 4.1 shows a schematic of the aerofoil, in which all length scales are normalised by the chord, with its apex position at $(x, y) = (0.3, 0.05)$, hereafter referred to as Reference aerofoil.

In the experiments, various quantities were measured including time-averaged lift, drag and pressure coefficients defined as

$$\overline{C}_L = \frac{\overline{F}_L}{q_\infty A}\,, \qquad \overline{C}_D = \frac{\overline{F}_D}{q_\infty A}\,, \qquad \overline{C}_P = \frac{\overline{p} - \overline{p}_a}{q_\infty}\,, \tag{4.1}$$

respectively, where $\overline{F}_L$ and $\overline{F}_D$ are the time-averaged lift and drag forces, respectively, measured with a force balance, $\overline{p}$ is the time-averaged static pressure obtained via mid-span pressure tappings and pressure-sensitive paint (PSP), $\overline{p}_a$ is a time-averaged reference static pressure measured at the aerofoil apex, A is the aerofoil planform area, and q_∞ is the time-averaged dynamic pressure. The time-averaged dynamic pressure was obtained via

$$q_\infty = \overline{p}_{Ts} - \overline{p}_e, \tag{4.2}$$

where $\overline{p}_{Ts}$ is the time-averaged total pressure measured with a pitot tube in the settling chamber of the wind tunnel and $\overline{p}_e$ is the time-averaged static pressure measured at the entrance of the test section.

For the PyFR simulations, instantaneous lift and drag coefficients are defined as

$$C_L = \frac{F_L}{q_\infty A}\,, \qquad C_D = \frac{F_D}{q_\infty A}\,, \tag{4.3}$$

respectively, where F_L and F_D are the instantaneous forces on the aerofoil per unit area measured as

the sum of viscous and pressure forces in the y and x directions, respectively, and q_∞ is obtained via

$$q_\infty = \frac{1}{2}\rho_\infty v_\infty^2 \tag{4.4}$$

where ρ_∞ is the free-stream density, measured at the centre of the inflow plane. Time-averaged lift and drag coefficients $\overline{C}_L$ and $\overline{C}_D$, can then be obtained by time-averaging C_L and C_D, respectively, over the Data Extraction Period.

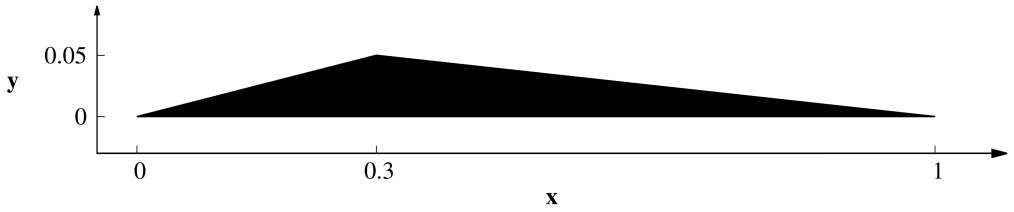


Figure 4.1: Schematic of the Reference aerofoil studied experimentally and numerically by Munday et al. [15] and used as validation case.

Both the experimental and computational studies of Munday et al. [15] were undertaken with $M = 0.15$ and $M = 0.5$, and $Re = 3,000$ and $Re = 10,000$, for various angles of attack α in the range $0° \leq \alpha \leq 15°$. In the present work, we focus on the case with $M = 0.15$ and $Re = 3,000$. Under these conditions, the triangular aerofoil has a highly nonlinear lift curve, and various flow regimes can be identified, including a laminar two-dimensional regime when $\alpha < 7°$ and a turbulent three-dimensional regime when $\alpha > 9°$. Specifically, when $\alpha < 7°$ the flow fully separates from the apex of the triangular aerofoil, followed by subsequent vortex roll-up. However, when $\alpha > 9°$, the flow fully separates from the leading edge, with larger and stronger vortices rolling up on the suction surface compared to those shed from the apex. These more energetic vortices induce a large area of low pressure on the suction surface, which enhances lift, but also increases drag. In the transition region between these two regimes, the point of full separation migrates from the apex to the leading edge, resulting in rapid variation of lift with α. In the experimental studies of Munday et al. [15], this transition occurs in the region $\alpha = 8° - 9°$. However, in the computational studies of Munday et al. [15] it occurs in the region $\alpha = 7° - 8°$. The computational studies of Munday et al. [15] comprised span-wise periodic DNS, with a domain-span to chord ratio of 0.3.

4.2 Effects of Domain Span

4.2.1 Overview

In this section the effect of domain span on the accuracy of span-wise periodic DNS is investigated. Specifically, results from two-dimensional (2D) PyFR simulations, and results from span-wise periodic three-dimensional (3D) PyFR simulations with domain span-to-chord ratios of 0.3, 0.6 and 0.9, are compared with previous experimental and computational results from Munday et al. [15]. All simulations were undertaken using PyFR v1.10.0. Simulations were undertaken using Nvidia Tesla V100-SXM2-16GB GPUs on Cirrus at the EPCC Advanced Computing Facility and Nvidia Tesla P100-16GB GPUs on Piz Daint at the Swiss National Supercomputing Centre (CSCS).

4.2.2 Setup

Startup Process and Data Extraction

All simulations were initiated at $t = 0$ with a uniform density $\rho = 1.0$, velocity $\mathbf{v} = \{v_x, v_y, v_z\} = \{1.0, 0.0, 0.0\}$ and pressure $p = 31.746$ throughout the entire domain. Simulations were advanced a period t_t to remove initial transients and then for a further t_e, henceforth referred to as the Data Extraction Period during which data was extracted for analysis. For 2D simulations $t_t = 10t_c$, $t_e = 10t_c$ when $\alpha < 8°$, and $t_t = 15t_c$, $t_e = 15t_c$ when $\alpha \geq 8°$, and for 3D simulations $t_t = 40t_c$, $t_e = 20t_c$ when $\alpha < 8°$, and $t_t = 100t_c$, $t_e = 50t_c$ when $\alpha \geq 8°$, and with, in all cases, $t_c = 1/v_\infty$ where v_∞ is the x-velocity magnitude measured at the centre of the inflow plane and time-averaged over the Data Extraction Period. Note that for the first $5t_c$ of each 3D simulation, the velocity prescribed at the inflow plane was modified to have a time-dependent component as follows $\mathbf{v} = \{1+0.2\sin(100t), 0.2\sin(100t), 0.2\sin(100t)\}$ to trigger flow instabilities.

Computational Domain

The origin in the streamwise-vertical xy-plane is located at the leading edge of the aerofoil when $\alpha = 0°$. When changing the angle of attack, the aerofoil is rotated about its trailing edge. The dimensions

of the computational domain are $x \in [-10, 20]$ in the streamwise direction and $y \in [-10, 10]$ in the vertical direction. These are the same as those used in the computational study of Munday et al. [15]. The span-wise extent of the domain is varied, from zero for the 2D cases to $z \in [0, \delta_z]$ for the 3D cases, where the domain span δ_z is set to be 0.3, 0.6 and 0.9.

Meshes

For the 2D simulations, meshes are comprised of structured and unstructured regions in the streamwise-vertical xy-plane. Specifically, structured quadrilateral meshes are located adjacent to the aerofoil surfaces, extending a distance of 0.2 normally from the upper surface and 0.1 normally from the lower surface into the domain. For high angles of attack, structured regions on the upper surface are augmented after the apex to extend a distance of 0.5 normally into the domain. Structured quadrilateral meshes are also located in the wake region, extending a distance of 6.0 downstream of the aerofoil. The remainder of the streamwise-vertical xy-plane meshes are tessellated with an unstructured mix of quadrilaterals and triangles. Figure 4.2 shows the mesh in the streamwise-vertical xy-plane for $\alpha = 12°$. The 2D meshes have $\sim 6 \times 10^3$ elements and $\sim 160 \times 10^3$ degrees of freedom per equation in total when fourth-order solution polynomials are used to represent the solution within each element.

For the 3D simulations, the analogous 2D mesh is extruded in the span-wise z direction, generating hexahedra and triangular prisms throughout the domain. The largest 3D meshes have $\sim 155 \times 10^3$ elements, and $\sim 19.4 \times 10^6$ degrees of freedom per equation in total when fourth-order solution polynomials are used to represent the solution within each element.

Finally, we note that a grid independence study was undertaken for the 2D case with $\alpha = 15°$, in which the mesh was refined isotropically to have 1.92 and then 5.13 times more elements. This resulted in values of $\overline{C}_L$ varying by less than 0.4%. Moreover, for the 3D case with $\alpha = 15°$ and $\delta_z = 0.9$ it was verified a posteriori in Figure 4.3 that $2.5\eta > \Delta$ everywhere in the wake, where

$$\Delta = \frac{\sqrt[3]{V}}{\wp + 1} \tag{4.5}$$

is an estimate of the local solution point spacing, with V the local element volume and $\wp$ the polynomial

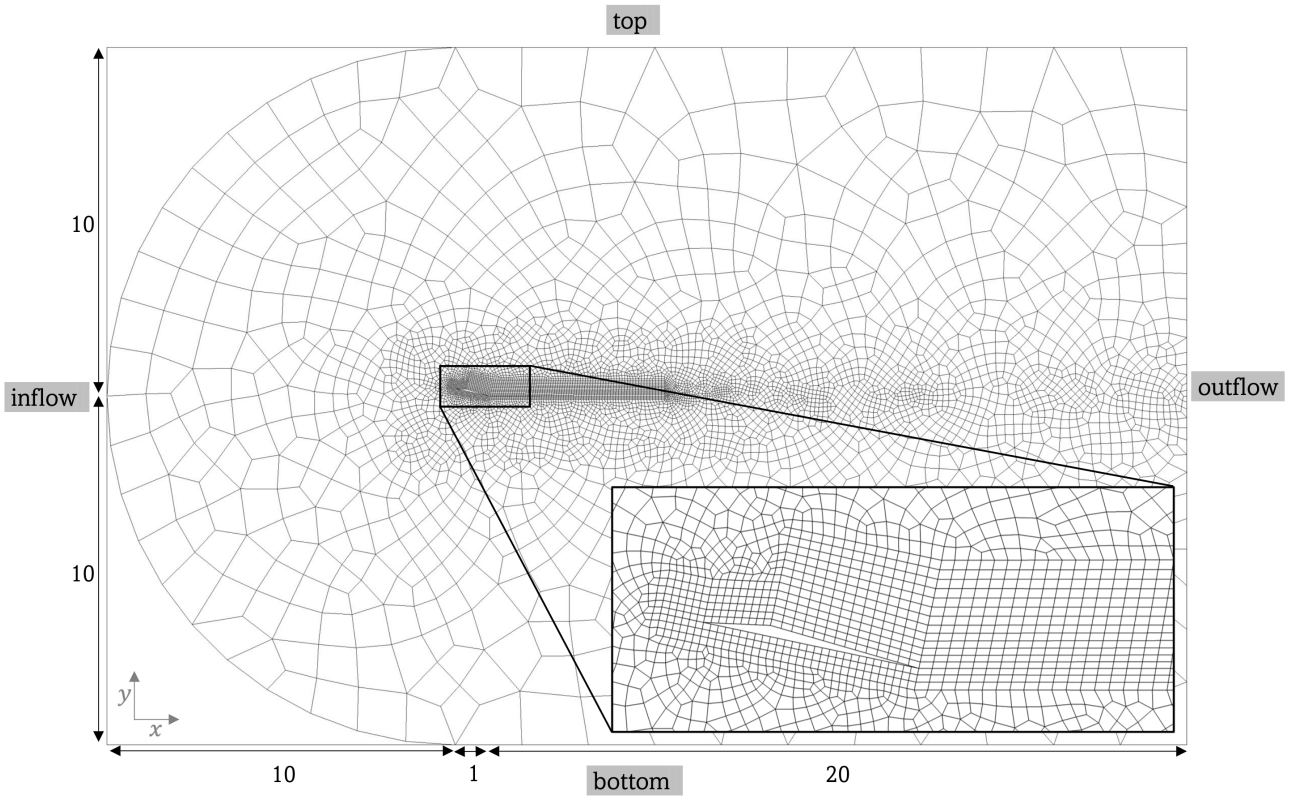


Figure 4.2: View of mesh in the streamwise-vertical xy-plane used for 2D and span-wise periodic 3D DNS with $\alpha = 12°$ of the Reference aerofoil. The origin in the streamwise-vertical xy-plane is located at the leading edge of the aerofoil when $\alpha = 0°$.

order used to represent the solution within each element of the mesh, and

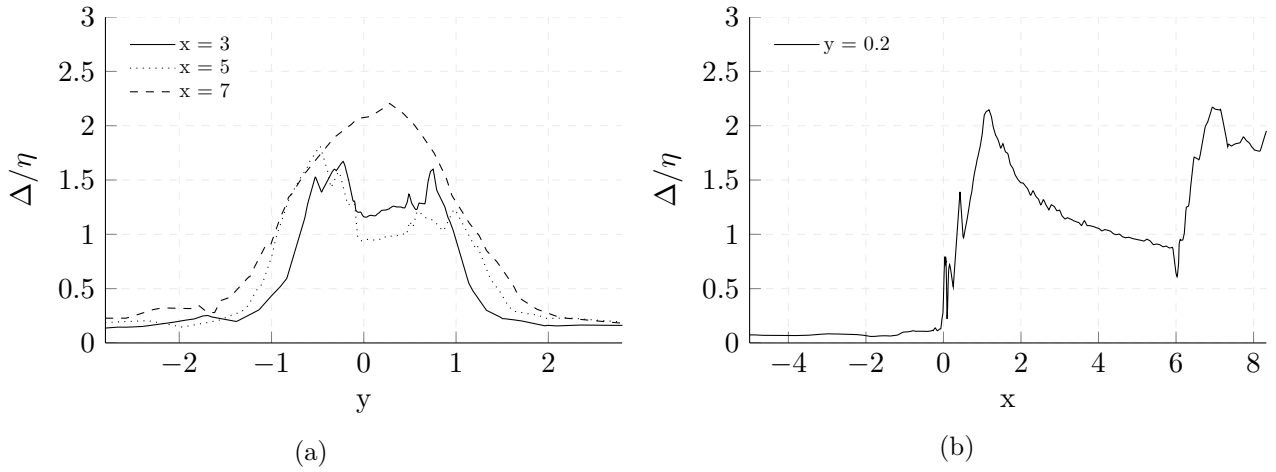
$$\eta = \left(\frac{\nu^3}{\varepsilon}\right)^{1/4} \tag{4.6}$$

is the Kolmogorov length scale, with ν the kinematic viscosity and

$$\varepsilon = 2\nu s_{ij} s_{ij} \tag{4.7}$$

the dissipation rate, where s_{ij} is the fluctuating rate-of-strain tensor. This is within the threshold required to achieve DNS resolution given the simulations are nominally fifth-order accurate in space [125]. Span-wise periodic DNS with $\alpha = 15°$ and $\delta_z = 0.9$ was re-started from $t = 100t_c$ and run for a further $400t_c$, during which data was extracted for analysis. Figure 4.3 shows plots of Δ/η along various mid-span lines for the span-wise periodic and virtual wind tunnel cases, respectively, where Δ is an estimate of the solution point spacing given by Eq. (4.5) and η is an estimate of the Kolmogorov

length scale given by Eq. (4.6).



(a) (b)

Figure 4.3: Plots of Δ/η in the mid-span plane as a function of y at $x = 3$, $x = 5$ and $x = 7$ (a) and as a function of x at $y = 0.2$ (b) for span-wise periodic 3D DNS with $\alpha = 15°$ and $\delta_z = 0.9$ of the Reference aerofoil.

Boundary Conditions

At the $x = -10$ inflow, $x = 20$ outflow, $y = -10$ bottom, and $y = 10$ top planes a characteristic boundary condition was applied. Specifically, a density $\rho = 1.0$, velocity $\mathbf{v} = \{v_x, v_y, v_z\} = \{1.0, 0.0, 0.0\}$ and pressure $p = 31.746$ were prescribed. An impermeable no-slip adiabatic boundary condition was prescribed at the aerofoil surface. For the 3D cases, periodic boundary conditions were applied in the span-wise direction. Taken together these conditions achieved $M = 0.15$ and $Re = 3,000$. Note that no turbulence was injected at the inflow.

4.2.3 Results

Figure 4.4 shows plots of $\overline{C}_L$ and $\overline{C}_D$ as a function of α for the 2D and span-wise periodic DNS undertaken with PyFR, as well as for the previous DNS and experimental studies of Munday et al. [15].

The 2D PyFR results are seen to be in reasonable agreement with the experimental $\overline{C}_L$ and good agreement with the experimental $\overline{C}_D$ for low α. However, as α increases and the flow becomes highly separated and unsteady, the 2D PyFR simulations start to significantly over-predict both $\overline{C}_L$ and $\overline{C}_D$ relative to the experimental results, with discrepancies in $\overline{C}_L$ reaching 80% when $\alpha = 15°$.

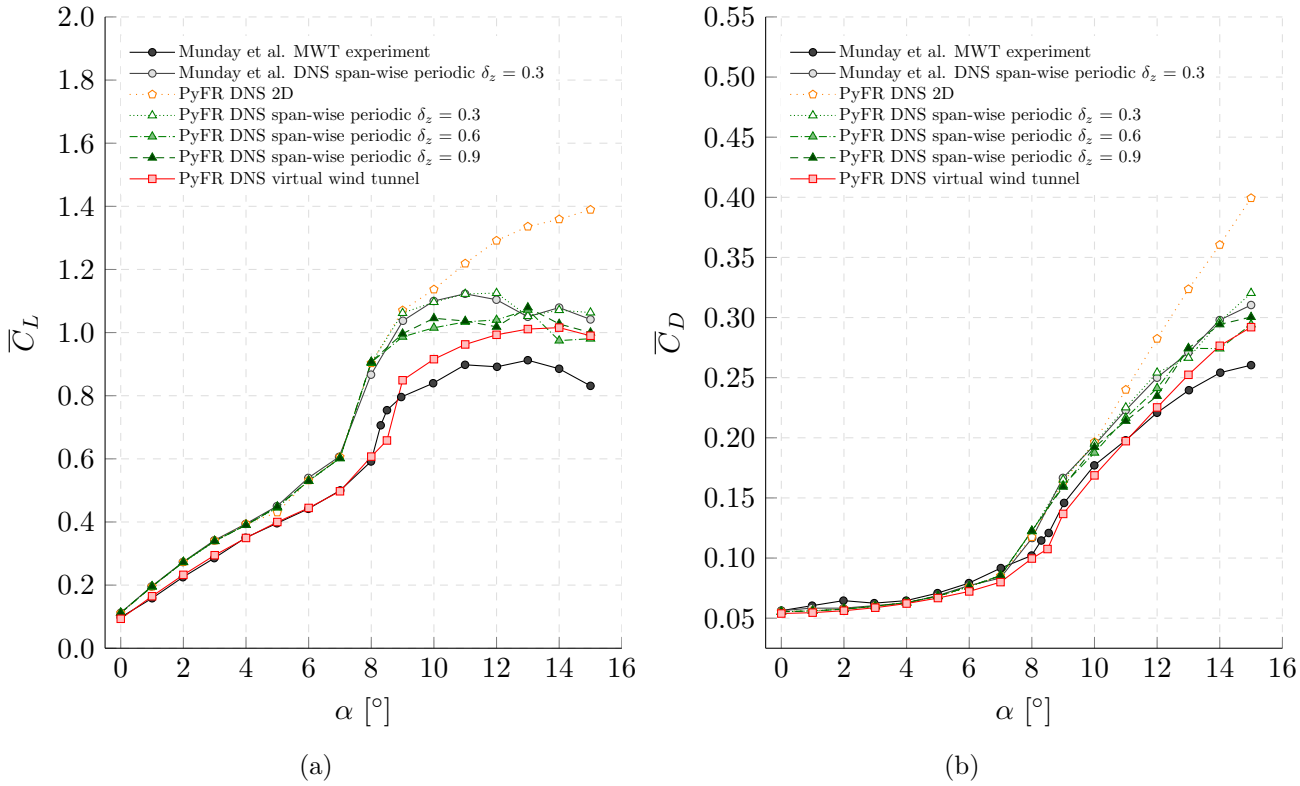


Figure 4.4: Plots of time-averaged lift coefficient $\overline{C}_L$ (a) and drag coefficient $\overline{C}_D$ (b) as a function of angle of attack α obtained from the MWT experiments of Munday et al. [15], span-wise periodic DNS with $\delta_z = 0.3$ of Munday et al. [15], 2D DNS using PyFR, span-wise periodic DNS with $\delta_z = 0.3$, $\delta_z = 0.6$, $\delta_z = 0.9$ using PyFR, and DNS in a virtual wind tunnel using PyFR.

The span-wise periodic DNS results obtained using PyFR with $\delta_z = 0.3$ are seen to be in excellent agreement with both $\overline{C}_L$ and $\overline{C}_D$ obtained from the previous DNS of Munday et al. [15], which were undertaken using the same domain span to chord ratio of 0.3. The trends in both $\overline{C}_L$ and $\overline{C}_D$ are also closer to the experimental data than the 2D PyFR results. This is because the span-wise periodic DNS can capture the breakdown of large vortical structures shed above the suction surface of the aerofoil. The importance of this effect becomes particularly apparent when $\alpha \geq 9°$ after the point of full separation has moved to the leading edge of the aerofoil. Capturing the de-correlation of these coherent vortical structures is of high importance to accurately predict the performance of these unconventional aerofoils since they are their primary lift-generating mechanism, as detailed in Chapter 2.

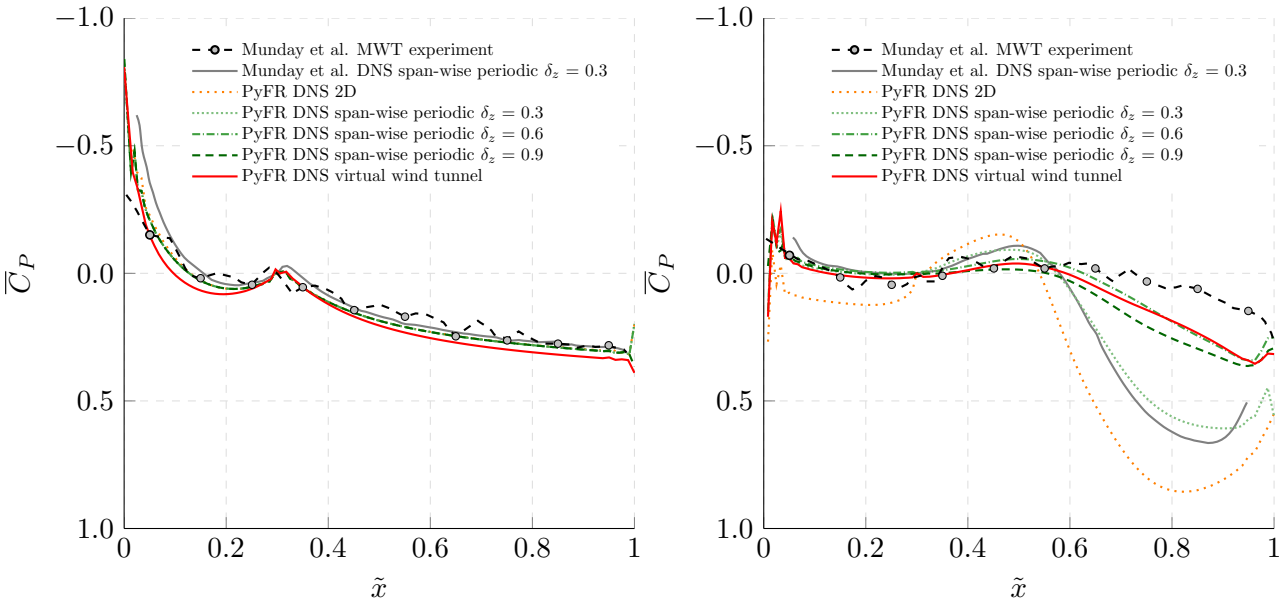
The span-wise periodic DNS results obtained using PyFR with $\delta_z = 0.6$ and $\delta_z = 0.9$ are similar to those obtained with $\delta_z = 0.3$ when $\alpha \leq 9°$. However, when $\alpha \geq 9°$ they achieve better agreement with the experimental $\overline{C}_L$ and $\overline{C}_D$. Specifically, except for when $\alpha = 13°$, discrepancies relative to

the experimental $\overline{C}_L$ and $\overline{C}_D$ are reduced by between 20% and 50%. However, we note that changing from $\delta_z = 0.6$ to $\delta_z = 0.9$ has little additional effect on both $\overline{C}_L$ and $\overline{C}_D$.

Figure 4.5 shows plots of $\overline{C}_P$ for $\alpha = 6^\circ$ and $\alpha = 12^\circ$ on the suction surface of the aerofoil as a function of $\tilde{x} = x/a$, where a is the x-wise distance between the leading and trailing edge of the aerofoil, for the 2D and span-wise periodic DNS undertaken with PyFR, as well as for the previous DNS and experimental studies of Munday et al. [15]. For the span-wise periodic DNS $\overline{C}_P$ was obtained using Eq. (4.3), where p was obtained at each $\tilde{x}$ by space-time-averaging static pressure on the suction surface of the aerofoil in span and over the Data Extraction Period, $\overline{p}_a$ was obtained by space-time-averaging static pressure within all mesh cells that had vertices coincident with the apex of the aerofoil and over the Data Extraction Period, and q_∞ was obtained via Eq. (4.4).

When $\alpha = 6^\circ$ the 2D and span-wise periodic DNS results obtained using PyFR are seen to be in good agreement with $\overline{C}_P$ obtained from the previous DNS and experiments of Munday et al. [15]. However, when $\alpha = 12^\circ$ differences occur. Specifically, the 2D PyFR simulations start to significantly over-predict $\overline{C}_P$ above the down-stream section of the aerofoil relative to the experimental results. Span-wise periodic DNS results obtained using PyFR with $\delta_z = 0.3$ are seen to reduce this discrepancy, and achieve good agreement with $\overline{C}_P$ distributions obtained from the previous DNS of Munday et al. [15], which were undertaken using the same domain span to chord ratio of 0.3. Increasing the domain span to $\delta_z = 0.6$ is seen to reduce the discrepancy further still, dramatically flattening the $\overline{C}_P$ distribution above the down-stream section of the aerofoil, and bringing it significantly closer to the experimental results. However, further increasing the domain span from $\delta_z = 0.6$ to $\delta_z = 0.9$ has little additional effect on $\overline{C}_P$.

Figure 4.6 shows instantaneous Q-criterion iso-surfaces, coloured by velocity magnitude, for the case with $\alpha = 12^\circ$ when $\delta_z = 0.3$ and $\delta_z = 0.9$, and at different points in the shedding cycle. Specifically, the left-hand column shows the instant of maximum lift in a specific shedding cycle, the middle column shows an instant of intermediate lift in the same cycle, and the right-hand column shows the instant of minimum lift in the same cycle. Figure 4.7 shows instantaneous density gradient, at the instant of maximum lift in a specific shedding cycle, for the case with $\alpha = 12^\circ$ when $\delta_z = 0.3$ and $\delta_z = 0.9$, and in different y-z planes. Specifically, the left-hand column shows a plane at the trailing edge, the middle column shows a plane half a chord downstream from the trailing edge, and the right-hand column



(a) (b)

Figure 4.5: Plots of pressure coefficient $\overline{C}_P$ as a function of $\tilde{x}$ for angles of attack $\alpha = 6°$ (a) and $\alpha = 12°$ (b) on the suction surface of the aerofoil obtained from the MWT experiments of Munday et al. [15], span-wise periodic DNS with $\delta_z = 0.3$ of Munday et al. [15], 2D DNS using PyFR, span-wise periodic DNS with $\delta_z = 0.3$, $\delta_z = 0.6$, $\delta_z = 0.9$ using PyFR, and DNS in a virtual wind tunnel using PyFR.

shows a plane one chord downstream from the trailing edge. Note that for the case with $\delta_z = 0.3$ the periodic data is repeated three times to facilitate comparison with the $\delta_z = 0.9$ case.

Taken together, Figures 4.6 and 4.7 show how using $\delta_z = 0.3$ imposes non-physical periodicity, and artificially suppresses the three-dimensional breakdown of coherent structures that form above the suction surface of the aerofoil and in the wake.

4.3 Effects of Wind Tunnel Walls

4.3.1 Overview

This section assesses the effect of simulating the wind tunnel walls on the DNS' ability to reproduce experimental results. Specifically, results from full-span DNS of the triangular aerofoil in a virtual wind tunnel, including all wind tunnel walls, are compared with previous experimental and computational results from Munday et al. [15].

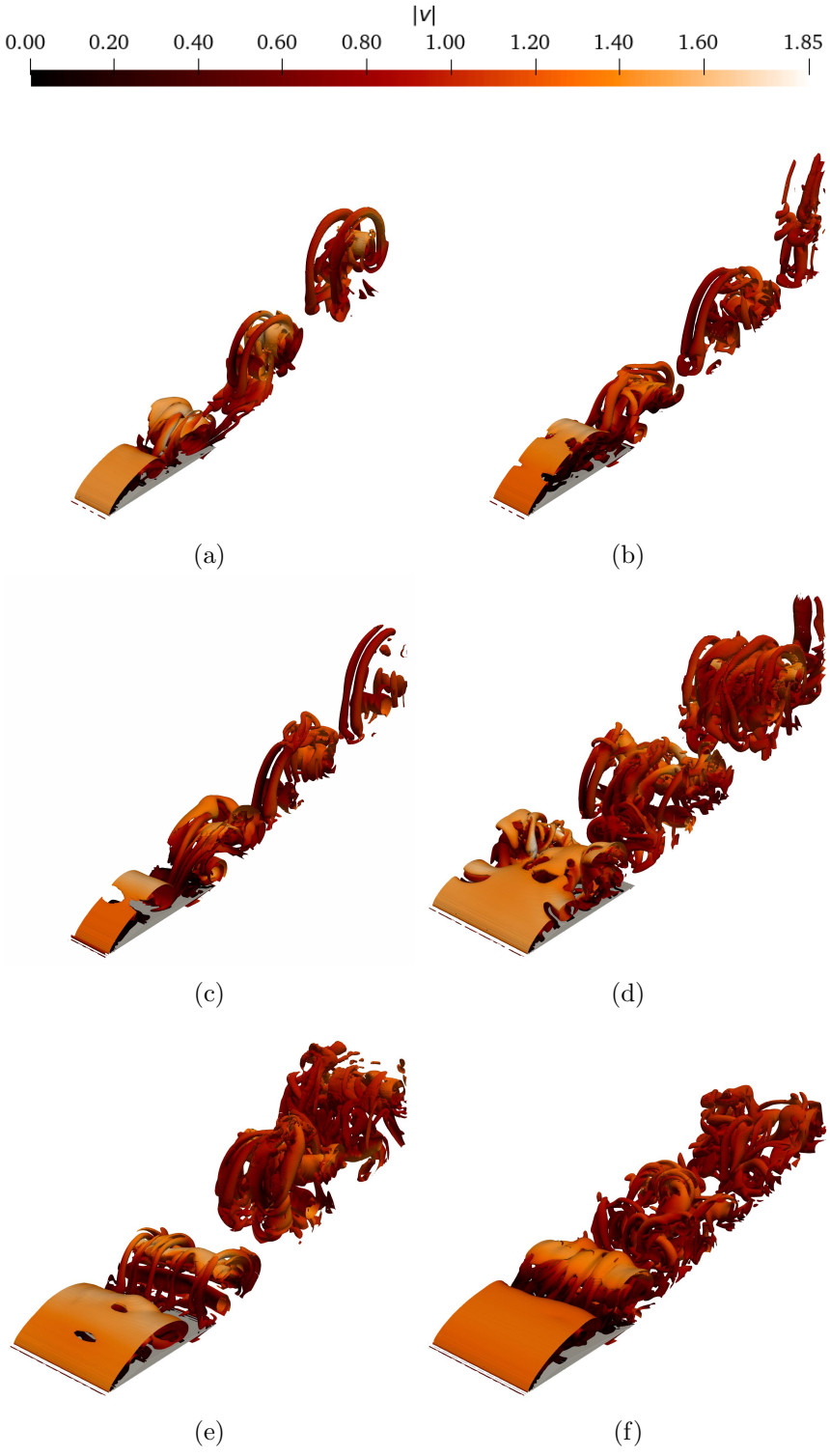


Figure 4.6: Images of instantaneous Q-criterion isosurfaces $Q = 1$, coloured by velocity magnitude $|v|$, for $\alpha = 12°$ when $\delta_z = 0.3$ (a), (b) and (c), and $\delta_z = 0.9$ (d), (e) and (f), at different points in the shedding cycle: maximum lift (a) and (d), intermediate lift (b) and (e), and minimum lift (c) and (f).

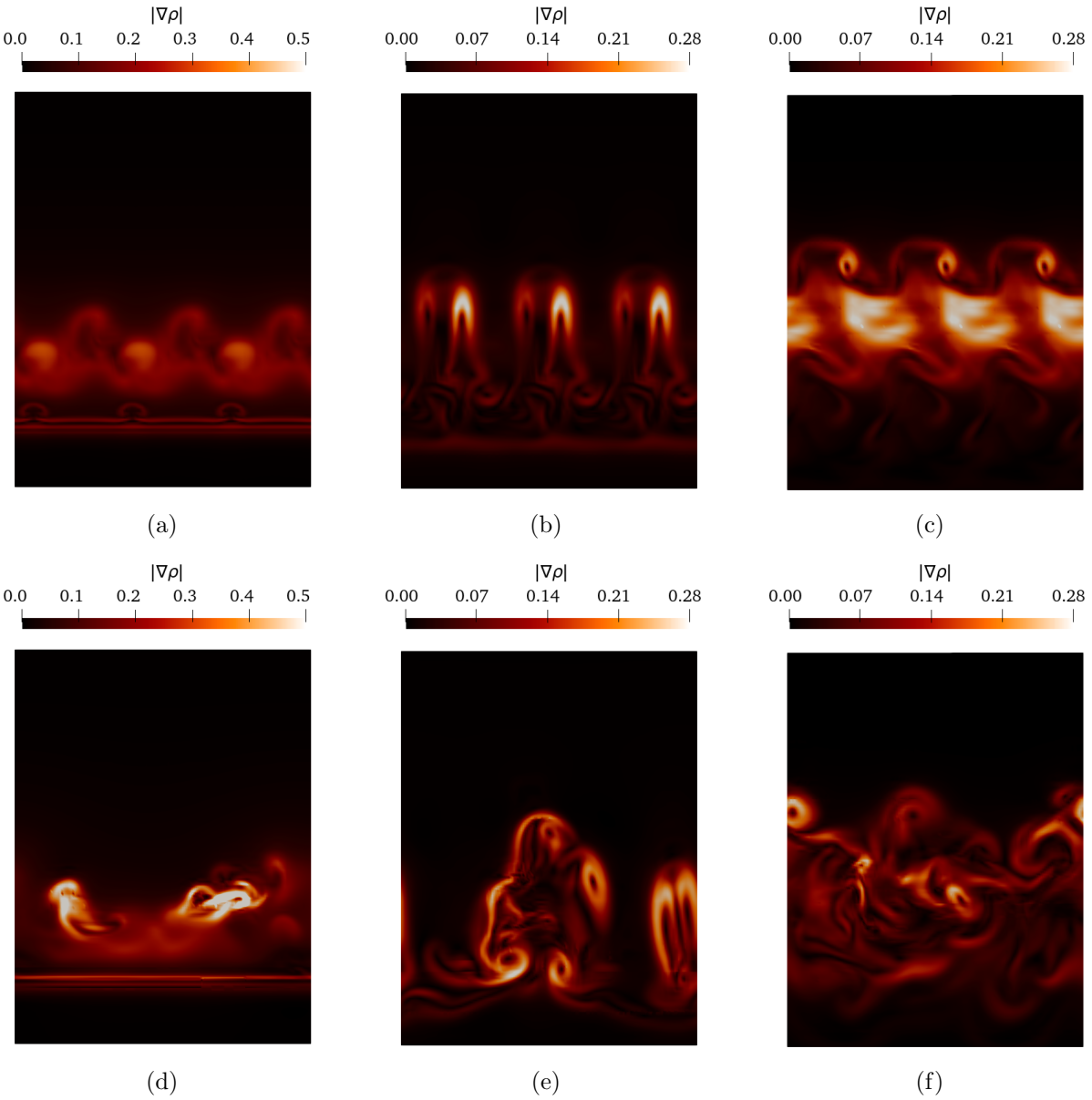


Figure 4.7: Images of instantaneous density gradient magnitude $|\nabla\rho|$, at the instant of maximum lift in a specific shedding cycle, for $\alpha = 12°$ when $\delta_z = 0.3$ (a), (b) and (c), and $\delta_z = 0.9$ (d), (e) and (f), in different y-z planes: (a) and (d) show a plane at the trailing edge, (b) and (e) show a plane half a chord downstream from the trailing edge, and (c) and (f) show a plane one chord downstream from the trailing edge. Note that for the case with $\delta_z = 0.3$ the periodic data is repeated three times to facilitate comparison with the $\delta_z = 0.9$ case.

4.3.2 Setup

Startup Process and Data Extraction

All simulations were initiated at $t = 0$ with a uniform density $\rho = 1.0$, velocity $\mathbf{v} = \{v_x, v_y, v_z\} = \{1.0, 0.0, 0.0\}$ and pressure $p = 34.337$ throughout the entire domain. Simulations were advanced a period t_t to remove initial transients, where $t_t = 96t_c$ when $\alpha < 8$ and $t_t = 144t_c$ when $\alpha \geq 8$, and then a further period t_e, henceforth referred to as the Data Extraction Period during which data was extracted for analysis, where $t_e = 48t_c$ when $\alpha < 8$ and $t_e = 72t_c$ when $\alpha \geq 8$, and with, in all cases, $t_c = 1/v_\infty$.

Computational Domain

As per Sec. 4.2.2, the origin in the streamwise-vertical xy-plane is located at the leading edge of the aerofoil when $\alpha = 0°$. When changing the angle of attack, the aerofoil is rotated about its trailing edge. The dimensions of the computational domain are $x \in [-5, 8.333]$ in the streamwise direction, $y \in [-2.5, 2.5]$ in the vertical direction at the inlet, and $z \in [0, 3.333]$ in the span-wise direction, with the top and bottom walls inclined at an angle of 1.3° to the streamwise direction. This configuration matches the working section of the MWT, in which the experiments of Munday et al. [15] were undertaken.

Meshes

Meshes are constructed by extruding 2D streamwise-vertical xy-plane meshes in the span-wise z direction. The streamwise-vertical xy-plane meshes are comprised of structured and unstructured regions. Specifically, structured quadrilateral meshes are located adjacent to the aerofoil surfaces, extending a distance of 0.2 normally from the upper surface and 0.1 normally from the lower surface into the domain. For high angles of attack structured regions on the upper surface are augmented after the apex to extend a distance 0.5 normally into the domain. Structured quadrilateral meshes are also located in the wake region, extending a distance of 6.0 downstream of the aerofoil, and adjacent to the top and bottom walls, extending a distance of 0.3 normally into the domain. The remainder of the

streamwise-vertical xy-plane meshes are tessellated with an unstructured mix of quadrilaterals and triangles. Extrusion of the 2D meshes in the span-wise z direction, generates hexahedra and triangular prisms throughout the domain. Figure 4.8 shows the external surface of the mesh for $\alpha = 12°$. The mesh has $\sim 1.3 \times 10^6$ elements, and $\sim 138 \times 10^6$ degrees of freedom per equation in total when fourth-order solution polynomials are used to represent the solution within each element.

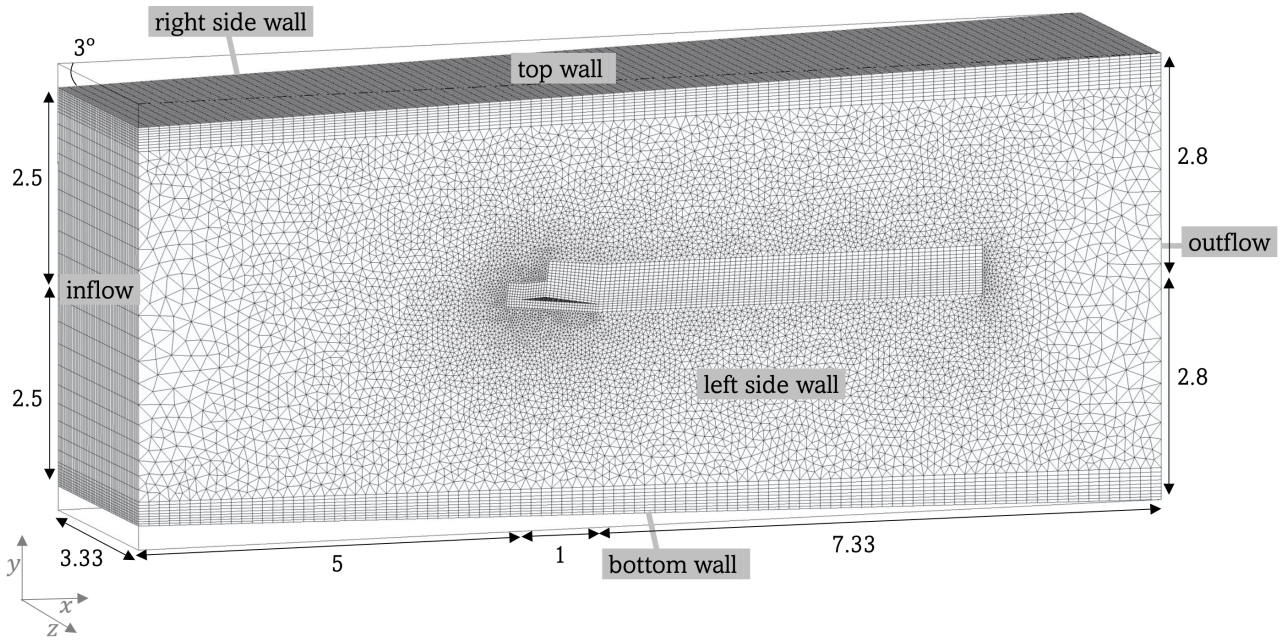
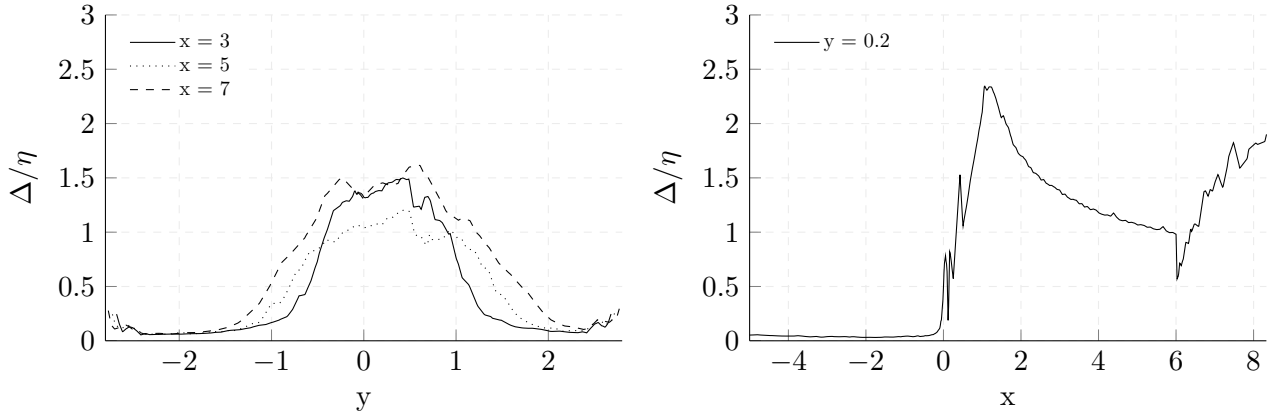


Figure 4.8: View of the computational mesh used for the virtual wind tunnel DNS with $\alpha = 12°$. The origin in the streamwise-vertical xy-plane is located at the leading edge of the aerofoil when $\alpha = 0°$.

Finally, we note that mesh cells adjacent to the wind tunnel walls are sized aiming for $\delta_\nu > \Delta$ in the boundary layer, where δ_ν is the local diffusive length scale of a Blasius boundary layer solution. Moreover, for the $\alpha = 15°$ case, it was verified a posteriori in Figure 4.9 that $2.5\eta > \Delta$ everywhere in the wake. This is within the threshold required to achieve DNS resolution given the simulations are nominally fifth-order accurate in space [125]. DNS in a virtual wind tunnel with $\alpha = 15°$ was re-started from $t = 144t_c$ and run for a further $383t_c$, during which data was extracted for analysis. Figure 4.9 shows plots of Δ/η along various mid-span lines for the virtual wind tunnel case, where Δ is an estimate of the solution point spacing given by Eq. (4.5) and η is an estimate of the Kolmogorov length scale given by Eq. (4.6).



(a) (b)

Figure 4.9: Plots of Δ/η in the mid-span plane as a function of y at $x = 3$, $x = 5$ and $x = 7$ (a) and as a function of x at $y = 0.2$ (b) for DNS in a virtual wind tunnel with $\alpha = 15°$.

Boundary Conditions

At the $x = -15$ inflow, a total pressure boundary condition was applied. Specifically, a total pressure $p_T = 34.8804$, a total temperature $T_T = 0.1196$ and an inflow angle normal to the inflow plane were prescribed uniformly. At the $x = 8.333$ outflow plane, a characteristic boundary condition was applied consisting of a uniform distribution of density $\rho = 1.0$ and pressure $p = 34.3365$, along with a spatially varying velocity $\mathbf{v} = \{v_x, v_y, v_z\} = \{(\tanh(8.307(y + 2.803)) - \tanh(8.307(y - 2.803)) - 1.0)(\tanh(8.307z) - \tanh(8.307(z - 3.333)) - 1.0), 0.0, 0.0\}$. This velocity profile was selected by fitting hyperbolic tangent functions to match the velocity distribution observed at the exit plane in a reference simulation with an extended domain. The use of this profile ensured that the laminar boundary layer could develop naturally in the domain, avoiding artificial perturbations at the exit, as shown in Fig. 4.10. An impermeable no-slip adiabatic boundary condition was prescribed at the aerofoil surface and the wind tunnel walls. Taken together these conditions achieved $M = 0.15$ and $Re = 3,000$. Note that no boundary layer and no turbulence was injected at the inflow.

4.3.3 Results

Full-span DNS in a virtual wind tunnel captures two important aspects of the flow physics that are not present in the previous span-wise periodic DNS. Specifically, blockage effects are captured, as are interactions between side wall boundary layers and the triangular aerofoil, which lead to span-wise

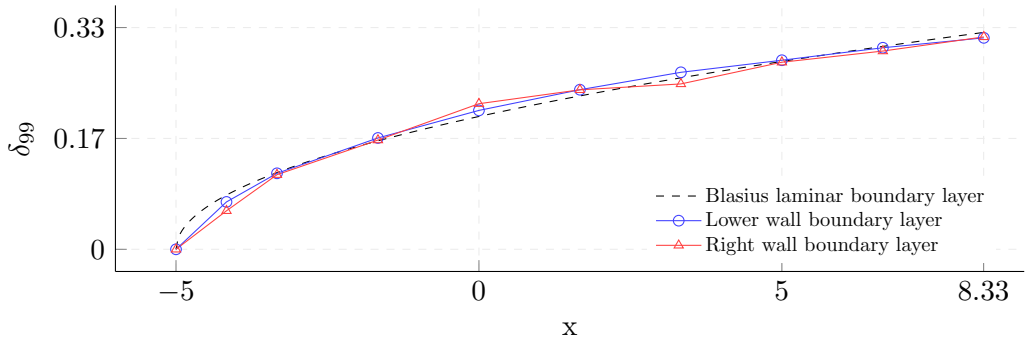


Figure 4.10: Plot of the boundary layer thickness δ_{99} as a function of $\mathbf{x}$ for the virtual wind tunnel DNS with $\alpha = 11°$ on the lower and right-hand-side walls, measured at the mid-span and mid-height respectively, alongside the Blasius laminar boundary layer thickness.

variations in the flow field.

Figure 4.4 shows plots of $\overline{C}_L$ and $\overline{C}_D$ as a function of α for DNS in a virtual wind tunnel undertaken with PyFR, as well as for the previous DNS and experimental studies of Munday et al. [15]. For the PyFR simulations $\overline{C}_L$ and $\overline{C}_D$ were obtained using Eq. (4.3), where $\overline{F}_L$ and $\overline{F}_D$ were obtained by time-averaging the sum of viscous and pressure forces on the aerofoil in the y and x directions, respectively, over the Data Extraction Period, and q_∞ was obtained via Eq. (4.4).

Results from DNS in a virtual wind tunnel are seen to be in excellent agreement with the experimental $\overline{C}_L$ and $\overline{C}_D$ for low α. This agreement is markedly better than that achieved using span-wise periodic DNS. Moreover, it extends through to $\alpha = 9°$, past the point at which full separation migrates from the apex to the leading edge of the aerofoil. Indeed, at e.g. $\alpha = 8°$ the resulting error in $\overline{C}_L$ relative to the experimental data is 95% less than that achieved using span-wise periodic DNS. Finally, we note that when $\alpha > 9°$ discrepancies begin to emerge between results from DNS in a virtual wind tunnel and the experimental $\overline{C}_L$ and $\overline{C}_D$. However, these discrepancies are on the whole less than, or at worst similar to, those achieved using span-wise periodic DNS.

Figure 4.5 shows plots of $\overline{C}_P$ for $\alpha = 6°$ and $\alpha = 12°$ on the suction surface of the aerofoil as a function of $\tilde{x}$, for DNS in a virtual wind tunnel undertaken with PyFR, as well as for the previous DNS and experimental studies of Munday et al. [15]. For the DNS in a virtual wind tunnel $\overline{C}_P$ was obtained using Eq. (4.3), where $\overline{p}$ was obtained at each $\tilde{x}$ by time-averaging mid-span static pressure on the suction surface of the aerofoil over the Data Extraction Period, $\overline{p}_a$ was obtained by space-time-averaging static pressure within the two mid-span mesh cells that had vertices coincident with the

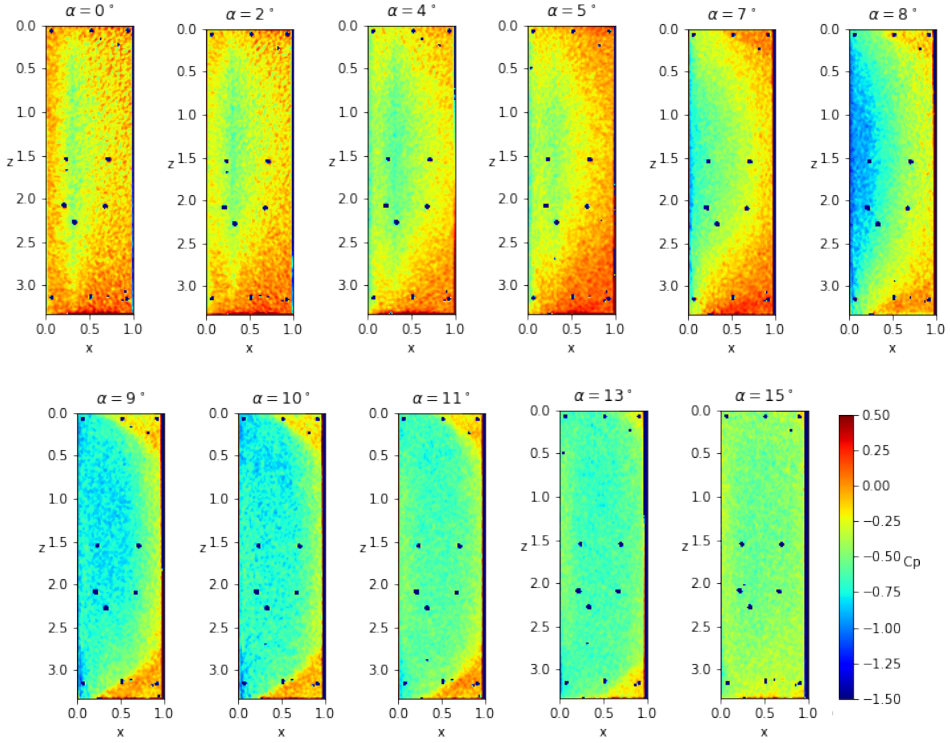
apex of the aerofoil and over the Data Extraction Period, and q_∞ was obtained via Eq. (4.4).

When $\alpha = 6^\circ$ results from DNS in a virtual wind tunnel are seen to be in good agreement with mid-span $\overline{C}_P$ obtained from the previous DNS and experiments of Munday et al. [15]. However, when $\alpha = 12^\circ$ differences occur. Specifically, DNS in a virtual wind tunnel over-predicts $\overline{C}_P$ above the down-stream section of the aerofoil relative to the experimental results. The discrepancies are similar to those that occur for span-wise periodic DNS with $\delta_z = 0.6$ and $\delta_z = 0.9$.

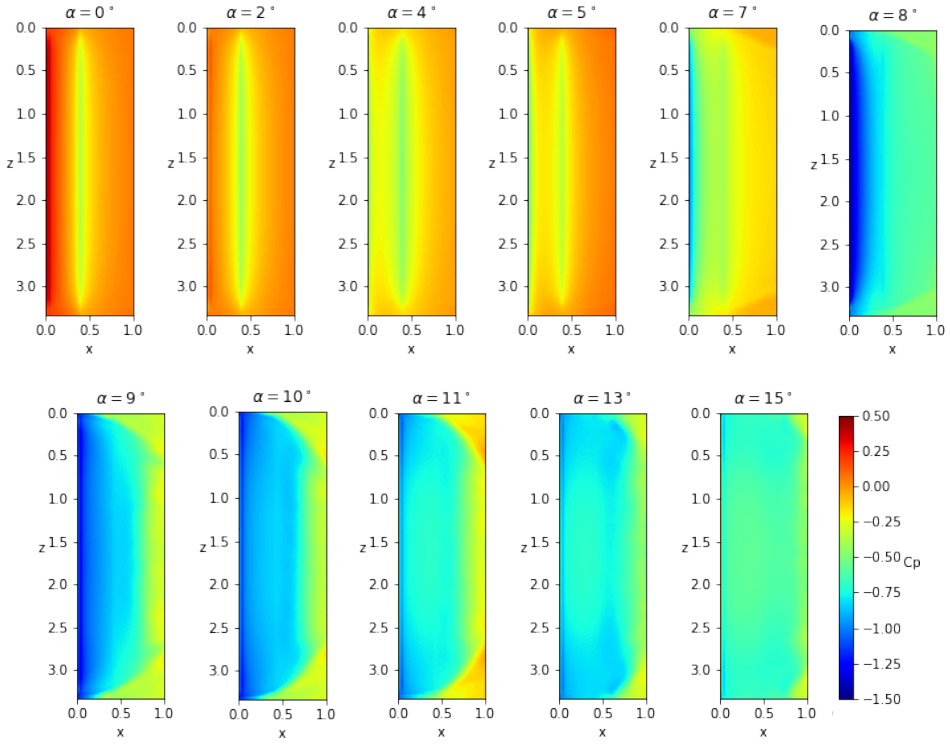
Figure 4.11 shows distributions of $\overline{C}_P$ on the suction surface of the aerofoil for DNS in a virtual wind tunnel undertaken with PyFR, as well as for the experimental studies of Munday et al. [15]. For the PyFR simulations, $\overline{C}_P$ distributions were obtained using Eq. (4.3), where $\overline{p}$ was obtained by time-averaging static pressure on the suction surface of the aerofoil over the Data Extraction Period, plus an additional constant but α dependent shift; calculated to ensure each distribution had the same span-wise average at the apex as the analogous experimental distribution. This shift was applied in order to enable (at least qualitative) comparison between results, under the constraint that precise values of the normalisation constants used to obtain the experimental $\overline{C}_P$ distributions were no longer available. For all α, results from DNS in a virtual wind tunnel are seen to be in good qualitative agreement with $\overline{C}_P$ distributions obtained experimentally by Munday et al. [15].

Figure 4.12 shows instantaneous Q-criterion iso-surfaces, coloured by velocity magnitude, for various α, obtained using span-wise periodic DNS with $\delta_z = 0.9$, and DNS in a virtual wind tunnel. It can be seen that even for low α, DNS in a virtual wind tunnel leads to the breakdown of span-wise uniform coherent structures, and hence 3D flow physics. In contrast, the flow remains entirely 2D for span-wise periodic DNS when α is low. The excellent matching between simulation results and experimental data at low angles of attack can be explained by this breakdown of 2D structures into 3D flow, and due to the blockage in the virtual wind tunnel.

Figure 4.13 shows time-averaged velocity magnitude in the mid-span plane with superimposed velocity Line Integral Convolutions (LICs), for various α, obtained using span-wise periodic DNS with $\delta_z = 0.9$, and DNS in a virtual wind tunnel. Figure 4.14 shows time-averaged wall shear stress magnitude $|\boldsymbol{\tau}|$ on the suction surface of the aerofoil with superimposed time-averaged wall shear stress Line Integral Convolutions (LICs), for various α, obtained using DNS in a virtual wind tunnel. Figure 4.15 shows



(a)



(b)

Figure 4.11: Plots of $\overline{C}_P$ distribution on the suction surface of the wing obtained by experimental studies of Munday et al. [15] (a) and DNS in a virtual wind tunnel using PyFR (b).

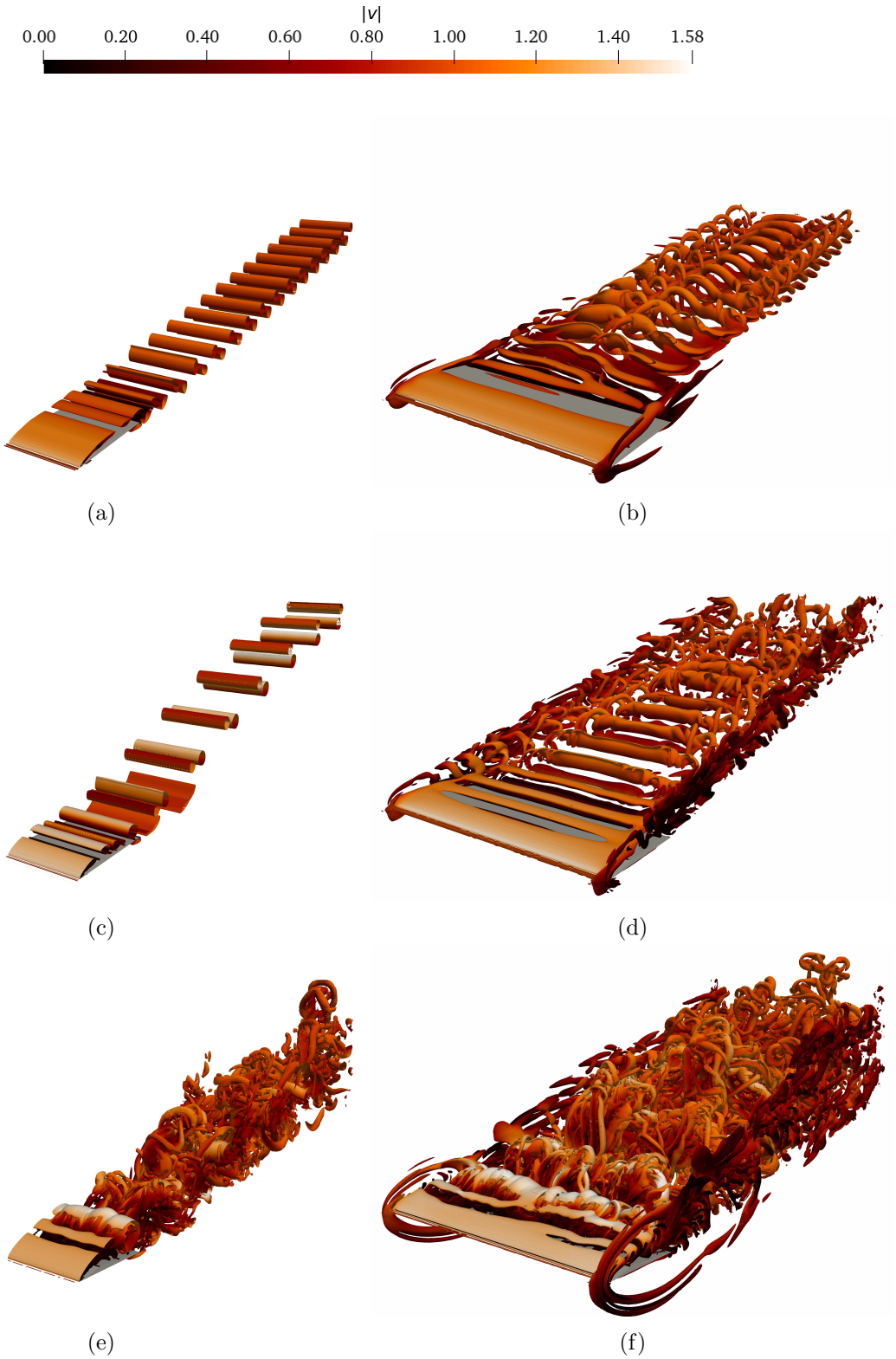


Figure 4.12: Images of instantaneous Q-criterion isosurfaces $Q = 1$, coloured by velocity magnitude $|v|$, for angles of attack $\alpha = 6°$ (a) and (b), $\alpha = 8°$ (c) and (d), and $\alpha = 15°$ (e) and (f), from span-wise periodic DNS with span $\delta_z = 0.9$ (a), (c) and (e), and virtual wind tunnel DNS (b), (d) and (f).

the time-averaged friction coefficient defined as

$$\overline{C}_f = \frac{\tau_s}{q_\infty}, \tag{4.8}$$

where τ_s is the stream-wise component of the time-averaged wall shear stress and q_∞ was obtained via Eq. (4.4), on the suction surface of the aerofoil in the mid-span plane as a function of $\tilde{\boldsymbol{x}}$, for various α, obtained using span-wise periodic DNS with $\delta_z = 0.9$, and DNS in a virtual wind tunnel.

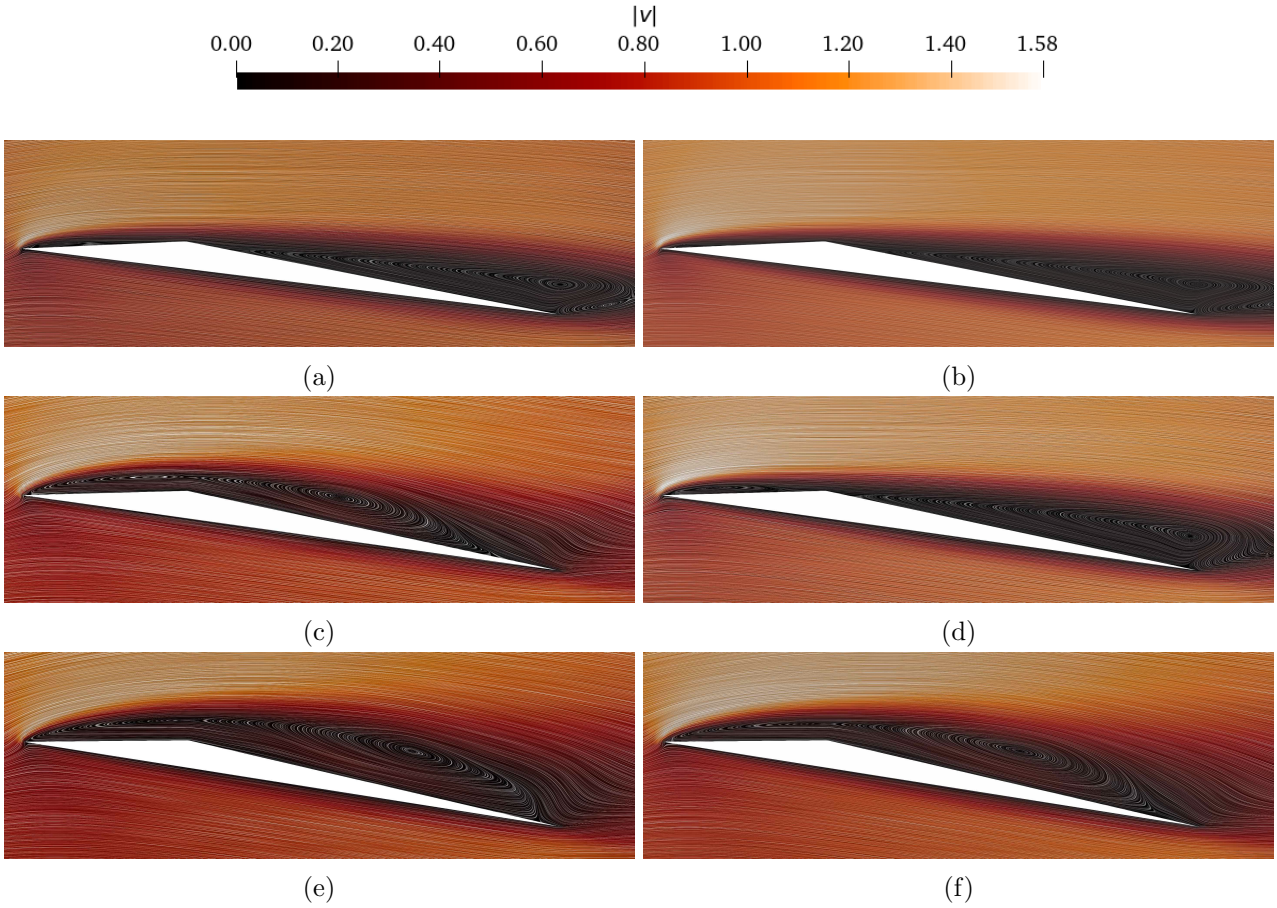
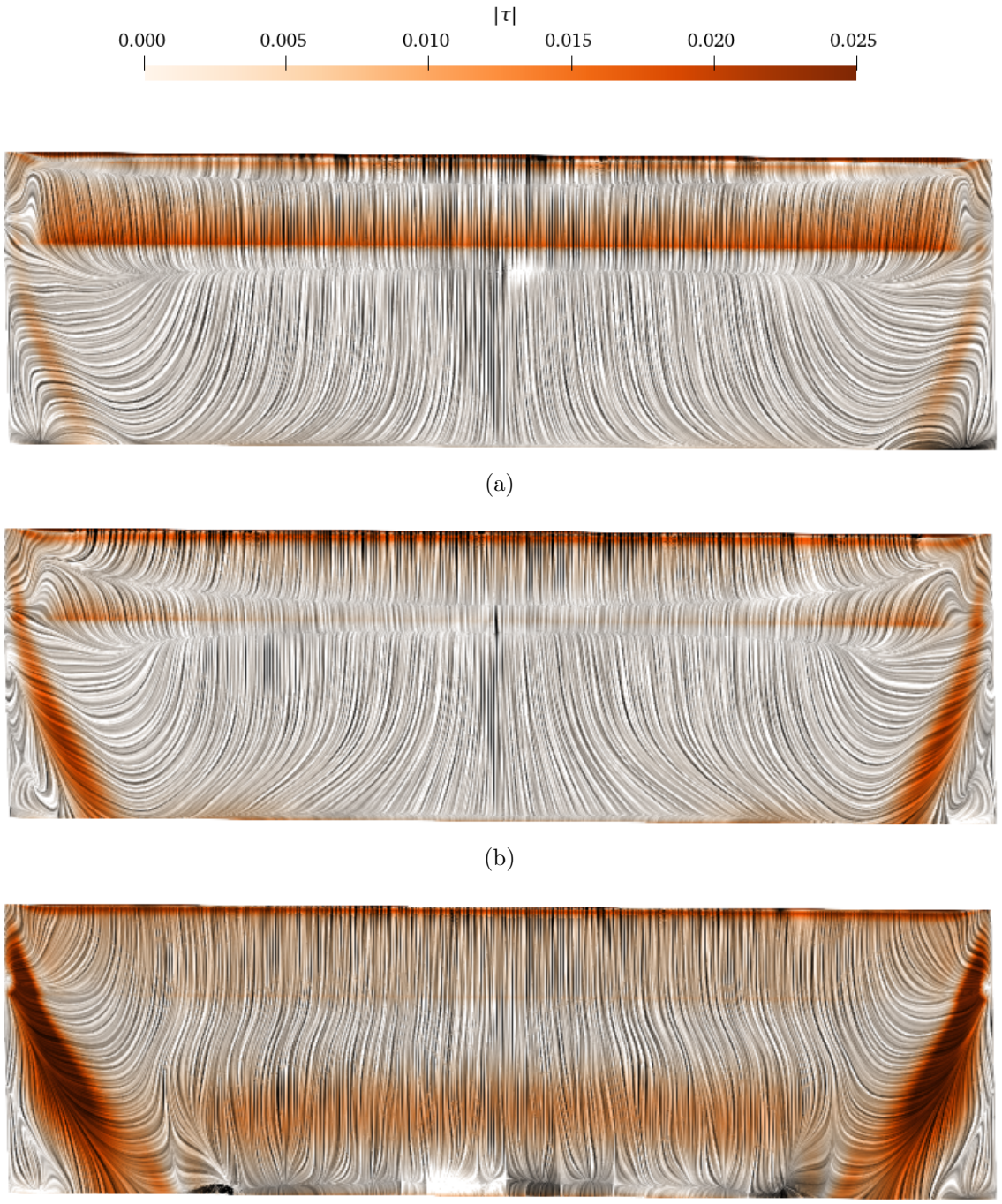


Figure 4.13: Images of time-averaged velocity magnitude $|v|$ in the mid-span plane with superimposed velocity Line Integral Convolutions (LICs) for angles of attack $\alpha = 7°$ (a) and (b), $\alpha = 8°$ (c) and (d), and $\alpha = 9°$ (e) and (f), from span-wise periodic DNS with span $\delta_z = 0.9$ (a), (c) and (e), and virtual wind tunnel DNS (b), (d) and (f).

It can be seen that when $\alpha = 7°$ and $\alpha = 9°$ both the span-wise periodic DNS with $\delta_z = 0.9$ and DNS in a virtual wind tunnel exhibit similar separation characteristics. Specifically, when $\alpha = 7°$ a small recirculation bubble develops after the leading edge, but full separation occurs from the apex, and when $\alpha = 9°$ full separation occurs from the leading edge. However, when $\alpha = 8°$ separation characteristics



(a)

(b)

(c)

Figure 4.14: Images of time-averaged wall shear stress magnitude $|\tau|$ on the suction surface of the aerofoil with superimposed time-averaged wall shear stress Line Integral Convolutions (LICs) for angles of attack $\alpha = 7°$ (a), $\alpha = 8°$ (b), and $\alpha = 9°$ (c) from virtual wind tunnel DNS.

differ. Specifically, for span-wise periodic DNS with $\delta_z = 0.9$, the point of full separation has migrated to the leading edge, whereas for DNS in a virtual wind tunnel, a small recirculation bubble remains after the leading edge, and full separation still occurs from the apex. It is this suppression of the point

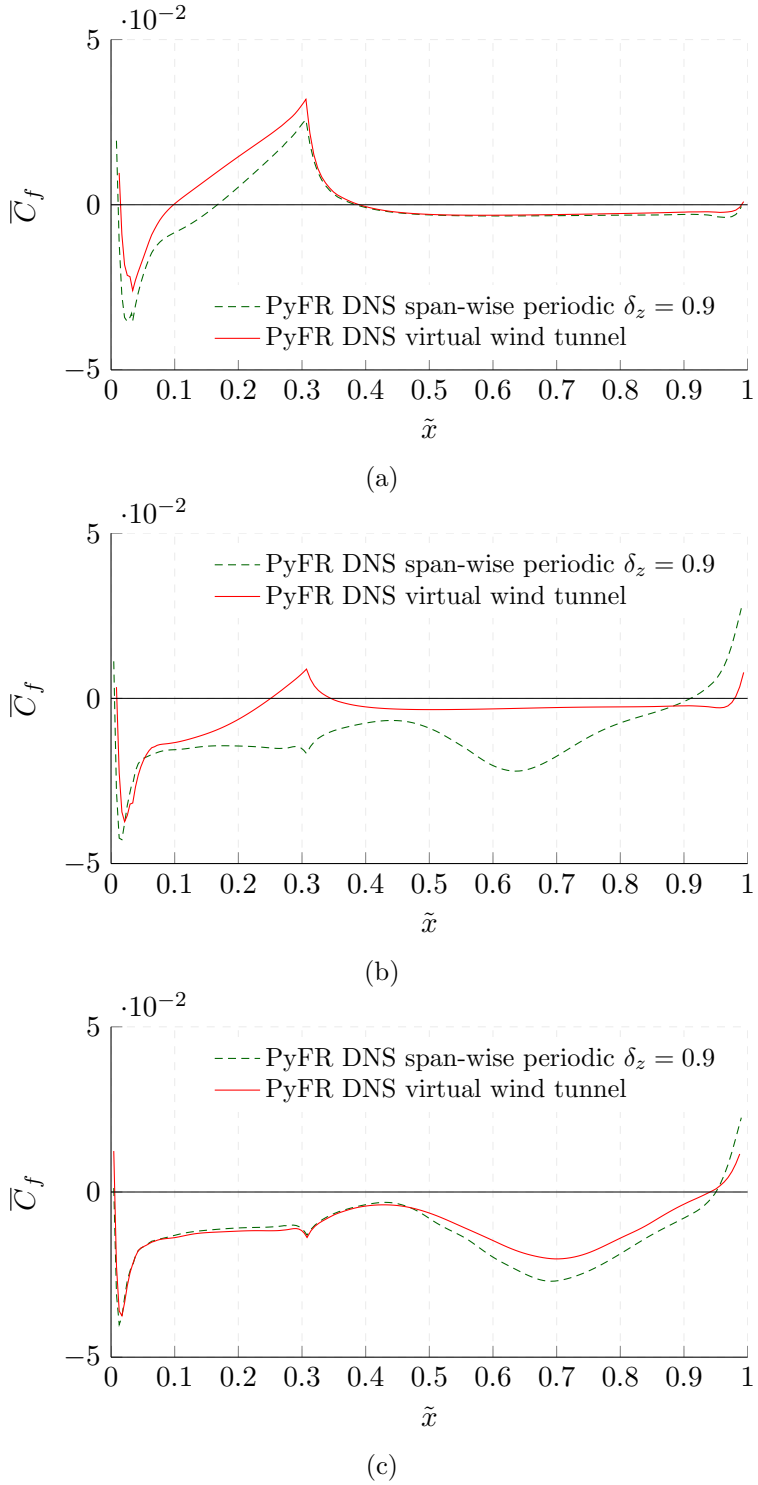


Figure 4.15: Plots of friction coefficient $\overline{C}_f$ on the suction surface of the aerofoil in the mid-span plane as a function of $\tilde{x}$ for angles of attack $\alpha = 7°$ (a), $\alpha = 8°$ (b), and $\alpha = 9°$ (c) from span-wise periodic DNS with $\delta_z = 0.9$ and virtual wind tunnel DNS.

at which full separation moves from the apex to the leading edge that results in DNS in a virtual wind tunnel achieving much better agreement with experimental $\overline{C}_L$ and $\overline{C}_D$ than span-wise periodic DNS

through to $\alpha = 9°$, as shown in Figure 4.4.

4.4 Summary

High-order GPU-accelerated PyFR DNS of flow over a triangular aerofoil, referred to as Reference aerofoil, have been validated against experiments by Munday et al. [15] at a range of angles of attack, with a fixed free-stream Mach number of 0.15 and chord-based Reynolds number of 3,000.

First, span-wise periodic DNS of the Reference aerofoil were undertaken. It was found that extending the domain span from $\delta_z = 0.3$ to $\delta_z = 0.6$ improved agreement with associated wind tunnel data. Extending it further to $\delta_z = 0.9$ provided little additional benefit. In particular, on extending δ_z from 0.3 to 0.6 better agreement with $\overline{C}_L$, $\overline{C}_D$ and mid-span $\overline{C}_P$ distributions were achieved at high angles of attack ($\alpha > 9°$), when the flow is separated. This is because $\delta_z = 0.3$ was found to artificially suppress the three-dimensional breakdown of coherent structures that form above the suction surface of the aerofoil and in the wake. These coherent motions are the primary lift-generating mechanism of these unconventional aerofoils, therefore, capturing their de-correlation in the spanwise direction is vital to accurately predicting the aerodynamic forces. Despite this improvement, discrepancies remained between the span-wise periodic DNS results and associated wind tunnel data for all angles of attack studied.

Subsequently, full-span DNS of the Reference aerofoil in a virtual wind tunnel were undertaken, including four no-slip walls representative of the experiment's wind tunnel walls. These simulations, which attempt to capture blockage effects and the interaction of wall boundary layers with the aerofoil, led to further improved agreement with the associated wind tunnel data. Specifically, better agreement with $\overline{C}_L$ and $\overline{C}_D$ was achieved for all angles of attack compared with the span-wise periodic DNS results. In particular, excellent agreement was achieved for low angles of attack ($\alpha < 7°$) and in the region where full separation moves from the apex to the leading edge ($7° < \alpha < 9°$). Moreover, good qualitative agreement was achieved with spatially resolved $\overline{C}_P$ distributions on the suction surface of the aerofoil for all angles of attack studied.

The results are important in terms of understanding discrepancies between previous span-wise periodic DNS of triangular aerofoils and associated wind tunnel data. They also demonstrated the utility of high-order DNS with PyFR as a tool for accurately resolving flow physics associated with triangular aerofoils under Martian atmospheric conditions.

Chapter 5

Optimisation of Aerofoils for Martian Rotorcraft using Direct Numerical Simulations and Genetic Algorithms

In this chapter, optimisation of Martian aerofoils is performed using high-order accurate DNS with PyFR and Genetic Algorithms (GAs) with `pymoo`, as described in Chapter 3. Specifically, triangular aerofoils are optimised under flow conditions of chord-based Reynolds number $Re = 3,000$ and Mach number $M = 0.15$. The chosen Reynolds number, Mach number and angles of attack α are representative of conditions at the root/mid-section of a rotor blade on a Martian helicopter. First, 2D and 3D DNS optimisations are run at $\alpha = 6^\circ$ and $\alpha = 12^\circ$ initialised with a Latin Hypercube Sampling (LHS), which will be referred to as 2D-DNS-6_{LHS}, 3D-DNS-6_{LHS}, 2D-DNS-12_{LHS} and 3D-DNS-12_{LHS}, respectively. Results are then compared, and the need for 3D DNS is discussed. Then, 3D DNS optimisation is performed at $\alpha = 12^\circ$ with the results of 2D-DNS-12_{LHS} used for the initial population of designs, which will be referred to as 3D-DNS-12_{2DS}. From each optimisation, optimal aerofoils are found with improved performance compared to the Reference aerofoil investigated in Chapter 4. Flow physics associated with the optimal aerofoils obtained from 3D-DNS-12_{2DS} are analysed and compared with the flow physics associated with the Reference aerofoil to understand how they achieve their improved performance. The work constitutes the first-ever use of DNS for aerodynamic shape optimisation. The work presented in this chapter has been published as a journal paper in the AIAA

Journal [126] and as a conference paper in the ICCFD11 conference [127].

5.1 Methodology

5.1.1 Optimisation

The optimisation process is as described in Chapter 3. The selected population size for all optimisations presented in this Chapter is 30 individuals and 15 offspring based on the nature and availability of the computational resources.

Design Variables and Objective Functions

The triangular aerofoil to be optimised is represented in Figure 5.1. The design variables are the x and y coordinates of the aerofoil's apex, x_a and y_a, respectively. The coordinates are measured from the leading edge of the aerofoil when $\alpha = 0°$.

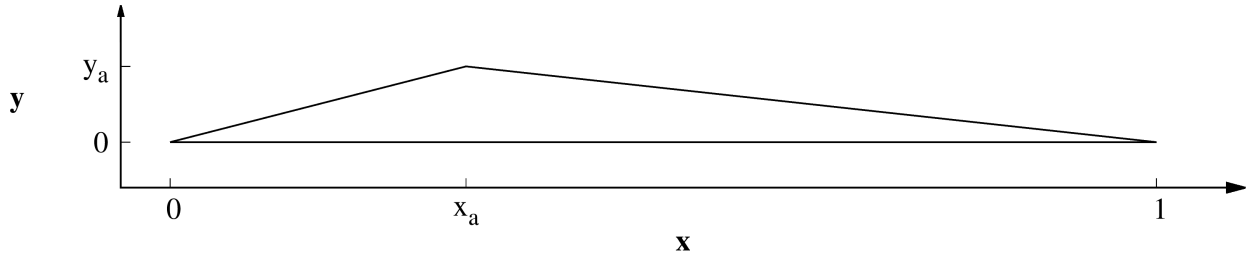


Figure 5.1: Triangular aerofoil with design variables x_a and y_a.

The objective functions are the time-averaged lift coefficient $\overline{C}_L$, which is to be maximised, and the time-averaged drag coefficient $\overline{C}_D$, which is to be minimised. C_L and C_D, and their respective time-averaged quantities, $\overline{C}_L$ and $\overline{C}_D$, are defined as in Chapter 4, Equation (4.3). These are obtained by automatically meshing each of the geometries with Gmsh [115], solving the flow physics with PyFR [17], and extracting the time-averaged aerodynamic forces. All simulations were undertaken using PyFR v1.15.0. The simulations ran on Nvidia Tesla P100-16GB GPUs on Piz Daint at the Swiss National Supercomputing Centre (CSCS).

5.1.2 Evaluation

Data Extraction

At $t = 0$, the simulations are initialised with uniform density $\rho = 1.0$, velocity $\mathbf{v} = \{v_x, v_y, v_z\} = \{1.0, 0.0, 0.0\}$ and pressure $p = 31.746$ throughout the domain. Simulations are advanced a period t_t to remove initial transients and then for a further t_e, referred to as the Data Extraction Period, during which data is extracted for analysis. For 2D-DNS-6_{LHS} and 2D-DNS-12_{LHS} optimisations $t_t = 50t_c$, $t_e = 50t_c$, and for the 3D-DNS-6_{LHS}, 3D-DNS-12_{LHS} and 3D-DNS-12_{2DS} optimisations $t_t = 75t_c$, $t_e = 75t_c$. Values for t_t and t_e were selected *a priori* through manual analysis of the behaviour of C_L and C_D for each aerofoil in the initial population. As a reference, Figure 5.2 illustrates C_L as a function of time for a subset of nine aerofoils from the initial population of the 2D-DNS-12_{2DS} optimisation. Additionally, the behaviour of C_L and C_D was manually reviewed *a posteriori* for each aerofoil to confirm the suitability of t_t and t_e.

While this manual approach was effective for this study, it may introduce inefficiencies or potential averaging errors. Future work should focus on automating the determination of t_t and t_e during simulations. Techniques for transient detection and averaging, such as those proposed by Bergmann et al. [128] and Mockett et al. [129], offer promising solutions to streamline this process and ensure consistency across simulations.

Computational Domain and Mesh

The computational domain and mesh for the triangular aerofoils are analogous to the ones in Chapter 4 for the Reference aerofoil (see Figure 4.2), which have been validated against experimental data. All triangular aerofoils are defined to have a chord of 1.0 and infinitely sharp leading and trailing edges. The origin in the streamwise-vertical xy-plane is located at the leading edge of the aerofoils when $\alpha = 0°$. The aerofoils are rotated about their trailing edges to achieve the desired angles of attack of $\alpha = 6°$ and $\alpha = 12°$. The dimensions of the computational domain are $x \in [-10, 20]$ in the streamwise direction, $y \in [-10, 10]$ in the vertical direction and for 3D DNS $z \in [0, 0.6]$ in the spanwise direction. The spanwise extent of 0.6 chords has been selected based on the findings of Chapter 4, which show that this length is required to avoid constraining the breakdown of coherent vortices at

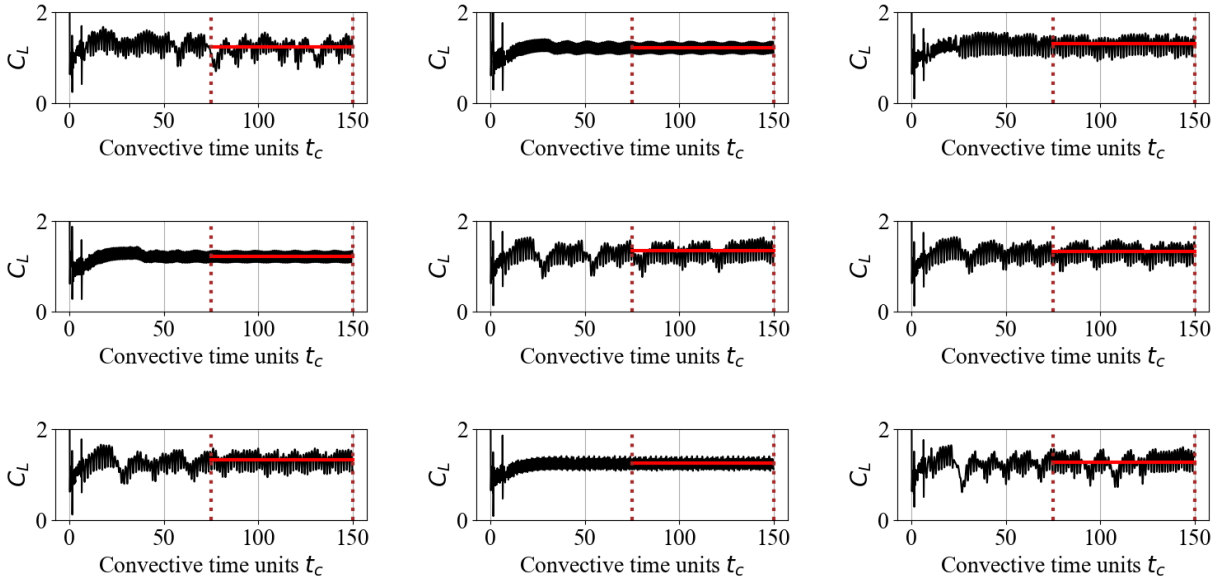


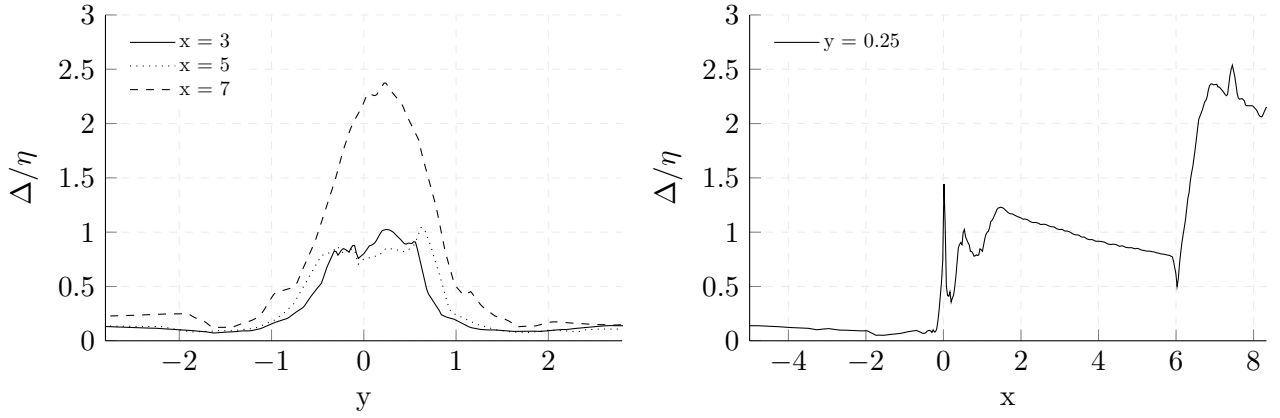
Figure 5.2: C_L as a function of time for a subset of 9 aerofoils from the initial population of the 2D-DNS-12$_{\text{2DS}}$ optimisation. The horizontal red line marks $\overline{C}_L$. The vertical dotted lines mark the start and end of the Data Extraction Period.

angles of attack $\alpha > 7°$ for a triangular aerofoil.

In terms of element count, the 2D DNS meshes have approximately $\sim 6 \times 10^3$ elements and $\sim 160 \times 10^3$ degrees of freedom per equation and the 3D DNS meshes have $\sim 155 \times 10^3$ elements and $\sim 19.4 \times 10^6$ degrees of freedom per equation. These are similar to or greater than those used in Chapter 4 for the Reference aerofoil.

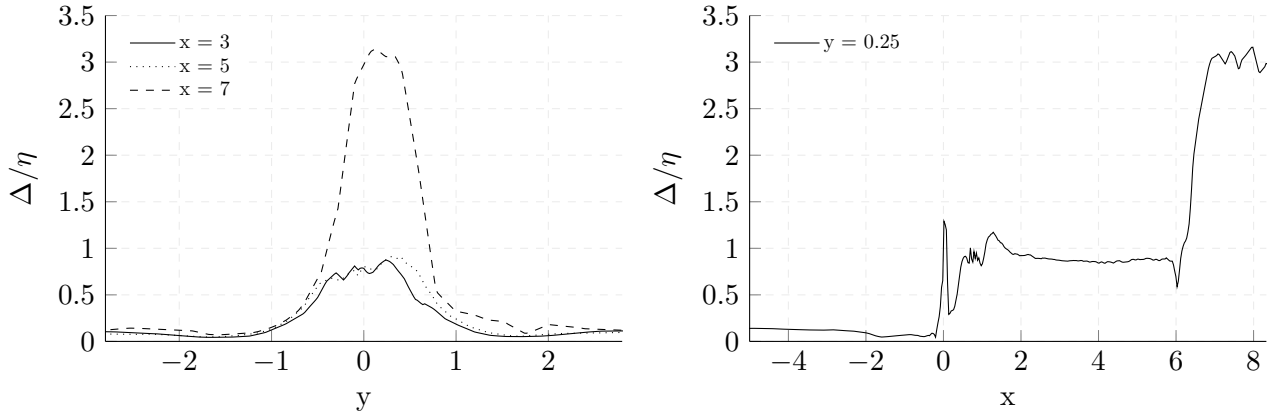
Moreover, for four representative aerofoils on the Pareto front from the 2D-DNS-12$_{\text{2DS}}$ optimisation, DNS resolution was verified a posteriori. Specifically, it was determined that $3.5\eta > \Delta$ throughout the wake, where Δ is an estimate of the solution point spacing given by Eq. (4.5) and η is an estimate of the Kolmogorov length scale given by Eq. (4.6). This is within the threshold required to achieve DNS resolution given the simulations are nominally fifth-order accurate in space [125]. 3D DNS for these four representative aerofoils were re-started from $t = 150t_c$ and ran for a further $400t_c$, during which data was extracted for analysis.

Figures 5.3, 5.4, 5.5 and 5.6 show plots of Δ/η along various mid-span lines for four optimised representative aerofoils, where Δ is an estimate of the solution point spacing given by Eq. (4.5) and η is an estimate of the Kolmogorov length scale given by Eq. (4.6).



(a) (b)

Figure 5.3: Plots of Δ/η in the mid-span plane as a function of y at $x = 3$, $x = 5$ and $x = 7$ (a) and as a function of x at $y = 0.2$ (b) for a representative Pareto optimal aerofoil from 3D-DNS-12_{2DS} (Group 1).

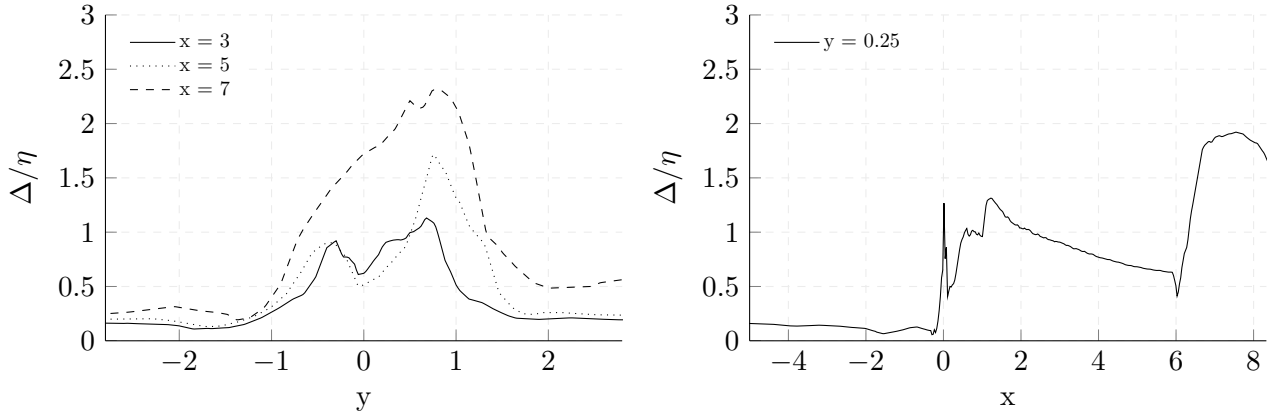


(a) (b)

Figure 5.4: Plots of Δ/η in the mid-span plane as a function of y at $x = 3$, $x = 5$ and $x = 7$ (a) and as a function of x at $y = 0.2$ (b) for a representative Pareto optimal aerofoil from 3D-DNS-12_{2DS} (Group 2).

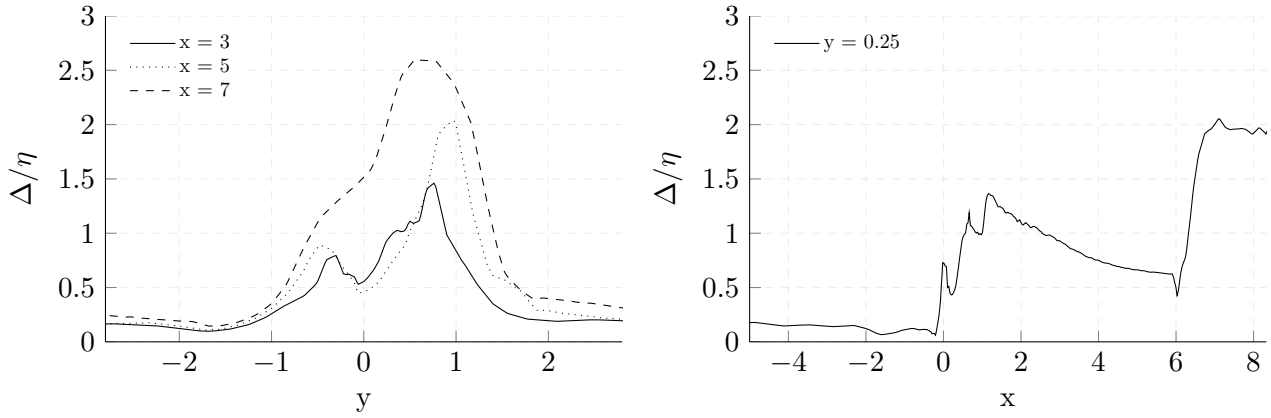
Boundary Conditions

Analogous to Chapter 4, a characteristic `char-riem-inv` PyFR boundary condition with density $\rho = 1.0$, velocity $\mathbf{v} = \{v_x, v_y, v_z\} = \{1.0, 0.0, 0.0\}$ and pressure $p = 31.746$, is applied at the $x = -10$ inflow, $x = 20$ outflow, $y = -10$ bottom, and $y = 10$ top boundaries to achieve $M = 0.15$ and $Re = 3,000$. An impermeable no-slip adiabatic `no-slp-adia-wall` PyFR boundary condition is applied at the aerofoil surface. A periodic boundary condition is applied at the side planes. No turbulence is injected at the inflow. Note that for an initial $5t_c$ of the 3D DNS, the velocity prescribed at the inflow plane is modified to have a time-dependent component as follows $\mathbf{v} = \{1 + 0.2\sin(100t), 0.2\sin(100t), 0.2\sin(100t)\}$ to



(a) (b)

Figure 5.5: Plots of Δ/η in the mid-span plane as a function of y at $x = 3$, $x = 5$ and $x = 7$ (a) and as a function of x at $y = 0.2$ (b) for a representative Pareto optimal aerofoil from 3D-DNS-12_{2DS} (Group 3).



(a) (b)

Figure 5.6: Plots of Δ/η in the mid-span plane as a function of y at $x = 3$, $x = 5$ and $x = 7$ (a) and as a function of x at $y = 0.2$ (b) for a representative Pareto optimal aerofoil from 3D-DNS-12_{2DS} (Group 4).

trigger flow instabilities to accelerate the transient period, with $t_c = 1.0/v_\infty$ where v_∞ is the free-stream velocity.

5.2 Comparison of 2D DNS vs 3D DNS as Evaluation

This section investigates the differences in results when optimising a triangular aerofoil using 2D and 3D high-order accurate DNS with PyFR at two different angles of attack. The aim is to assess the need for resolving the three-dimensionality of the flow when optimising triangular aerofoils under Martian

conditions. Specifically, 2D and 3D DNS optimisations are run at $\alpha = 6°$, referred to as 2D-DNS-6_{LHS} and 3D-DNS-6_{LHS} respectively, and at $\alpha = 12°$, referred to as 2D-DNS-12_{LHS} and 3D-DNS-12_{LHS} respectively, under the conditions of chord-based Reynolds number $Re = 3,000$ and Mach number $M = 0.15$.

5.2.1 Low Angle of Attack, $\alpha = 6°$

2D-DNS-6_{LHS} was run for 15 generations, with 15 individuals in each generation except for the first, which had 30 individuals, resulting in 240 2D DNS evaluations. Each 2D DNS took approximately 2 hours to run on one Tesla P100-16GB GPU, hence, 2D-DNS-6_{LHS} required approximately 480 GPUhs. 3D-DNS-6_{LHS} was run for 10 generations due to its higher cost, resulting in 165 3D DNS evaluations in total. Each 3D DNS took approximately 23 hours to run on 20 Tesla P100-16GB GPUs, therefore, 3D-DNS-6_{LHS} required approximately 80,000 GPUhs. Note that the 3D DNS were run on 20 Tesla P100-16GB GPUs to achieve a run time below 24h, which is the maximum job duration limit on Piz Daint. This avoided re-queuing to complete a given run.

Convergence is assessed using a hypervolume metric [120], which is calculated as the area dominated by the Pareto front at a particular generation with respect to a reference point. Figure 5.7 shows the hypervolume value, normalised by its value at the final generation, as a function of the number of generations for 2D-DNS-6_{LHS} (a) and 3D-DNS-6_{LHS} (b). 2D-DNS-6_{LHS} can be considered converged by generation 13 as the hypervolume reaches a plateau. 3D-DNS-6_{LHS} is approaching convergence by generation 10, but more generations should be run to confirm convergence. This was not done due to limited resources.

Figure 5.8 shows the design space with plots of x_a, y_a (a) and $\overline{C}_L$, $\overline{C}_D$ (b) for the initial population of 2D-DNS-6_{LHS} and 3D-DNS-6_{LHS}. 2D-DNS-6_{LHS} and 3D-DNS-6_{LHS} were seeded via the same Latin Hypercube Sampling of the region $0.1 < x_a < 0.9, 0.02 < y_x < 0.1$. The limits of the design space were selected to avoid unfeasible/unrealistic geometries such as aerofoils too thin to manufacture, or aerofoils with very blunt leading/trailing edges, whilst retaining substantive coverage of the design space.

Figure 5.8 (b) shows that most of the aerofoils in the initial population result in very similar $\overline{C}_L$ and $\overline{C}_D$ when evaluated with 2D or 3D DNS, with some aerofoils showing significant differences in $\overline{C}_L$.

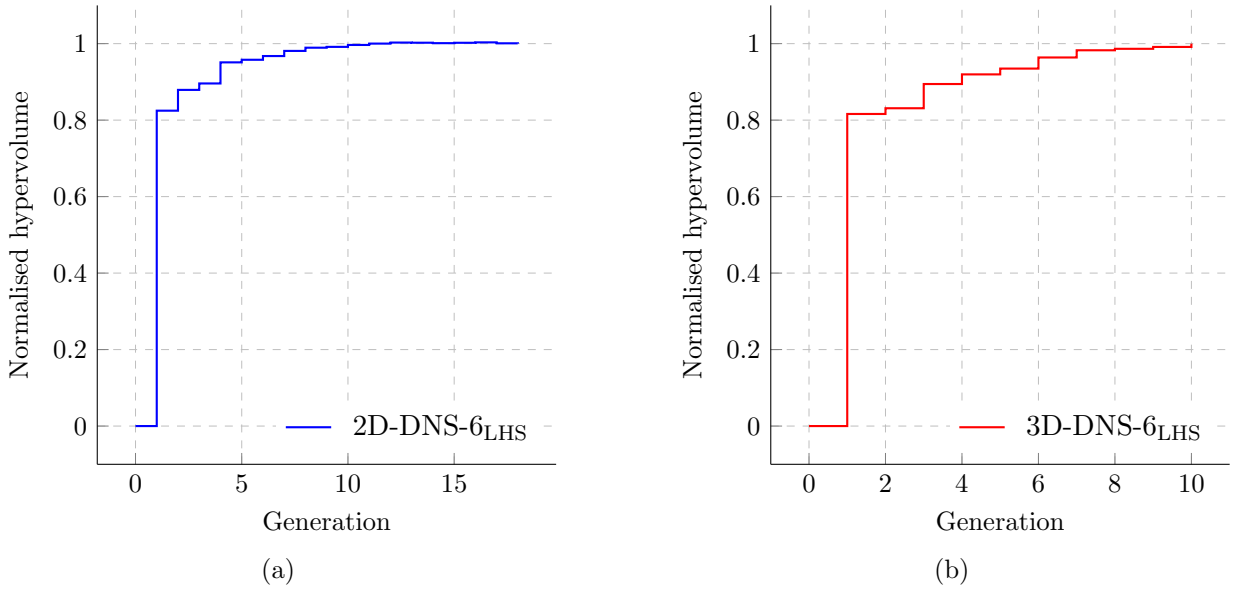


Figure 5.7: Normalised hypervolume convergence as a function of the number of generations for 2D-DNS-6_{LHS} (a) and 3D-DNS-6_{LHS} (b).

Based on the findings of Chapter 4, large differences in aerodynamic coefficients were not anticipated at $\alpha = 6°$ when using 2D or 3D DNS due to finding a mostly two-dimensional flow for the Reference aerofoil when $\alpha < 7°$. Clearly, some of the tested aerofoils exhibit three-dimensional properties that can not be captured by 2D DNS, which result in an over-prediction of $\overline{C}_L$ in most cases. Nonetheless, the set of aerofoils that are non-dominated in this initial population, and hence, that form the Pareto front at generation 1, show comparable aerodynamic coefficients.

Figure 5.9 shows plots of x_a, y_a (a) and $\overline{C}_L$, $\overline{C}_D$ (b) for the Pareto optimal aerofoils of 2D-DNS-6_{LHS} and 3D-DNS-6_{LHS}. Figure 5.9 (a) also shows, represented with lines, the Pareto optimal aerofoils with minimum $\overline{C}_D$, maximum $\overline{C}_L/\overline{C}_D$, and maximum $\overline{C}_L$ and the Reference aerofoil. Additionally, Figure 5.9 (b) shows the Reference aerofoil at $\alpha = 6°$ and 2D-DNS-6_{LHS} Pareto optimal aerofoils run with 3D DNS. Even though 2D-DNS-6_{LHS} and 3D-DNS-6_{LHS} evolve differently due to the slight differences in $\overline{C}_L$ and $\overline{C}_D$ from generation 1, which leads to testing different aerofoil shapes, both optimisations evolve to overlapping Pareto fronts of non-dominated solutions, see Figure 5.9 (b). However, these overlapping Pareto fronts correspond to slightly different aerofoil shapes, see Figure 5.9 (a). To verify if Pareto optimal aerofoils found from 2D-DNS-6_{LHS} are optimal when considering three-dimensional physics, they were run with 3D DNS. Figure 5.9 (b) shows that they are still optimal as they are within the Pareto front of 3D-DNS-6_{LHS}.

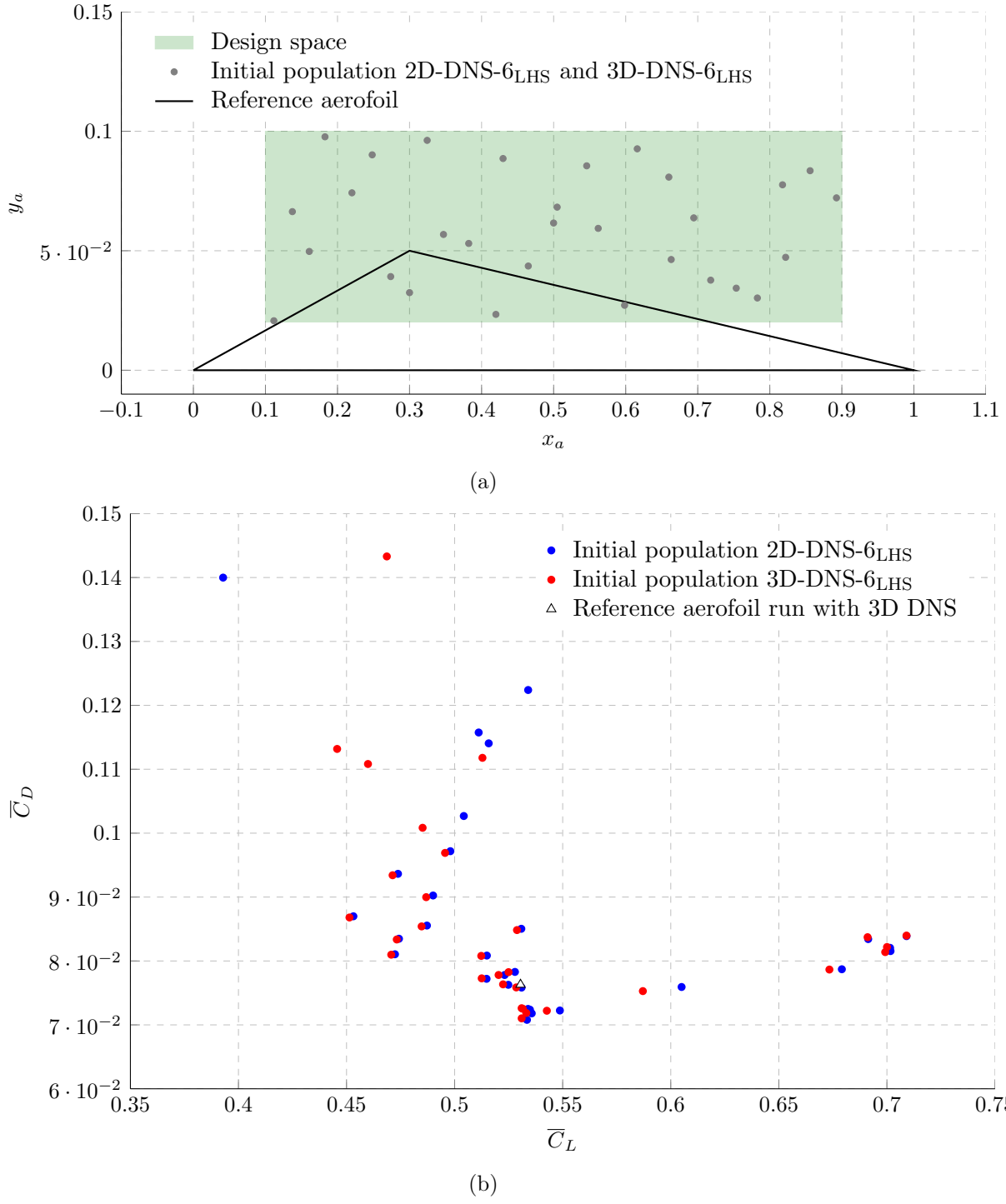
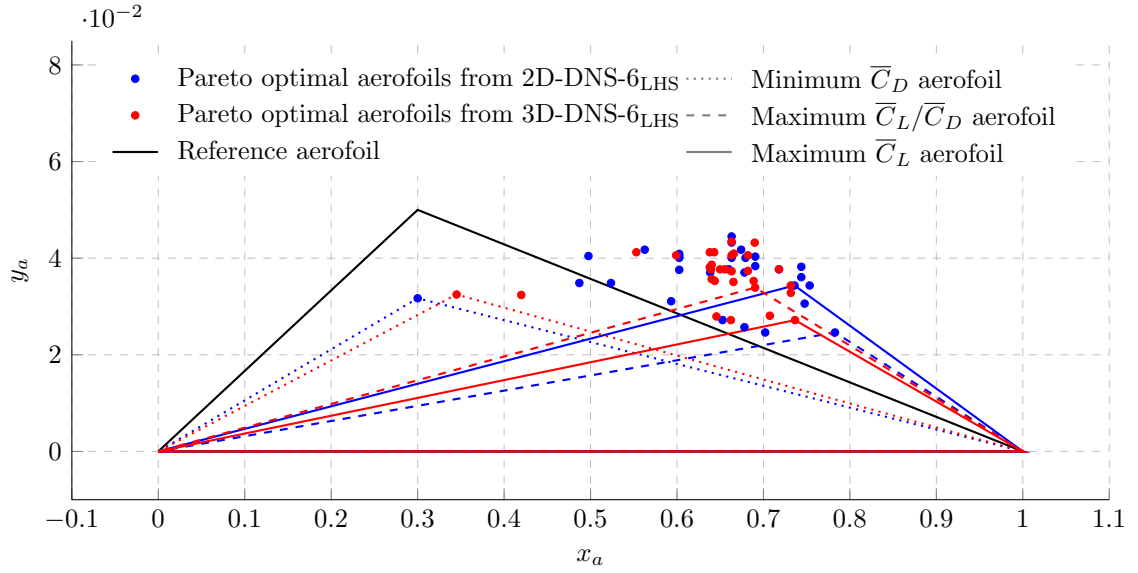
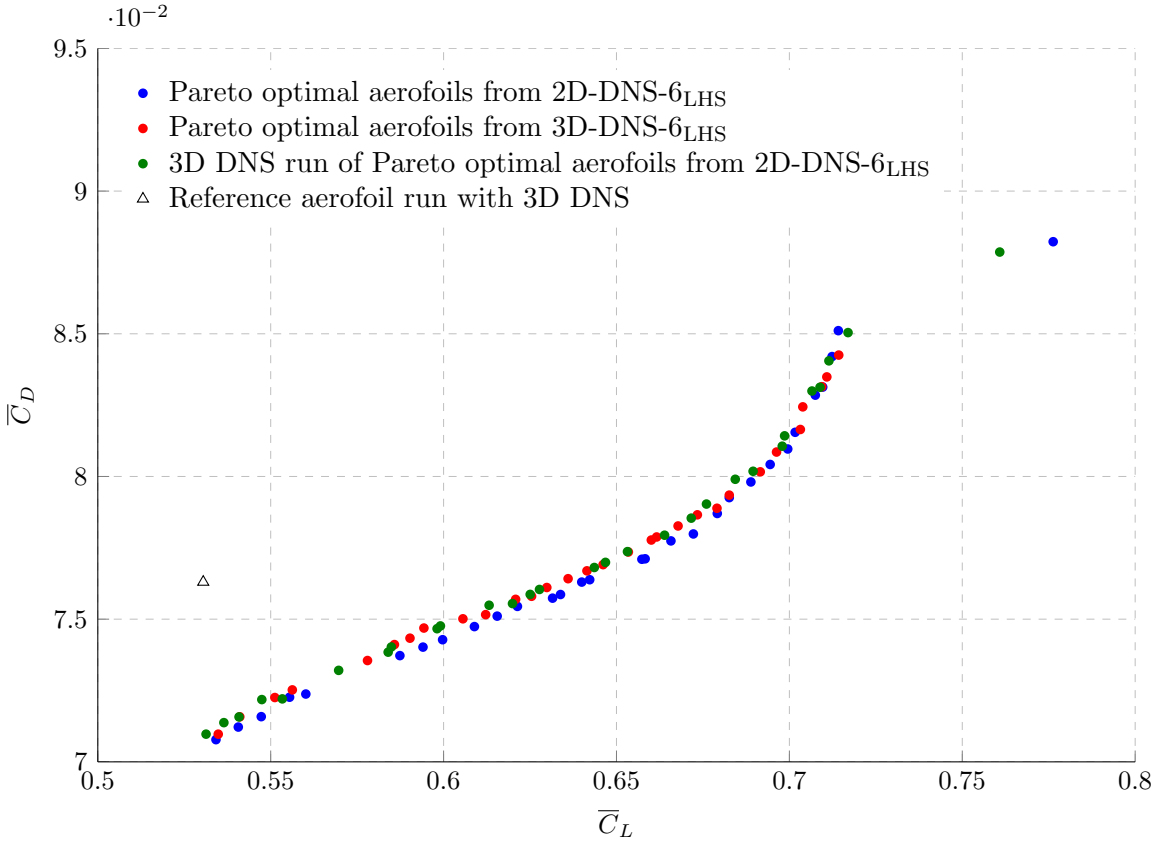


Figure 5.8: Design space with plots of x_a, y_a (a) and plots of $\overline{C}_L$, $\overline{C}_D$ (b) for the initial population of 2D-DNS-6_{LHS} and 3D-DNS-6_{LHS}, and the Reference aerofoil at $\alpha = 6°$.

Figures 5.10 (a), (c), (e) show the time-averaged velocity magnitude in the midspan plane with superimposed velocity line integral convolutions (LICs) for the Pareto optimal aerofoils with minimum drag (a), maximum lift-to-drag ratio (b) and maximum lift (c) from 2D-DNS-6_{LHS} run with 3D DNS.



(a)



(b)

Figure 5.9: Plots of x_a, y_a for the Pareto optimal aerofoils of 2D-DNS-6$_{\text{LHS}}$ and 3D-DNS-6$_{\text{LHS}}$, with the minimum $\overline{C}_D$, maximum $\overline{C}_L/\overline{C}_D$, and maximum $\overline{C}_L$ aerofoils and the Reference aerofoil represented with lines (a). Plots of $\overline{C}_L$, $\overline{C}_D$ (b) for the Pareto optimal aerofoils of 2D-DNS-6$_{\text{LHS}}$ and 3D-DNS-6$_{\text{LHS}}$, the Reference aerofoil at $\alpha = 6°$ and 2D-DNS-6$_{\text{LHS}}$ Pareto optimal aerofoils run with 3D DNS (b).

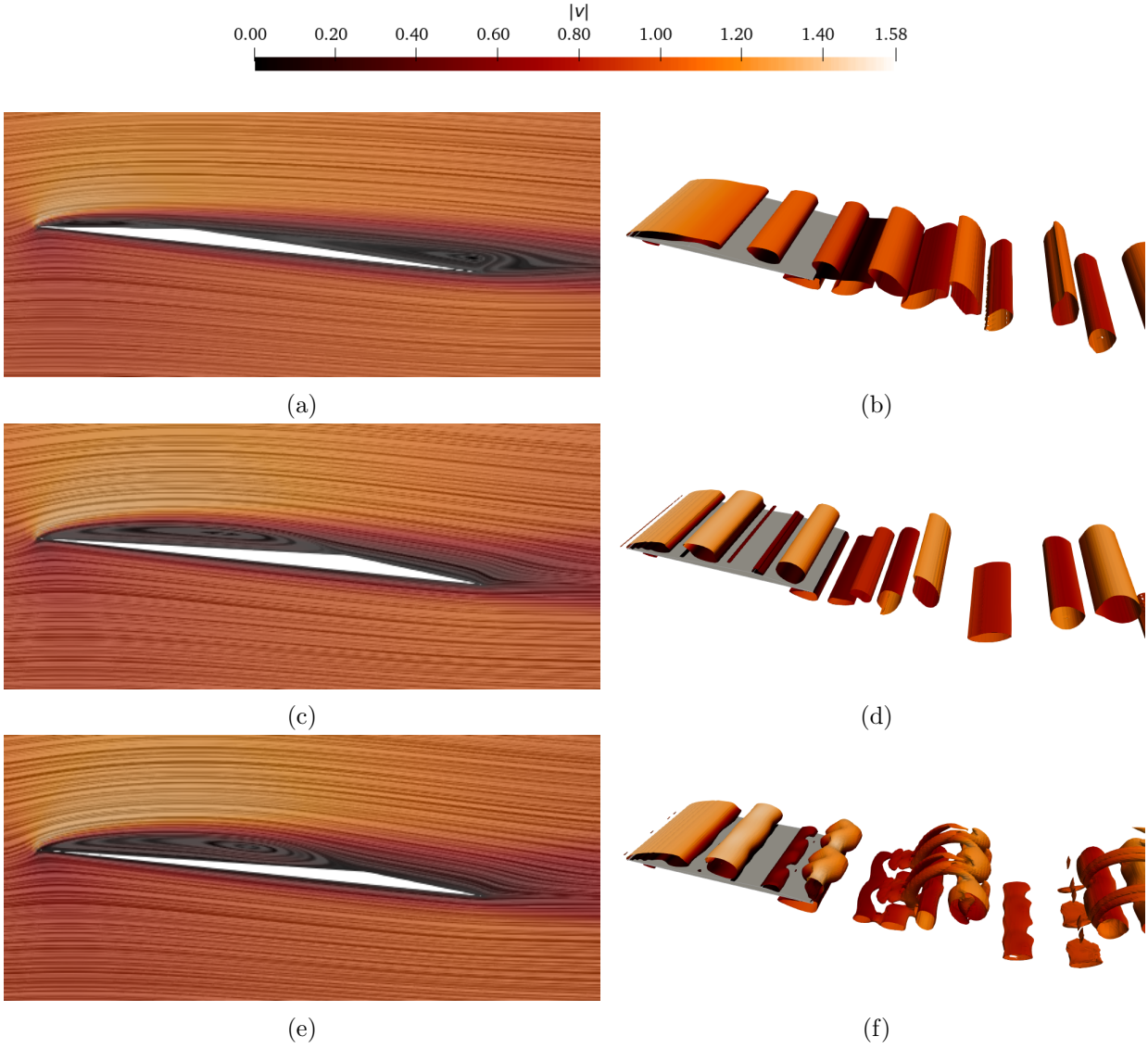


Figure 5.10: Images of time-averaged velocity magnitude in the midspan plane with superimposed velocity line integral convolutions (LICs) on the left (a),(c),(e) and images of instantaneous Q-criterion isosurfaces $Q = 1$, coloured by velocity magnitude $|\mathbf{v}|$, on the right (b),(d),(f) for the Pareto optimal aerofoils with minimum $\overline{C}_D$ (a),(b), maximum $\overline{C}_L/\overline{C}_D$ (c),(d), and maximum $\overline{C}_L$ (e),(f) obtained from 2D-DNS-6_{LHS} run with 3D DNS.

Figures 5.10 (b), (d), (f) show images of instantaneous Q-criterion, $Q = \frac{1}{2}(||\Omega||^2 - ||S||^2)$, isosurfaces of $Q = 1$, coloured by velocity magnitude over the same three Pareto front aerofoil shapes from 2D-DNS-6_{LHS} run with 3D DNS.

The minimum drag aerofoil, Figures 5.10 (a) and (b), exhibits a small laminar separation bubble near the leading edge and flow separation from the apex of the aerofoil, similar to the Reference aerofoil at $\alpha \leq 7°$. Instead, the maximum lift-to-drag ratio aerofoil, Figures 5.10 (c) and (d), and maximum

lift aerofoil, Figures 5.10 (e) and (f), exhibit flow separation from the leading edge with subsequent roll-up of vortices, similar to the Reference aerofoil when $\alpha > 7°$, with the flow appearing reattached at the apex in the time-averaged sense from the LIC images. The Q-criterion images show mostly two-dimensional flow over the aerofoils for all three cases, even if there is vortex roll-up shedding from the leading edge for (c) and (f). Three-dimensional structures can be identified towards the trailing edge in Figure 5.10 (c) for the maximum lift aerofoil, which explains the larger differences in $\overline{C}_L$ for the maximum lift aerofoil in Figure 5.9 (b).

Given that the three examined aerofoils inhabit the extremes in the objective space, it may be assumed that all the aerofoils in the Pareto front have similar flow structures, with two-dimensional flow over most of the aerofoil surface. This corroborates the ability of using 2D DNS evaluations for triangular aerofoil optimisation at an angle of attack of $\alpha = 6°$ and flow conditions of $Re = 3,000$ and Mach number $M = 0.15$ and, presumably, at lower angles of attack and/or lower Reynolds numbers. Using 2D DNS for cost-function evaluation in the optimisation allows a reduction in cost of approximately 150 times.

5.2.2 High Angle of Attack, $\alpha = 12°$

2D-DNS-12_{LHS} was run for 25 generations, with 15 individuals in each generation except for the first, which had 30 individuals, totalling 390 2D DNS evaluations. Each 2D DNS took approximately 2 hours to run on one Tesla P100-16GB GPU, hence, 2D-DNS-12_{LHS} required approximately 780 GPUhs. 3D-DNS-12_{LHS} was run for 15 generations, resulting in 240 3D DNS evaluations. Each 3D DNS took approximately 23 hours to run on 36 Tesla P100-16GB GPUs, therefore, 3D-DNS-12_{LHS} required approximately 200,000 GPUhs. Note that the 3D DNS were run on 36 Tesla P100-16GB GPUs to achieve a run time below 24h, which is the maximum job duration limit on Piz Daint. This avoided re-queuing to complete a given run.

Similarly to before, convergence is assessed using the hypervolume metric [120]. Figure 5.11 shows the hypervolume value, normalised by its value at the final generation, as a function of the number of generations for 2D-DNS-12_{LHS} (a) and 3D-DNS-12_{LHS} (b). 2D-DNS-12_{LHS} can be considered converged from generation 20 as the hypervolume reaches a plateau. 3D-DNS-12_{LHS} does not show convergence after 15 generations and more generations should be run. This was not done due to limited resources.

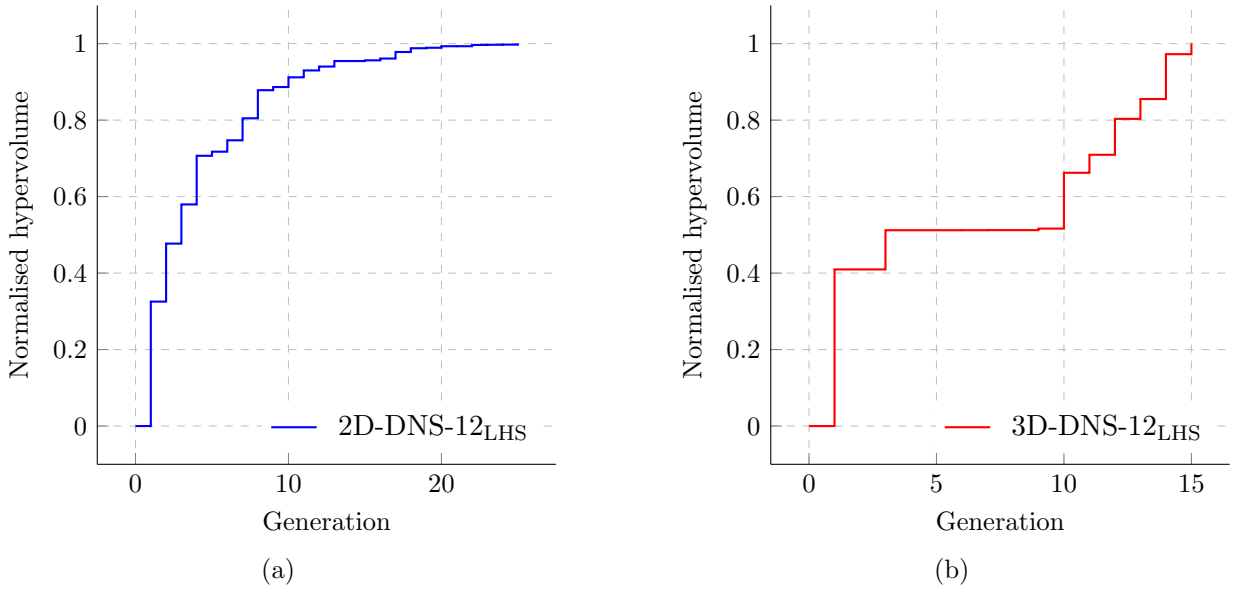


Figure 5.11: Normalised hypervolume convergence as a function of the number of generations for 2D-DNS-12_{LHS} (a) and 3D-DNS-12_{LHS} (b). Note that 3D-DNS-12_{LHS} does not show convergence and was not run further due to limited resources.

Figure 5.12 shows the design space with plots of x_a, y_a (a) and $\overline{C}_L$, $\overline{C}_D$ (b) for the initial population of 2D-DNS-12_{LHS} and 3D-DNS-12_{LHS}. 2D-DNS-12_{LHS} and 3D-DNS-12_{LHS} were seeded via a Latin Hypercube Sampling of the constrained design space. Design space constraints were applied such that

$$0.1 \leq x_a \leq 0.9, \quad 0.02 \leq y_a \leq 0.4, \quad y_a - x_a \leq 0, \quad x_a + y_a - 1 \leq 0. \tag{5.1}$$

These avoid unfeasible/unrealistic geometries such as aerofoils that are too thin to manufacture, or aerofoils with very blunt leading/trailing edges, whilst retaining substantive coverage of the design space. A restriction step was applied in which any individuals violating the design space constraints were moved to the nearest point within the design space. Note that the constrained design space for the current optimisations has been extended compared to $\alpha = 6°$ since preliminary tests showed aerofoils evolving towards the boundaries of a smaller design space.

Figure 5.12 (b) shows large differences in the aerodynamic coefficients obtained from the initial population of 2D-DNS-12_{LHS} and 3D-DNS-12_{LHS}. Specifically, 3D DNS evaluations show lower $\overline{C}_L$ and $\overline{C}_D$ compared to 2D DNS evaluations. This aligns with the findings in Chapter 4 for the Reference aerofoil at various high angles of attack, where the spanwise breakdown of the coherent vortices shed from the leading edge resulted in a weaker suction.

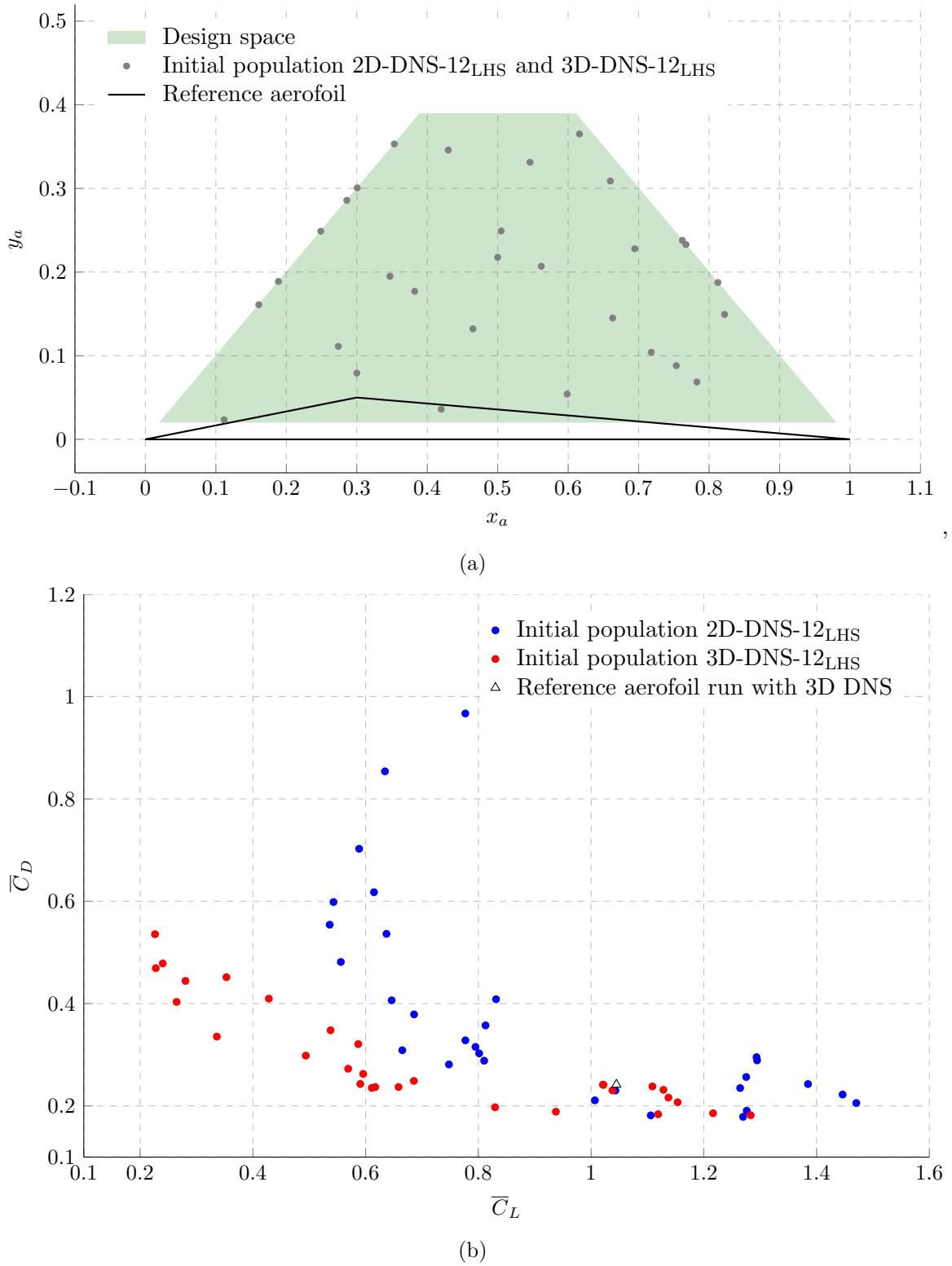
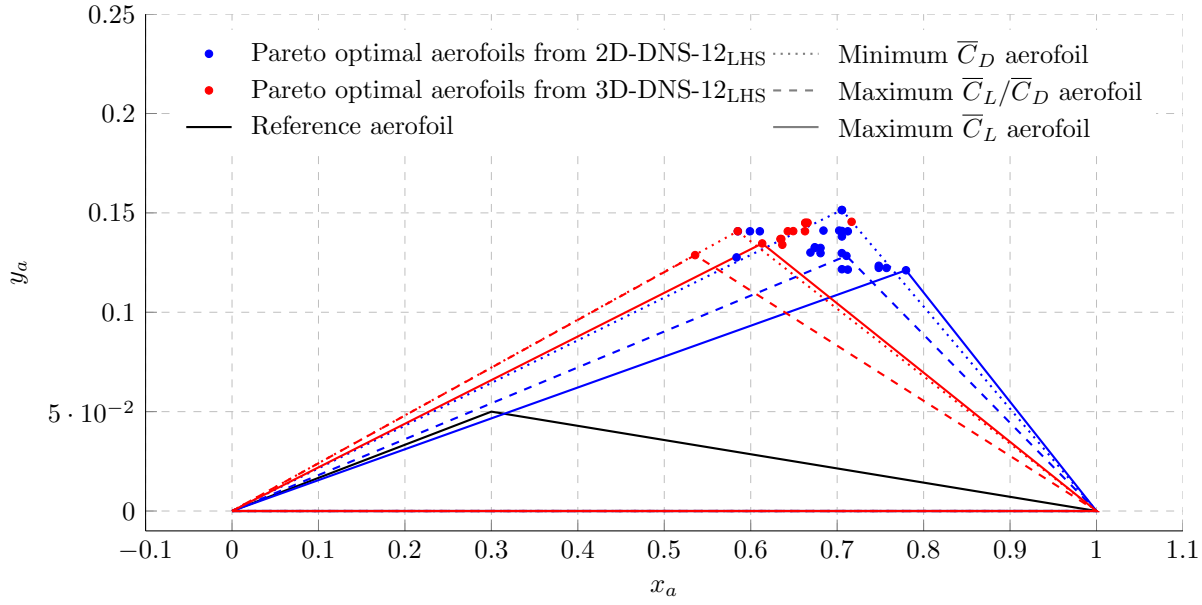
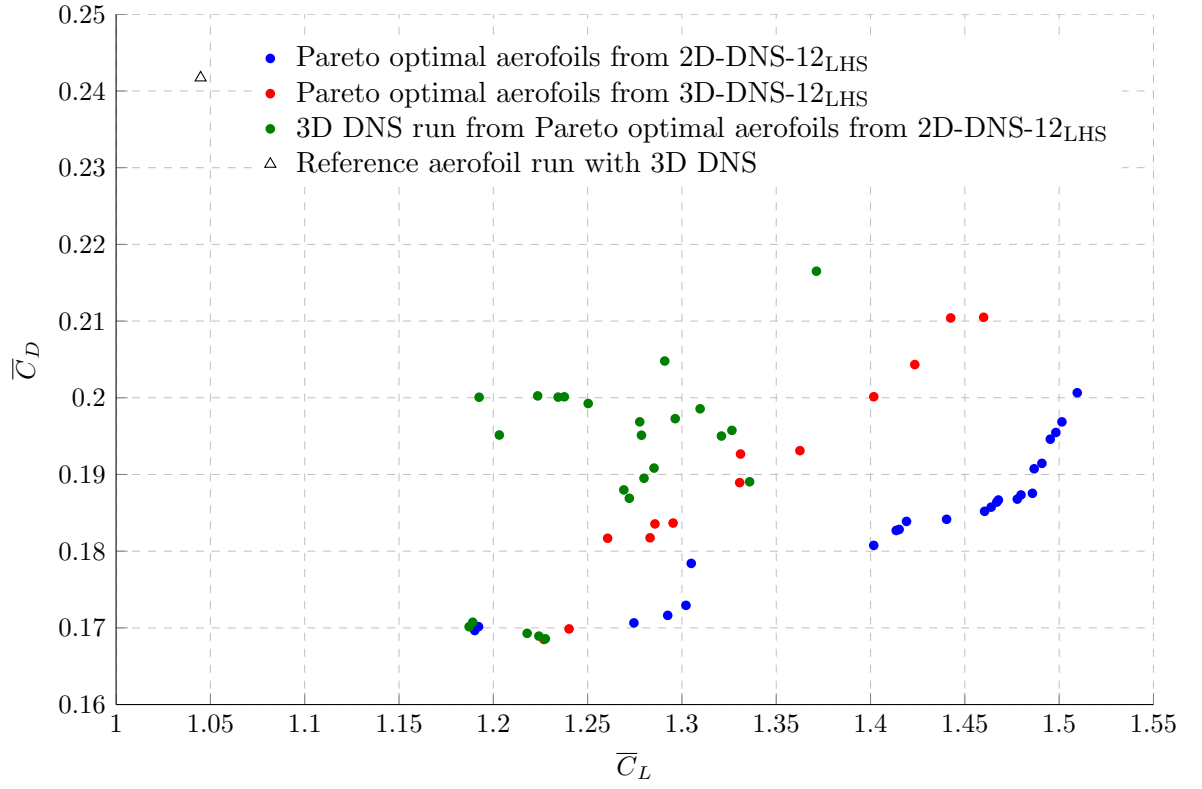


Figure 5.12: Design space with plots of x_a, y_a (a) and plots of $\overline{C}_L$, $\overline{C}_D$ (b) for the initial population of 2D-DNS-12$_{\text{LHS}}$ and 3D-DNS-12$_{\text{LHS}}$, and the Reference aerofoil at $\alpha = 12°$.

Figure 5.13 shows plots of x_a, y_a (a) and $\overline{C}_L$, $\overline{C}_D$ (b) for the Pareto optimal aerofoils of 2D-DNS-12$_{\text{LHS}}$ and 3D-DNS-12$_{\text{LHS}}$. Figure 5.13 (a) also shows, represented with lines, the Pareto optimal aerofoils



(a)



(b)

Figure 5.13: Plots of x_a, y_a for the Pareto optimal aerofoils of 2D-DNS-12$_{\text{LHS}}$ and 3D-DNS-12$_{\text{LHS}}$, with the minimum $\overline{C}_D$, maximum $\overline{C}_L/\overline{C}_D$, and maximum $\overline{C}_L$ aerofoils and the Reference aerofoil represented with lines (a). Plots of $\overline{C}_L$, $\overline{C}_D$ (b) for the Pareto optimal aerofoils of 2D-DNS-12$_{\text{LHS}}$ and 3D-DNS-12$_{\text{LHS}}$, the Reference aerofoil at $\alpha = 12°$ and 2D-DNS-12$_{\text{LHS}}$ Pareto optimal aerofoils run with 3D DNS (b).

with minimum $\overline{C}_D$, maximum $\overline{C}_L/\overline{C}_D$, and maximum $\overline{C}_L$ and the Reference aerofoil. Additionally, Figure 5.13 (b) shows the Reference aerofoil at $\alpha = 12°$ and 2D-DNS-12$_{\text{LHS}}$ Pareto optimal aerofoils run with 3D DNS. Pareto optimal aerofoils from 2D-DNS-12$_{\text{LHS}}$ in Figure 5.13 (a) show apex positions (x_a, y_a) closer to the trailing edge compared to Pareto optimal aerofoils from 3D-DNS-12$_{\text{LHS}}$. Contrary to the results for $\alpha = 6°$, Pareto fronts from 2D-DNS-12$_{\text{LHS}}$ and 3D-DNS-12$_{\text{LHS}}$ in Figure 5.13 (b) do not overlap. Instead, 2D-DNS-12$_{\text{LHS}}$ shows higher $\overline{C}_L$ and lower $\overline{C}_D$ values.

Evaluating the Pareto optimal aerofoils from 2D-DNS-12$_{\text{LHS}}$ using 3D DNS reveals a shift in the aerodynamic coefficients by 5 to 15%. This shift reiterates the previous findings that 2D DNS constrains the flow, failing to simulate the flow physics accurately. Aside from this shift, most Pareto optimal aerofoils from 2D-DNS-12$_{\text{LHS}}$ are positioned in the dominated region of the 3D-DNS-12$_{\text{LHS}}$ Pareto front, with a few exceptions. Notably, one exception dominates a solution found by 3D-DNS-12$_{\text{LHS}}$, while others extend the Pareto front to the left of the objective domain. These indicate that the 3D-DNS-12$_{\text{LHS}}$ optimisation has not fully converged, as denoted by the hypervolume metric. Despite these findings, most aerofoils identified by 2D-DNS-12$_{\text{LHS}}$ are non-optimal when evaluated with 3D DNS. This serves as evidence that optimisation using 3D DNS is necessary to achieve the optimal set of aerofoil designs at $\alpha = 12°$ under flow conditions of $Re = 3,000$ and Mach number $M = 0.15$.

Figures 5.14 (a), (c), (e) show the time-averaged velocity magnitude in the midspan plane with superimposed velocity line integral convolutions (LICs) for the Pareto optimal aerofoils with minimum $\overline{C}_D$ (a),(b), maximum $\overline{C}_L/\overline{C}_D$ (c),(d), and maximum $\overline{C}_L$ (e),(f) obtained from 3D-DNS-12$_{\text{LHS}}$. Figures 5.10 (b), (d), (f) show images of instantaneous Q-criterion, $Q = \frac{1}{2}(||\Omega||^2 - ||S||^2)$, isosurfaces of $Q = 1$, coloured by velocity magnitude over the same three Pareto front aerofoil shapes from 3D-DNS-12$_{\text{LHS}}$. The time-averaged LICs show that, for all three cases, the flow separates from the leading edge, with a vortex rolling up on the suction side of the aerofoil, acting as the lifting mechanism. The Q-criterion iso-surfaces show the unsteady nature of the flow, with a three-dimensional breakdown of the streamwise vortices in the spanwise direction. The next section investigates the flow mechanisms of optimum aerofoils in more depth.

As the examined aerofoils inhabit the extremes of the 3D-DNS-12$_{\text{LHS}}$ Pareto front, it may be assumed that all aerofoils found in the Pareto front experience similar separation phenomena with three-dimensional flow structures breaking the coherence of the streamwise vortices. Also, findings

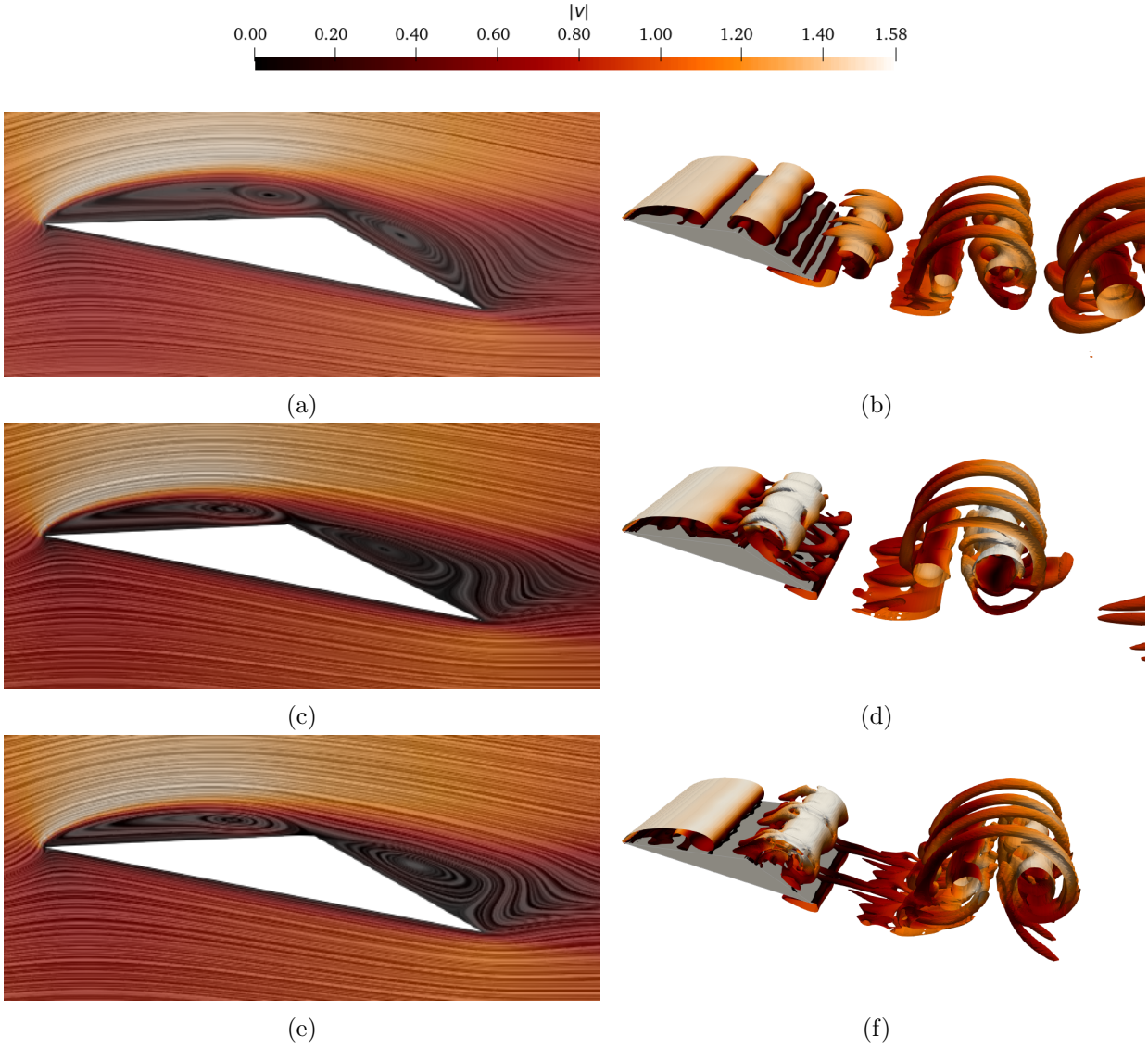


Figure 5.14: Images of time-averaged velocity magnitude in the midspan plane with superimposed velocity line integral convolutions (LICs) on the left (a),(c),(e) and images of instantaneous Q-criterion isosurfaces $Q = 1$, coloured by velocity magnitude $|\mathbf{v}|$, on the right (b),(d),(f) for the Pareto optimal aerofoils with minimum $\overline{C}_D$ (a),(b), maximum $\overline{C}_L/\overline{C}_D$ (c),(d), and maximum $\overline{C}_L$ (e),(f) obtained from 3D-DNS-12$_{\text{LHS}}$.

show that Pareto optimal aerofoils from 2D-DNS-12$_{\text{LHS}}$ evaluated with 3D DNS show similar three-dimensional physics with spanwise breakdown, but do not maintain optimality. Therefore, it can be concluded that when optimising triangular aerofoils at $\alpha = 12°$ under flow conditions of $Re = 3,000$ and Mach number $M = 0.15$, 3D DNS should be used to capture the fundamentally three-dimensional nature of the lifting mechanism. Finally, given that the breakdown is expected to be more acute the higher the angle of attack or the higher the Reynolds number, this statement presumably holds for

higher angles of attack and/or higher Reynolds numbers.

5.3 Optimisation Results at $\alpha = 12^\circ$ using 3D DNS

Whilst it has been well established that 2D DNS can miss important flow physics at $\alpha = 12^\circ$, t is reasonable to assume that the 2D-DNS-12_{LHS} results retain enough relevant information to significantly accelerate the convergence of the 3D-DNS-12_{2DS} optimisation. This approach is expected to reduce the overall computational cost, as 2D DNS calculations are approximately 100 times cheaper than 3D DNS calculations. Using the 2D-DNS-12_{LHS} results as the initial sampling introduces meaningful physical insights, in contrast to a Latin Hypercube Sampling (LHS) approach, which lacks this added physical context.

2D-DNS-12_{LHS} required approximately 780 GPUhs as previously stated. 3D-DNS-12_{2DS} was run for 16 generations, with 15 individuals in each generation except for the first, which had 30 individuals. Each 3D DNS took approximately 23 hours to run on 36 Tesla P100-16GB GPUs, therefore, 3D-DNS-12_{2DS} required approximately 210,000 GPUhs. In total, the overall cost of the optimisation was $\sim$ 212,000 GPUhs.

Convergence of 3D-DNS-12_{2DS} is assessed using a hypervolume metric [120]. Figure 5.15 shows the hypervolume value, normalised by its value at the final generation, as a function of the number of generations for 3D-DNS-12_{2DS}. Additionally, the plot shows the hypervolume for 3D-DNS-12_{LHS} normalised by the hypervolume at the final generation of 3D-DNS-12_{2DS}. Note how 3D-DNS-12_{2DS} converges faster than 3D-DNS-12_{LHS} since the former is seeded with a biased set of aerofoils closer to the optimum solution.

5.3.1 Optimal Aerofoils

Figure 5.16 (a) plots apex locations in the x_a, y_a design space for the initial population (hollow circles), and Pareto optimal aerofoils (solid circles) from 3D-DNS-12_{2DS}, along with the Reference aerofoil. The optimal aerofoils are thicker than the Reference aerofoil, and their apexes are shifted downstream. Figure 5.16 (b) plots the initial population (hollow circles) and the Pareto front of optimal aerofoils (solid circles) from 3D-DNS-12_{2DS} and the Reference aerofoil at $\alpha = 12^\circ$ in the $\overline{C}_L$,

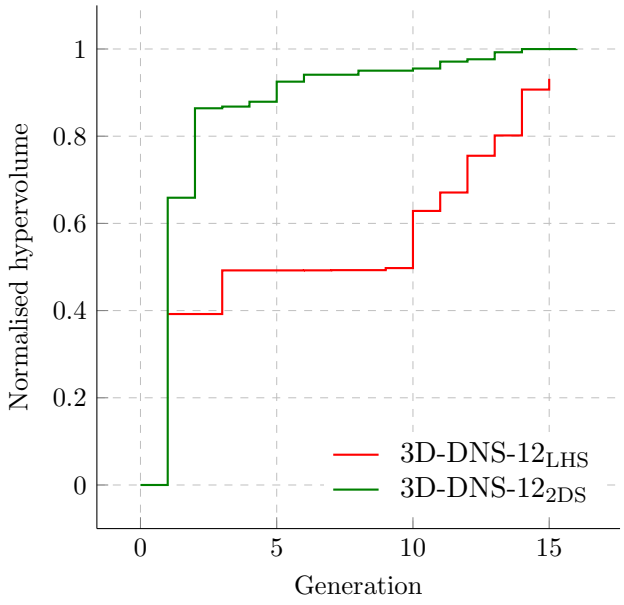


Figure 5.15: Normalised hypervolume convergence as a function of the number of generations for 3D-DNS-12_{LHS} and 3D-DNS-12_{2DS}. Note that it is normalised by its value at the last generation of 3D-DNS-12_{2DS}.

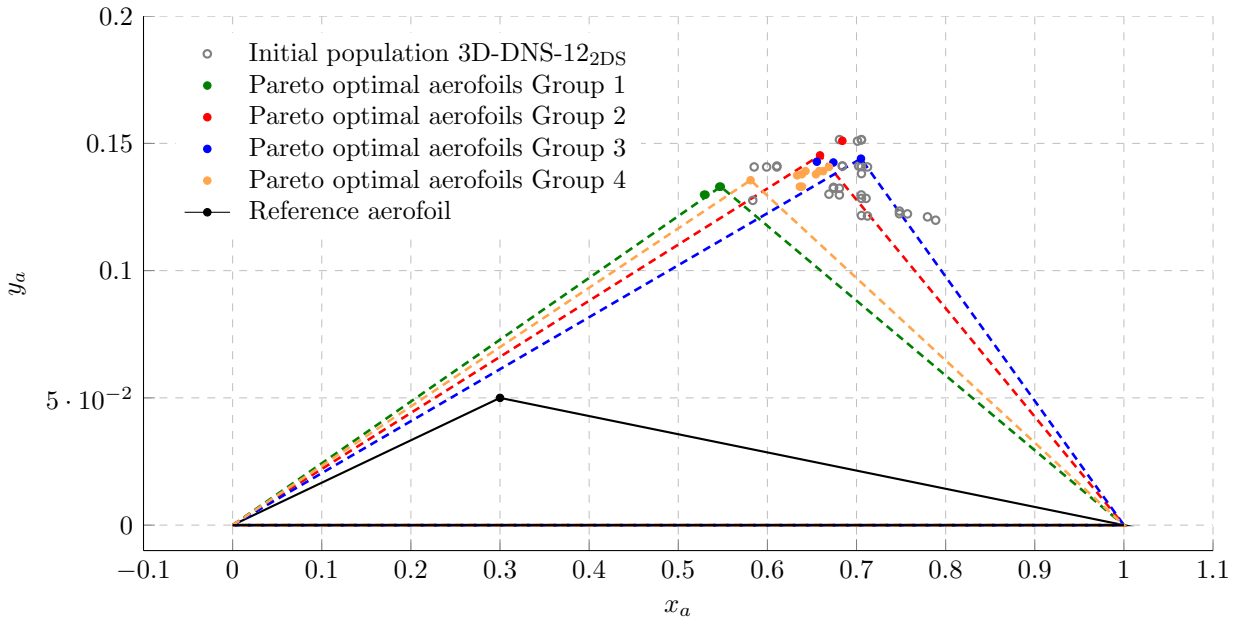
$\overline{C}_D$ objective space. All the aerofoils on the Pareto front have improved $\overline{C}_L$ and $\overline{C}_D$ compared to the Reference aerofoil. Specifically, $\overline{C}_L$ is increased by up to 48% and $\overline{C}_D$ is reduced by up to 28%.

Based on associated flow characteristics, four distinct groups of aerofoils can be identified on the Pareto front, defined as per Table 5.1. A detailed discussion of the flow physics associated with each group, including analyses of Q-criterion isosurfaces, lift coefficient C_L, time-averaged pressure coefficient $\overline{C}_p$, time-averaged velocity line integral convolutions (LICs) and time-averaged skin friction coefficient $\overline{C}_f$, are presented below.

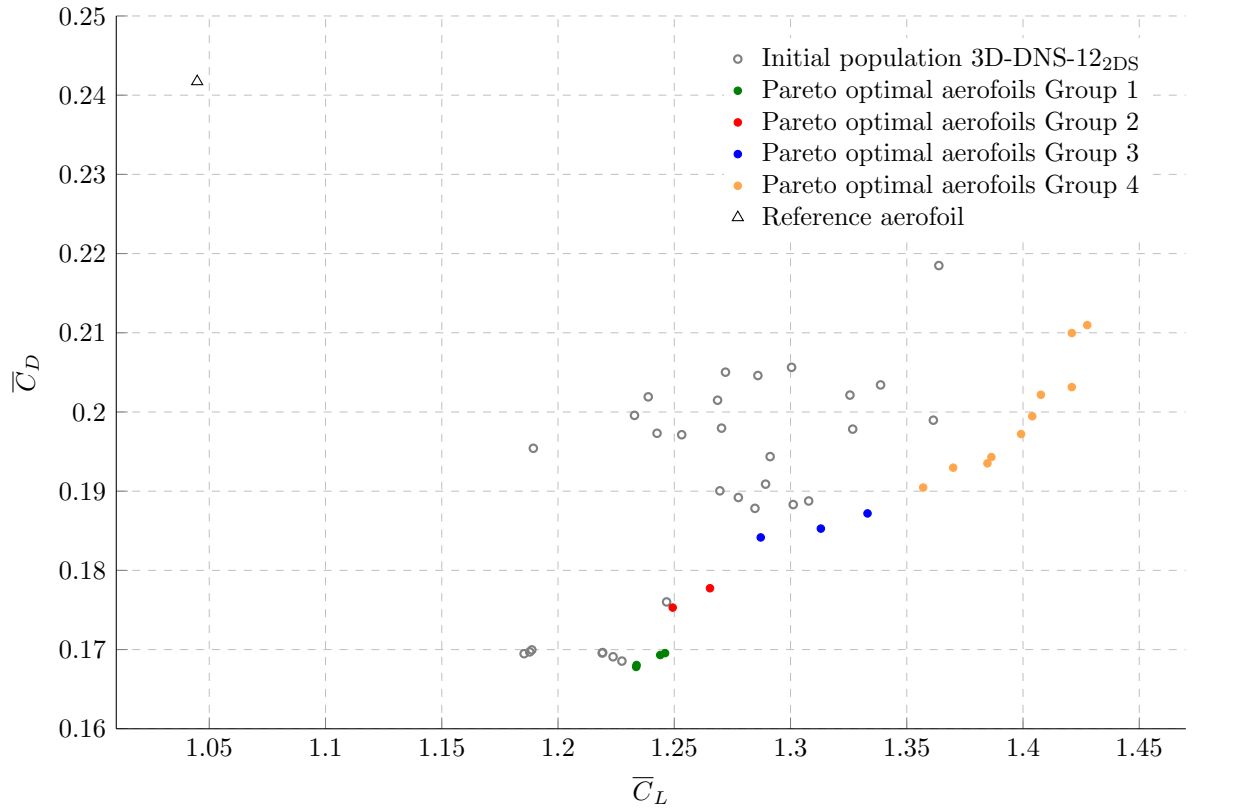
5.3.2 Q-criterion Isosurfaces and Lift Time Series

Figure 5.17 shows, for a representative aerofoil of each group and the Reference aerofoil, instantaneous Q-criterion isosurfaces coloured by velocity magnitude $|v|$ (left), C_L time series for the Data Extraction Period (middle) and C_L spectra for the Data Extraction Period (right).

The Q-criterion isosurfaces show the inherently unsteady nature of the flow over all aerofoils, with separation from the sharp leading edge and subsequent roll-up of large coherent structures on the suction side of the aerofoils. In all cases, the flow breaks down in the spanwise direction and becomes three-dimensional. For Groups 1 and 2, it is easy to identify the rib-roller vortex structure in the wake,



(a)



(b)

Figure 5.16: Plots of x_a, y_a for the initial population (hollow circles), and optimal aerofoils (solid circles), from 3D-DNS-12$_{2DS}$ and the Reference aerofoil (a). Plots of $\overline{C}_L$, $\overline{C}_D$ for the initial population (hollow circles), and optimal aerofoils (solid circles), forming the Pareto front, from 3D-DNS-12$_{2DS}$ and the Reference aerofoil (b).

Group	$\overline{C}_L$ and $\overline{C}_D$	Spanwise breakdown	C_L temporal behaviour	$\overline{C}_p$ distribution	$\overline{C}_f$ distribution
1	Lowest	Rib-roller vortex structure	Low amplitude with dominant freq. St $\approx$ 1.1	Plateau with early fall	Change of sign at trailing edge
2	Intermediate	Rib-roller vortex structure	Low amplitude with dominant freq. St $\approx$ 1.1	Plateau with later fall	Change of sign at apex and trailing edge
3	Intermediate	Spanwise unstructured	High amplitude with dominant freq. St $\approx$ 0.65	Plateau with later fall	Change of sign at apex and trailing edge
4	Highest	Spanwise unstructured	High amplitude with dominant freq. St $\approx$ 0.65	Plateau with later fall	Change of sign at trailing edge
Reference aerofoil	-	Spanwise unstructured	High amplitude with dominant freq. St $\approx$ 1.1 and energy content at low freq.	Plateau with smooth fall and lower suction	Change of sign at trailing edge and weaker recirculation

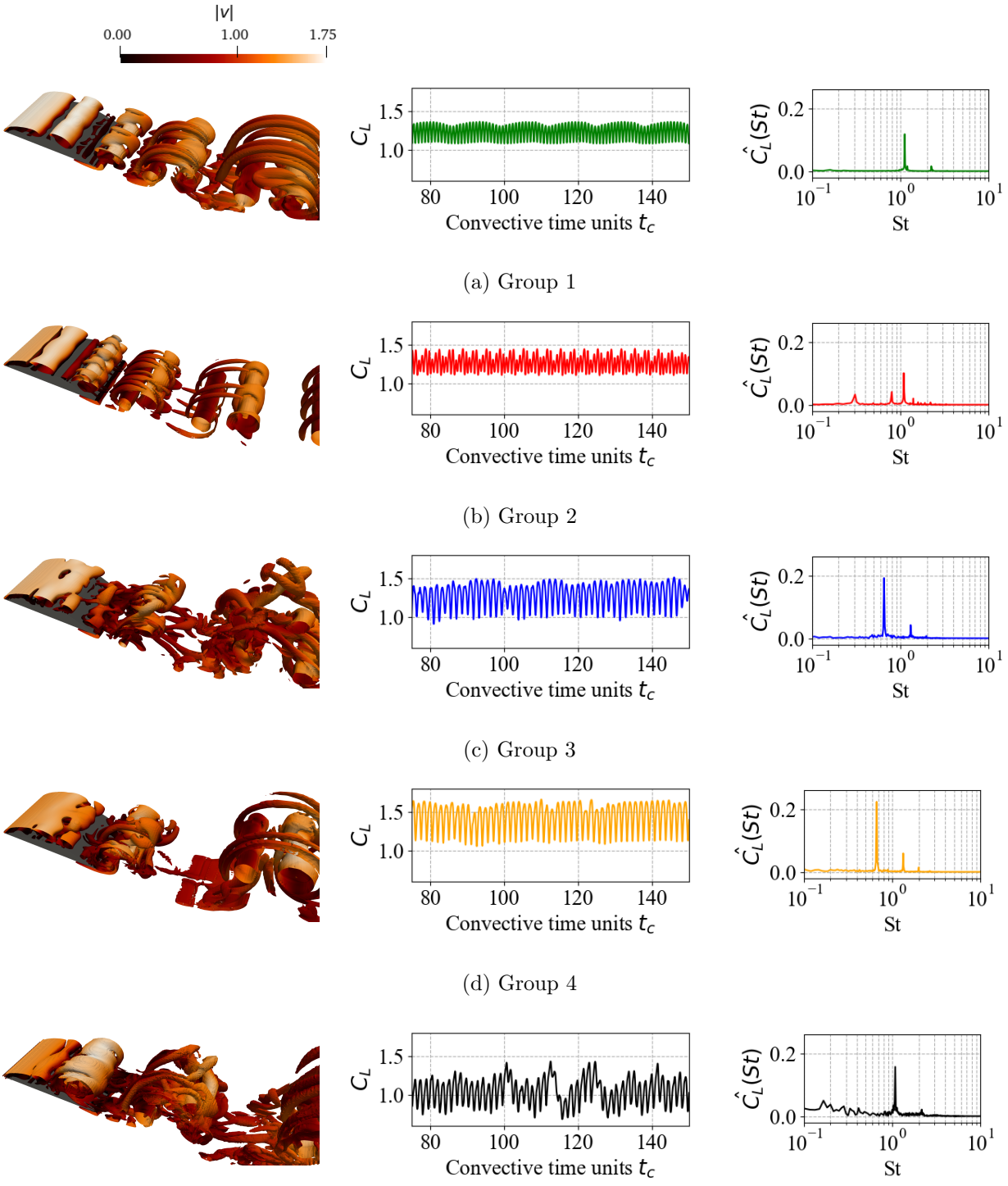
Table 5.1: Flow characteristics associated with each of the four distinct groups of aerofoils on the Pareto front from 3D-DNS-12_{2DS}, and flow characteristics associated with the Reference aerofoil.

typical of a mixing layer [130], with periodically repeating cells of span ∼0.3 chords. For Groups 3 and 4, the breakdown is unstructured, with no repeating spanwise structures. The C_L time series also reflect the unsteadiness of the flow that is characteristic of these sharp-leading-edge aerofoils, with large-amplitude oscillations corresponding to the vortex roll-up. Groups 1 and 2 show lower amplitude fluctuations than Groups 3 and 4. A correlation between large amplitude fluctuations and high $\overline{C}_L$ can be identified from the plots, with Groups 3 and 4 having the highest of both. The spectra show the dominant frequencies of the C_L time series for the representative aerofoils of each group. Groups 1 and 2 have a dominant frequency at $St \approx 1.1$, while Groups 3 and 4 have a dominant frequency at $St \approx 0.6$. The Reference aerofoil induces similar flow behaviour to Groups 3 and 4 in terms of span-wise breakdown and C_L time series. However, its dominant frequency of $St \approx 1.1$ is closer to that of Groups 1 and 2.

5.3.3 Pressure Coefficient Distribution

Time-averaged pressure coefficient $\overline{C}_p$ is defined as in Chapter 4, Equation (4.1). Figure 6.7 plots mid-span $\overline{C}_p$ distributions on the surface of a representative aerofoil from each group on the Pareto front, and the Reference aerofoil, as a function of $\tilde{x} = x/a$, where a is the x-wise distance between the leading and trailing edge of the aerofoil. The vertical dashed lines show the position of the apex for each aerofoil.

The optimal aerofoils exhibit a region of lower $\overline{C}_p$ above the upstream portion of the suction surface,



(a) Group 1

(b) Group 2

(c) Group 3

(d) Group 4

(e) Reference aerofoil

Figure 5.17: Instantaneous Q-criterion isosurfaces coloured by velocity magnitude $|v|$ (left), C_L time-series (middle) and C_L spectra (right) for one representative aerofoil of each group on the Pareto front from 3D-DNS-12_{2DS} and the Reference aerofoil.

followed by a downstream pressure recovery region, which is typical of a laminar separation bubble [25, 45, 131, 132]. Specifically, $\overline{C}_p$ remains broadly constant over the upstream portion of the suction surface. There is then a rapid pressure recovery region immediately upstream of the apex, followed by a final slower recovery region downstream of the apex; although in all cases $\overline{C}_p$ does not fully recover to the free-stream value prior to the trailing edge.

The Reference aerofoil exhibits a relatively much flatter $\overline{C}_p$ distribution over the suction surface of the aerofoil, attaining significantly higher $\overline{C}_p$ than the optimal aerofoils over the upstream portion of the suction surface, but a slightly lower value over the downstream portion of the suction surface.

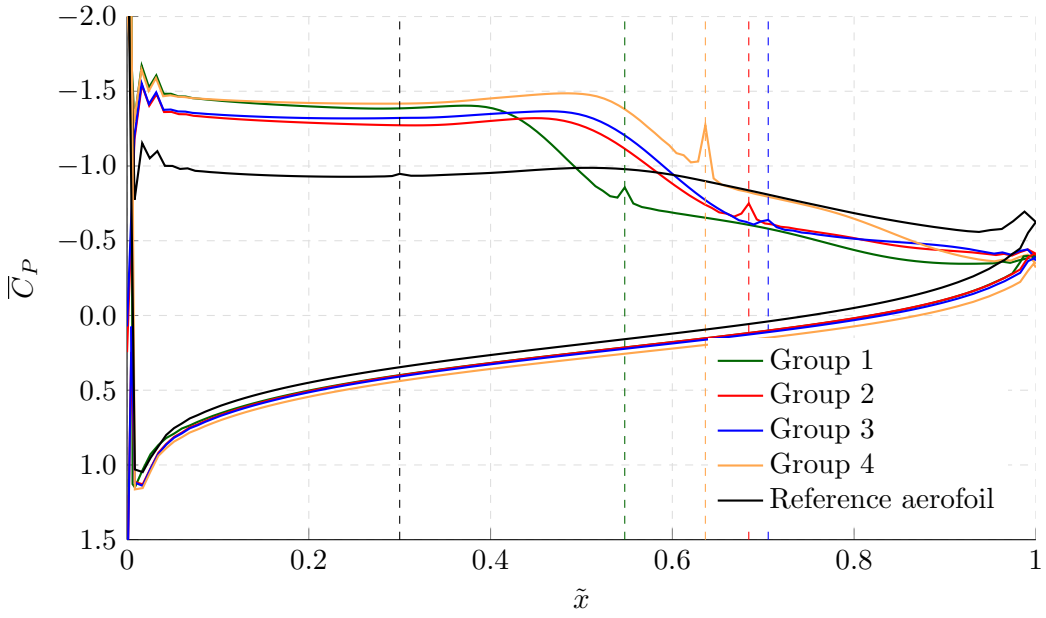
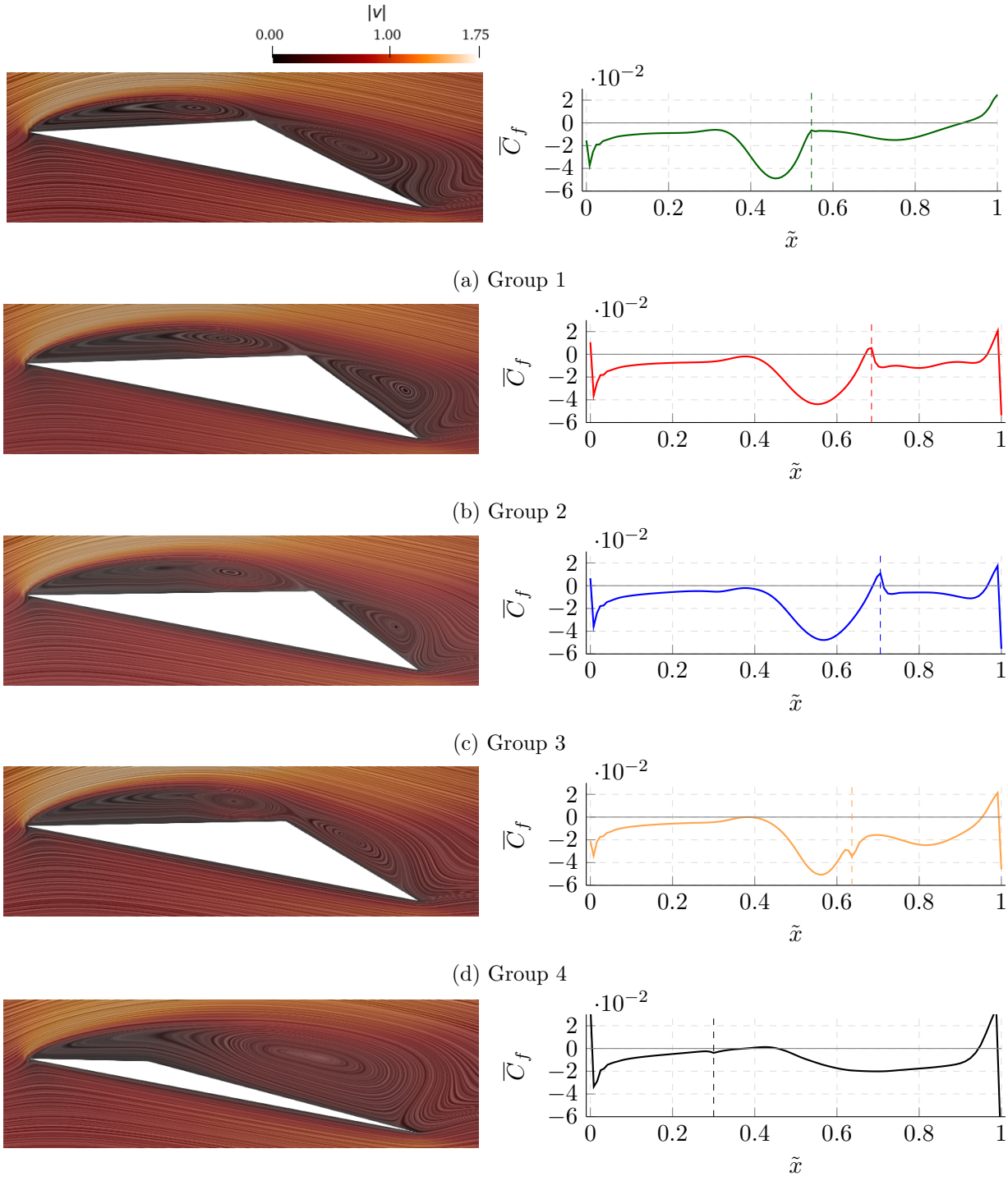


Figure 5.18: Plots of mid-span $\overline{C}_p$ distributions on the surface of a representative aerofoil from each group on the Pareto front from 3D-DNS-12$_{\text{2DS}}$, and the Reference aerofoil, as a function of $\tilde{x}$. The dashed lines show the position of the apex for each aerofoil.

5.3.4 Velocity Line Integral Convolutions (LICs) and Skin Friction Distribution

The time-averaged skin friction coefficient $\overline{C}_f$ is defined as in Chapter 4, Equation (4.8). Figure 6.8 plots time-averaged velocity magnitude $|v|$ in a span-wise constant plane, with superimposed time-averaged velocity Line Integral Convolutions (LICs) [133] (left), and $\overline{C}_f$ distributions on the suction surface as a function of $\tilde{x}$ (right), for a representative aerofoil from each group on the Pareto front, and the Reference aerofoil. The dashed lines show the position of the apex for each aerofoil.

For the optimal aerofoils, the LIC plots show two large recirculation regions adjacent to the suction



(a) Group 1

(b) Group 2

(c) Group 3

(d) Group 4

(e) Reference aerofoil

Figure 5.19: Time-averaged velocity magnitude $|v|$ in a span-wise constant plane, with superimposed time-averaged velocity LICs (left), and mid-span $\overline{C}_f$ distributions on the suction surface as a function of $\tilde{x}$ (right), for a representative aerofoil from each group on the Pareto front from 3D-DNS-12_{2DS}, and the Reference aerofoil. The dashed lines show the position of the apex for each aerofoil.

surface, which are responsible for the increased lift. The recirculation regions can also be identified from the two pronounced negative peaks in the $\overline{C}_f$ distributions. aerofoils in Groups 2 and 3 experience a change in sign of $\overline{C}_f$ near the apex, which signifies reattachment in the time-averaged sense. The flow then separates again downstream of the apex, with vortices rolling up on the downstream suction surface of the aerofoil. aerofoils in Groups 1 and 4 show a similar $\overline{C}_f$ distribution to those in Groups 2 and 3, but without reattachment; they induce separated flow, in the time-averaged sense, for the entirety of the chord. All the aerofoils induce a change of sign of $\overline{C}_f$ near the trailing edge due to the vortex generated by the flow coming from the pressure surface being sucked upwards to the suction surface.

The Reference aerofoil exhibits fully separated flow from the leading edge with a recirculation region further downstream and further away from the suction surface compared to the Pareto optimal aerofoils. Consequently, the Reference aerofoil is unable to create such a strong overall suction effect, as observed in the $\overline{C}_p$ distribution in Fig. 6.7.

5.4 Summary

Triangular aerofoil shapes with sharp leading edges have been optimised for Martian atmospheric conditions, targeting aerodynamic performance. Optimisations have been performed with both 2D and 3D DNS with PyFR, at angles of attack $\alpha = 6°$ and $\alpha = 12°$, with a chord-based $Re = 3,000$ and Mach number $M = 0.15$. Specifically, multi-objective optimisation was performed to maximise lift and minimise drag, yielding a Pareto front of non-dominated aerofoils.

For low angles of attack ($\alpha = 6°$), it has been shown that the optimal aerofoils induce predominantly two-dimensional flow. 2D and 3D DNS evaluations have given similar aerodynamic coefficients, which resulted in similar optimum aerofoil shapes for both optimisations. Furthermore, the 2D DNS Pareto optimal aerofoils evaluated with 3D DNS are still within the 3D DNS Pareto optimal set of solutions. Thus, 2D DNS optimisation can be used to optimise triangular aerofoils at low angles of attack such as $\alpha = 6°$, under the conditions tested.

On the other hand, at an angle of attack of $\alpha = 12°$, optimisation with 2D and 3D DNS yields different results. It has been shown that 2D DNS evaluations over-predict lift and under-predict drag at $\alpha = 12°$

due to the lack of capturing the three-dimensional breakdown of vortices. When evaluated with 3D DNS, the 2D DNS Pareto optimal aerofoils fall into the dominated area of the 3D DNS Pareto front. Furthermore, Pareto optimal aerofoils rely on the vortex roll-up shed from the leading edge with a three-dimensional breakdown in the spanwise direction. Hence, 3D DNS optimisation is necessary to optimise triangular aerofoils at high angles of attack such as $\alpha = 12^\circ$, under the conditions tested.

A set of Pareto optimal aerofoils is obtained from 3D DNS optimisation at $\alpha = 12^\circ$ with 2D DNS optimisation results as the initial sampling. The resulting aerofoil shapes are investigated in terms of Q-criterion isosurfaces, lift coefficient spectra, pressure coefficient distributions, velocity line integral convolutions and skin friction distributions to elucidate the flow physics that yield optimal performance.

The aerofoils on the Pareto front achieve optimal performance by exploiting vortex roll-up as a lifting mechanism. Specifically, they aim to retain a strong vortex close to the upstream portion of the suction surface, prior to the apex, whilst avoiding excessive inclination of the downstream portion of the suction surface, which would result in a high-pressure drag. This is achieved by positioning their apexes downstream of $x \approx 0.5$ and at $y \approx 0.15$; setting the upstream portion of the suction surface approximately parallel to the free-stream flow when $\alpha = 12^\circ$.

Aerofoils in Group 1 have the lowest $\overline{C}_L$ values since their apexes are upstream of those in Groups 2, 3 and 4, which reduces the extent of the low-pressure region on the upstream portion of the suction surface. Group 1 aerofoils also have the lowest $\overline{C}_D$ values, likely because the downstream portion of their upper surface is less steeply inclined. Aerofoils in this Group exhibit a rib-roller vortex structure with low amplitude C_L fluctuations and a dominant frequency at $St = 1.1$.

Aerofoils in Groups 2 and 3 are in the middle of the Pareto front, with intermediate values of $\overline{C}_L$ and $\overline{C}_D$. The aerofoils in these groups are characterised by reattachment of the flow near the apex in the time-averaged sense. They have intermediate values of $\overline{C}_L$ and $\overline{C}_D$ because the low-pressure region on the upstream portion of their suction surface is larger than for Group 1, but their vortices roll up further from the suction surface compared to Group 4. Groups 2 and 3 differ in their vortex structures and C_L behaviour. Aerofoils in Group 2 have a rib-roller vortex structure with low-amplitude C_L fluctuations and a dominant frequency at $St = 1.1$, similar to Group 1. Group 3 aerofoils show higher values of $\overline{C}_L$ and $\overline{C}_D$ compared to those in Group 2, and they exhibit an unstructured spanwise breakdown of the

coherent motions shed into the wake, with high-amplitude C_L fluctuations and a dominant frequency at $St = 0.65$.

Finally, aerofoils in Group 4 have the highest values of $\overline{C}_L$ and $\overline{C}_D$ because the low-pressure region on the upstream portion of their suction surface is larger than for Group 1, and their vortices roll-up closer to the suction surface compared to Groups 2 and 3. Aerofoils in this Group exhibit similar flow structures and C_L behaviour to those in Group 3, with an unstructured spanwise breakdown of the coherent motions shed into the wake, high amplitude C_L fluctuations and a dominant frequency at $St = 0.65$.

The optimised aerofoils that form the Pareto front achieve up to a 48% increase in lift or a 28% reduction in drag compared to the Reference aerofoil. This work marks the first-ever use of DNS for aerodynamic shape optimisation.

Chapter 6

Effects of Free-Stream Eddies on Genetic Algorithm Optimisation of Aerofoils for Martian Rotorcraft using Direct Numerical Simulations

This chapter is divided into the following investigations. First, it examines the effect of free-stream eddies on the performance of optimised triangular aerofoils for Martian atmospheric conditions. Then, it explores the impact that optimising triangular aerofoils affected by free-stream eddies has on the resulting optimal aerofoil shapes. The aim is to understand to what extent physics are modified when the inflow contains free-stream eddies, and whether optimal designs remain the same.

To this end, Pareto optimal aerofoils from 3D-DNS-12_{2DS} from Chapter 5 - optimised for steady, uniform inflow - have been re-evaluated under the effects of injected free-stream eddies with target values of turbulence intensity of TI = 0.5% and TI = 1% and target values of characteristic length scales of $ls = 0.05$ and $ls = 0.1$ chords at chord-based Reynolds number $Re = 3,000$ and Mach number $M = 0.15$ using high-order 3D DNS with the PyFR framework, described in Chapter 3. Results show that free-stream eddies do affect the performance of optimum aerofoils. Consequently, 3D DNS optimisation of triangular aerofoils using GAs with `pymoo`, detailed in Chapter 3, is run with injected

free-stream eddies with target values of turbulence intensity of TI = 1% and a characteristic length scale of $ls = 0.1$ chords at $Re = 3,000$, $M = 0.15$ and $\alpha = 12°$ with Pareto optimal aerofoils from 3D-DNS-12_{2DS} as the initial sampling. This optimisation is referred to as 3D-DNS-12-FSE_{3DS}. Flow physics from Pareto optimal aerofoils from 3D-DNS-12-FSE_{3DS} are then investigated and compared against Pareto optimal aerofoils from 3D-DNS-12_{2DS}.

6.1 Methodology

Synthetic turbulence is generated via a source term following the extended Synthetic Eddy Method (SEM) as described in Chapter 3. The source term is based on a superimposition of fictitious turbulent eddies with prescribed geometrical shapes, random signs and random positions, which are advected with constant velocity across a predetermined region of space. The injected free-stream eddies are not referred to as injected synthetic turbulence in this work since they do not develop into turbulence due to the very low Reynolds number (3,000 based on the chord). The aim is to simulate conditions similar to the unsteady flow affecting a rotor blade on Mars due to atmospheric perturbations or the wake of an upstream blade. All simulations in this Chapter were undertaken using PyFR commit `bbaaefd` on the `develop` branch. The simulations ran on Nvidia Tesla P100-16GB GPUs on Piz Daint at the Swiss National Supercomputing Centre.

The meshes used in this Chapter are analogous to the ones used in Chapter 5, with an additional structured quadrilateral fine mesh in the area of injected eddies and downstream of it. Figure 6.1 shows the computational mesh used for the simulations with injected free-stream eddies, in particular for the Reference aerofoil. The centre plane of the box of injected eddies is located at a distance of 1.0 upstream of the leading edge when the aerofoil is at an angle of attack of $\alpha = 12°$. The streamwise extent of the box is 0.2, the vertical extent is 1.0 and the spanwise extent is the same as the domain size, 0.6. Figure 6.1 shows the box of injected eddies illustrated in red. The resulting three-dimensional meshes have $\sim 200 \times 10^3$ elements and $\sim 25 \times 10^6$ degrees of freedom per equation in total. The boundary conditions, initial conditions and Data Extraction Period are analogous to the ones in Chapter 5.

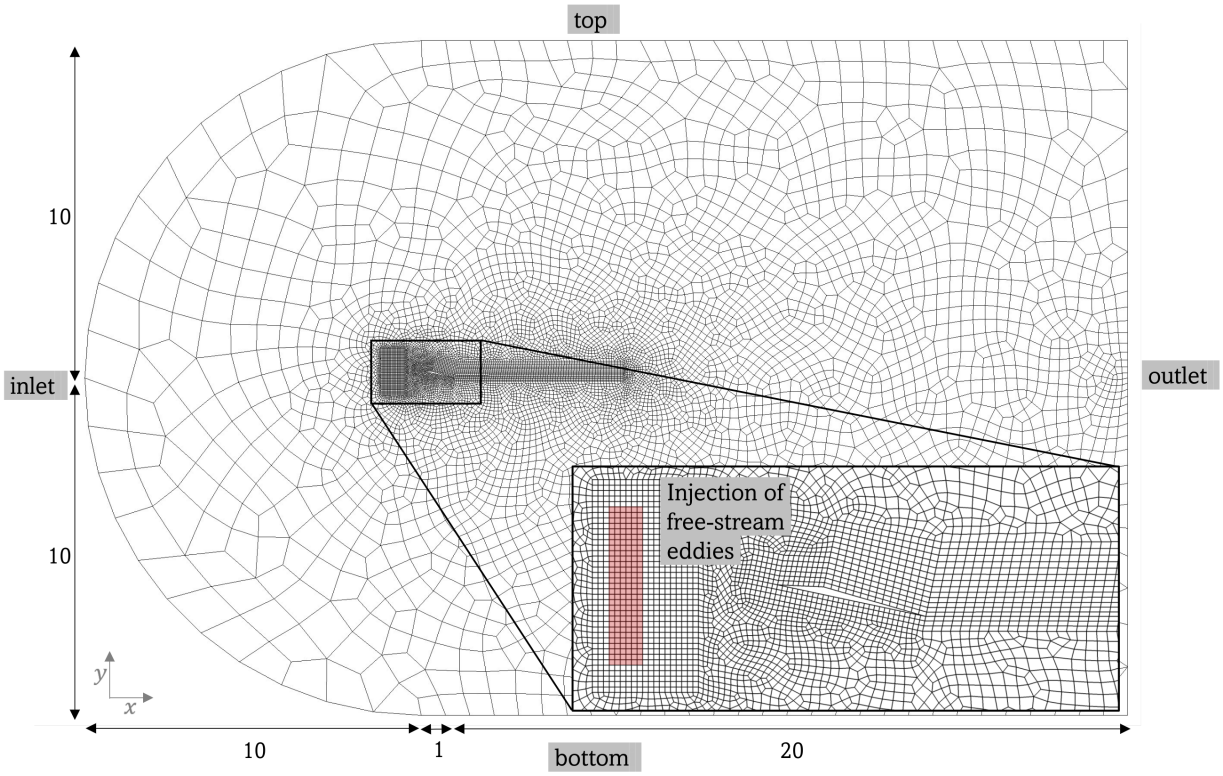


Figure 6.1: Computational mesh for the Reference aerofoil. The box within which free-stream eddies were injected is shaded red for a specific characteristic length scale of $ls = 0.1$.

6.2 Effects of Free-Stream Eddies on Optimised Aerofoils from 3D-DNS-12_{2DS}

The work presented in Chapters 4 and 5 investigated the flow physics that enhance performance of triangular aerofoils for Martian Rotorcraft. Findings indicate that the aerodynamic forces of optimal aerofoils are influenced by the coherence of the large vortical structures that roll on the suction side of the aerofoils, as well as on the dynamics of flow separation and reattachment. It is anticipated that optimal aerofoils are sensitive to free-stream perturbations since these can affect the flow around the aerofoils in various ways. Free-stream eddies may interact with the separated shear layer, influencing the large-scale vortices on the suction side and altering the flow reattachment. This interaction can also prompt an earlier transition, leading to a reattachment of the flow. Moreover, free-stream eddies can impact the large-scale vortices in the wake, thereby affecting the aerodynamic forces. This section aims to investigate the extent to which these physical phenomena are affected and altered.

Optimal airfoils from 3D-DNS-12_{2DS} from Chapter 5 - optimised for steady, uniform inflow - have been used to investigate the effects of free-stream eddies with various turbulence intensities and length scales on optimal Martian Rotorcraft triangular aerofoils. Due to a lack of published data on free-stream turbulence measurements in the Martian atmosphere, the target values of turbulence intensity and characteristic length scales for the injected eddies have been chosen intuitively. The length scales of the eddies are selected to be comparable to the chord length to maximise their impact on the flow over the aerofoils. It is assumed that eddies larger than the chord would induce quasi-steady conditions, while the influence of eddies smaller than the chord would average out across the span of the wing, thereby having a less significant effect. The injected free-stream eddies in this investigation have target values of turbulence intensity of 0.5% and 1% and target values of integral length scales of 0.05 and 0.1 chords. All simulations are run at chord-based Reynolds number $Re = 3,000$ and Mach number $M = 0.15$ using high-order 3D DNS with PyFR.

6.2.1 Aerodynamic Performance

Figure 6.2a plots apex locations in the x_a, y_a design space for the Pareto optimal aerofoils from 3D-DNS-12_{2DS}, with a representative aerofoil from each of the groups identified in Chapter 5 delineated with dashed lines, using distinct colours for the different groups. Figures 6.2b, 6.2c, 6.2d, 6.2e and 6.2f plot the Pareto front of optimal aerofoils in the $\overline{C}_L$, $\overline{C}_D$ objective space, with the representative aerofoil from each group coloured, as well as the $\overline{C}_L$, $\overline{C}_D$ values of the aerofoil when run with injected free-stream eddies of various turbulence intensities, TI=1% and TI=0.5%, and characteristic length scales, $ls = 0.1$ and $ls = 0.05$.

When exposed to free-stream eddies, all tested aerofoils exhibit a decrease in $\overline{C}_L$, ranging between 1% and 27% lower than under uniform conditions. In most cases, a reduction in $\overline{C}_D$ is also observed, with variations between +3% and -24%. In general, with the exception of Group 1, a trend can be identified where, as turbulence intensity and/or characteristic length scale of the free-stream eddies is increased, the aerodynamic coefficients decrease. The increase in turbulence intensity, in particular, has a more pronounced impact.

Additionally, by looking at the cases affected by the highest values of turbulence intensity and length scales, it can be seen that all aerofoils exhibit similar aerodynamic coefficients independently of their

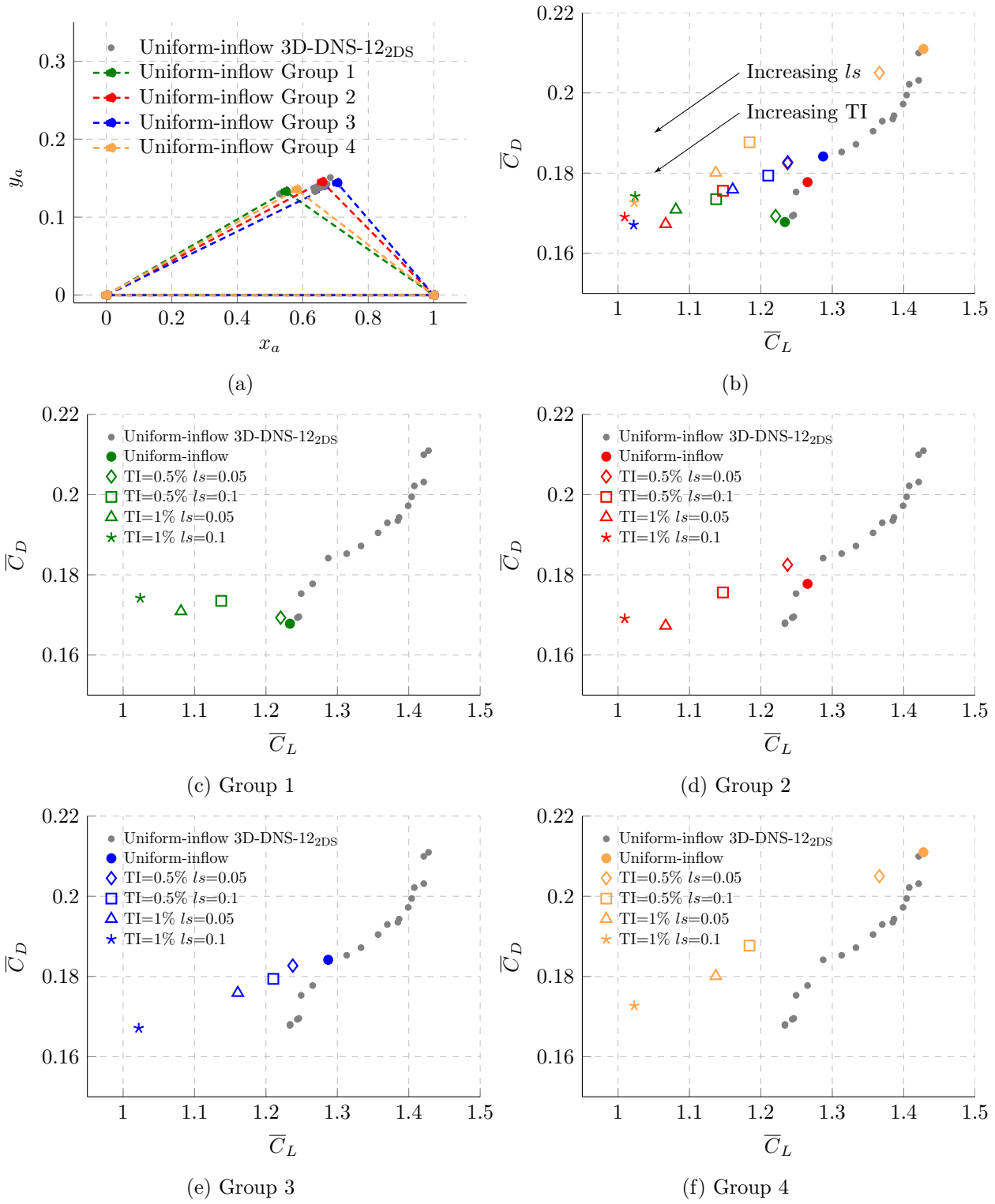


Figure 6.2: Plots of x_a, y_a for the optimal aerofoils from 3D-DNS-12$_{2DS}$ in grey with one aerofoil representative from each of the groups identified delineated with dashed lines and colours (a). Plots of $\overline{C}_L$, $\overline{C}_D$ (b), (c), (d), (e), (f) for the optimal aerofoils from 3D-DNS-12$_{2DS}$ in grey with values of the representative (coloured) aerofoils under the influence of free-stream eddies with target values of turbulent intensity of TI=1% and TI=0.5% and characteristic length scales of $ls = 0.1$ and $ls = 0.05$.

initial positions in the objective space. This suggests that high levels of turbulence intensity and length scale can regularise aerofoil performance for the Pareto optimal aerofoils. Conversely, lower levels of these parameters result in minor variations in the aerodynamic coefficients, leading to positions in the objective space closer to the uniform-inflow cases.

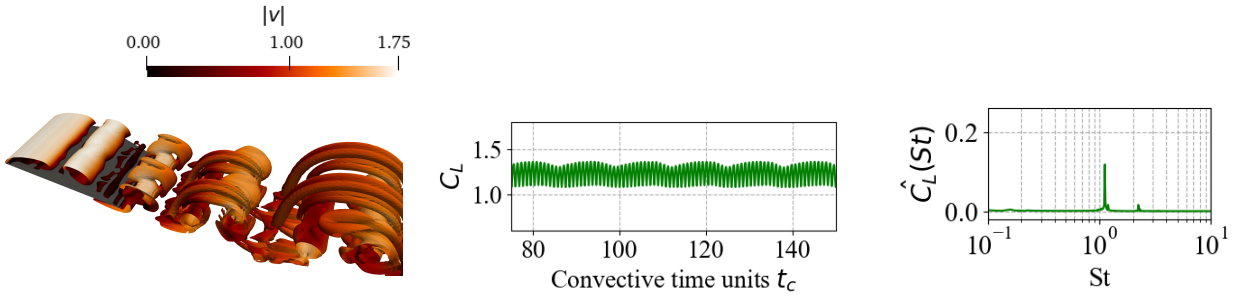
It is also important to note that the tested aerofoils do not maintain a Pareto-front relationship when subjected to different free-stream eddies as observed in Figure 6.2b. Some aerofoils become dominated by others, and their relative positioning within the Pareto front is not preserved. Therefore, not all optimised aerofoil shapes under uniform-inflow conditions remain optimal when influenced by different free-stream conditions.

In order to examine how the injection of different free-stream eddies affects the associated flow physics of the optimal aerofoils, results are analysed and compared against results from uniform-inflow conditions. A detailed discussion of the flow physics associated with each group, including analysis of Q-criterion isosurfaces, lift coefficient C_L, time-averaged pressure coefficient $\overline{C}_p$, time-averaged velocity line integral convolutions (LICs) and time-averaged skin friction $\overline{C}_f$, is presented below.

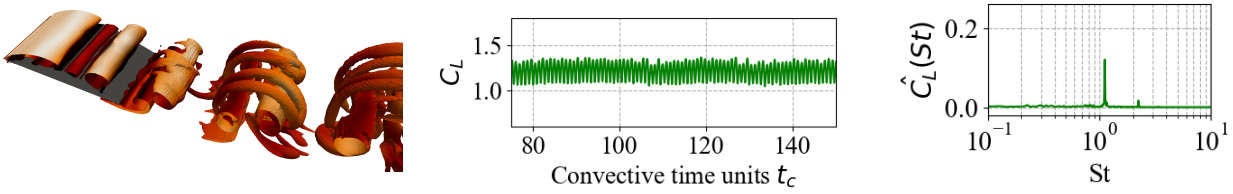
6.2.2 Q-criterion Isosurfaces and Lift Time Series

Figures 6.3, 6.4, 6.5 and 6.6 show, for each of the representative aerofoils of each group, instantaneous Q-criterion isosurfaces coloured by velocity magnitude $|v|$ (left), C_L time series for the Data Extraction Period (middle) and C_L spectra for the Data Extraction Period (right) for different free-stream conditions: uniform-inflow (a), free-stream eddies with TI=0.5% and $ls = 0.05$ (b), free-stream eddies with TI=1% and $ls = 0.05$ (c), free-stream eddies with TI=0.5% and $ls = 0.1$ (d) and free-stream eddies with TI=1% and $ls = 0.1$ (e).

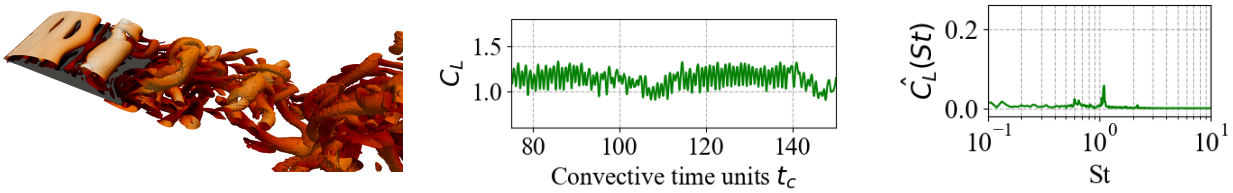
In all cases, the Q-criterion isosurfaces show the inherently unsteady nature of the flow over all aerofoils, with separation from the sharp leading edge and subsequent roll-up of large coherent structures on the suction side of the aerofoils. Additionally, in all cases, the flow breaks down in the spanwise direction and becomes three-dimensional. Under the influence of free-stream eddies, the flow exhibits less spanwise coherence and more unstructured behaviour, an effect that intensifies with higher turbulence intensity and larger characteristic length scales.



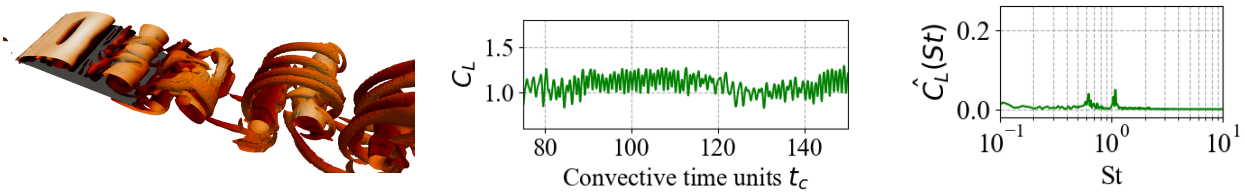
(a) Uniform-inflow Group 1



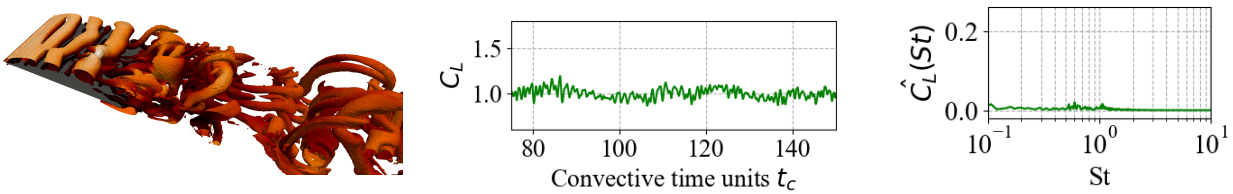
(b) Free-stream eddies TI=0.5% ls=0.05 Group 1



(c) Free-stream eddies TI=0.5% ls=0.1 Group 1

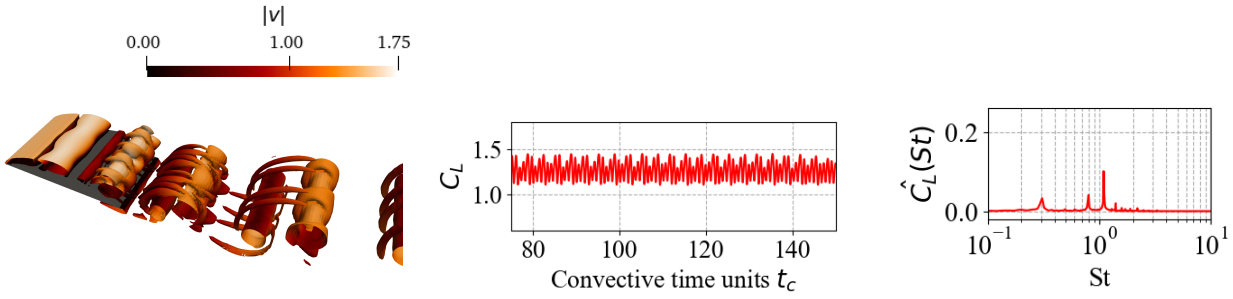


(d) Free-stream eddies TI=1% ls=0.05 Group 1

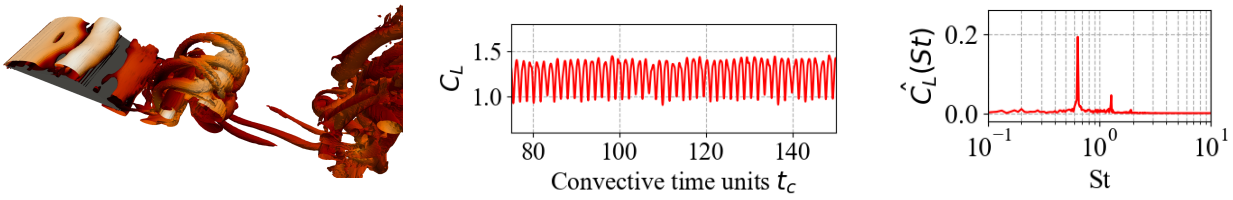


(e) Free-stream eddies TI=1% ls=0.1 Group 1

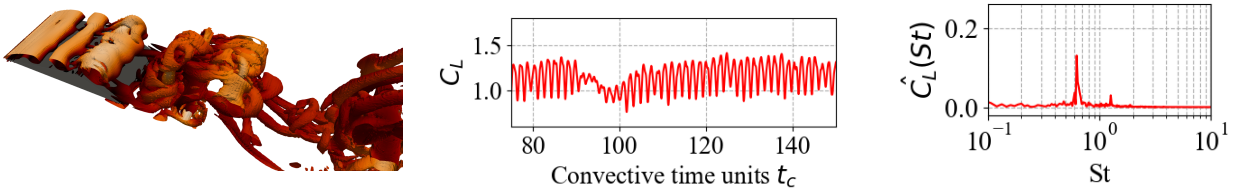
Figure 6.3: Instantaneous Q-criterion isosurfaces coloured by velocity magnitude $|v|$ (left), C_L time series (middle) and C_L spectra (right) for different free-stream conditions for the representative aerofoil from Group 1 on the Pareto front from 3D-DNS-12$_{2DS}$.



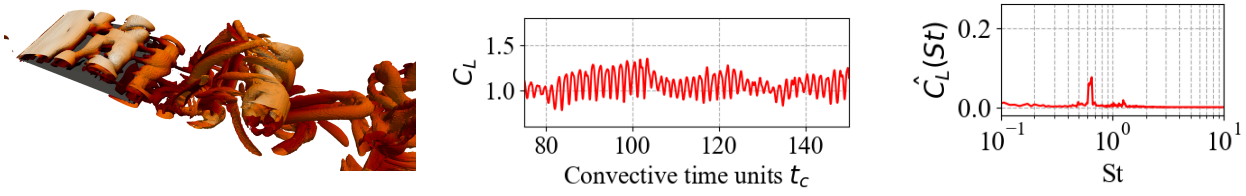
(a) Uniform-inflow Group 2



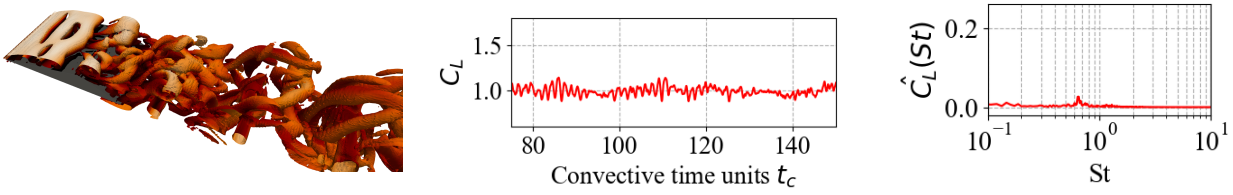
(b) Free-stream eddies TI=0.5% ls=0.05 Group 2



(c) Free-stream eddies TI=0.5% ls=0.1 Group 2

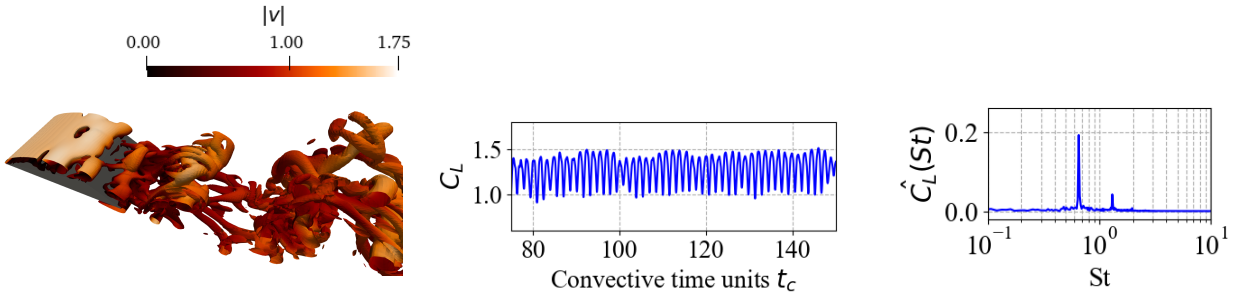


(d) Free-stream eddies TI=1% ls=0.05 Group 2

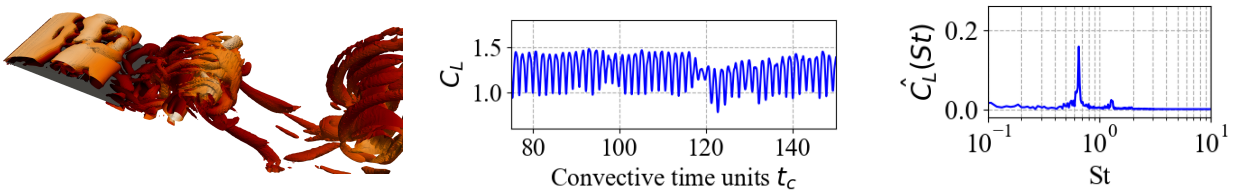


(e) Free-stream eddies TI=1% ls=0.1 Group 2

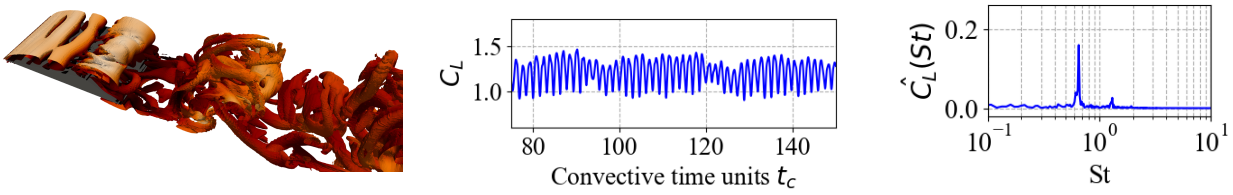
Figure 6.4: Instantaneous Q-criterion isosurfaces coloured by velocity magnitude $|v|$ (left), C_L time series (middle) and C_L spectra (right) for different free-stream conditions for the representative aerofoil from Group 2 on the Pareto front from 3D-DNS-12$_{2DS}$.



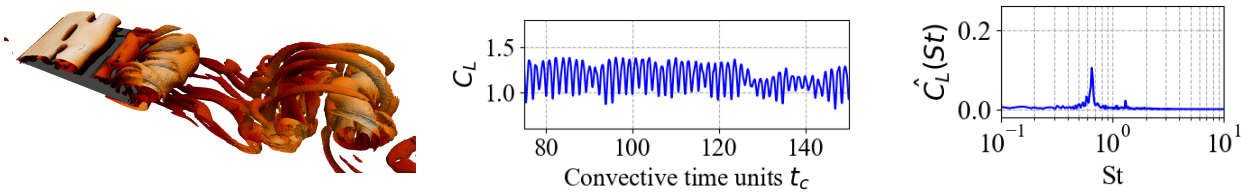
(a) Uniform-inflow Group 3



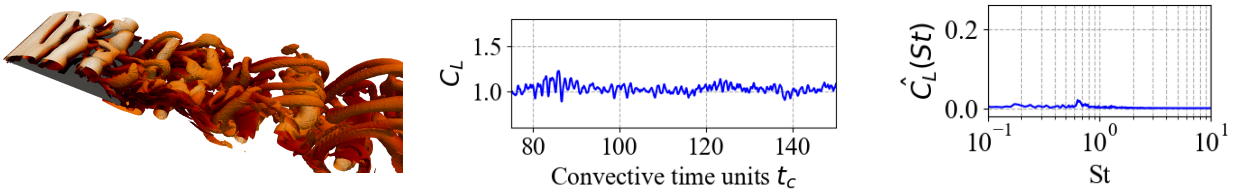
(b) Free-stream eddies TI=0.5% ls=0.05 Group 3



(c) Free-stream eddies TI=0.5% ls=0.1 Group 3

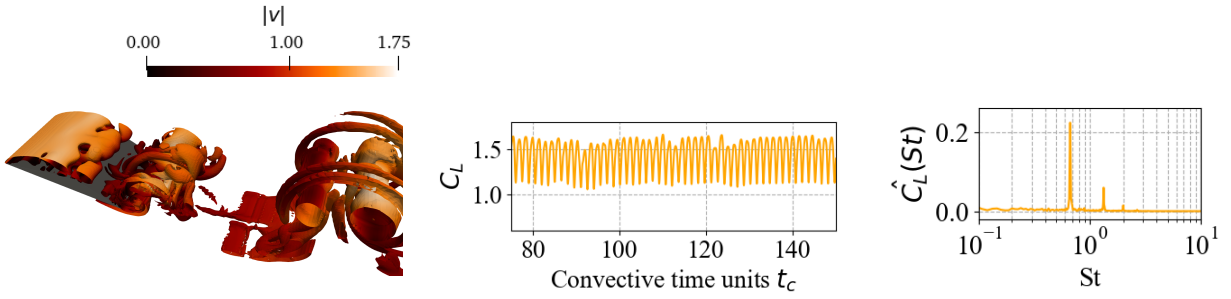


(d) Free-stream eddies TI=1% ls=0.05 Group 3

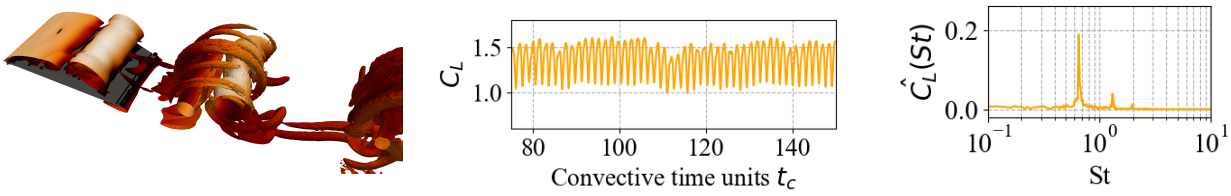


(e) Free-stream eddies TI=1% ls=0.1 Group 3

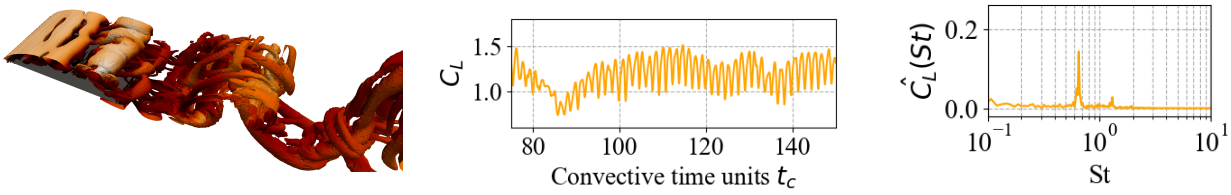
Figure 6.5: Instantaneous Q-criterion isosurfaces coloured by velocity magnitude $|v|$ (left), C_L time series (middle) and C_L spectra (right) for different free-stream conditions for the representative aerofoil from Group 3 on the Pareto front from 3D-DNS-12$_{2DS}$.



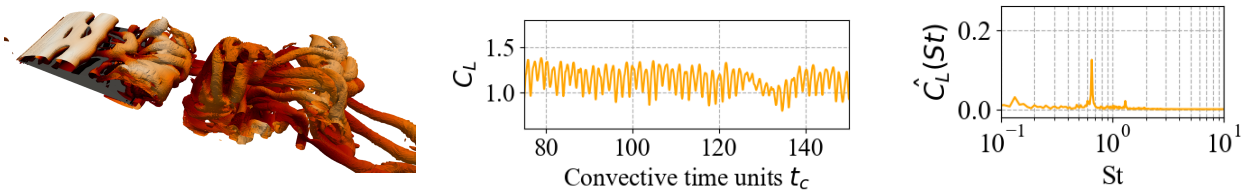
(a) Uniform-inflow Group 4



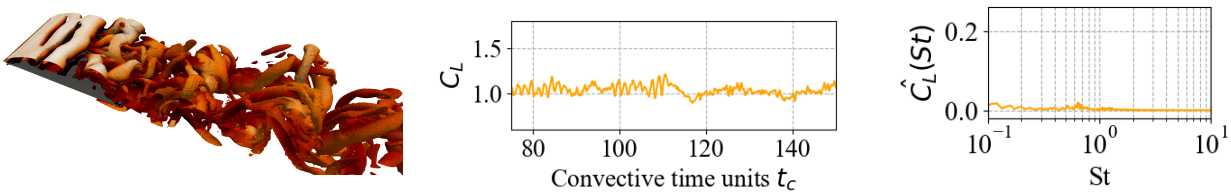
(b) Free-stream eddies TI=0.5% ls=0.05 Group 4



(c) Free-stream eddies TI=0.5% ls=0.1 Group 4



(d) Free-stream eddies TI=1% ls=0.05 Group 4



(e) Free-stream eddies TI=1% ls=0.1 Group 4

Figure 6.6: Instantaneous Q-criterion isosurfaces coloured by velocity magnitude $|v|$ (left), C_L time series (middle) and C_L spectra (right) for different free-stream conditions for the representative aerofoil from Group 4 on the Pareto front from 3D-DNS-12$_{2DS}$.

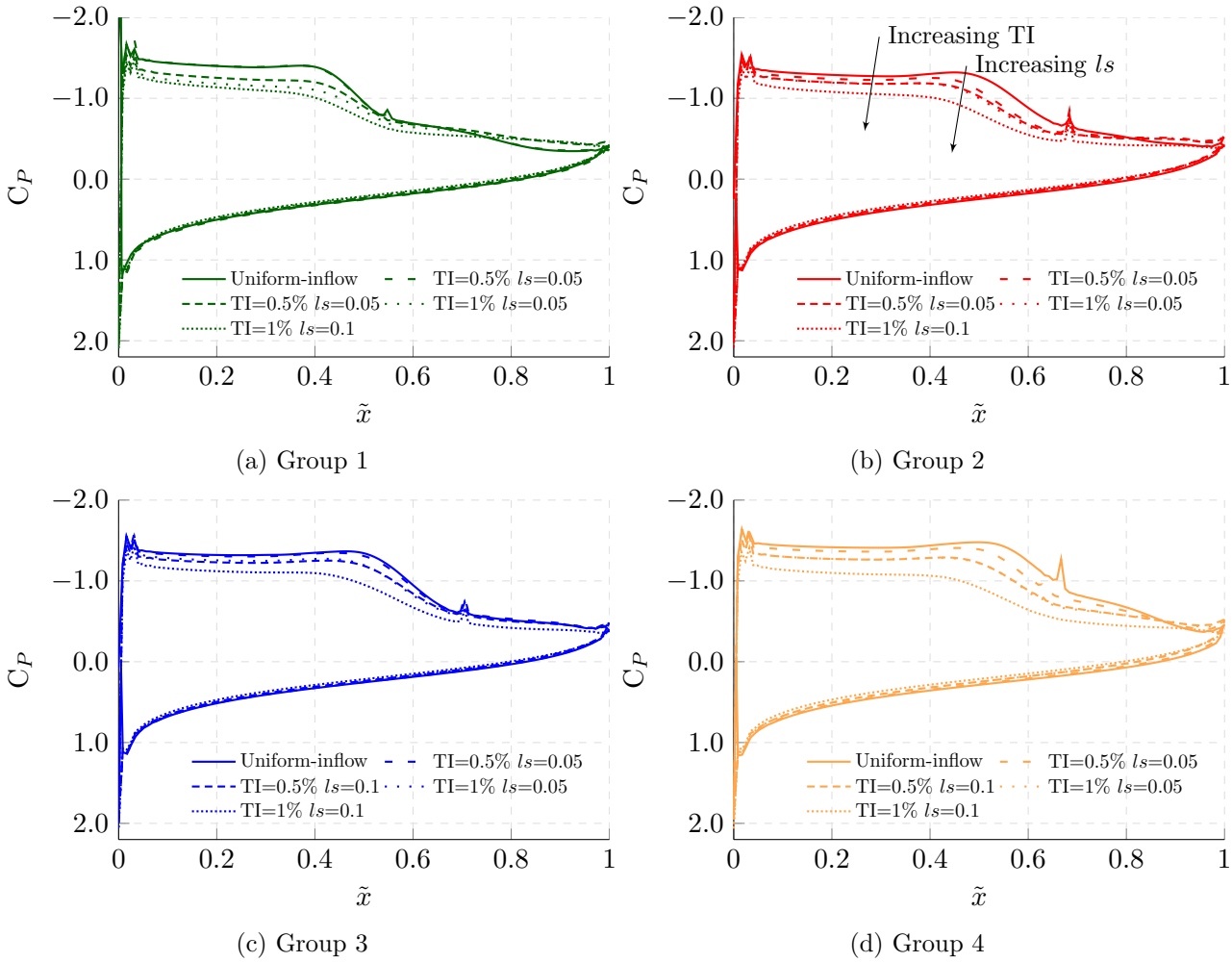
The C_L time series also reflect the unsteadiness of the flow that is characteristic of these sharp-leading-edge aerofoils. Uniform inflow conditions result in higher amplitude fluctuations and a higher $\overline{C}_L$ than those seen with injected free-stream eddies. This difference arises from the interaction of free-stream eddies with the large coherent vortices on the suction side, leading to their breakdown and resulting in weaker suction due to spanwise de-correlation, as evidenced by the Q-criterion isosurfaces. The spectra show the dominant frequencies of the C_L time series. For all groups, when run with uniform inflow, the spectra show much clearer dominant frequencies than when affected by free-stream eddies. The higher the turbulence intensity and the higher the characteristic length scale of the injected eddies, the lesser periodicity is maintained in the C_L signal. Interestingly, the TI=0.5% $ls = 0.1$ combination seems to have a similar effect on the C_L time series, and therefore its spectra, to the TI=1% $ls = 0.05$ combination across all groups. The most extreme TI and ls values notably disrupt periodicity and, as shown in Figure 6.2, lead to a significant reduction in both aerodynamic coefficients due to the breakdown of vortex coherence. Analysis of the Q-criterion isosurfaces, C_L time series, and spectra under these conditions reveals similar flow features across different groups. Moreover, all aerofoils exhibit notably similar behaviour under the influence of the highest tested values of TI and ls, reinforcing the observation that free-stream eddies increasingly regularise the performance of diverse Pareto optimal aerofoils as the TI and ls values are raised.

Examining each aerofoil individually yields additional insights. The aerofoil in Group 1 retains the dominant frequency that characterised this group of $St \approx 1.1$. In contrast, the Group 2 aerofoil shows a shift in dominant frequency from uniform-inflow to injected free-stream eddies, aligning its dominant frequency ($St \approx 0.65$) with those of Groups 3 and 4. The dominant frequencies in Groups 3 and 4 remain the same, regardless of the free-stream eddy conditions.

6.2.3 Pressure Coefficient Distribution

The time-averaged pressure coefficient $\overline{C}_p$ is defined as in Chapter 4, Equation (4.1). Figure 6.7 plots mid-span $\overline{C}_p$ distributions on the surface of the representative aerofoil from each group on the Pareto front from 3D-DNS-12_{2DS} under the five different free-stream conditions as a function of $\tilde{x} = x/a$, where a is the x-wise distance between the leading and trailing edge of the aerofoil.

As described in Chapter 5, the optimal aerofoils exhibit a region of low $\overline{C}_p$ above the upstream



(a) Group 1

(b) Group 2

(c) Group 3

(d) Group 4

Figure 6.7: Plots of mid-span $\overline{C}_p$ distributions as a function of $\tilde{x}$ on the surface of the representative aerofoil from each group on the Pareto front from 3D-DNS-12$_{2DS}$ when evaluated with uniform inflow as well as when affected by free-stream eddies with different target turbulence intensities, TI, and different target characteristic length scales, ls.

portion of the suction surface, followed by a downstream pressure recovery region, typical of a laminar separation bubble. Specifically, for all groups, $\overline{C}_p$ remains broadly constant over the upstream portion of the suction surface, with uniform-inflow conditions showing the highest suction. Under the influence of injected free-stream eddies, as previously noted, the flow de-correlates in the spanwise direction, which causes a reduction in suction. This effect amplifies with increasing TI and ls values. Groups 1 and 3 show minimal changes in their $\overline{C}_p$ distribution with the smallest values of TI and ls. Thus, it can be said that they are more robust to low-intensity, small perturbations in the incoming flow.

After the plateau $\overline{C}_p$ region, there is a rapid pressure recovery region immediately upstream of the apex. The reduced suction in aerofoils impacted by free-stream eddies results in a less steep pressure

recovery, reaching similar $\overline{C}_p$ values downstream of the apex. The $\overline{C}_p$ distribution on the downstream portion of the upper surface when comparing cases influenced by uniform inflow and injected free-stream eddies shows mixed results. In some instances, free-stream eddies increase suction near the trailing edge, while in others, they decrease it. The influence of free-stream eddies is less pronounced closer to the trailing edge given that the coherent vortices on the suction surface are already broken down at this point for the uniform-inflow cases.

The $\overline{C}_p$ distribution parallels observations from the Q-criterion isosurfaces, C_L time series, and $\overline{C}_L$ and $\overline{C}_D$ values, where aerofoils in different groups exhibit similar patterns when exposed to the highest tested TI and ls values.

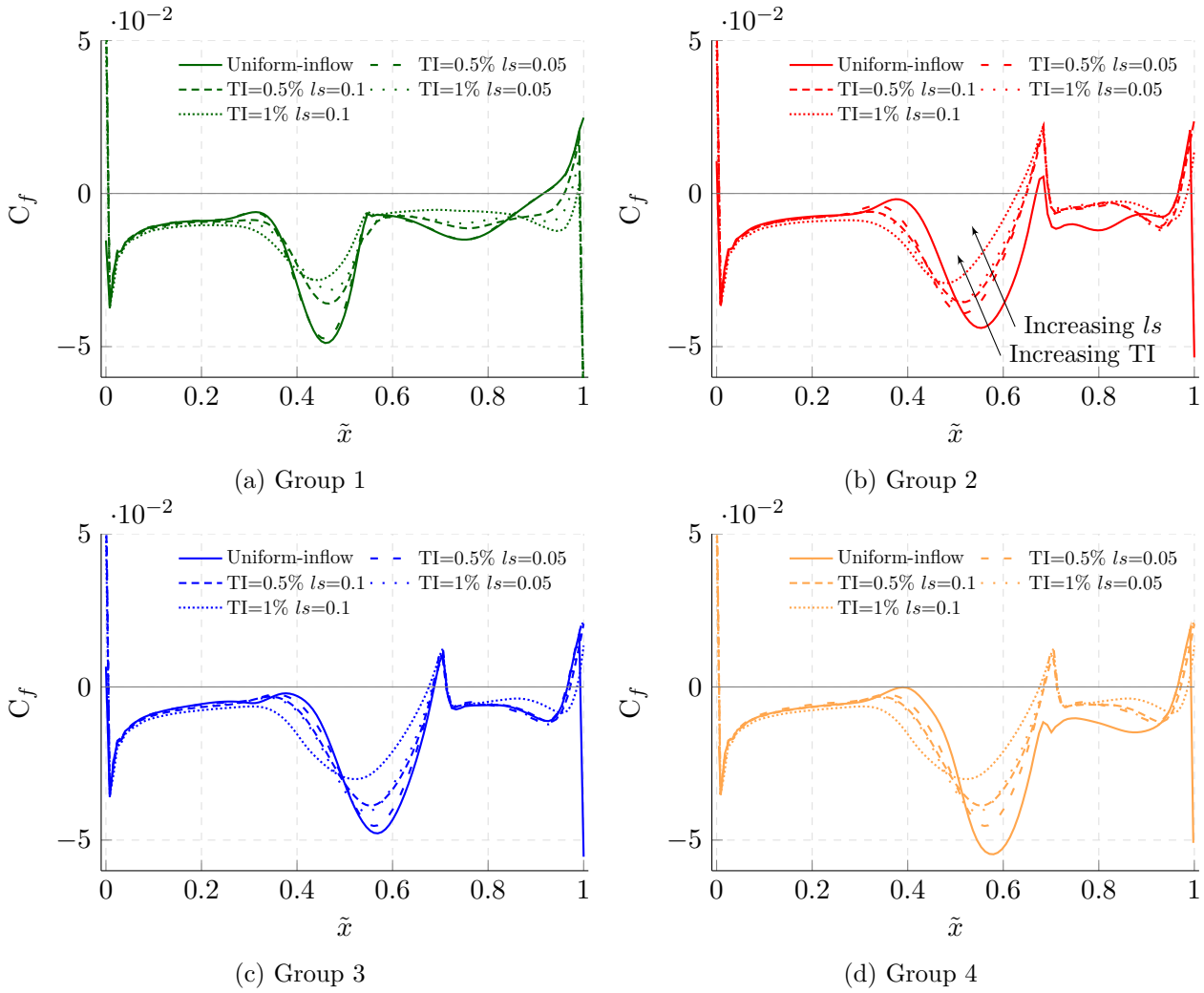
Despite the reduction in suction and vortex breakdown due to the influence of free-stream eddies, the optimal aerofoils still leverage vortex roll-up as a lifting mechanism, preserving a low-pressure region near the suction surface's upstream section.

6.2.4 Skin Friction Distribution

The time-averaged skin friction coefficient $\overline{C}_f$ is defined as in Chapter 4, Equation (4.8). Figure 6.8 plots mid-span $\overline{C}_f$ distributions on the suction surface as a function of $\tilde{x}$, for the representative aerofoil from each group on the Pareto front from 3D-DNS-12_{2DS} under the five different free-stream conditions.

As described in Chapter 5 for the optimal aerofoils when evaluated with uniform inflow, a strong recirculation region can be identified before the apex by the negative peak in $\overline{C}_f$, and another, much weaker, recirculation region can be identified after the apex. When injecting free-stream eddies, the strength of the recirculation regions is reduced as the target TI and ls values rise, and the negative peak before the apex expands over a wider area.

In the uniform-inflow cases, aerofoils in Groups 2 and 3 are characterised by a change in sign of $\overline{C}_f$ near the apex, which signifies reattachment in the time-averaged sense, while aerofoils in Groups 1 and 4 are characterised by not showing time-averaged reattachment at the apex. When injecting free-stream eddies, the aerofoil representative of Group 1 still shows no reattachment of the flow at the apex in the time-averaged sense for any of the TI and ls values tested. Therefore, aerofoils in Group 1 induce



(a) Group 1

(b) Group 2

(c) Group 3

(d) Group 4

Figure 6.8: Plots of mid-span $\overline{C}_f$ distributions on the suction surface as a function of $\tilde{x}$ for the representative aerofoils from each group on the Pareto front from 3D-DNS-12$_{2DS}$ when evaluated with uniform inflow as well as when affected by free-stream eddies with different target turbulence intensities, TI, and different target characteristic length scales, *ls*.

separated flow, in the time-averaged sense, for the entirety of the chord for all tested free-stream conditions, with generally weaker vortices when injecting free-stream eddies. Aerofoils from Groups 2 and 3 show the same behaviour as for uniform-inflow conditions regarding reattachment of the flow at the apex. The aerofoil representative of Group 4 shows a change of behaviour with flow reattachment at the apex in the time-averaged sense for all TI and *ls* values tested. For aerofoils in Groups 2, 3 and 4, after reattachment, the flow separates again downstream of the apex, with vortices rolling up on the downstream suction surface of the aerofoil. All aerofoils with all free-stream conditions tested induce a change of sign of $\overline{C}_f$ near the trailing edge due to the vortex generated by the flow coming from the pressure surface being sucked upwards to the suction surface. The strength and size of this

trailing edge vortex are reduced when injecting free-stream eddies, with a higher impact as the TI and ls values are raised.

6.2.5 Outcomes

This investigation shows that free-stream eddies affect the performance and flow physics of Pareto optimal triangular aerofoils from 3D-DNS-12_{2DS} under Martian conditions. The injected eddies interact with the separated shear layer of these aerofoils, resulting in a breakdown of the coherent structures rolling on the suction surface, which these aerofoils use as their lifting mechanism. As a result, both aerodynamic coefficients are reduced due to the weaker and less coherent vortices, with a reduction of the high amplitude fluctuations and the friction on the aerofoil's surface. Free-stream eddies also influence the separation and reattachment of the flow and tend to homogenise the behaviour of the 3D-DNS-12_{2DS} Pareto optimal aerofoils. Furthermore, when evaluated with the effects of free-stream eddies, the 3D-DNS-12_{2DS} Pareto optimal aerofoils no longer form a set of non-dominated solutions.

The outcomes of this study motivated running a 3D DNS optimisation with injected free-stream eddies with the highest values of tested turbulence intensity and characteristic length scale upstream of the aerofoils to investigate if a new set of aerofoils could be found that are optimally adapted for the flow physics produced by the presence of free-stream eddies.

6.3 Optimisation with Free-Stream Eddies

A 3D DNS GA optimisation of triangular aerofoils was run with injected free-stream eddies with target values of turbulence intensity of 1% and characteristic length scale of 0.1 chords at $Re = 3,000$, $M = 0.15$ and $\alpha = 12°$, referred to as 3D-DNS-12-FSE_{3DS}. 3D-DNS-12-FSE_{3DS} was initialised with Pareto optimal aerofoils from 3D-DNS-12_{2DS} re-run under conditions of free-stream eddies with target values of turbulence intensity of 1% and characteristic length scale of 0.1 chords. It was then run for 18 generations, with 15 individuals in each generation, totalling 270 3D DNS evaluations with injected free-stream eddies. Each 3D DNS took approximately 23 hours to run on 36 Tesla P100-16GB GPUs, therefore, 3D-DNS-12-FSE_{3DS} required approximately 220,000 GPUhs. Note that the 3D DNS were run on 36 Tesla P100-16GB GPUs to achieve a run time below 24h - the maximum job duration limit

on Piz Daint. This avoided re-queuing to complete a given run.

Convergence is again assessed using the hypervolume metric [120]. Figure 6.9 shows the hypervolume value, normalised by its value at the final generation, as a function of the number of generations for 3D-DNS-12-FSE$_{3DS}$. 3D-DNS-12-FSE$_{3DS}$ can be considered converged from generation 17 as the hypervolume reaches a plateau. It is presumed that using the Pareto optimal aerofoils from 3D-DNS-12$_{2DS}$ as initial sampling for 3D-DNS-12-FSE$_{3DS}$ allows for a rapid convergence and reduced costs compared to initialising it from a well-distributed LHS set of aerofoils across the design space.

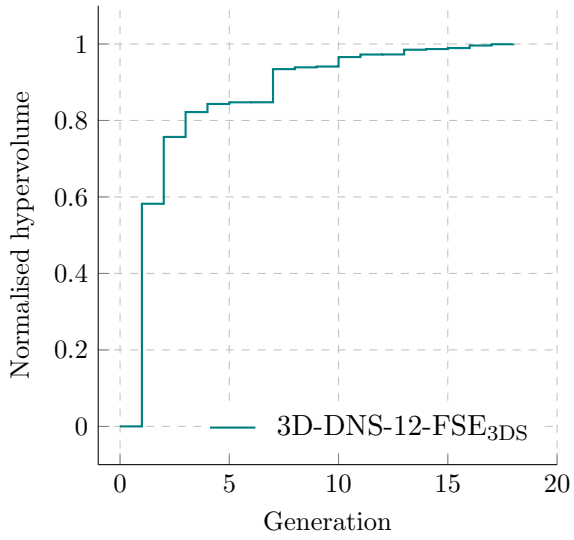


Figure 6.9: Normalised hypervolume convergence as a function of the number of generations for 3D-DNS-12-FSE$_{3DS}$.

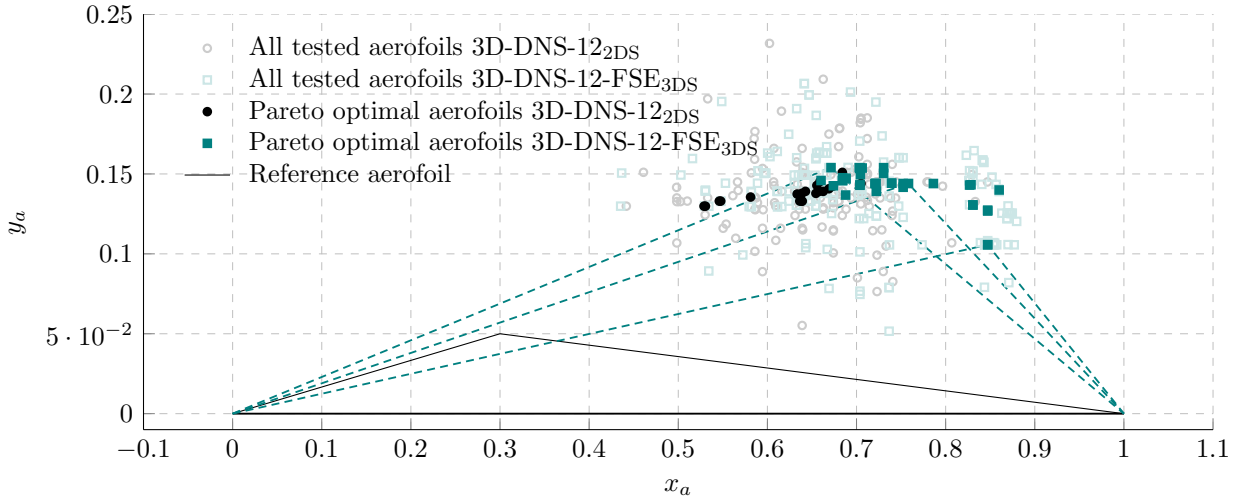
6.3.1 Optimal Aerofoils

Figure 6.10 (a) plots apex locations in the x_a, y_a design space for all tested aerofoils (hollow) and Pareto optimal aerofoils (filled) for 3D-DNS-12$_{2DS}$ (circles) and 3D-DNS-12-FSE$_{3DS}$ (squares) with three Pareto optimal aerofoils from 3D-DNS-12-FSE$_{3DS}$ represented with dashed lines, along with the Reference aerofoil. The aerofoils delineated with dashed lines represent the minimum $\overline{C}_D$ aerofoil (left), the maximum $\overline{C}_L/\overline{C}_D$ aerofoil (middle) and the maximum $\overline{C}_L$ aerofoil (right). The Pareto optimal aerofoils from 3D-DNS-12-FSE$_{3DS}$ have their apexes close to the Pareto optimal aerofoils from 3D-DNS-12$_{2DS}$ with a tendency, in general, to be situated closer to the trailing edge, with comparable or lower y_a locations.

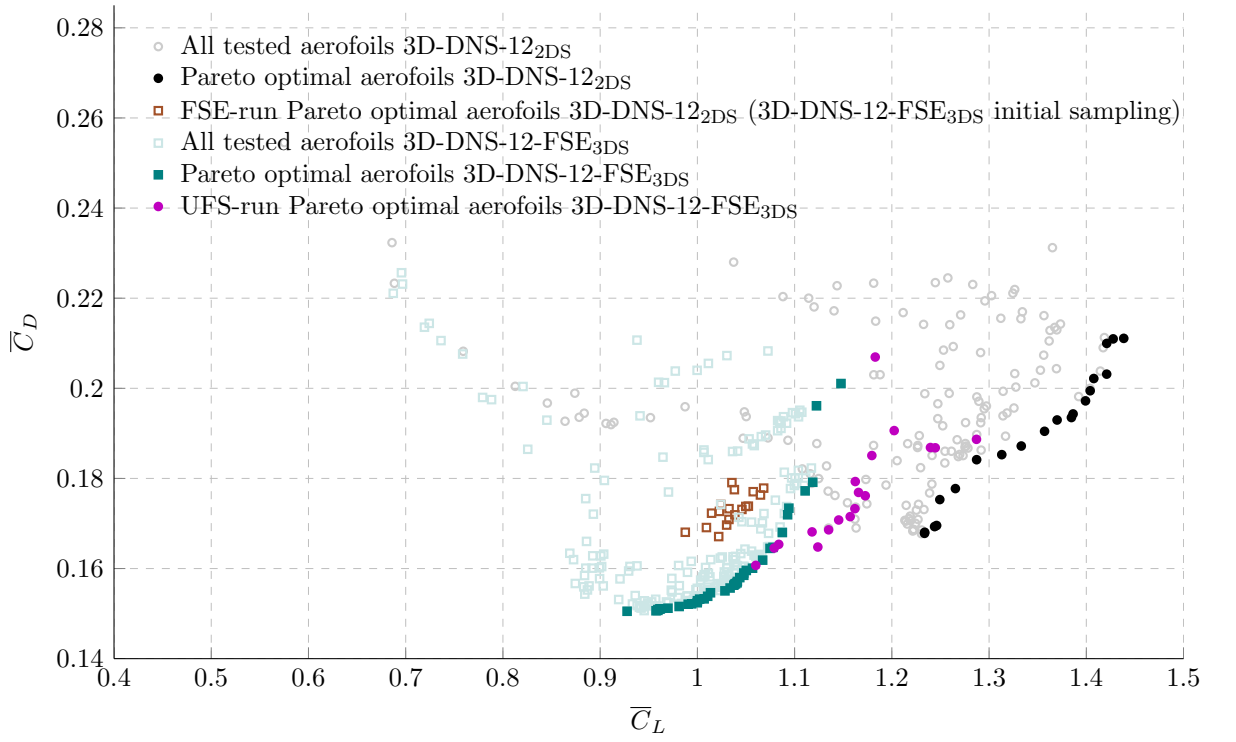
Figure 6.10 (b) plots $\overline{C}_L$, $\overline{C}_D$ for all tested aerofoils (hollow) and Pareto optimal aerofoils (filled) for

3D-DNS-12_{2DS} (circles) and 3D-DNS-12-FSE_{3DS} (squares), as well as 3D-DNS-12_{2DS} Pareto optimal aerofoils run with free-stream eddies (brown squares) and 3D-DNS-12-FSE_{3DS} Pareto optimal aerofoils run with uniform free-stream (magenta circles). As discussed previously, when the 3D-DNS-12_{2DS} Pareto optimal aerofoils are evaluated under the effects of free-stream eddies, they show reduced values of $\overline{C}_L$ and $\overline{C}_D$, with different aerofoils yielding very similar performance (brown squares). Nonetheless, after optimising them under the effects of free-stream eddies, a range of different Pareto optimal aerofoils with trade-off values of $\overline{C}_L$ and $\overline{C}_D$ are found (turquoise squares), dominating the Pareto optimal aerofoils from 3D-DNS-12_{2DS} when affected by free-stream eddies. Still, 3D-DNS-12-FSE_{3DS} Pareto optimal aerofoils obtain lower $\overline{C}_L$ and $\overline{C}_D$ values compared to Pareto optimal aerofoils from 3D-DNS-12_{2DS} under steady, uniform free-stream conditions. When the 3D-DNS-12-FSE_{3DS} Pareto optimal aerofoils are evaluated under steady, uniform free-stream conditions, they generally exhibit higher values of both $\overline{C}_L$ and $\overline{C}_D$ (purple circles). Still, they are dominated by the 3D-DNS-12_{2DS} Pareto optimal aerofoils under steady, uniform free-stream conditions. This implies that one needs to carefully set the free-stream conditions under which these unconventional aerofoils are designed since optimal designs appear to be very sensitive to them.

To understand the physics behind the improved performance of the Pareto optimal aerofoils from 3D-DNS-12-FSE_{3DS} and the differences with the Pareto optimal aerofoils from 3D-DNS-12_{2DS}, flow physics are investigated and compared for three aerofoils from each set of Pareto optimal aerofoils. The analysis includes snapshots of instantaneous density gradient magnitude $|\nabla\rho|$ and static pressure p, time-averaged pressure coefficient $\overline{C}_p$, Q-criterion isosurfaces, lift coefficient C_L time series, time-averaged velocity line integral convolutions (LICs) and time-averaged skin friction coefficient $\overline{C}_f$. No groupings of aerofoils were identified based on their associated flow physics for 3D-DNS-12-FSE_{3DS} as opposed to for 3D-DNS-12_{2DS} in Chapter 5 since the effect of free-stream eddies tends to homogenise the flow behaviour for all the Pareto optimal aerofoils. For this reason, the aerofoils selected for the analysis are the minimum $\overline{C}_D$ aerofoil, the maximum $\overline{C}_L/\overline{C}_D$ aerofoil and the maximum $\overline{C}_L$ aerofoil, represented with dashed lines in Figure 6.10. These will be compared against the representative aerofoils from Group 1 (minimum $\overline{C}_D$ aerofoil), Group 2 (intermediate values of $\overline{C}_L$ and $\overline{C}_D$) and Group 4 (maximum $\overline{C}_L$ aerofoil) from 3D-DNS-12_{2DS} as described in Chapter 5.



(a)



(b)

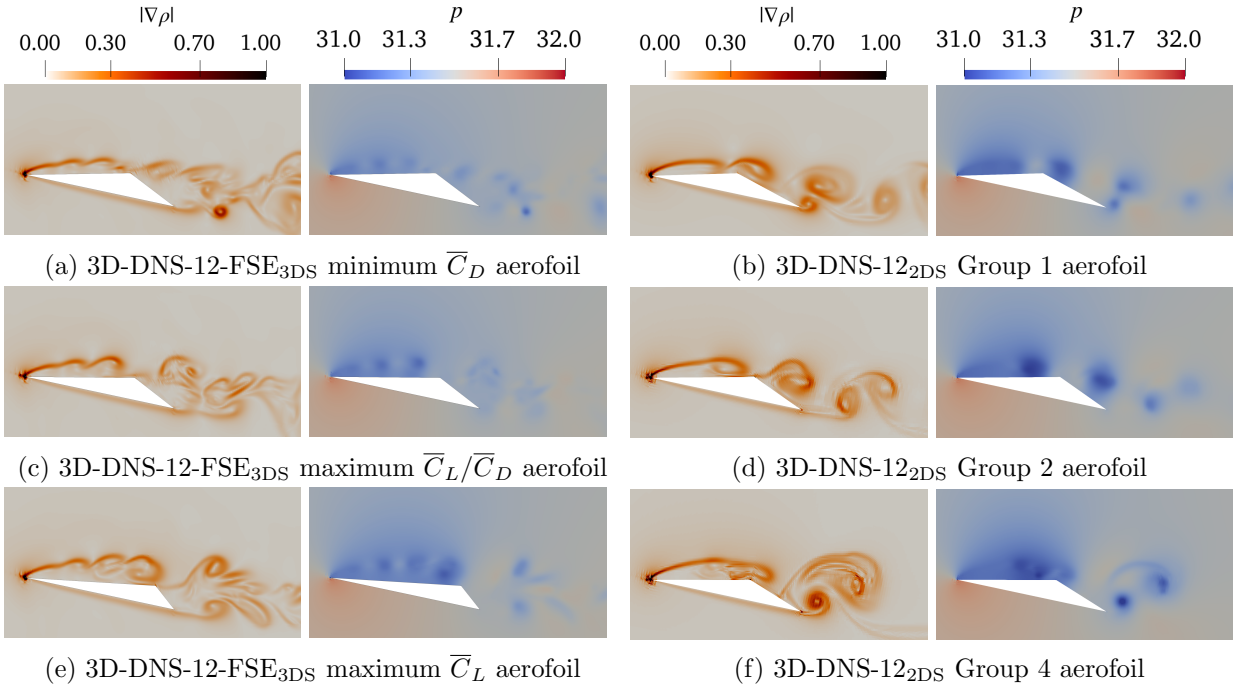
Figure 6.10: Plots of x_a, y_a for all tested aerofoils (hollow) and Pareto optimal aerofoils (filled) for 3D-DNS-12$_{2DS}$ (circles) and 3D-DNS-12-FSE$_{3DS}$ (squares) with the minimum $\overline{C}_D$ aerofoil (left), the maximum $\overline{C}_L/\overline{C}_D$ aerofoil (middle) and the maximum $\overline{C}_L$ aerofoil (right) represented with dashed lines (a). Plots of $\overline{C}_L$, $\overline{C}_D$ for all tested aerofoils (hollow) and Pareto optimal aerofoils (filled) for 3D-DNS-12$_{2DS}$ (circles) and 3D-DNS-12-FSE$_{3DS}$ (squares), and 3D-DNS-12$_{2DS}$ Pareto optimal aerofoils run with free-stream eddies (brown squares) and 3D-DNS-12-FSE$_{3DS}$ Pareto optimal aerofoils run with uniform free-stream (magenta circles) (b).

6.3.2 Instantaneous Density Gradient and Static Pressure

Figure 6.11 shows instantaneous density gradient magnitude $|\nabla\rho|$ (left) and instantaneous static pressure p (right) for three Pareto optimal aerofoils from 3D-DNS-12-FSE$_{3DS}$ (a), (c), (e) and three from 3D-DNS-12$_{2DS}$ (b), (d), (f). As previously discussed, the free-stream eddies interact with the separated shear layer and break down the large streamwise coherent vortices rolling on the suction surface of the optimum aerofoils, which results in weaker, smaller, less coherent vortices. The snapshots in Figure 6.11 demonstrate this effect by distinctly showing the weaker vortices on the 3D-DNS-12-FSE$_{3DS}$ aerofoils, (a), (c), (e), as opposed to the large coherent vortices on the 3D-DNS-12$_{2DS}$ aerofoils, (b), (d), (f).

When optimising under conditions of free-stream eddies, optimum aerofoils aim to exploit these smaller vortices as the lifting mechanism, similarly to 3D-DNS-12$_{2DS}$ exploiting the large coherent vortices. To do this, the position of the apex is moved closer to the trailing edge to allow these vortices to grow and energise as they roll on the first upper surface of the triangular aerofoil, as observed in the maximum $\overline{C}_L$ aerofoil in Figure 6.11 (e). The second upper surface avoids a steep inclination to prevent high-pressure drag, especially in the low $\overline{C}_D$ aerofoils, see Figure 6.11 (a), similarly to what was observed for low-$\overline{C}_D$ optimal aerofoils from 3D-DNS-12$_{2DS}$ from Chapter 5.

Due to the larger extent of the first upper surface and the weaker, smaller vortices, Pareto optimal aerofoils from 3D-DNS-12-FSE$_{3DS}$ show multiple (three/four) vortices rolling on this first upper surface. Instead, Pareto optimal aerofoils from 3D-DNS-12$_{2DS}$ under steady, uniform free-stream conditions result in one-to-two strong coherent vortices on the first upper surface, with the position of the apex aiming to maintain them close to the airfoil's surface to maximise their suction. The flow on the second upper surface also differs for the two sets of aerofoils. For the aerofoils from 3D-DNS-12$_{2DS}$, when the vortices reach the apex, they keep rolling close to the surface, generating an area of low pressure, until they interact with the trailing-edge vortex to produce a more uniform wake, characterised by distinct shed vortices. Instead, for the aerofoils from 3D-DNS-12-FSE$_{3DS}$, the vortices separate and mix with the trailing-edge vortex, resulting in a transitional/turbulent wake.



(a) 3D-DNS-12-FSE$_{3DS}$ minimum $\overline{C}_D$ aerofoil

(b) 3D-DNS-12$_{2DS}$ Group 1 aerofoil

(c) 3D-DNS-12-FSE$_{3DS}$ maximum $\overline{C}_L/\overline{C}_D$ aerofoil

(d) 3D-DNS-12$_{2DS}$ Group 2 aerofoil

(e) 3D-DNS-12-FSE$_{3DS}$ maximum $\overline{C}_L$ aerofoil

(f) 3D-DNS-12$_{2DS}$ Group 4 aerofoil

Figure 6.11: Images of instantaneous density gradient magnitude $|\boldsymbol{\nabla}\rho|$ (left) and instantaneous static pressure p (right) for three aerofoils on the Pareto front from 3D-DNS-12-FSE$_{3DS}$ (a), (c) and (e), and three from 3D-DNS-12$_{2DS}$ (b), (d) and (f).

6.3.3 Time-Averaged Pressure Coefficient on the Surface

The time-averaged pressure coefficient $\overline{C}_p$ is defined as in Chapter 4, Equation (4.1). Figure 6.12 plots mid-span $\overline{C}_p$ distributions on the surface of three aerofoils on the Pareto front from 3D-DNS-12-FSE$_{3DS}$ and three from 3D-DNS-12$_{2DS}$ as a function of $\tilde{x} = x/a$, where a is the x-wise distance between the leading and trailing edge of the aerofoil.

Pareto optimal aerofoils from 3D-DNS-12-FSE$_{3DS}$ exhibit weaker suction compared to those from 3D-DNS-12$_{2DS}$, attributable to the presence of smaller and weaker vortices on their first upper surface due to the interaction of free-stream eddies with the separated shear layer. Despite the closer proximity of the apex position of the Pareto optimal aerofoils from 3D-DNS-12-FSE$_{3DS}$ to the trailing edge compared to those from 3D-DNS-12$_{2DS}$, the extent of the high-suction area of the chord remains similar. In the case of the Pareto optimal aerofoils from 3D-DNS-12-FSE$_{3DS}$, the majority of suction occurs before the apex, beyond which the vortices break down and separate, unlike aerofoils from 3D-DNS-12$_{2DS}$, where a large vortex rolls up on the second upper surface, generating suction at the apex and downstream of it. A tendency can be identified with the Pareto optimal aerofoils from 3D-

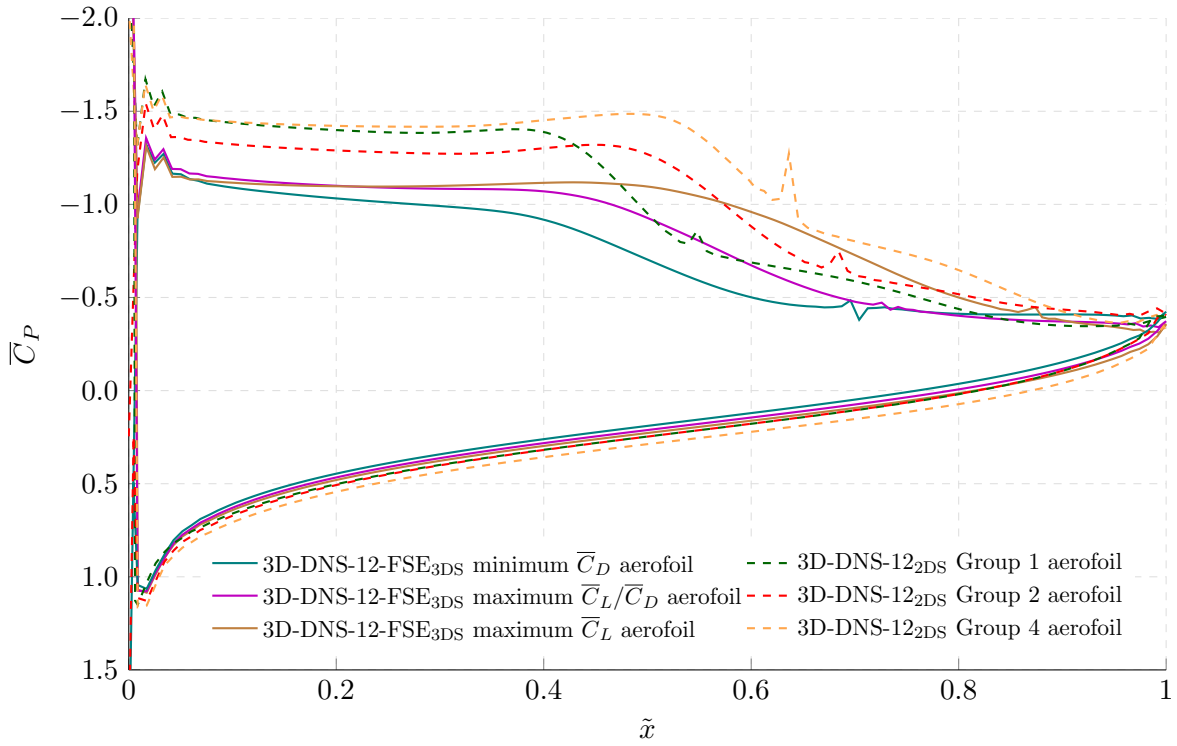


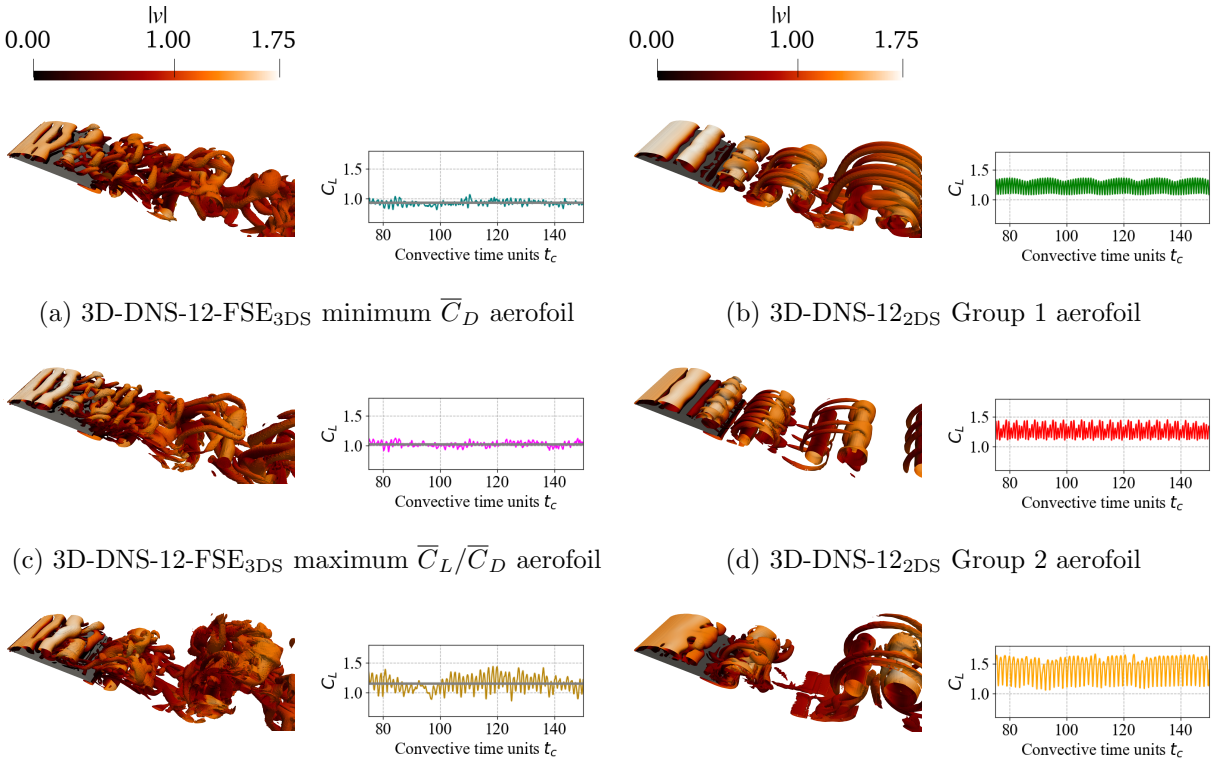
Figure 6.12: Plots of mid-span $\overline{C}_p$ distributions on the surface of three aerofoils on the Pareto front from 3D-DNS-12-FSE$_{3DS}$ and three from 3D-DNS-12$_{2DS}$ as a function of $\tilde{x}$.

DNS-12-FSE$_{3DS}$, where the closer the apex is to the trailing edge, the larger the area of high suction and consequently, the higher the $\overline{C}_L$. However, this is not observed in the case of the Pareto optimal aerofoils from 3D-DNS-12$_{2DS}$, where the Group 4 aerofoil apex - associated with the maximum $\overline{C}_L$ - is positioned between the apexes of Groups 1 and 2. The higher $\overline{C}_L$ from Group 4 aerofoils does not result from a larger area of vortex roll-up but instead from the vortices rolling closer to the surface.

6.3.4 Q-criterion Isosurfaces and Lift Time Series

Figure 6.13 shows instantaneous Q-criterion isosurfaces coloured by velocity magnitude $|v|$ (left) and C_L time series for the Data Extraction Period (right) for three aerofoils on the Pareto front from 3D-DNS-12-FSE$_{3DS}$ and three from 3D-DNS-12$_{2DS}$.

The Q-criterion isosurfaces show the interaction of the free-stream eddies with the large coherent vortices shed from the leading edge which, as explained before, results in their breakdown into smaller, weaker and less coherent vortices. These display similar structures to those observed for the Pareto optimal aerofoils from 3D-DNS-12$_{2DS}$ exposed to free-stream eddies of TI= 1% and $ls = 0.1$, see



(a) 3D-DNS-12-FSE$_{3DS}$ minimum $\overline{C}_D$ aerofoil

(b) 3D-DNS-12$_{2DS}$ Group 1 aerofoil

(c) 3D-DNS-12-FSE$_{3DS}$ maximum $\overline{C}_L/\overline{C}_D$ aerofoil

(d) 3D-DNS-12$_{2DS}$ Group 2 aerofoil

(e) 3D-DNS-12-FSE$_{3DS}$ maximum $\overline{C}_L$ aerofoil

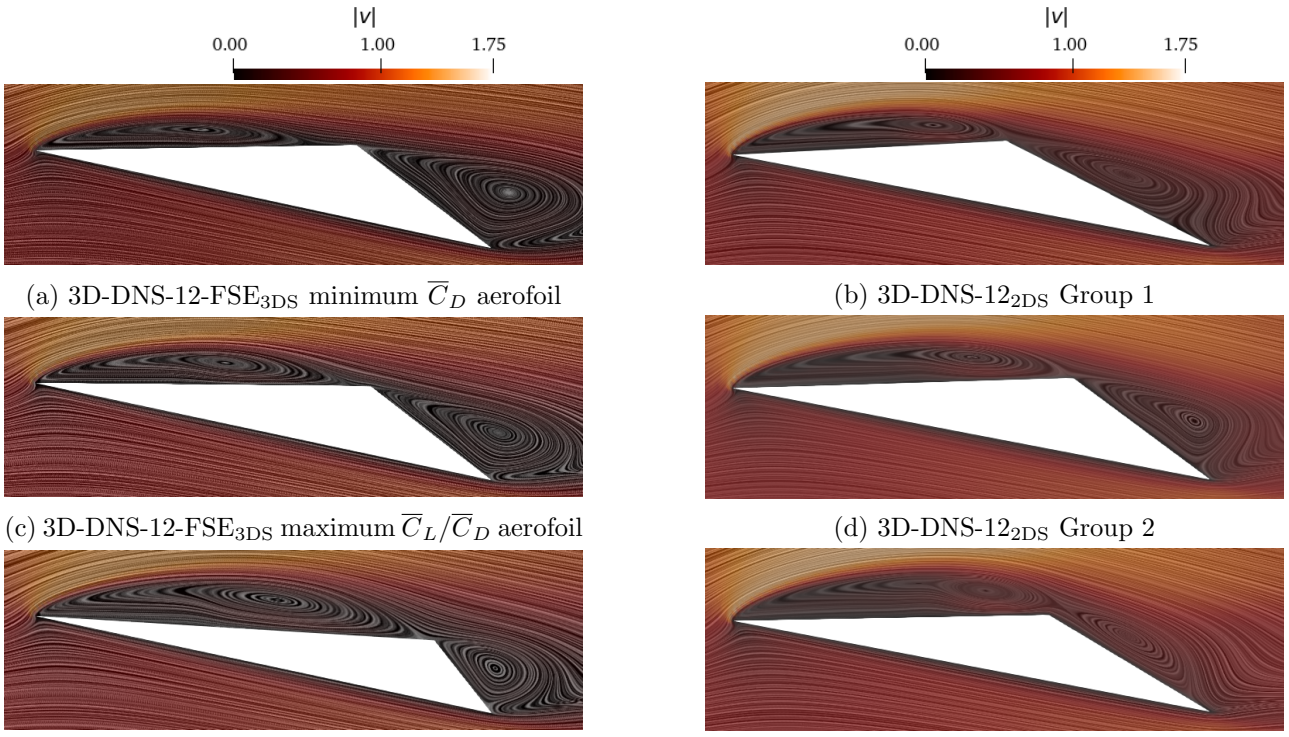
(f) 3D-DNS-12$_{2DS}$ Group 4 aerofoil

Figure 6.13: Instantaneous Q-criterion isosurfaces coloured by velocity magnitude $|v|$ (left) and lift time series C_L (right) for three aerofoils on the Pareto front from 3D-DNS-12-FSE$_{3DS}$ (a), (c) and (e), and three from 3D-DNS-12$_{2DS}$ (b), (d) and (f).

Figures 6.3 (d), 6.4 (d), 6.5 (d) and 6.6 (d). As seen for the Pareto optimal aerofoils from 3D-DNS-12$_{2DS}$ exposed to free-stream eddies, the interaction of free-stream eddies with the separated shear layer results in lower amplitude fluctuations, lower $\overline{C}_L$, and less periodicity in the C_L signal. This is also the case for the Pareto optimal aerofoils from 3D-DNS-12-FSE$_{3DS}$, which can reduce the negative structural impact of the unsteadiness associated with these aerofoils on helicopter blades. The maximum $\overline{C}_L$ aerofoil, Figure 6.13 (e), shows higher amplitude fluctuations in the C_L time series with increased vertical suction due to its delayed apex location which, as discussed previously, allows the vortices to grow and energise. It should be noted that this also results in higher drag, which is why the minimum $\overline{C}_D$ aerofoil (a) and the maximum $\overline{C}_L/\overline{C}_D$ aerofoil (c) do not promote this effect.

6.3.5 Velocity Line Integral Convolutions (LICs) and Skin Friction Distribution

Figure 6.8 plots time-averaged velocity magnitude $|v|$ in a span-wise constant plane, with superimposed time-averaged velocity Line Integral Convolutions (LICs) for three aerofoils on the Pareto front from 3D-DNS-12-FSE$_{3DS}$ and three from 3D-DNS-12$_{2DS}$.



(a) 3D-DNS-12-FSE$_{3DS}$ minimum $\overline{C}_D$ aerofoil

(b) 3D-DNS-12$_{2DS}$ Group 1

(c) 3D-DNS-12-FSE$_{3DS}$ maximum $\overline{C}_L/\overline{C}_D$ aerofoil

(d) 3D-DNS-12$_{2DS}$ Group 2

(e) 3D-DNS-12-FSE$_{3DS}$ maximum $\overline{C}_L$ aerofoil

(f) 3D-DNS-12$_{2DS}$ Group 4

Figure 6.14: Time-averaged velocity magnitude $|v|$ in a span-wise constant plane, with superimposed time-averaged velocity LICs for three aerofoils on the Pareto front from 3D-DNS-12-FSE$_{3DS}$ (a), (c) and (e), and three from 3D-DNS-12$_{2DS}$ (b), (d) and (f).

The LIC images show two large recirculation regions adjacent to each suction surface in the time-averaged sense for all the aerofoils, with aerofoils from 3D-DNS-12-FSE$_{3DS}$, (a), (c) and (e), having a much lower velocity magnitude $|v|$ than aerofoils from 3D-DNS-12$_{2DS}$, (b), (d) and (f). The first recirculation region for the 3D-DNS-12-FSE$_{3DS}$ aerofoils occupies a broader area and is more centred compared to the 3D-DNS-12$_{2DS}$ aerofoils, where the centre is closer to the apex. The second recirculation region for the 3D-DNS-12-FSE$_{3DS}$ aerofoils is larger and further from the surface, while in the 3D-DNS-12$_{2DS}$ aerofoils, the centre is closer to the apex and nearer to the surface. As demonstrated by the instantaneous snapshots in Figure 6.14, the recirculation regions in aerofoils from 3D-DNS-12-FSE$_{3DS}$ and 3D-DNS-12$_{2DS}$ are caused by different flow mechanisms. For 3D-DNS-12-FSE$_{3DS}$

aerofoils, the first time-averaged recirculation region results from multiple vortices rolling on the first upper surface, while for 3D-DNS-12_{2DS} aerofoils, it results from a single large, strong vortex rolling on this surface. The second time-averaged recirculation region for 3D-DNS-12-FSE_{3DS} aerofoils is caused by flow separation at the apex and trailing edge, leading to a transitional/turbulent wake. In contrast, for 3D-DNS-12_{2DS} aerofoils, it is caused by the same large, coherent vortex from the first upper surface rolling onto the second upper surface and interacting with the trailing-edge vortex into a wake characterised by distinct vortex shedding.

The time-averaged skin friction coefficient $\overline{C}_f$ is defined as in Chapter 4, Equation (4.8). Figure 6.15 plots $\overline{C}_f$ distributions on the suction surface as a function of $\tilde{x}$, for three aerofoils on the Pareto front from 3D-DNS-12-FSE_{3DS} and three from 3D-DNS-12_{2DS}.

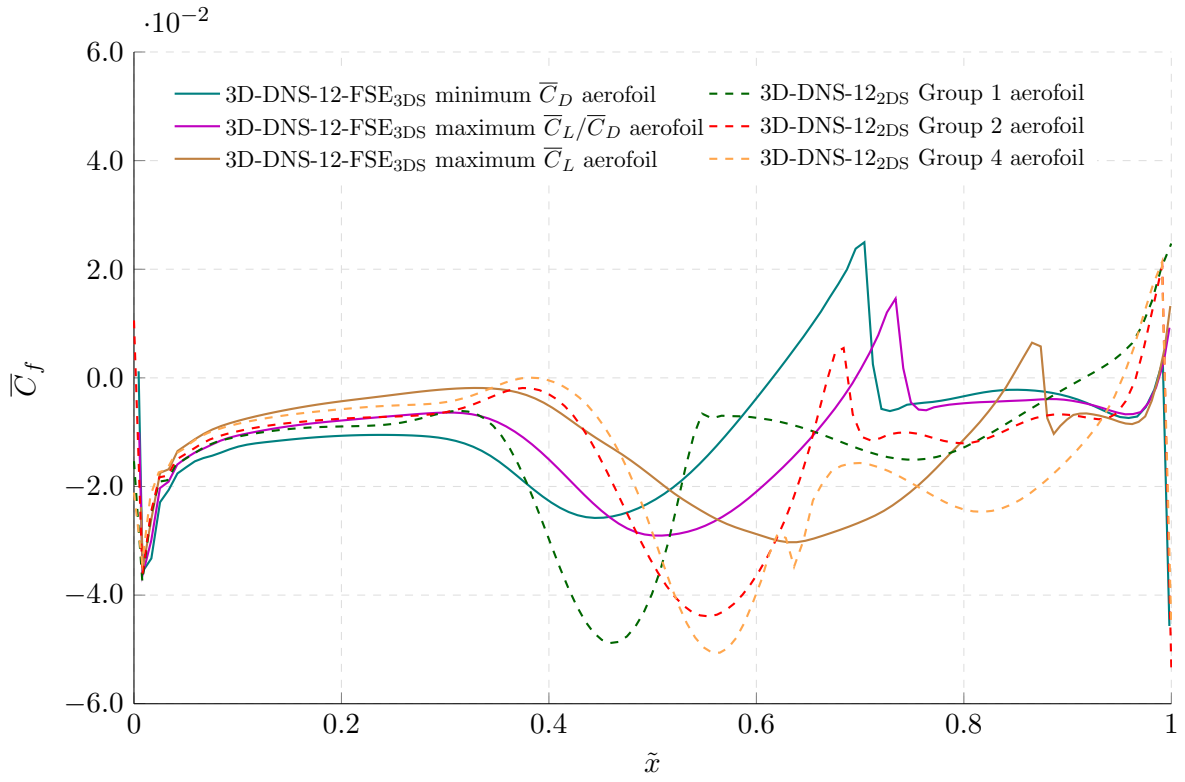


Figure 6.15: Plots of mid-span $\overline{C}_f$ distributions on the suction surface of three aerofoils on the Pareto front from 3D-DNS-12-FSE_{3DS} and three from 3D-DNS-12_{2DS} as a function of $\tilde{x}$.

The time-averaged recirculation regions identified in the LIC images in Figure 6.14 can be recognised from the two negative peaks in the $\overline{C}_f$ distributions. On the first upper surface, the smaller, weaker vortices on the 3D-DNS-12-FSE_{3DS} aerofoils are reflected in the $\overline{C}_f$ plots with weaker peaks compared to the 3D-DNS-12_{2DS} aerofoils. Additionally, as highlighted by the LIC images, the recirculation

region is wider for the 3D-DNS-12-FSE$_{3DS}$ aerofoils due to the downstream shift of the apex and the larger number of vortices occupying the suction surface, as opposed to a strong, more localised vortex in the time-averaged sense for the 3D-DNS-12$_{2DS}$ aerofoils. On the second upper surface, the negative peak is almost non-existent for the 3D-DNS-12-FSE$_{3DS}$ aerofoils due to the flow being separated in a transitional/turbulent wake, while it is much more pronounced for the 3D-DNS-12$_{2DS}$ aerofoils due to the vortex rolling on the second surface. The trailing edge vortex, rolling upwards from the pressure surface, also shows weaker strength for the 3D-DNS-12-FSE$_{3DS}$ aerofoils, influenced by the free-stream eddies. These differences are similar to the effects of free-stream eddies on Pareto optimal aerofoils from 3D-DNS-12$_{2DS}$. All Pareto optimal aerofoils from 3D-DNS-12-FSE$_{3DS}$ exhibit reattachment of the flow at the apex in the time-averaged sense, with higher friction compared to the Pareto optimal aerofoils from 3D-DNS-12$_{2DS}$.

6.4 Summary

Pareto optimal aerofoils from 3D-DNS-12$_{2DS}$ from Chapter 5 - optimised for steady, uniform inflow - have been re-evaluated under the effects of injected free-stream eddies with target values of turbulence intensity of TI = 0.5% and TI = 1% and target values of characteristic length scales of $ls = 0.05$ and $ls = 0.1$ chords at chord-based Reynolds number $Re = 3,000$ and Mach number $M = 0.15$ using high-order 3D DNS with PyFR.

It is found that free-stream eddies break the structure and periodicity of the flow present in the uniform-inflow cases, with a stronger effect the higher the TI and ls values. Additionally, free-stream eddies tend to regularise the behaviour of the different optimum aerofoil designs, especially at the highest levels of TI and ls tested, TI=1% and $ls = 0.1$. Results also showed that not all optimised aerofoil shapes under uniform-inflow conditions remain non-dominated when influenced by free-stream eddies, which motivated optimisation under the effect of free-stream eddies at the highest TI and ls values tested.

3D-DNS-12-FSE$_{3DS}$ optimisation is run with injected free-stream eddies with target values of turbulence intensity of 1% and characteristic length scale of 0.1 chords at $Re = 3,000$, $M = 0.15$ and $\alpha = 12^{\circ}$ with Pareto optimal aerofoils from 3D-DNS-12$_{2DS}$ as the initial sampling. New Pareto optimal aerofoils are found which dominate Pareto optimal aerofoils from 3D-DNS-12$_{2DS}$ evaluated with

free-stream eddies. These new aerofoils have their apex positions shifted towards the trailing edge in x, with similar or lower y positions. The delayed apex position allows for the weaker, smaller vortices to grow and energise, producing a higher suction, especially for the aerofoils optimised for high lift. Still, the interaction of the free-stream eddies with the separated shear layer results in a lower suction and lower amplitude fluctuations of the lift in comparison to aerofoils optimised for steady, uniform free-stream conditions. As the free-stream eddies break the large coherent vortices rolling over the aerofoils, the new Pareto optimal designs exhibit flow reattachment at the apex in a time-averaged sense. This is followed by a subsequent flow separation, leading to a transitional/turbulent wake.

Interestingly, when exposed to free-stream eddies, aerofoils with similar apex positions exhibit comparable behaviour, and, as the apex is moved in one direction, one can predict its effect on the performance of the aerofoil. This makes aerofoils exposed to free-stream eddies more predictable and less sensitive to variations in the angle of attack, free-stream velocity or gusts compared to aerofoils under steady, uniform free-stream conditions.

When the 3D-DNS-12-FSE$_{\text{3DS}}$ Pareto optimal aerofoils are evaluated under steady, uniform free-stream conditions, they generally exhibit higher values of both $\overline{C}_L$ and $\overline{C}_D$. However, they are still outperformed by the 3D-DNS-12$_{\text{2DS}}$ Pareto optimal aerofoils under these same conditions. This suggests that free-stream conditions must be carefully considered when designing these unconventional aerofoils as they are highly sensitive to off-design conditions. Since aerofoils on a Martian rotorcraft will experience a range of different conditions, future work should involve multi-point design optimisation to improve the robustness of the output designs.

As a general note on the design outcomes from this study, one can conclude that perturbations in the flow tend to break down the large coherent vortices that Martian aerofoils use as their lift-generation mechanism and promote reattachment of the flow at the apex. The interaction of free-stream eddies with the separated shear layer results in a lower suction due to the weaker vortices, but also in a decreased unsteadiness with lower amplitude fluctuations. This reduction in fluctuations can mitigate the negative structural impact of unsteady aerodynamic forces on helicopter blades.

Chapter 7

Conclusions and Future Work

7.1 Conclusions

This thesis presented a comprehensive study on the aerodynamic optimisation of unconventional aerofoils for Martian rotorcraft using high-order Direct Numerical Simulations (DNS) via PyFR and Genetic Algorithms (GAs) via `pymoo`. This study marks the first use of DNS for aerodynamic shape optimisation. The key findings and contributions from each chapter are summarised below:

In Chapter 4, high-order GPU-accelerated DNS of a triangular aerofoil under Martian atmospheric conditions were conducted using PyFR. These simulations aimed to validate PyFR against experimental wind tunnel data and to understand the flow physics associated with a specific triangular aerofoil, used as reference throughout the thesis, at various angles of attack.

To begin, span-wise periodic DNS of the triangular aerofoil were undertaken. It was found that extending the domain span from 0.3 to 0.6 chords improved agreement with associated wind tunnel data. However, extending it further to 0.9 chords provided little additional benefit. In particular, on extending the domain span from 0.3 to 0.6 chords, better agreement with lift and drag coefficients, and mid-span pressure coefficient distributions were achieved at high angles of attack ($\alpha > 9°$), when the flow is separated from the leading edge. This improvement is attributed to 0.3 chords of domain span artificially suppressing the three-dimensional breakdown of coherent structures that form above the suction surface of the aerofoil and in the wake. Despite this improvement, discrepancies remained

between the span-wise periodic DNS results and associated wind tunnel data for all angles of attack studied.

Subsequently, full-span DNS of the triangular aerofoil in a virtual wind tunnel were undertaken, mimicking the wind tunnel test section from the experiments. These simulations, which aimed to properly capture blockage effects and the interaction of wall boundary layers with the aerofoil, led to further improved agreement with the associated wind tunnel data. Specifically, better agreement with lift and drag coefficients was achieved for all angles of attack compared with the span-wise periodic DNS results. Excellent agreement was achieved for low angles of attack ($\alpha < 7°$) and for angles of attack where full separation shifts from the apex to the leading edge in the time-averaged sense ($7° < \alpha < 9°$). For higher angles of attack ($\alpha > 9°$) results showed improvement, but some discrepancies still remained. Recommended future work to investigate the physics behind these discrepancies is presented in the subsequent section. Finally, good qualitative agreement was achieved with pressure coefficient distributions on the suction surface of the aerofoil for all angles of attack studied compared to experimental data obtained through Pressure Sensitive Paint (PSP).

These results contributed to the understanding of previously published discrepancies between span-wise periodic DNS and associated wind tunnel data of a triangular aerofoil under Martian atmospheric conditions, highlighting the wind tunnel effects on the aerofoil's flow physics and performance. Additionally, they demonstrated the utility of high-order DNS with PyFR as a tool for accurately resolving flow physics associated with triangular aerofoils under Martian atmospheric conditions.

Based on the findings from Chapter 4, Chapter 5 focused on the optimisation of triangular aerofoil shapes for Martian atmospheric conditions at low ($\alpha = 6°$) and high ($\alpha = 12°$) angles of attack with a chord-based Reynolds number $Re = 3,000$ and Mach number $M = 0.15$. These chosen parameters are representative of conditions at the root/mid-section of a rotor blade on a Martian helicopter. Specifically, multi-objective optimisation was performed to maximise lift and minimise drag, resulting in a Pareto front of non-dominated aerofoils.

The investigation showed that 2D DNS optimisation is effective for low angles of attack ($\alpha = 6°$), as the flow remains predominantly two-dimensional in nature. 2D and 3D DNS evaluations resulted in similar aerodynamic coefficients and, consequently, both optimisations resulted in similar optimal aerofoil shapes, although the 2D optimisation was a factor of 150 times less computationally expensive.

However, at higher angles of attack ($\alpha = 12°$), the 2D DNS evaluations over-predicted lift and under-predicted drag due to the lack of three-dimensional physics. 3D DNS optimisation was necessary to accurately represent the spanwise breakdown of the coherent vortices that roll up over these aerofoils, which acts as their lifting mechanism, and obtain the optimal aerofoil designs. As 2D DNS fails to represent the flow physics over the aerofoils tested in the optimisation, the Pareto optimal aerofoils obtained from the 2D DNS optimisation fell into the dominated area of the 3D DNS Pareto front when evaluated with 3D DNS.

Detailed analyses were conducted on aerofoils on the Pareto front for the 3D DNS optimisation at $\alpha = 12°$, including Q-criterion isosurfaces, lift coefficient spectra, pressure coefficient distributions, velocity line integral convolutions, and skin friction distributions, to elucidate the flow physics underlying their optimal performance. The optimal aerofoils were seen to exploit vortex roll-up as a lifting mechanism. They achieved this by maintaining a strong vortex close to the upstream portion of the suction surface to increase lift, while avoiding excessive inclination of the downstream portion of the suction surface, which would otherwise result in high pressure drag. This configuration was achieved by positioning the apexes downstream of $x \approx 0.5$ and at $y \approx 0.15$, setting the upstream portion of the suction surface approximately parallel to the free-stream flow when $\alpha = 12°$. The optimised aerofoils on the Pareto front demonstrated significant performance improvements, achieving up to a 48% increase in lift or a 28% reduction in drag compared to the reference aerofoil.

Results from Chapter 5 showed that the performance of Pareto optimal aerofoils was very susceptible to small variations in the location of their apex, with small changes in the design variables having a large impact on the flow physics and performance of the aerofoil. To further understand the physics and performance of these unconventional triangular aerofoils under Martian conditions and improve their robustness, Chapter 6 focused on investigating the effects of free-stream eddies.

First, Pareto optimal aerofoils from the 3D DNS optimisation at $\alpha = 12°$ in Chapter 5 evaluated with steady, uniform inflow were re-evaluated under the effects of injected free-stream eddies. The turbulence intensities tested were 0.5% and 1%, with characteristic length scales of 0.05 and 0.1 chords, at a chord-based Reynolds number of $Re = 3,000$ and a Mach number of $M = 0.15$ with high-order 3D DNS with PyFR. The findings suggest that perturbations in the flow break down the large coherent vortices that yield the lift-generation mechanism for sharp-leading-edge aerofoils. The interaction of

free-stream eddies with the separated shear layer results in lower suction and reduced unsteadiness, with lower amplitude fluctuations, which can mitigate negative structural impacts on helicopter blades. Compared to uniform-inflow conditions, free-stream eddies disrupt the structure and periodicity of the flow, with stronger effects at higher turbulence intensities (TI) and larger characteristic length scales (ls). Additionally, the investigation showed that free-stream eddies tend to regularise the behavior of different optimal aerofoil designs, especially at the highest levels of TI and ls tested (TI = 1% and $ls = 0.1$). Notably, many aerofoils optimised under uniform-inflow conditions did not remain non-dominated when subjected to free-stream eddies.

To address this, a further optimisation was conducted with free-stream eddies of TI = 1% and $ls = 0.1$ at $Re = 3,000$, $M = 0.15$, and $\alpha = 12°$. The new optimisation identified aerofoils that dominated the original steady, uniform free-stream optimal aerofoils when evaluated with free-stream eddies. These new optimal aerofoils exhibited apex positions shifted towards the trailing edge in the x direction, with similar or lower y positions. As expected, the interaction of free-stream eddies with the separated shear layer resulted in lower suction and reduced amplitude fluctuations of the lift compared to optimal aerofoils under steady, uniform free-stream conditions. The delayed apex position in the new optimal aerofoils allowed weaker, smaller vortices to grow and energise, producing higher suction compared to aerofoils optimised for steady, uniform free-stream conditions under the effects of free-stream eddies. Additionally, the new Pareto optimal aerofoils showed reattachment of the flow at the apex in the time-averaged sense, followed by subsequent separation leading to a transitional/turbulent wake. When evaluated under steady, uniform free-stream conditions, these aerofoils generally exhibited higher values of both lift and drag coefficients. However, they were still outperformed by the original Pareto optimal aerofoils under steady, uniform free-stream conditions, indicating the significant impact of the free-stream conditions used in the evaluation when optimising aerofoils, and the sensitivity of these aerofoils to off-design conditions. Considering the effects of free-stream perturbations in the design process is crucial for the practical application of these aerofoils on a Martian rotorcraft that will experience variable conditions due to atmospheric perturbations, changes in the operating conditions, wake effects, etc.

7.2 Future Work

7.2.1 Discrepancies between the Virtual Wind Tunnel DNS and Associated Mars Wind Tunnel Data

One avenue for future work is to investigate further the discrepancies between the virtual wind tunnel DNS and the associated Mars Wind Tunnel data at high angles of attack ($\alpha > 9°$) for the specific triangular aerofoil presented in Chapter 4. Hypotheses for the discrepancies are:

I Dissimilarity in the leading and trailing edges between simulations and experiments. All aerofoils simulated in this work, including those for the DNS virtual wind tunnel, had infinitely sharp leading and trailing edges. The sharpness of the aerofoil's edges tested in the experiments was limited by fabrication tolerances, with a radius of approximately 0.3% of the chord, estimated by the authors of the experiments. The difference in leading and trailing edges can impact the separation of the flow and subsequent flow behaviour, which could account for the observed differences in the aerodynamic forces. A preliminary test has been carried out in this work which involved rounding the edges of the aerofoil with a radius of 0.3% of the chord while maintaining the same chord length as in the simulations presented in Chapter 4. The aerodynamic forces obtained for the rounded-edges aerofoil at angles of attack $\alpha = 12°$ and $\alpha = 15°$ are presented in Figure 7.1, alongside the data presented in Figure 4.4 in Chapter 4. These results do not show much difference compared to previous PyFR DNS virtual wind tunnel data, except for a small reduction in the forces for $\alpha = 15°$, getting closer to the experimental data. The reduction in aerodynamic forces is possibly caused by the delay in flow separation from a rounded edge compared to an infinitely sharp edge due to a weaker adverse pressure gradient. This delayed separation with a weaker adverse pressure gradient would generate weaker vortices rolling on the suction side of the aerofoil, resulting in lower lift and drag. However, the reduction is very slight and additional simulations should be run testing different radii and possibly increasing the resolution near the edges. Additionally, these tests should be run for all angles of attack and flow physics should be analysed to be able to extract conclusive findings.

II Chapter 6 revealed the impact of free-stream eddies on the performance and associated flow physics of various triangular aerofoils. Virtual wind tunnel DNS in Chapter 4 were run with

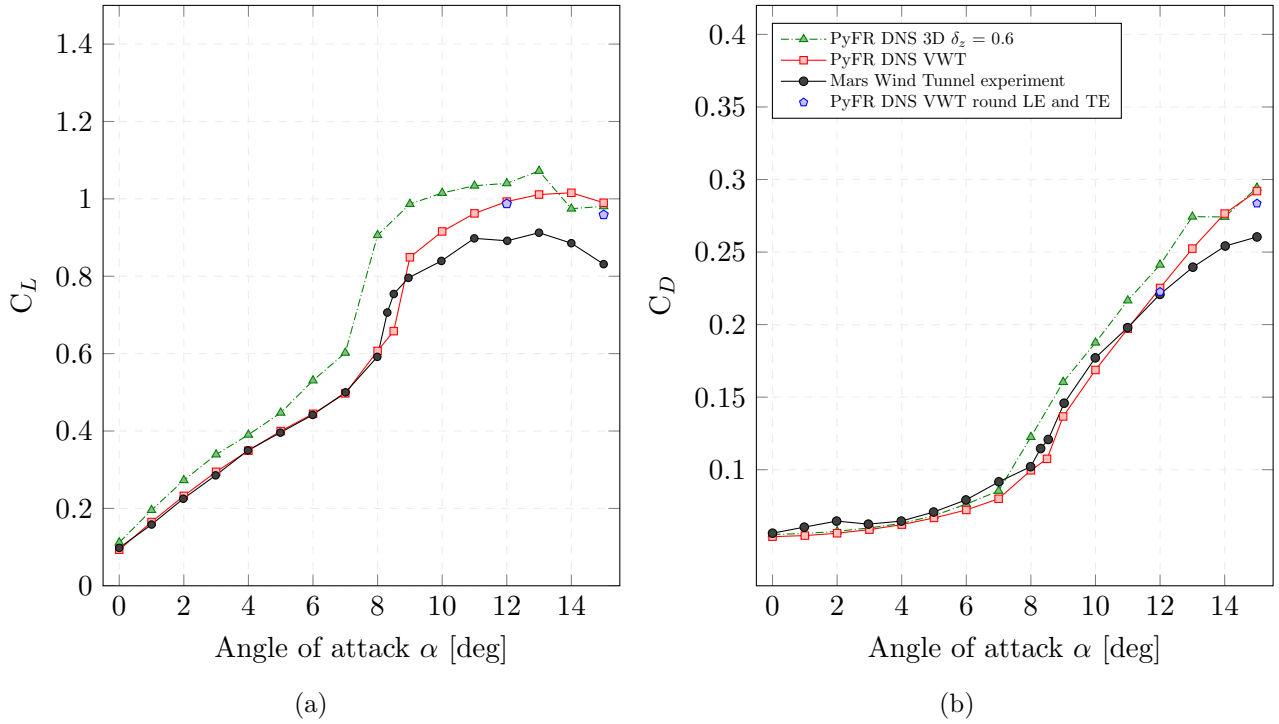
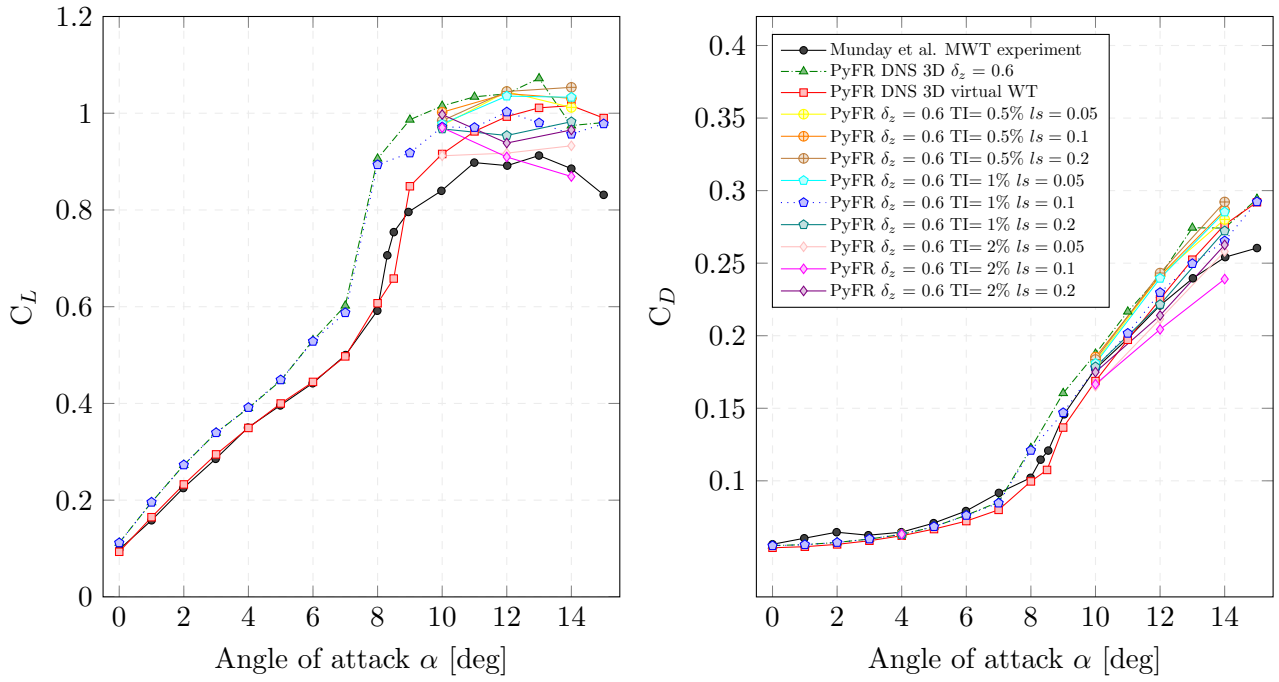


Figure 7.1: Plots of time-averaged lift coefficient $\overline{C}_L$ (a) and drag coefficient $\overline{C}_D$ (b) as a function of angle of attack α showing the data presented in Chapter 4 Figure 4.4 including DNS of the triangular aerofoil with rounded leading and trailing edges in a virtual wind tunnel using PyFR.

steady, uniform inflow conditions, which is unlikely to be the case for the experiments at the Mars Wind Tunnel. Free-stream eddies interacting with the separated shear layer could be responsible for the differences in the aerodynamic forces between simulations and experiments. A preliminary study has been pursued by running PyFR DNS with periodic boundary conditions at the sides and a span of 0.6 chords – due to limited resources – with free-stream eddies of various turbulence intensities and characteristic length scales, due to the lack of measurements of the actual values in the experiments. This has been done for angles of attack of $\alpha = 10°$, $\alpha = 12°$ and $\alpha = 14°$ where the discrepancies lay. Additionally, for one of the injected free-stream eddy conditions (TI=1% and ls=0.1), simulations have been run for angles of attack between $\alpha = 0°$ and $\alpha = 9°$ to ascertain if free-stream eddies would perturb the flow at low angles of attack, which would alter the agreement between simulations and experiments. Results show no variation in the aerodynamic forces for angles of attack $\alpha < 9°$, and a reduction in both aerodynamic forces for angles of attack $\alpha > 8°$, with results approaching the experimental data the higher the turbulence intensity and characteristic length scale of the eddies. These preliminary results motivate further investigation of the effects of free-stream eddies on this particular triangular aerofoil in a virtual

wind tunnel setup.



(a) (b)

Figure 7.2: Plots of time-averaged lift coefficient $\overline{C}_L$ (a) and drag coefficient $\overline{C}_D$ (b) as a function of angle of attack α showing the data presented in Chapter 4 Figure 4.4 including DNS of the triangular aerofoil with periodic boundary conditions at the sides and a span of 0.6 chords using PyFR with injected free-stream eddies of various turbulence intensities and characteristic length scales.

III Finally, the virtual wind tunnel simulations presented in Chapter 4 allowed for the boundary layer at the no-slip walls to grow from zero thickness. This could be a reason for discrepancies between simulations and the experiments since the boundary layer at the walls of the Mars Wind Tunnel test section may already have formed prior to the wind tunnel test section. Results in Chapter 4 have demonstrated the impact of the boundary layers at the side walls, interacting with the flow on the aerofoil, and on the top and bottom walls, causing a blockage effect on the flow. The investigation should look at the effect of imposing various wall boundary layer profiles at the no-slip walls of the virtual wind tunnel, looking at the effect on the aerofoil's flow physics and performance.

These investigations should focus on whether these factors can account for the remaining discrepancies between DNS results and wind tunnel data at high angles of attack ($\alpha > 9°$). Furthermore, unsteady flow physics associated with the point at which full separation moves from the apex to the leading edge in the region $7° < \alpha < 9°$ should be examined in greater detail, including the effect of wind tunnel

walls on this process. Investigating these phenomena will significantly enhance the understanding of the flow over unconventional aerofoil designs under Martian conditions and how different tools (experimental and numerical) can provide different insights into flow physics.

7.2.2 Acceleration Techniques for DNS Optimisation

Chapter 5 looked into reducing the cost and time of DNS optimisation by assessing the need for 3D DNS at different angles of attack and by using a biased set of aerofoils as the initial population. However, the computational cost of a three-dimensional DNS-based optimisation is still high, and it should be minimised by making use of efficient optimisation techniques. One way to accelerate the optimisation process is by fitting a surrogate model to high-fidelity data, which is then used as the cost function. Aerodynamic design through surrogate-assisted optimisation is becoming an increasingly popular technique [134, 135]. Several studies [136–141] have used surrogate models with various levels of CFD fidelity as sampling and infill data for aerofoil shape optimisation to reduce the overall computational resources that are required. However, these studies have focused on conventional aerofoils. Unconventional aerofoils with sharp edges can cause discontinuities in the cost function, since, as observed in Chapter 5, small variations in the design space (apex position) cause large differences in the objectives (lift and drag coefficients). Surrogate models struggle with discontinuities, which worsens the model's ability to predict accurately.airfoils

An initial study on the use of a Kriging surrogate model for DNS GA optimisation of triangular aerofoils has been conducted and presented as a conference paper in the Vertical Flight Society Forum 78 [142]. The Kriging model was used as the surrogate model due to its local approximation property and higher accuracy compared to other methods [123]. For the generation of the model, `pydacefit` [143] was used; a Python toolbox. This work involved comparing two strategies for high-order accurate DNS-based multi-objective optimisation of unconventional aerofoils under Martian conditions. The first strategy utilised GA optimisation with DNS for cost function evaluation. The second strategy employed GA optimisation with a Kriging surrogate model – generated and updated using DNS — for cost function evaluation. The work only considered 2D simulations due to their significantly reduced cost. The local accuracy of the model is enhanced periodically using DNS as infill or update points to rebuild the model, in addition to the initial sampling dataset.

Results showed that the surrogate-assisted optimisation with DNS infill converged to a Pareto front close to the 25th generation (390 DNS evaluations) Pareto front from DNS-based optimisation, but it struggled to cover the entire Pareto front. When the non-dominated aerofoils from the surrogate-assisted optimisation – which were obtained from the model – were run with DNS, new individuals were found dominating some of the DNS-based optimisation aerofoils. The convergence of the strategies to a reference Pareto front was assessed using the IGD+ performance indicator proposed by Ishibushi et al. [144]. The reference Pareto front consists of a combined set of non-dominated individuals from both strategies, with the ones obtained from the surrogate-assisted optimisation evaluated with DNS. The IGD+ metric was computed differently for each strategy as the comparison relies on the cost, which primarily depends on the DNS evaluations. IGD+ was computed at each generation for the DNS-based GA optimisation, while, for the surrogate-assisted optimisation, it was computed at each model update.

Figure 7.3 shows the IGD+ metric as a function of DNS evaluations for both strategies. One can observe that surrogate-assisted optimisation initially converged much more rapidly towards the reference Pareto front. However, as the optimisation progressed, the convergence of the surrogate-assisted optimisation stagnated and lost its advantage against DNS-based optimisation without a surrogate model. Consequently, for the case presented here, the utility of the surrogate model for DNS optimisation is seen to depend on the termination criteria. For example, if one plans to use a termination criterion that requires 100 DNS evaluations, the surrogate assistance significantly improves the obtained Pareto front. The benefits of surrogate-assisted optimisation can likely be improved by optimising its parameters.

Future work should look into improving the efficiency of the surrogate model used, including enhancing the sampling plan and the infill criteria. More sophisticated approaches for sampling a constrained design space with LHS should be explored. Blank et al. [145] propose different well-spaced space-filling methods, for instance, discarding unfeasible points and generating new ones from multiple LHS iterations until the number of desired points is reached. Regarding the infill criteria, different combinations of the number of exploitation and exploration infill points should be evaluated to improve the overall efficiency. Additionally, there are methods [145] that drive the infill points towards the extremes of the Pareto front and, thus, pursue diversity in the objective space.

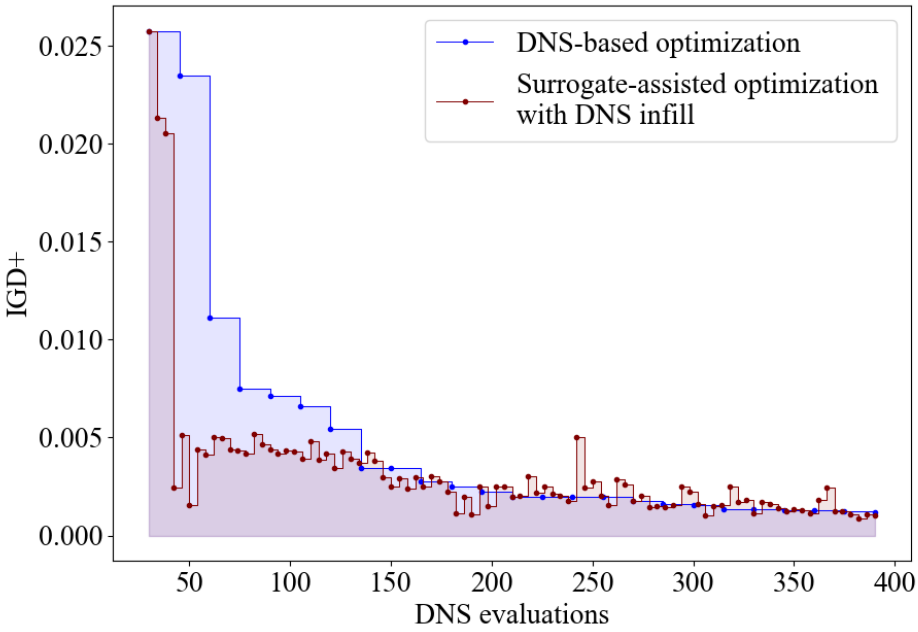


Figure 7.3: IGD+ metric as a function of DNS evaluations comparing the convergence of DNS-based optimisation against surrogate-assisted optimisation DNS infill.

7.2.3 Multi-Point Optimisation

Another proposed avenue for future work is to consider multi-point optimisation, given the sensitivity that unconventional aerofoils optimised in Chapters 5 and 6 showed to free-stream conditions. When in operation, the Martian rotorcraft will experience a range of various conditions, including different turbulence levels, upstream wake effects, varying rotational speeds, diverse pitch angles, gusts, and other perturbations. To enhance the robustness of the designs, it is important to account for various expected conditions. Multi-point optimisation involves evaluating aerofoil performance across a range of operating conditions and considering them through a weighted sum for a single objective function or through different objective functions.

7.2.4 Increased Design Complexity

Finally, as the field of Martian aerodynamics advances, future research should focus on increasing the complexity of the optimisation process. This could involve testing more sophisticated aerofoil shapes and including a range of angles of attack in the optimisation. Moreover, it is important

to consider objective functions that not only target aerodynamic performance but also address other critical factors such as structural integrity and weight. Incorporating more complex aerofoil geometries, additional design variables and/or additional objectives into the optimisation will inevitably increase the computational cost. Therefore, as mentioned previously, it is imperative to develop and implement techniques to accelerate and reduce the cost of the optimisation.

These avenues for future work are expected to lead to a deeper understanding of the aerodynamics of unconventional aerofoil shapes under Martian conditions. Additionally, they will enhance optimisation techniques for aerodynamic shape design and result in a more comprehensive and robust set of Martian aerofoils. This will significantly advance and expand the field of Martian rotorcraft design.

Bibliography

[1] Genova A., Goossens S., Lemoine F. G., Mazarico E., Neumann G. A., Smith D. E., and Zuber M. T. Seasonal and static gravity field of Mars from MGS, Mars Odyssey and MRO radio science. *Icarus*, 272, 2016.

[2] P. Lee, M. Bicay, A. Colaprete, R. Elphic, A. Genova, B. Hine, M. Horanyi, B. Jaroux, D. Korsmeyer, B. S. Lewis, and S. P. Worden. Phobos and Deimos and Mars environment (PADME): A LADEE-derived mission to explore Mars's moons and the Martian orbital environment. *Lunar and Planetary Science Conference*, 45, 2014.

[3] K. H. Williford, K. A. Farley, K. M. Stack, A. C. Allwood, D. Beaty, L. W. Beegle, R. Bhartia, A. J. Brown, M. De la Torre Juarez, S. E. Hamran, M. H. Hecht, J. A. Hurowitz, J. A. Rodriguez-Manfredi, S. Maurice, S. Milkovich, and R. C. Wiens. The NASA Mars 2020 rover mission and the search for extraterrestrial life. *From Habitability to Life on Mars*, 2018.

[4] A. R. Vasavada. Mission overview and scientific contributions from the Mars Science Laboratory Curiosity rover after eight years of surface operations. *Space Science Reviews*, 218, 2022.

[5] R. E. Arvidson, J. W. Ashley, J. F. Bell, M. Chojnacki, J. Cohen, T. E. Economou, W. H. Farrand, R. Fergason, I. Fleischer, P. Geissler, R. Gellert, M. P. Golombek, J. P. Grotzinger, E. A. Guinness, R. M. Haberle, K. E. Herkenhoff, J. A. Herman, K. D. Iagnemma, B. L. Jolliff, J. R. Johnson, G. Klingelhöfer, A. H. Knoll, A. T. Knudson, R. Li, S. M. McLennan, D. W. Mittlefehldt, R. V. Morris, T. J. Parker, M. S. Rice, C. Schröder, L. A. Soderblom, S. W. Squyres, R. J. Sullivan, and M. J. Wolff. Opportunity Mars rover mission: Overview and selected results from Purgatory ripple to traverses to Endeavour crater. *Journal of Geophysical Research: Planets*, 116, 2011.

[6] K. Sanderson. Mars rover Spirit (2003-10). *Nature*, 463, 2010.

[7] M. Bajracharya, M. W. Maimone, and D. Helmick. Autonomy for Mars rovers: Past, present, and future. *Computer*, 41, 2008.

[8] Mark W. Siebert and Theo G. Keith. The NASA Mars pathfinder mission. *Lubrication Engineering*, 54, 1998.

[9] J. B. Balaram, T. Canham, C. Duncan, M. Golombek, H. Fjær Grip, W. Johnson, J. Maki, A. Quon, R. Stern, and D. Zhu. Mars helicopter technology demonstrator. *AIAA Atmospheric Flight Mechanics Conference*, 2018.

[10] Brian K. Muirhead, Austin K. Nicholas, Jeffrey Umland, Orson Sutherland, and Sanjay Vijendran. Mars Sample Return campaign concept status. *Acta Astronautica*, 176, 2020.

[11] S. Withrow-Maser, W. Johnson, T. Tzanetos, H. Grip, W. Koning, N. Schatzman, L. Young, A. Chan, A. Ruan, H. Cummings, B. Allan, C. Malpica, L. Meyn, B. Pipenberg, and M. Keennon. Mars Sample Recovery Helicopter: Rotorcraft to retrieve the first samples from the Martian surface. In *Forum 2023 - Vertical Flight Society 79th Annual Forum and Technology Display*, 2023.

[12] W.J.F. Koning, E. A. Romander, and W. Johnson. Performance optimization of plate airfoils for Martian rotor applications using a genetic algorithm. *45th European Rotorcraft Forum 2019, ERF 2019*, 1, 2019.

[13] W. J. F. Koning, E. A. Romander, and W. Johnson. Optimization of low Reynolds number airfoils for Martian rotor applications using an evolutionary algorithm. *AIAA Science and Technology Forum and Exposition (AIAA SciTech)*, 2020.

[14] W.J.F. Koning, E. A. Romander, H. V. Cummings, B. N. Perez Perez, and P. G. Buning. On improved understanding of airfoil performance evaluation methods at low Reynolds numbers. *Journal of Aircraft*, 60, 2023.

[15] P. Munday, K. Taira, T. Suwa, D. Numata, and K. Asai. Non-linear lift on a triangular airfoil in low-Reynolds-number compressible flow. *Journal of Aircraft*, 52:924–931, 2015.

[16] Gaku Sasaki, Tomoaki Tatsukawa, T. Nonomura, A. Oyama, Takaaki Matsumoto, and Koichi Yonemoto. Multi-objective optimization of airfoil for Mars exploration aircraft using genetic algorithm. *Transactions of the Japan Society for Aeronautical and Space Sciences, Aerospace Technology Japan*, 12:59–64, 2014.

[17] F. Witherden, A. Farrington, and P.E. Vincent. PyFR: An open source framework for solving advection–diffusion type problems on streaming architectures using the flux reconstruction approach. *Computer Physics Communications*, 185:3028–3040, 2014.

[18] S. Withrow, W. Johnson, L. A. Young, W. Koning, W. Kuang, C. Malpica, J. Balaram, and T. Tzanetos. Mars science helicopter conceptual design. 2020.

[19] S. Withrow-Maser, W. Johnson, L. Young, W. Koning, W. Kuang, C. Malpica, J. Balaram, and T. Tzanetos. Mars science helicopter: Conceptual design of the next generation of Mars rotorcraft. In *Accelerating Space Commerce, Exploration, and New Discovery Conference, ASCEND 2020*. American Institute of Aeronautics and Astronautics Inc, AIAA, 2020.

[20] S. Withrow-Maser, W. Johnson, L. Young, H. Cummings, A. Chan, T. Tzanetos, J. Balaram, and Jonathan Bapst. An advanced Mars helicopter design. In *Accelerating Space Commerce, Exploration, and New Discovery Conference, ASCEND 2020*. American Institute of Aeronautics and Astronautics Inc, AIAA, 2020.

[21] W. Johnson, S. Withrow-Maser, L. Young, C. Malpica, W. J. F. Koning, W. Kuang, M. Fehler, A. Tuano, A. Chan, A. Datta, C. Chi, R. Lumba, D. Escobar, J. Balaram, T. Tzanetos, and H. Fjaer Grip. Mars science helicopter conceptual design, 2020.

[22] H. Cummings, B. N. Perez Perez, W. Koning, W. Johnson, L. Young, Farid Haddad, Ethan Romander, J. Balaram, T. Tzanetos, Joshua Bowman, Lauren Wagner, S. Withrow-Maser, Eb Isaacs, Savannah Toney, Dorsa Shirazi, Sarah Conley, B. Pipenberg, A. Datta, R. Lumba, C. Chi, J. Ken Smith, Charles Cornelison, Alfredo Perez, T. Nonomura, and K. Asai. Overview and introduction of the Rotor Optimization for the Advancement of Mars eXploration (ROAMX) Project. In *Aeromechanics for Advanced Vertical Flight Technical Meeting 2022*, 2022.

[23] H. Schlichting and K. Gersten. *Boundary-Layer Theory*. 2016.

[24] J. Mcmasters and M. Henderson. Low speed single element airfoil synthesis. *Technical Soaring*, 6, 1980.

[25] J. C.Muti Lin and Laura L. Pauley. Low-reynolds-number separation on an airfoil. *AIAA Journal*, 34, 1996.

[26] L. L. Pauley, P. Moin, and W. C. Reynolds. The instability of two-dimensional laminar separation. *Low Reynolds Number Aerodynamics Proceedings*, 1989.

[27] Serhiy Yarusevych, Pierre E. Sullivan, and John G. Kawall. Coherent structures in an airfoil boundary layer and wake at low Reynolds numbers. *Physics of Fluids*, 18, 2006.

[28] Serhiy Yarusevych and Michael S.H. Boutilier. Vortex shedding of an airfoil at low Reynolds numbers. *AIAA Journal*, 49, 2011.

[29] A. Michalke. The instability of free shear layers. *Progress in Aerospace Sciences*, 12, 1972.

[30] Jonathan H. Watmuff. Evolution of a wave packet into vortex loops in a laminar separation bubble. *Journal of Fluid Mechanics*, 397, 1999.

[31] M. Gaster. The structure and behaviour of laminar separation bubbles. *Aeronautical Research Council Reports and Memoranda*, 1967.

[32] S Wang, Y Zhou, Md. Mahbub Alam, and H Yang. Turbulent intensity and Reynolds number effects on an airfoil at low Reynolds numbers. *Physics of fluids (1994)*, 26(11):115107, 2014.

[33] Ibrahim E. Abdalla and Zhiyin Yang. Numerical study of the instability mechanism in transitional separating-reattaching flow. *International Journal of Heat and Fluid Flow*, 25, 2004.

[34] Michael S.H. Boutilier and Serhiy Yarusevych. Separated shear layer transition over an airfoil at a low Reynolds number. *Physics of Fluids*, 24, 2012.

[35] Yang Zhang, Zhou Zhou, Kelei Wang, and Xu Li. Aerodynamic characteristics of different airfoils under varied turbulence intensities at low Reynolds numbers. *Applied Sciences*, 10:1706, 03 2020.

[36] N. Fard Afshar. High-order implicit large eddy simulation of flow over a low-Reynolds turbine cascade. *PyFR Seminar Series*, 10.52843/cassyni.pw9418 2021.

[37] Shu Wang. Turbulent intensity and Reynolds number effects on an airfoil at low Reynolds numbers. *Physics of Fluids*, 26, 11 2014.

[38] M. N. Izakov. Turbulence in the free atmospheres of Earth, Mars, and Venus: A review. *Solar System Research*, 41, 2007.

[39] Aymeric Spiga. Turbulence in the lower atmosphere of Mars enhanced by transported dust particles. *Journal of Geophysical Research: Planets*, 126, 2021.

[40] C. Wilson, A. Camilletti, S. Calcutt, and P.M. Ligrani. A wind tunnel for the calibration of Mars wind sensors. *Planetary and Space Science*, 56:1532–1541, 2008.

[41] J. Merrison, H. Bechtold, H. Gunnlaugsson, A. Jensen, K. Kinch, P. Nørnberg, and K. Rasmussen. An environmental simulation wind tunnel for studying Aeolian transport on Mars. *Planetary and Space Science*, 56:426–437, 2008.

[42] M. Anyoji, K. Nose, S. Ida, D. Numata, H. Nagai, and K. Asai. Development of a low-density wind tunnel for simulating Martian atmospheric flight. *Transactions of the Japanese Society for Artificial Intelligence, Aerospace Technology Japan*, 9, 2011.

[43] M. Anyoji, K. Nose, S. Ida, D. Numata, H. Nagai, and K. Asai. Low Reynolds number airfoil testing in a Mars wind tunnel. *40th Fluid Dynamics Conference and Exhibit*, Chicago, Illinois: 2010.

[44] H. Nagai, K. Asai, D. Numata, T. Suwa, and M. Anyoji. Characteristics of low-Reynolds number airfoils in a Mars wind tunnel. *51st AIAA Aerospace Sciences Meeting including the New Horizons Forum and Aerospace Exposition*, 2013.

[45] M. Anyoji, T. Nonomura, H. Aono, A. Oyama, K. Fujii, H. Nagai, and K. Asai. Computational and experimental analysis of a high-performance airfoil under low-reynolds-number flow condition. *Journal of Aircraft*, 51, 2014.

[46] H. Aono, M. Anyoji, Daiki Hamada, Shotaro Wakui, and Tomoaki Tatsukawa. A study on development of airfoil shape toward low Reynolds-number dependence of aerodynamic characteristics under low-Reynolds-number-flow conditions. In *AIAA Aerospace Sciences Meeting, 2018*, 2018.

[47] T. Suwa, K. Nose, D. Numata, H. Nagai, and K. Asai. Compressibility effects on airfoil aerodynamics at low Reynolds number. *30th AIAA Applied Aerodynamics Conference*, New Orleans, Louisiana: 2012.

[48] Robert J. McGhee, Betty S. Walker, and Betty F. Millard. Experimental results for the Eppler 387 airfoil at low Reynolds numbers in the Langley Low-Turbulence Pressure Tunnel. *NASA Technical Memorandum*, 1988.

[49] Michael V. Ol, Brian R. McAuliffe, Ernest S. Hanff, Ulrich Scholz, and Christian Kähler. Comparison of laminar separation bubble measurements on a low Reynolds number airfoil in three facilities. In *35th AIAA Fluid Dynamics Conference and Exhibit*, 2005.

[50] M. Anyoji, T. Nonomura, H. Aono, A. Oyama, K. Fujii, H. Nagai, and K. Asai. Computational and experimental analysis of a high-performance airfoil under low-Reynolds-number flow condition. *Journal of Aircraft*, 51(6):1864–1872, 2014.

[51] M. Anyoji, M. Okamoto, H. Hidaka, T. Nonomura, A. Oyama, and K. Fujii. Planetary atmosphere wind tunnel tests on aerodynamic characteristics of a Mars airplane scale model. *Transactions of the Japan Society for Aeronautical and Space Sciences, Aerospace Technology Japan*, 12:7–12, 2014.

[52] Zhao Pengyue, Qiquan Quan, Shuitian Chen, Tingting Yang, Deen Bai, Dewei Tang, and Zongquan Deng. Geometry shape selection of NACA airfoils for Mars rotorcraft. *Acta Astronautica*, 157, 2018.

[53] Robin Shrestha, Moble Benedict, Vikram Hrishikeshavan, and Inderjit Chopra. Hover performance of a small-scale helicopter rotor for flying on Mars. *Journal of Aircraft*, 53:1–8, 2016.

[54] Atsushi Yamaguchi, Raoul Sunil Golani, Koji Fujita, and H. Nagai. Experimental investigation on aerodynamic performance of coaxial rotor at low Reynolds numbers. *AIAA Scitech 2021 Forum*, 2021.

[55] I. S. Bensignor, D. Seth, and M. McCrink. Rotor propulsion modeling for low Reynolds number flow ($\mathrm{Re} < 10^5$) for Martian rotorcraft flight. *AIAA Aviation 2022 Forum*, 2022.

[56] D. Escobar, Inderjit Chopra, and A. Datta. High-Fidelity aeromechanical analysis of coaxial Mars helicopter. *Journal of Aircraft*, 58, 2021.

[57] Pengyue Zhao, Qiquan Quan, Shuitian Chen, Dewei Tang, and Zongquan Deng. Experimental investigation on hover performance of a single-rotor system for Mars helicopter. *Aerospace Science and Technology*, 86, 2019.

[58] K Kanou, K Fujita, and H Nagai. Experimental study on high efficiency of aerodynamic performance of rotor blades for Mars helicopter. *AIAA Scitech 2019 Forum*, 2019.

[59] A. Obata and S. Sinohara. Flow visualization study of the aerodynamics of modeled dragonfly wings. *AIAA Journal*, 47:3043–3046, 2009.

[60] M. Okamoto and A. Azuma. Experimental study on aerodynamic characteristics of unsteady wings at low Reynolds number. *AIAA Journal*, 43:2526–2536, 2005.

[61] H. Hidaka and M. Okamoto. An experimental study of triangular airfoils for Mars airplane. *Transactions of the Japan Society for Aeronautical and Space Sciences, Aerospace Technology Japan*, 12:21–27, 2014.

[62] Marshall C. Galbraith and Miguel R. Visbal. Implicit large eddy simulation of low-Reynolds-number transitional flow past the SD7003 airfoil. In *40th AIAA Fluid Dynamics Conference*, 2010.

[63] C. Carton De Wiart and K. Hillewaert. DNS and ILES of transitional flows around a SD7003 using a high order discontinuous Galerkin method. In *7th International Conference on Computational Fluid Dynamics, ICCFD 2012*, 2012.

[64] Y. Han and A. Ramesh. CFD simulations of a triangular airfoil for Martian atmosphere in low-Reynolds number compressible flow. 06 2019.

[65] T. Désert, T. Jardin, H. Bézard, and J. M. Moschetta. Numerical predictions of low Reynolds number compressible aerodynamics. *Aerospace Science and Technology*, 92, 2019.

[66] R.M. Hicks, E.M. Murman, and G.N. Vanderplaats. An assessment of airfoil design by numerical optimization. *NASA TM X-3092*, 126, 1974.

[67] R. M. Hicks and P. A. Henne. Wing design by numerical optimization. *Journal of Aircraft*, 15, 1978.

[68] D. E. Goldberg. *Genetic Algorithms in Search, Optimization and Machine Learning*, chapter 2, pages 27–54. Addison-Wesley Longman Publishing Co., Inc., Boston, MA, United States, 1st edition, 1989.

[69] A. Oyama, S. Obayashi, K. Nakahaski, and N. Hirose. Aerodynamic wing optimization via evolutionary algorithms based on structured coding. *Computational Fluid Dynamics Journal*, 8, 2000.

[70] A. Vicini and D. Quagliarella. Inverse and direct airfoil design using a multi-objective genetic algorithm. *AIAA Journal*, 35, 1997.

[71] N. Macro, J. a. Desideri, and S. Lanteri. Multi-objective optimization in CFD by genetic algorithm. *Institut National de Recherche en Informatique et en Automatique (INRIA)*, 1999.

[72] T. L. Holst and T. H. Pulliam. Aerodynamic shape optimization using a real-number-encoded genetic algorithm. In *19th AIAA Applied Aerodynamics Conference*, 2001.

[73] K. C. Giannakoglou. Design of optimal aerodynamic shapes using stochastic optimization methods and computational intelligence, 2002.

[74] O. Polat and I. H. Tuncer. Aerodynamic shape optimization of wind turbine blades using a parallel genetic algorithm. In *Procedia Engineering*, volume 61, 2013.

[75] A. P. Antunes and J. L. F. Azevedo. Studies in aerodynamic optimization based on genetic algorithms. *Journal of Aircraft*, 51, 2014.

[76] A. Boutemedjet, M. Samardžić, L. Rebhi, Z. Rajić, and T. Mouada. UAV aerodynamic design involving genetic algorithm and artificial neural network for wing preliminary computation. *Aerospace Science and Technology*, 84:464–483, 1 2019.

[77] A. Dina, S. Danaila, M. V. Pricop, and I. Bunescu. Using genetic algorithms to optimize airfoils in incompressible regime. *INCAS Bulletin*, 11, 2019.

[78] A. Saleem and M. H. Kim. Aerodynamic performance optimization of an airfoil-based airborne wind turbine using genetic algorithm. *Energy*, 203, 2020.

[79] X. Zhao, Z. Tang, F. Cao, C. Zhu, and J. Periaux. An efficient hybrid evolutionary optimization method coupling cultural algorithm with genetic algorithms and its application to aerodynamic shape design. *Applied Sciences (Switzerland)*, 12, 2022.

[80] T. Yan, H. Chen, J. Fang, and P. Yan. Research on 3D Design of high-load counter-rotating compressor based on aerodynamic optimization and CFD coupling method. *Energies*, 15, 2022.

[81] A. Porta Ko, S. Smidt, R. Schmehl, and M. Mandru. Optimisation of a multi-element airfoil for a fixed-wing airborne wind energy system. *Energies*, 16, 2023.

[82] J. C. Tyacke, Y. Dai, R. Watson, and P. G. Tucker. Design optimisation of labyrinth seals using les. *Mathematical Modelling of Natural Phenomena*, 16, 2021.

[83] Rob Watson and Paul Tucker. Perfectly parallel optimization for cutback trailing edges. *AIAA Journal*, 54, 2016.

[84] Kazufumi Uwatoko, Masahiro Kanazaki, H. Nagai, Koji Fujita, and A. Oyama. Blade Element Theory coupled with CFD applied to optimal design of rotor for Mars exploration helicopter. *AIAA Scitech 2020 Forum*, 1 PartF, 2020.

[85] Masahiko Sugiura, Yasutada Tanabe, Hideaki Sugawara, Keita Kimura, A. Oyama, Makoto Sato, Kota Yoshikawa, Yuta Buto, Masahiro Kanazaki, Yuki Kishi, Daisuke Kikuchi, and Takuma Minajima. Blade shape optimization of Mars helicopter exploring pit craters. *78th Vertical Flight Society Annual Forum and Technology Display, Forum 2022*, 2022.

[86] T. Yamaguchi and M. Anyoji. Numerical study on low-Reynolds compressible flows around Mars helicopter rotor blade airfoil. *Journal of Flow Control, Measurement amp; Visualization*, 11, 2023.

[87] Pengyue Zhao, Xifeng Gao, Bo Zhao, Huan Liu, Jianwei Wu, and Zongquan Deng. Machine Learning assisted prediction of airfoil lift-to-drag characteristics for Mars helicopter. *Aerospace*, 10, 2023.

[88] Henri Fuhrmann. Design optimization of a class of low Reynolds, high Mach number airfoils for use in the Martian atmosphere. *Collection of Technical Papers - AIAA Applied Aerodynamics Conference*, 1, 2005.

[89] Benjamin T. Pipenberg, Matthew T. Keennon, Sara A. Langberg, and Jeremy D. Tyler. Development of the Mars helicopter rotor system. *The Vertical Flight Society - Forum 75: The Future of Vertical Flight - Proceedings of the 75th Annual Forum and Technology Display*, 2019.

[90] J. Fuentes and R. P. Kaluarachchi. Martian RHOVER feasibility study. *53rd AIAA Aerospace Sciences Meeting*, 2015.

[91] D. Escobar, Inderjit Chopra, and A. Datta. Vacuum chamber testing of 1.5 foot diameter Mars rotor. *Proceedings of the AHS International Technical Meeting on Aeromechanics Design for Transformative Vertical Flight 2018*, 2018.

[92] C. Chi, R. Lumba, and A. Datta. Structural design and aeromechanical analysis of a next-generation Mars hexacopter rotor. *77th Annual Vertical Flight Society Forum and Technology Display, Forum 2021: The Future of Vertical Flight*, 2021.

[93] C. Chi, R. Lumba, Yong Su Jung, and A. Datta. Aeromechanical analysis of a next-generation Mars hexacopter rotor. *Journal of Aircraft*, 59, 2022.

[94] R. Lumba, C. Chi, A. Datta, W. Koning, N. Perez Perez, and H. Cummings. Structural design and aeromechanical analysis of unconventional blades for future Mars rotorcraft. *Aeromechanics for Advanced Vertical Flight Technical Meeting 2022*, 2022.

[95] Cuyler Dull, Lauren Wagner, L. Young, and W. Johnson. Hover and forward flight performance modeling of the Ingenuity Mars helicopter. *Aeromechanics for Advanced Vertical Flight Technical Meeting 2022*, 2022.

[96] L. A. Young, Jeff Delaune, W. Johnson, S. Withrow-Maser, H. Cummings, Evgeniy Sklyanskiy, Jacob Izraelevitz, Aaron Schutte, Abigail Fraeman, and Raghav Bhagwat. Design considerations for a Mars highland helicopter. *Accelerating Space Commerce, Exploration, and New Discovery Conference, ASCEND 2020*, 2020.

[97] J. Blank and K. Debmoy. Pymoo: multi-objective optimization in Python. *IEEE Access*, PP:1–1, 04 2020.

[98] H.T. Huynh. A flux reconstruction approach to high-order schemes including discontinuous Galerkin methods. *AIAA Paper 4079*, pages 1–42, 2007.

[99] P. E Vincent, P Castonguay, and A Jameson. A new class of high-order energy stable Flux Reconstruction schemes. *Journal of Scientific Computing*, 47(1):50–72, 2010.

[100] Kopriva D. A. A staggered-grid multidomain spectral method for the compressible Navier–Stokes equations. *Journal of Computational Physics*, 143:125–158, 6 1998.

[101] Sun Y., Wang Z. J., and Liu Y. High-order multidomain spectral difference method for the Navier-Stokes equations on unstructured hexahedral grids. *Communications in Computational Physics*, 2, 2007.

[102] Cem Pekardan and Alina Alexeenko. Rarefaction effects for transonic airfoil flows at low Reynolds numbers. *AIAA Journal*, 56(2), February 2018.

[103] Sighard F. Hoerner. *Fluid-dynamic drag*, chapter Drag at high speeds as affected by viscosity and rarefraction, pages 410–412. Published by the Author, Bakersfield, CA 93390, 1965.

[104] N. Jarrin, S. Benhamadouche, D. Laurence, and R. Prosser. A synthetic-eddy-method for generating inflow conditions for large-eddy simulations. *International Journal of Heat and Fluid Flow*, 27, 2006.

[105] N. Jarrin, R. Prosser, J. C. Uribe, S. Benhamadouche, and D. Laurence. Reconstruction of turbulent fluctuations for hybrid RANS/LES simulations using a Synthetic-Eddy Method. *International Journal of Heat and Fluid Flow*, 30, 2009.

[106] M. Pamiès, P. E. Weiss, E. Garnier, S. Deck, and P. Sagaut. Generation of synthetic turbulent inflow data for large eddy simulation of spatially evolving wall-bounded flows. *Physics of Fluids*, 21, 2009.

[107] F.D. Witherden G. Giangaspero and P.E. Vincent. Synthetic turbulence generation for high-order scale-resolving simulations on unstructured grids. *AIAA Journal*, 60, February 2022.

[108] S.Schmidt and M. Breuer. Source term based synthetic turbulence inflow generator for eddy-resolving predictions of an airfoil flow including a laminar separation bubble. *Computers & Fluids*, 146:1–22, 2017.

[109] M. V. Morkovin. Effects of compressibility on turbulent flows. *Mécanique de la Turbulence*, 367, 1962.

[110] R. Lechner, J. Sesterhenn, and R. Friedrich. Turbulent supersonic channel flow. *Journal of Turbulence*, 2, 2001.

[111] J. E Marsden, L Sirovich, and S. S Antman. *Nodal Discontinuous Galerkin Methods: Algorithms, Analysis, and Applications*, volume 54 of *Texts in Applied Mathematics*. Springer New York, New York, 2008.

[112] Christopher A. Kennedy, Mark H. Carpenter, and R. Michael Lewis. Low-storage, explicit Runge-Kutta schemes for the compressible Navier-Stokes equations. *Applied Numerical Mathematics*, 35(3):177–219, 2000.

[113] P. Vincent, F. Witherden, B. Vermeire, J. S. Park, and A. Iyer. Towards green aviation with Python at Petascale. In *SC '16: Proceedings of the International Conference for High Performance Computing, Networking, Storage and Analysis*, pages 1–11, Nov 2016.

[114] J. S. Park, F. D. Witherden, and P. E. Vincent. High-order implicit large-eddy simulations of flow over a NACA0021 aerofoil. *AIAA Journal*, 55(7), 2017.

[115] Christophe Geuzaine and Jean François Remacle. Gmsh: A 3-D finite element mesh generator with built-in pre- and post-processing facilities. *International Journal for Numerical Methods in Engineering*, 79, 2009.

[116] N. Siinivas and K. Deb. Multi-objective optimization using non-dominated sorting in genetic algorithms. *Evolutionary Computation*, 2:221–248, 1994.

[117] K. Deb, A. Sameer, and T. Meyarivan. A fast elitist non-dominated sorting genetic algorithm for multi-objective optimization NSGA-II. *IEEE Transaction on Evolutionary Compution*, 6:182–197, 2002.

[118] Goldberg D. E. and K. Deb. *A Comparative Analysis of Selection Schemes Used in Genetic Algorithms*, volume 1 of *Foundations of Genetic Algorithms*, pages 69–93. Elsevier, Amsterdam, The Netherlands, 1991.

[119] K. Deb, Karthik Sindhya, and Tatsuya Okabe. Self-adaptive simulated binary crossover for real-parameter optimization. *Proceedings of GECCO 2007: Genetic and Evolutionary Computation Conference*, 2007.

[120] Eckart Zitzler and Lothar Thiele. Multiobjective optimization using evolutionary algorithms — a comparative case study. In *Parallel Problem Solving from Nature — PPSN V*, volume 1498 LNCS, pages 292–301, Berlin, Heidelberg, 1998. Springer Berlin Heidelberg.

[121] Nery Riquelme, Christian Von Lücken, and Benjamin Baran. Performance metrics in multi-objective optimization. *2015 Latin American Computing Conference (CLEI)*, pages 1–11, 2015.

[122] Eckart Zitzler, Dimo Brockhoff, and Lothar Thiele. The hypervolume indicator revisited: On the design of Pareto-compliant indicators via weighted integration. *Lecture Notes in Computer Science*, 4403 LNCS, 2007.

[123] Timothy W. Simpson, Timothy M. Mauery, John J. Korte, and Farrokh Mistree. Comparison of response surface and kriging models for multidisciplinary design optimization. *7th AIAA USAF NASA ISSMO Symposium on Multidisciplinary Analysis and Optimization*, 1998.

[124] L. Caros, O.R.H. Buxton, T. Shigeta, T. Nagata, T. Nonomura, K. Asai, and P.E. Vincent. Direct numerical simulation of flow over a triangular airfoil under Martian conditions. *AIAA Journal*, March 2022.

[125] O.R.H. Buxton, S. Laizet, and B. Ganapathisubramani. The effects of resolution and noise on kinematic features of fine-scale turbulence. *Experiments in Fluids*, 51(5):1417–1437, November 2011.

[126] L. Caros, O.R.H. Buxton, and P.E. Vincent. Optimization of triangular airfoils for Martian helicopters using Direct Numerical Simulations. *Submitted to AIAA Journal*, 2023.

[127] L. Caros, O.R.H. Buxton, and P.E. Vincent. Optimization of non-conventional airfoils for Martian rotorcraft using Direct Numerical Simulations. *11th International Conference on Computational Fluid Dynamics (ICCFD11)*, July 2022.

[128] Michael Bergmann, Christian Morsbach, Graham Ashcroft, and Edmund Kugeler. Statistical error estimation methods for engineering-relevant quantities from scale-resolving simulations. *Journal of Turbomachinery*, 144, 2022.

[129] Charles Mockett, T Knacke, and F Thiele. Detection of initial transient and estimation of statistical error in time - resolved turbulent flow data. *8th International Symposium on Engineering Turbulence Modelling and Measurements - ETMM8*, 2010.

[130] Michael M. Rogers and Robert D. Moser. The three-dimensional evolution of a plane mixing layer: The Kelvin-Helmholtz rollup. *Journal of Fluid Mechanics*, 243:183–226, 1992.

[131] Joshua N.N. Counsil and Kiari Goni Boulama. Low-Reynolds-number aerodynamic performances of the NACA 0012 and Selig-Donovan 7003 airfoils. *Journal of Aircraft*, 50, 2013.

[132] Ilyas Karasu M. Serdar Genc. Numerical study on low Reynolds number flows over an aerofoil. *Journal of Applied Mechanical Engineering*, 02, 2013.

[133] Brian Cabral and Leith Casey Leedom. Imaging vector fields using Line Integral Convolution. *Proceedings of the 20th Annual Conference on Computer Graphics and Interactive Techniques*, page 263–270, 1993.

[134] Nestor V. Queipo, Raphael T. Haftka, Wei Shyy, Tushar Goel, Rajkumar Vaidyanathan, and P. Kevin Tucker. Surrogate-based analysis and optimization. *Progress in Aerospace Sciences*, 41, 2005.

[135] Andy Keane, Alexander Forrester, and Andras Sobester. *Engineering Design via Surrogate Modelling: A Practical Guide*. 2008.

[136] Vishal Raul and Leifur Leifsson. Surrogate-based aerodynamic shape optimization for delaying airfoil dynamic stall using Kriging regression and infill criteria. *Aerospace Science and Technology*, 111:106555, 2021.

[137] Qing Wang and Qijun Zhao. Rotor blade aerodynamic shape optimization based on high-efficient optimization method. *Proceedings of the Institution of Mechanical Engineers, Part G: Journal of Aerospace Engineering*, 234, 2020.

[138] Jiwei Tang, Yu Hu, Bifeng Song, and Hui Yang. Unsteady aerodynamic optimization of airfoil for cycloidal propellers based on surrogate model. *Journal of Aircraft*, 54, 2017.

[139] Zhong Hua Han, Ke Shi Zhang, Jun Liu, and Wen Ping Song. Surrogate-based aerodynamic shape optimization with application to wind turbine airfoils. *51st AIAA Aerospace Sciences Meeting including the New Horizons Forum and Aerospace Exposition 2013*, 2013.

[140] Yu Liang, Xiao Quan Cheng, Zheng Neng Li, and Jin Wu Xiang. Robust multi-objective wing design optimization via CFD approximation model. *Engineering Applications of Computational Fluid Mechanics*, 5, 2011.

[141] Liang Xu, Zhili Tang, and Wenliang Feng. An adaptive searching Kriging surrogate model for aerodynamic optimization. *Journal of Physics: Conference Series*, 1600, 2020.

[142] L. Caros, J. Blank, O.R.H. Buxton, and P.E. Vincent. Comparing strategies for DNS based optimization of airfoils for Martian rotorcraft. *Vertical Flight Society Forum 78*, May 2022.

[143] J. Blank. pydacefit. https://github.com/msu-coinlab/pydacefit, 2019.

[144] Hisao Ishibuchi, Hiroyuki Masuda, Yuki Tanigaki, and Yusuke Nojima. Modified distance calculation in generational distance and inverted generational distance. *Lecture Notes in Computer Science*, 9019, 2015.

[145] J. Blank and K. Deb. Constrained bi-objective surrogate-assisted optimization of problems with heterogeneous evaluation times: Expensive objectives and inexpensive constraints. *Lecture Notes in Computer Science*, 12654 LNCS, 2021.